Cosmic radiation measurements in the southern hemisphere, with the focus on aviation altitudes

MG Mosotho

orcid.org/0000-0003-0669-0869

Thesis accepted in fulfilment of the requirements for the degree *Doctor of Philosophy in Space Physics* at the North-West University

Promoter: Prof RD Strauss

Co-promoter: Prof MJ Kosch

Graduation May 2021

23853786

"Unless you believe, you will not understand."

-St. Aurelius Augustinus Augustine

Abstract

The radiation environment around the Earth is intense and complex. During the dawn of the aviation age in 1903, when the Wright brothers Orville and Wilbur invented, built, and flew the world's first successful aircraft, little was known about atmospheric radiation and its dependence on altitude. In early 1912 Victor Hess discovered that cosmic-ray intensity increases with altitude. The radiation field at and above aviation altitudes differs significantly from the radiation environment on Earth's surface. On the Earth's surface it is dominated by terrestrial radiation which stems from radionuclides in the Earth's crust and secondary by-products produced by cosmic-rays interaction with the Earth's atmosphere. In the atmosphere, the radiation field consists of a complex mixture of charged and neutral secondary particles. However, above the atmosphere, primary galactic cosmic-rays, particles from the Sun, and from the radiation belts around Earth, play a significant role. Hence, the radiation exposure is high at and above the atmosphere, especially over the poles and the South Atlantic Anomaly, because of the orientation of the Earth's geomagnetic field lines. The study of cosmic-ray interaction with the atmosphere is of great importance; such a study can address the essential science concerning long-term human space exploration risks and aviation radiation exposure for flight personnel and passengers. Most important is how the future of aviation is threatened by these increasing levels of radiation at and above the atmosphere. Given that, in the atmosphere, radiation is very high during solar minimum and low during solar maximum conditions (transient solar events can potentially increase atmospheric radiation even during this solar period), measuring radiation levels during these periods both in the atmosphere and on the Earth's surface is absolutely essential. This is also important in the Southern Hemisphere, where little or no such information is available at present.

In this thesis, a portable active dosimetry device based on two silicon semiconductor diodes is assembled, tested, and calibrated. This dosimeter is used to study the dose rate distributions from mid to low latitudes at various altitudes. Field tests on board commercial aircraft within the mixed radiation field at aviation altitudes are successfully performed and important dosimetric quantities calculated. Investigations on whether models currently used to analyze (or predict) radiation exposure of flight personnel are satisfactory will also be discussed and compared to measurements.

As part of the public awareness, a campaign initiated by the North-West University's Centre for Space Research in 2017, a battery powered detector known as HARM is used to monitor atmospheric radiation evolution with altitude from ground-level to aviation altitudes in commercial aircraft or higher altitudes (in principle up to a residual atmosphere of about 2.83 g/cm^2, i.e. $\sim$ 40 km) by means of launching balloons.

Keywords: Aviation radiation dosimetry, absorbed dose, Geiger-Müller counter, silicon detector, active dosimeter, solar activity

Acknowledgements

I would like to thank, in no particular order:

- My supervisors: Prof. R. DT. Strauss and Prof. M. Kosch, for their dedication, guidance, moral support and forever encouraging me throughout this project. I have greatly benefited from them and I am pleased to acknowledge my debt to them.
- Prof. Stephan Böttcher of the *Christian-Albrechts-Universität zu Kiel* for making the RPiRENA design available.
- Mr Corrie Diedericks for technical assistance and tirelessly helping with re-assembling the RPiRENA.
- Ms Hettie Sieberhagen for language editing this work.
- The South African Space Agency (SANSA) and the National Research Foundation of South Africa (NRF) for their financial support.
- Mrs M. P. Sieberhagen, Mrs E. van Rooyen, Mr L. Fransman, and Mrs L. van Wyk from NWU for their help with administration and also Ms Juchelle Ontong from SANSA.
- The physics department for this study opportunity and for their generous support, and providing me with all the necessary things needed to conduct research.
- Matplotlib *Hunter* [2007], all the figures were prepared using this library.
- My parents and parents-in-law for supporting me, also my wife Ncebakazi, for her love and support and above all, for putting a smile on my face whenever the chips were down.

Above all, I would like to thank my heavenly Father, to whom I am eternally grateful for His grace to have allowed me to complete this work. To my pastor Anita Mpofu and my church Christ Embassy (Potchefstroom 2), thank you for putting me in your prayers throughout. May God richly bless you all one-by-one.

Moshe Godfrey Mosotho
Center for Space Research
North-West University
May 2021

Contents

Abstract ii

Acknowledgements iii

Contents iv

Acronyms and Abbreviations vii

1 Introduction 1

2 The Sun-Earth Relationship 3
- 2.1 Introduction . . . 3
- 2.2 The Sun's Features and Solar Activity . . . 4
  - 2.2.1 Sunspots . . . 6
  - 2.2.2 Solar Flares . . . 8
  - 2.2.3 Coronal Mass Ejections . . . 8
- 2.3 Cosmic-rays . . . 9
- 2.4 Charged Particle Propagation in the Geomagnetic Field . . . 11
- 2.5 Atmosphere and Primary Cosmic-ray by-Products . . . 15
- 2.6 Cosmic-ray Observations . . . 17
- 2.7 Summary . . . 22

3 Radiation Dosimetry 23
- 3.1 Dosimetry Instruments . . . 23
- 3.2 Radiation Interaction with Matter . . . 25
  - 3.2.1 Charged Particles Interaction with Matter . . . 26
  - 3.2.2 Neutrons . . . 28
  - 3.2.3 Photons . . . 29
- 3.3 Radiation Protection and Exposure Assessment . . . 31
- 3.4 Basic Dosimetric Concepts and Quantities . . . 33
  - 3.4.1 Absorbed Dose . . . 33
  - 3.4.2 Linear Energy Transfer . . . 34
  - 3.4.3 Quality Factor . . . 35
  - 3.4.4 Dose Equivalent . . . 37
  - 3.4.5 Effective Dose . . . 37
  - 3.4.6 Ambient Dose Equivalent . . . 38
- 3.5 Effects of Ionizing Radiation . . . 38
  - 3.5.1 Stochastic and Deterministic Effects . . . 40

3.6 Summary . . . 41

4 Aviation Radiation Model **42**
4.1 Introduction . . . 42
4.2 The CARI Model . . . 43
4.3 Flight Routes Information . . . 45
4.4 Flight Simulation Settings . . . 46
4.4.1 The Longitude Flight Effect . . . 47
4.4.2 The Latitude Flight Effect . . . 49
4.4.3 The Altitude Flight Effect . . . 51
4.5 Summary . . . 55

5 The High Altitude Radiation Monitor **56**
5.1 Introduction . . . 56
5.2 Background and Motivation . . . 57
5.3 Housing and Electronics . . . 57
5.3.1 Raspberry Pi . . . 59
5.3.2 The $J305\beta$ Geiger-Müller Counter . . . 60
5.3.3 The Raspberry Pi Sense HAT . . . 61
5.4 Measurement on board an Aircraft . . . 61
5.4.1 The First Flight From Johannesburg to Windhoek . . . 62
5.5 Measurement on board a Stratospheric Balloon . . . 64
5.5.1 Launch Permit . . . 65
5.5.2 Payload Tracking . . . 65
5.5.3 Payload Box . . . 66
5.5.4 Flight Trajectory Prediction . . . 67
5.5.5 Electronics Testing and Location Tracker . . . 69
5.5.6 Launch Site . . . 70
5.6 Recovery . . . 71
5.7 Balloon Flight Results . . . 71
5.8 Summary . . . 73

6 The RPiRENA Dosimeter **74**
6.1 Introduction . . . 74
6.2 RPiRENA Historical Background . . . 74
6.3 Silicon PIN Diodes . . . 75
6.4 RPiRENA Housing . . . 77
6.5 Readout Electronics . . . 77
6.5.1 Detection . . . 77
6.5.2 Signal Processing Chain . . . 79
6.5.3 Storage . . . 80
6.6 Low-energy Calibrations: Laboratory Radioactive sources . . . 80
6.6.1 Americium-241 source . . . 82
6.6.2 Caesium-137 source . . . 83
6.6.3 Barium-133 source . . . 84
6.6.4 Bismuth-207 Source . . . 85
6.7 Energy Calibration . . . 86
6.8 Summary . . . 87

7 RPiRENAs Flight Measurements **88**
7.1 Introduction . . . 88
7.2 Measurement on board an Aircraft: RPiRENA . . . 89
7.3 Medium-haul and Long-haul International Flight Measurements . . . 89
7.3.1 Count Rates . . . 91
7.3.2 Energy Deposition Spectra . . . 97
7.4 Linear Energy Transfer Spectra and Quality Factor . . . 99
7.4.1 Dose Rates . . . 100
7.4.2 Directionality Measurements . . . 102
7.5 Short-haul Flight Measurements . . . 104
7.6 Cutoff Rigidity and Altitude Dependence . . . 105
7.7 Summary . . . 107

8 Summary, Conclusions, and Outlook **108**

A Approximate Analytical Solutions of the Parker Transport Equation **112**
A.1 Parker's Transport Equation . . . 112
A.2 Local Interstellar Spectrum . . . 115
A.2.1 Top-of-Atmosphere Parameterization: Spacecraft Data . . . 115
A.3 Modulation Parameters: Spacecrafts Data . . . 119
A.3.1 Time Dependent Modulation Parameters . . . 119
A.3.2 Time Dependence Diffusion Coefficients . . . 121
A.3.3 Rigidity Dependent Diffusion Coefficients . . . 123
A.4 Modulation Parameters: Neutron Monitor Data . . . 123
A.5 Summary . . . 128

B Portable Electronic Devices **130**

C Geometric Factor and Effective Thickness **133**
C.1 Single Diode . . . 133
C.2 Telescope Diode . . . 135
C.3 Effective Diode Thickness . . . 135

Bibliography **137**

Acronyms and Abbreviations

β	The Ratio Of Particle Speed To The Speed Of Light ($\beta \equiv v/c$)
ISN	International Sunspot Number
eV	Electron Volt[1]
GCR	Galactic Cosmic-Ray
GLE	Ground Level Enhancement
CME	Coronal Mass Ejections
SEP	Solar Energetic Particle
SN	Sunspot Number
NM	Neutron Monitor
PIN	Positive-Intrinsic-Negative
P_c	Cutoff Rigidity
TOA	Top Of The Atmosphere
FF	Force-Field
CD	Convection-Diffusion
SD	Silicon Diode
$\mathcal{E}_{\mathcal{DR}}$	Effective Dose Rate
PED	Portable Electronic Devices
LIS	Local Interstellar Spectra
HARM	High Altitude Radiation Monitor
ICRP	International Commission On Radiological Protection
CSTool	Computer Software Tools
c	Speed Of Light
T	Kinetic Energy Per Nucleus
E_0	Rest Mass Energy
RPiRENA	Raspberry Pi and Read-out Electronics For Nuclear Applications

[1] Defined to be the energy gained by a particle with the elemental charge when accelerated by a potential difference of 1 V, i.e. 1 eV $= 1.602 \times 10^{-19}$ J.

CHAPTER 1

Introduction

Radiation at aviation altitudes is unavoidable. This radiation consists of high energy subatomic particles which comes from two sources, i.e. (1) galactic cosmic-rays which originate from outer space and (2) solar energetic particle which are occasionally released from the Sun. When these particles interact with the Earth's atmosphere they produce high energy secondary particles. During commercial aircraft flights, these primary and secondary high energy particles interact with aircraft components to further produce more high energy secondary particles. Scientists have been assessing the exposure of crew members and commercial aircraft passengers to ionizing radiation ever since it was identified as a health risk in the 1920s. Since then, progress has been made over the years in measuring and monitoring radiation at flight altitudes.

When exposed to radiation from these highly energetic particles, the time-dependent amount of energy absorbed by our bodies, referred to as the dose rate, can be harmful because it can damage our DNA make-up. Even though our bodies are capable of repairing these damages, errors can occur during the repair processes, leading to a mutation of cells that can potentially result in cancer. The amount of damage when exposed to ionising radiation is dependent on the duration of the flight and geographic position at the time of exposure, as well as the period of solar activity. Post-exposure effects and radiation risk estimation for commercial aircrafts is still work in progress and therefore measurements of these secondaries can help us improve our knowledge and understanding.

To emphasize the importance of obtaining the high-altitude radiation measurements during commercial aircraft flights, a portable and light-weight dosimeter based on two silicon semiconductor diodes, has been assembled.[1] The assembled dosimeter prototype is similar to that assembled in the Ph.D. thesis of Birgit Ritter's Mobile Dosimetric Telescope project.[2] The

[1] http://www.ieap.uni-kiel.de/et/people/stephan/RPiRENA/
[2] https://nbn-resolving.org/urn:nbn:de:gbv:8-diss-131340

aim of re-assembling this kind of dosimeter for this work is to characterize the radiation environment in the Southern Hemisphere at aviation altitudes due to its capability of measuring routinely operational dosimetric quantities.

To measure radiation, at least up to the Regener-Pfotzer maximum, a small, portable and lightweight instrument was assembled, known as HARM.[3] This instrument uses a Geiger-Müller counter, capable of detecting ionising radiation.

As part of the South African National Space Agency's (SANSAs)[4,5] vision to provide space weather warnings as recommended by the International Civil Aviation Organization (ICAO),[6] the work presented in this thesis is an effort to further improve pre-existing measurements essential for calculations or estimation of dosimetric quantities at aviation altitudes with focus on the Southern Hemisphere. Also, shown in this work, is how the application of pre-existing models to describe the radiation fields dosimetric quantities compares with measurements.

This thesis is structured as follows: Cosmic-rays, the Sun-Earth relationship, propagation of particles in the Earth's magnetic field, production of secondary particles in the atmosphere to instruments capable of detecting these particles are discussed in Chapter 2, while Chapters 3 and 4 introduce radiation dosimetry and aviation radiation models used for this work, respectively. The High Altitude Radiation Monitor programme as well as its progress up to date is discussed in Chapter 5. The assembling of the RPiRENA dosimeter, testing and energy calibration are presented in Chapter 6. The flight tests of the dosimeter on long-haul flights and short-haul measurements on board an aircraft, and model estimates are presented in Chapter 7. A brief summary of the main results is given and conclusions drawn from these results, as well as possible avenues of future research are discussed in Chapter 8. The appendices provide additional information omitted from the chapters and results deemed unnecessary for inclusion in chapters. Aspects of this work were presented at:

- The South African Institute of Physics (SAIP) conference, hosted in Bloemfontein, South Africa, from 25$^{\text{th}}$ to 29$^{\text{th}}$ June 2018.
- The South African National Antarctic Programme (SANAP) Symposium, hosted in Hermanus, South Africa, from 13$^{\text{th}}$ to 16$^{\text{th}}$ August 2018.
- The Solar and Heliospheric Observatory (SOHO)/Solar Terrestrial Relations Observatory (STEREO) workshop, hosted in Kiel, Germany, from 11$^{\text{th}}$ to 14$^{\text{th}}$ June 2019.
- The International Space Weather Camp (ISWC), hosted in Hermanus, South Africa, from 30$^{\text{th}}$ June to 13$^{\text{th}}$ July 2019.

[3] HARM is an acronym meaning High Altitude Radiation Monitor
[4] https://www.sansa.org.za/
[5] https://tinyurl.com/y29ykjv7
[6] https://www.icao.int/Pages/default.aspx

CHAPTER 2

The Sun-Earth Relationship

2.1 Introduction

In this and the following chapters, the necessary background in order to understand the essential science concerning aviation radiation exposure for commercial personnel and passengers is discussed. The Sun is the source of energy for life on Earth and its influence extends throughout the entire heliosphere by a continuous outward expansion of the Sun's coronal magnetized plasma, known as the solar wind, and through photons which provide ionization, heat and light.

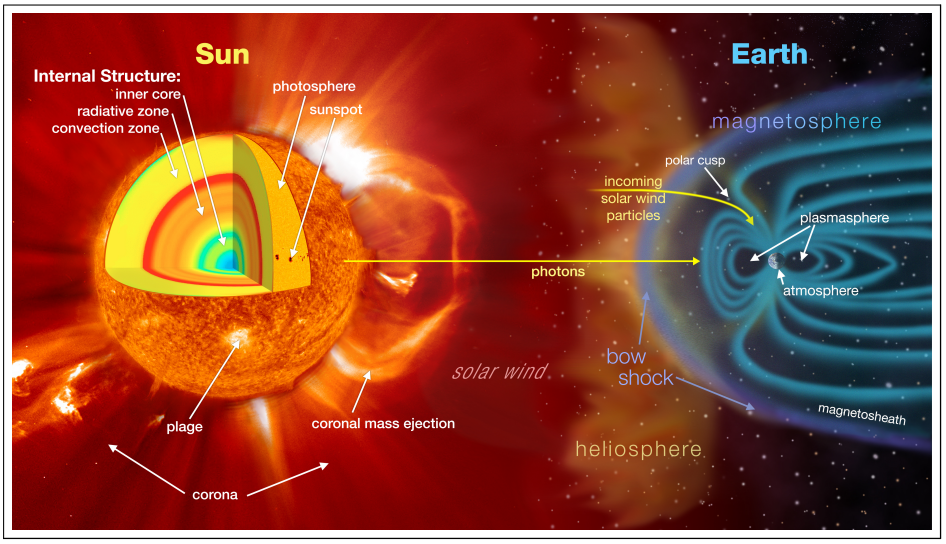

FIGURE 2.1: Different features observed on the Sun and Earth. Image credit: NASA's Goddard Space Flight Center (https://svs.gsfc.nasa.gov/30481).

Figure 2.1, demonstrates a phenomenon known as the Sun-Earth connection. The first step of understanding of the Sun-Earth connection was made by Edmund Halley following a spectacular natural light display in the sky known as the aurora (see, *Halley* [1692] for insights) in

Europe in March 1716. To illustrate the Sun-Earth connection, space weather can be classified into four basic parts, i.e. [1] solar flares and [2] coronal mass ejections, which both can erupt in any direction, but if released it the direction of Earth, they will continue in that direction, "plowing" right through the [3] high speed magnetized solar wind which potentially interacts with the Earth's magnetic field. [4] Solar energetic particles released by shocks form at the front of coronal mass ejections, and through the reconnecting magnetic field in solar flares, follow the magnetic field lines and result in impacts at Earth; this kind of event is called a Sun-Earth connection event. The term space weather broadly describes solar events and conditions at the Earth's magnetic field (and upper atmosphere) that can disrupt the reliability and performance (or damage in extreme cases) of space-borne, aviation, and ground-based modern technological systems, see *Baker* [1998], *Hanslmeier* [2002], *Eastwood* [2008], *Cade III and Chan-Park* [2015], *Hands et al.* [2018], *Zheng et al.* [2019], *Hapgood* [2019], and compromise the health of the Earthly inhabitants [*Hellweg and Baumstark-Khan*, 2007, *Seedhouse*, 2018]. Also, space weather is a serious concern for manned space missions to Mars (see, *Foullon et al.* [2005], *Kühl et al.* [2017], *Hassler et al.* [2018], *Guo et al.* [2019]). Space weather is now recognized as a world-wide concern (*Mann et al.* [2018] and references therein).

This chapter commences with an overview on the Sun. Subsequently discussed in this chapter is how the Sun's coronal magnetized plasma and sporadic transient eruptions in the solar atmosphere can significantly alter the radiation levels in the Earth's atmosphere at aviation altitudes which can potentially become hazardous for aircraft electronics, flight personnel, and passengers, as well as the impact of these solar events at ground-level.

2.2 The Sun's Features and Solar Activity

The nearest star at 1 astronomical unit (AU) away from the Earth is the Sun. The region of space influenced by this star is known as the heliosphere. This star is not a perfect sphere, but oblate as a result of solar rotation. The Sun's rotation rate inside the heliosphere steadily declines from the solar equator to the poles and due to this, its rotation takes about 25 days at the equator and about 36 days towards the poles [*Bartusiak*, 1994]. As seen from Figure 2.1, the Sun can be divided mainly into different regions, enumerated as $1-5$, i.e. the core, the radiative zone, the convection zone, the photosphere and the corona: [1] The core is the innermost region of the Sun and its energy and heat production takes place in this region. About half of the solar mass is contained in this region and its radius is one fourth of the solar radius [*Castellani et al.*, 1997, *Koskinen*, 2011]. [2] The region outside core of the Sun is known as the radiative zone. In this region, the energy transfer mechanism from the core is by

gamma-ray diffusion. This region extends from about 0.25 to 0.72 solar radii [*Koskinen*, 2011]. [3] The convection zone is above the radiative zone. This region extends from about 0.25 solar radii to the surface of the Sun. Throughout this zone, energy is transferred to the solar surface by convection [*Koskinen*, 2011]. [4] The surface of the Sun is called the photosphere, which is about 500 km thick. The temperature at an altitude less than 500 km is greater than that at an altitude of about 500 km. At the bottom of the photosphere, its temperature is about 6600 K and at an altitude of about 500 km the temperature is about 4300 K [*Koskinen*, 2011]. [5] The solar material consists mostly of ionised matter known as plasma. The extended plasma and the uppermost atmosphere of the Sun is called the corona. Compared to the photosphere, the corona is about 10^6 times less bright than photosphere. As a result of this, the corona can only be seen during a total solar eclipse.[1] Its temperature is higher than that of the photosphere about (10^6 K) and the outward expansion of the Sun's coronal magnetized plasma extends into the interplanetary space where it becomes the solar wind.

The existence of the solar wind came from the study of *Biermann* [1951, 1957] based on comet tail orientation. Biermann argued that the ion tails of comets passing close by the Sun always point radially away from the Sun, and that such a phenomenon could not result from solar radiation pressure. The name "solar wind" as we know it nowadays was introduced by Eugene Parker in the late 1950s when he identified the solar wind as a supersonic flow of plasma in heliosphere [*Parker*, 1958c]. The supersonic solar wind was later confirmed by in-situ observations by different spacecraft. The solar wind was directly observed in the heliosphere for the first time by Soviet spacecrafts Lunas 2 and 3 in 1959 and by Venera I in 1960 [*Verigin and Axford*, 2000] and has been the object of study ever since. Post confirmation of the existence of the solar wind by the Lunas and Venera spacecrafts, *Parker* [1963] showed that the solar corona could not be in static equilibrium and had to expand, at supersonic speeds. Due to the fact that the solar wind originates from the solar coronal, its composition is very similar, mainly containing ionised hydrogen (protons), a small percentage of fully ionised helium (alpha particles) and are traces of fully or partially ionised heavier elements and atomic nuclei [*Galvin et al.*, 1996, *Feldman et al.*, 1998, *Wurz*, 2005, *Bochsler*, 2008].

The Sun's magnetic fields were first observed in sunspots by *Hale* [1908]. Insides the heliosphere, the dark regions of the coronal holes give rise to the interplanetary magnetic fields (discussed later in section 2.2.1), which is frozen into the solar wind, that extends outward from the photosphere to the boundary of the heliosphere known as the local interstellar medium. This field is weak compared to other astrophysical bodies, but it extends over the whole heliosphere.

[1] https://www.nasa.gov/eclipse

2.2.1 Sunspots

Dark, visible and "planet-sized" areas of irregular shapes on the photosphere are known as sunspots. Nowadays, it is known that these sunspots occur as a result of solar magnetic flux tubes piercing the photosphere; an effect described by *Parker* [1955] and known as magnetic buoyancy. The less dark surrounding region on the photosphere enclosing the umbra is called penumbra. The lifetime of a sunspot is typically several days to about a week, although larger ones may last for several weeks to about a month. Sunspots usually originate as a pair, with one sunspot having a positive (or north) magnetic field while the other one will have a negative (or south) magnetic field [*Moore and Rabin*, 1985, *Baumann and Solanki*, 2005]. Due to the direction of solar rotation, all the leading sunspots groups in the northern hemisphere tends to have the same polarity, while those in the southern hemisphere have an opposite polarity with respect to those in the northern hemisphere.

The temperature in the sunspot umbra, i.e. the dark central region of sunspots, is about 3700 K compared to the surrounding temperature of the photosphere which is about 6000 K. Sunspots first form at mid-latitudes and later move towards the solar equator. When these sunspots fade, sunspots of the new cycle start appearing at mid-latitudes. The early historical records of "naked-eye" observation of sunspots dates back over 2000 years ago from Asia [*Clark and Stephenson*, 1978, *Wittmann and Xu Zhentao*, 1988]. To the rest of the world, the existence of sunspots came post the invention of European telescopes, publicly credited to Hans Lippershey in 1608, Italy. The discovery of sunspots in the telescope era was and still an ongoing debate, with many observers (including undocumented records) claiming to have been the first to record sunspots. The most notable observers are Simon Marius, Galileo Galileo, Thomas Harriot, Johannes Fabricius and Christoph Scheiner; see *Neuhaeuser and Neuhaeuser* [2016] for more information.

A representation of sunspots numbers with time can illustrate their temporal behaviour. The discovery of the sunspots fluctuations forming a cycle remained hidden until the early 19th century. This was reported in Astronomische Nachrichten by Heinrich Schwabe, showing the yearly number of sunspots visible on the photosphere as sunspot groups over the previous $\sim$ 18 years [*Schwabe*, 1844]. The cyclic appearance of sunspots, known as solar activity, was discovered by Schwabe after he noticed a periodic variation in the average number of sunspots. The cyclic form is assumed to be the result of the solar differential rotation and the related internal solar dynamo [*Babcock*, 1961, *Schwadron et al.*, 2008].

Since the 1980s, and continuing through the present, sunspot numbers are widely used in space science. Prior to 1885, the sunspot numbers representation, however, widely differed. In 1848

Rudolph Wolf developed what nowadays is known as the "international sunspot numbers" (ISN) by counting the number of individual and group sunspots recorded by various observers and extended the records to previous years [*Wolf*, 1850, *Wolf*, 1856, *Wolf*, 1861]. In the late 1990s, Hoyt and Schatten developed a new reconstruction of solar activity from sunspot observations known as the group sunspot number [*Hoyt and Schatten*, 1998]. Nowadays sunspots time series form a direct record used to retrace the long-term evolution of the solar cycles and probably their long-term influence on the Earth's environment. In this work, for demonstration, the ISN is used. The up-to-date datasets are available at daily to yearly scale from 1818 and is maintained and updated by the Solar Influence Data Analysis Center (SIDC).[2] The SIDC is a department of the Royal Observatory of Belgium. This ISN uses a weighted average of many observers from single, primary to tertiary observers, while the weighted average is tied to the primary observer.

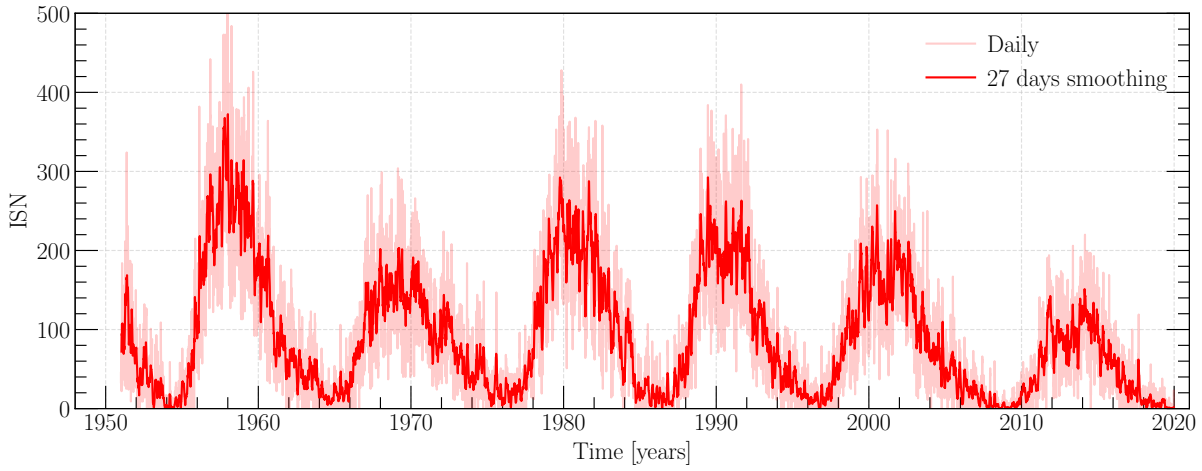

FIGURE 2.2: International sunspot number (ISN) record from early 1950s to early 2020. The original daily time resolution of the ISN is shown in light colour, while the 27 days moving averages are shown in dark colour. Data source: http://www.sidc.oma.be/silso/.

Figure 2.2 shows a record of the sunspot numbers from early 1950s to early 2020. The fading red colour shows the daily sunspot numbers, while the dark red colour shows the 27 days simple moving average data. From the figure, a peak in the sunspot count is called a solar maximum period and the time when few sunspots appear is called a solar minimum period. During this period, coronal holes are randomly scattered on the photosphere, while during solar minimum periods they are mainly found at the polar regions. When comparing sunspot cycles, they are asymmetric with respect to their maxima [*Waldmeier*, 1935, 1939]. The time elapsed from maximum down to minimum is almost always longer than the elapsed time from minimum up to maximum. From the figure, it is clear that solar cycles vary in length, shape and amplitude as illustrated. Also, these sunspot numbers show that since $\sim$ 1980 the solar maximum amplitude has been decreasing, giving an indication that the next solar maximum

[2] http://www.sidc.oma.be/silso/

might potentially be lower than the previous solar maxima since the 1950s. An informative review on the Sun, the long-term behaviour of the solar activity, and its cycle are given by *Hathaway* [2010], *Solanki* [2003], *Clette et al.* [2015], *Vaquero* [2007], *Usoskin* [2017].

2.2.2 Solar Flares

Solar activity can manifests itself as many different phenomena apart from the Schwabe sunspot cycle including also solar flares (and the possible subsequent coronal mass ejections) vary on several distinct time scales. Solar flare dynamics, similar to sunspots, also change approximately every 11 years, from minimum solar activity periods (where there are few or no flares during the period), leading to a period of maximum solar activity (where these activities occur more of frequently). A solar flare is an explosive eruption and the most powerful magnetic event on the Sun, which can potentially release $\sim 10^{25}$ J (6.24×10^{13} MeV) of energy on a time scale ranging from several tens of seconds to several tens of minutes [*Gordovskyy et al.*, 2019]. Solar flares impact Earth only when they occur on the side of the Sun facing Earth.

Carrington [1859] and *Hodgson* [1859] reported the first observations of a solar flare from white light observations on September 1, 1859. While observing the Sun; projected onto a viewing screen, Carrington noticed a brightening that lasted for about 5 minutes. Hodgson also noted a nearly simultaneous magnetic disturbance. Flares can be divided into two classes namely impulsive and gradual. "Gradual" events are large flares which occur high in the corona. These flares produce long duration soft and hard X-rays and gamma rays. However, small "impulsive" events relatively occur on the lower corona and produce radiation of short duration [*Miller*, 1998, *Hudson*, 2011].

2.2.3 Coronal Mass Ejections

In the early 1970s, coronal mass ejections (CMEs), were discovered through measurements obtained from the spacecraft observations OSO 7 [*Tousey*, 1973] and from Skylab [*MacQueen et al.*, 1974]. CMEs are often accompanied by solar flares, but their existence does not come about as a result of the solar flares because they can occur in their absence. Compared to solar flares, CMEs are extremely large clouds of plasma which erupt from the Sun and appear as bright loops moving away from the Sun as shown in Figure 2.1. CME driven shocks accelerate charged particles from close to the Sun and in the interplanetary medium. Far away from the Sun, they are called interplanetary CMEs (ICMEs) (see *Klein and Burlaga* [1982], *Huttunen et al.* [2005], *Manchester et al.* [2017], *Richardson and Cane* [2010]). One possible driver of a CMEs is a flux rope, which in principle it can be identified with a magnetic cloud in the

ICME structure [*Cheng et al.*, 2013, *Grechnev et al.*, 2019]. These magnetic clouds are used to characterize the ICME with a specific configuration in which the magnetic field average is lower than the magnetic field strength [*Grechnev et al.*, 2019]. The ability of flux ropes to drive CMEs have been shown theoretically [*Anzer*, 1978, *Gibson and Low*, 1998, *Chen*, 2017]. CMEs occur on a time scale ranging from minutes to days. These CMEs are responsible for dumping large quantities of mass ($\sim 10^{12} - 10^{13}$ kg) from the solar corona [*Webb and Howard*, 2012].

2.3 Cosmic-rays

Daily exposure to cosmic-rays and background radiation from the Earth's surface is a natural part of the environment in which the Earthly inhabitants live. Cosmic-rays, contrary to what may be implicated, are not "rays[3]" from the cosmos,[4] but are broadly defined as highly energetic, non-thermal and charged sub-atomic particles capable of ionizing matter as they propagate through at speeds close to the speed of light. Charles de Coulomb in 1785 recognized the presence of an ionizing radiation at the Earth's surface [*Coulomb*, 1785]. For more than half a century after this discovery, the conclusion that radioactivity mostly originate from the Earth's surface was questioned by many. One in particular, Domenico Pacini, compared the rate of ionization at sea-level (and deep in the sea), on ground-level, on iron towers, and on mountains. After Pacini's experiments, it was gradually and clearly recognized that the source that causes air to ionize was not from the Earth's surface. In February 1912, he (Pacini) concluded that "*a sizeable cause of ionization exists in the atmosphere, originating from penetrating radiation, independent of the direct action of radioactive substances in the soil*" [*Pacini*, 1912]. Being aware of Pacini's work (see *De Angelis* [2011], *Carlson and De Angelis* [2011]), Victor Hess conducted a series of balloon flights from 1911 and discovered that ionisation rates increased with increasing altitude. Hess obtained his measurements with an electroscope carried on a hydrogen filled balloon. In August 1912, Hess observed that at an altitude about 5 km (i.e. $\sim 550.85\ g/cm^2$) above the ground the measured rate was more than twice the value on Earth's surface [*Hess*, 1912, 2018]. Based on these observations, Hess concluded that this high altitude radiation (or Höhenstrahlung, a term he coined after the 1912 flights) which nowadays is called cosmic-rays (courtesy of Robert Millikan in 1925), was originating from a source outside the Earth's atmosphere. For this discovery, Hess was awarded the Nobel Prize in December 1936.

After Hess' discovery, all balloons (and subsequent satellite and spacecraft missions) equipped with particle detectors confirmed his claims and more discoveries on cosmic-rays were made

[3] https://www.dictionary.com/browse/ray?s=t
[4] https://www.dictionary.com/browse/cosmos?s=t

soon after. In the 1930s, *Clay* made measurements of the Earth's magnetic latitude effect, and coincidence measurements by *Bothe and Kolhörster* [1929], using two Geiger-Müller counters, uncovered that this ionizing radiation consisted mainly of charged particles. In 1934 Bruno Rossi found that devices located in different positions could record the cosmic-ray events simultaneously [*Rossi*, 1933]. This experiment was crucial for the discovery and study of extensive air showers, see *Auger et al.* [1939b,a]. Measurements obtained in the 1940s using photographic plates and cloud chambers carried along during stratospheric balloon flights pointed out that these charged particles mainly consist of relativistic protons and with a fraction of heavier nuclei [*Schein et al.*, 1941]. For the early history of cosmic particles and the timeline of these discoveries, see *de Angelis* [2014], *Walter and Wolfendale* [2012].

Cosmic-rays originate from two well-known sources, i.e. those that originate from within the heliosphere and those from outside the heliosphere. Within the heliosphere, four different cosmic-rays populations can be identified. The particle populations relevant for this work are:

1. Galactic cosmic-rays (GCRs): This population of energetic particles come from outside the heliosphere. These energetic particles are believed to be accelerated during supernova explosions (and pulsars, neutron stars, and other high energy, yet-to-be-discovered sources) and blast waves are responsible for the acceleration (see *Jones and Ellison* [1991]). These supernova blast wave origins were first inferred by *Krymskii* [1977] and *Axford et al.* [1977], while experimental evidence of these blast waves was discovered by *Koyama et al.* [1995] and confirmed by *Tanimori et al.* [1998]. These particle are isotropic (close to the Earth's environment), with energies that range up to 10^{20} eV. These particles consist of $\sim 2\%$ electrons and positrons and $\sim 98\%$ fully ionised nuclei. The nucleus component is composed of $\sim 1\%$ heavier nuclei, $\sim 9\%$ helium and $\sim 90\%$ protons [*Simpson*, 1983, *Gaisser et al.*, 2016]. Above 10^{20} eV, particles are considered as extragalactic cosmic-rays which originate from extragalactic sources [*Schlaepfer*, 2003, *Aharonian et al.*, 2011, *Bykov et al.*, 2018].
2. Solar energetic particles (SEPs): This particle population originates from the Sun. According to *Reames* [1999] "*solar energetic particles* (SEPs) *are accelerated in coronal mass ejections, solar flares, or at interplanetary shocks from close to the Sun*". SEPs, similar to the solar wind plasma, has a composition close to that of the corona. They are observed only occasionally at Earth (usually only for several hours) mainly during maximum solar activity periods, where extreme SEP events can potentially result in an enhanced radiation field. The SEP events are rarely observed reaching high energies of about 1 GeV for protons and about 100 MeV for electrons [*Forbush*, 1946, *Hathaway and Suess*, 2008, *Cliver*, 2009]. Above these energies, secondary particles can reach ground-level to produce a Ground-level enhancement (GLE).

The magnetized solar plasma plays a major role in the transport of cosmic-rays in the heliosphere [*Parker*, 1965]. Inside the heliosphere, as a result of the radially expanding solar wind, cosmic-rays experience changes in their intensities with time as a function of position and energy. This process is known as cosmic-ray modulation [*Parker*, 1965, *Caballero-Lopez and Moraal*, 2004]. The analysis of these cosmic-ray intensity variations is important for understanding not only their modulation processes and acceleration, but also the essential science related to both aviation radiation exposure for commercial personnel and passengers.

2.4 Charged Particle Propagation in the Geomagnetic Field

The Earth's magnetic field (also known as the geomagnetic field or magnetosphere) has a larger effect than the Sun's magnetic field on cosmic-rays approaching the Earth's atmosphere. This field is roughly represented by a not so perfect magnetic dipole. The boundary shape of this field is determined by a radial expansion from the solar corona. Inside the geomagnetic field, the magnetic field dominates, while outside the geomagnetic field, the solar wind is the controlling energy mechanism. The magnetopause around the Earth is in the form of an elongated teardrop with a long tail pointed away from the Sun. Figure 2.1 shows a version of the geomagnetic field. Depending on the particles' rigidity, angle of incidence, the geomagnetic latitude, and altitude of the entry point, they can either penetrate or diffuse through the geomagnetic field, or can get deflected, while some can get trapped in the geomagnetic field lines, thus constituting regions with high radiation fields known as the Van Allen belts [*van Allen et al.*, 1958, *van Allen et al.*, 1959a,b, *Stern*, 1996, *Kimigis*, 2014, *Bakhtiyarov*, 2015].

The so-called rigidity, P, of the particle is described as

$$\mathrm{P} = \frac{pc}{q} = \frac{mvc}{Ze}, \tag{2.1}$$

where

$$p = m\mathbf{v} = \frac{m_0\mathbf{v}}{\sqrt{1 - v^2/c^2}}, \tag{2.2}$$

is the particle's momentum. From the equation, $q = Ze$ is the charge, $v(= |\mathbf{v}|)$ is the speed, m is the relativistic mass, m_0 the rest-mass and c the speed of light in a vacuum. For a relativistic particle, total energy of particles, Ep, in terms of momentum is given by

$$\mathrm{E}p^2 = (\ \mathrm{T}p^2 + \ \mathrm{E}_0^2) = p^2c^2 + m_0^2c^4, \tag{2.3}$$

where $\mathrm{T}p$ is the total kinetic energy of particles and E_0 (i.e. $\mathrm{E}_0 = 0.938$ GeV, $\mathrm{E}_0 = 0.00511$ GeV and $\mathrm{E}_0 = 0.93185$ GeV for protons, electrons and helium) is their rest-mass energy.

Assuming that A represents the number of nucleons in the particle (i.e. the mass number), T is the kinetic energy per nucleon and E is the total energy per nucleon, therefore, the total energy per particle can be written as

$$\mathrm{A}^2\ \mathrm{E}^2 = (\ \mathrm{A}\ \mathrm{T} + \ \mathrm{A}\ \mathrm{E}_0)^2 = \ \mathrm{P}^2(Ze)^2 + \ \mathrm{A}^2\ \mathrm{E}_0^2, \tag{2.4}$$

where the A/Ze ratio is 1/1, 2/1 and 1/1 for protons, helium and electrons, respectively. For relativistic particles, the kinetic energy per nucleon can therefore be written as

$$\mathrm{T} = \left(\frac{Ze}{\mathrm{A}}\right)^2 \sqrt{\mathrm{P}^2 + \ \mathrm{E}_0^2} - \ \mathrm{E}_0, \tag{2.5}$$

or rigidity can be written with respect to kinetic energy per nucleon as

$$\mathrm{P} = \left(\frac{\mathrm{A}}{Ze}\right) \sqrt{\mathrm{T}(\ \mathrm{T} + 2\ \mathrm{E}_0)}. \tag{2.6}$$

Equation 2.6 and Figure 2.3 describe the relationship between rigidity and kinetic energy per nucleon. Here P is the rigidity in GV, and the cosmic-ray has electric charge Ze, atomic mass A, and the rest-mass energy E_0 and kinetic energy T are units of GeV/nucleon.

Figure 2.3, shows that for the same kinetic energy per nucleon, a helium cosmic-ray has about two times the rigidity of a proton with the same kinetic energy per nucleon. This implies that protons are more likely to be deflected by the geomagnetic field than helium and may not penetrate the geomagnetic field more easily compared to a helium particle of the same kinetic energy per nucleon.

In a geocentric dipole field there is a "cutoff rigidity", corresponding to each location (i.e. geomagnetic latitude, $\mathrm{G_L}$) and direction of arrival (i.e. angle of incidence, θ) for particles [*Störmer*, 1955], analytically this is expressed as

$$\mathrm{P_c} = \frac{M}{r_e^2} \frac{\cos^2(\ \mathrm{G_L})}{\left[\sqrt{(1 + \cos(\theta)\cos^3(\ \mathrm{G_L})} + 1\right]^2}, \tag{2.7}$$

where M represents the dipole moment, r_e the distance from the dipole center (in units of Earth radii) and θ is the angle of incidence. The ratio M/r_e^2 is approximated to 59.6 GV. For cosmic-rays arriving at the top of the atmosphere (TOA) from the vertical direction, with $\theta = 90°$, Equation 2.7 is approximated to

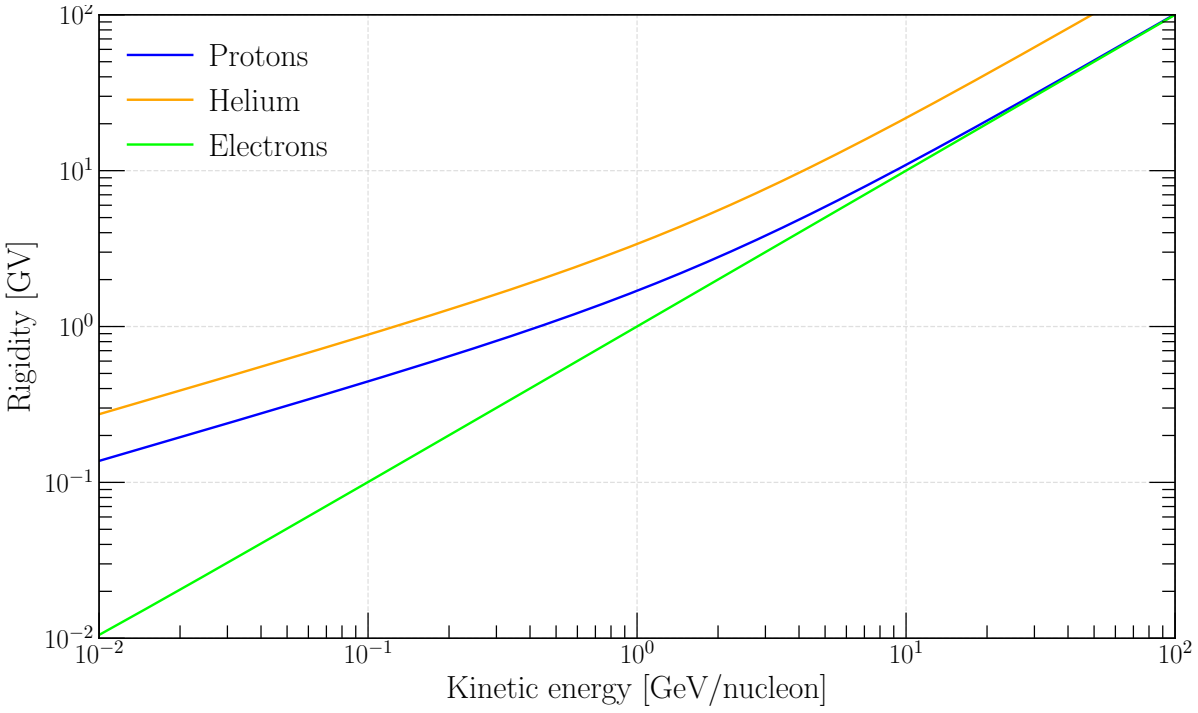

FIGURE 2.3: Relationship between rigidity and energy per nucleon, determined from Equation 2.6.

$$\mathrm{P_c} = \mathrm{P_0}\frac{\cos^4(\mathrm{G_L})}{r_e^2}, \tag{2.8}$$

where $\mathrm{P_0} = 14.9$ GV and $\mathrm{G_L}$ is the geomagnetic latitude in unit of radians. The parameter r_e is the distance from the Earth's dipole center in unit of Earth radii given by

$$r_e = \left(\frac{1}{a}\right)\left(\frac{a_0}{\sqrt{(1 - F^2\cos(\mathrm{G_L})}} + a_1\right), \tag{2.9}$$

where $a = 6371.2$ km is the average radius of the Earth, $a_0 = 6356.9$ km is the minimum polar radius of the Earth and $a_1 = 6.725 \times 10^{-3}$ km is the eccentricity. The parameter F is the altitude above the Earth's surface.

The term "vertical cutoff rigidity, $\mathrm{P_c}$" is described as the minimum rigidity a vertically incident particle can have and still reach a given altitude. Equation 2.8 is widely used, but it does not take into account the field geometry. In addition, the Earth's magnetic field configuration is much more complex than a simple dipole. For cosmic-ray modelling, $\mathrm{P_c}$ describing both quiet and very disturbed geomagnetic conditions is mostly used. Equations 2.7 and 2.8 do not account for these conditions, hence they were modified to take into account a geomagnetic activity parameter described by the planetary Kp index.[5] Kp is a common index used to indicate the severity of the global magnetic disturbances in near Earth space. The values of

[5] https://omniweb.gsfc.nasa.gov/form/dx1.html

the Kp range from 0 (very quiet geomagnetic storm) to 9 (very disturbed geomagnetic storm). A disturbed geomagnetic field can potentially lead to a significant shift in P_c, see *Smart* [2003], which in turn can potentially lead to more particles detected at lower altitudes. *Al Anid et al.* [2009] developed an analytical approximation for P_c to account for any ongoing geomagnetic disturbance based on the Kp index [*Al Anid et al.*, 2009, *Al Anid*, 2012]. For Kp index ≥ 5 (during a geomagnetic storm), this analytical approximation is given as

$$P_c = 0.5\left(1 + vP_c - 0.54e^{(-_v P_c/2.9)}\right). \tag{2.10}$$

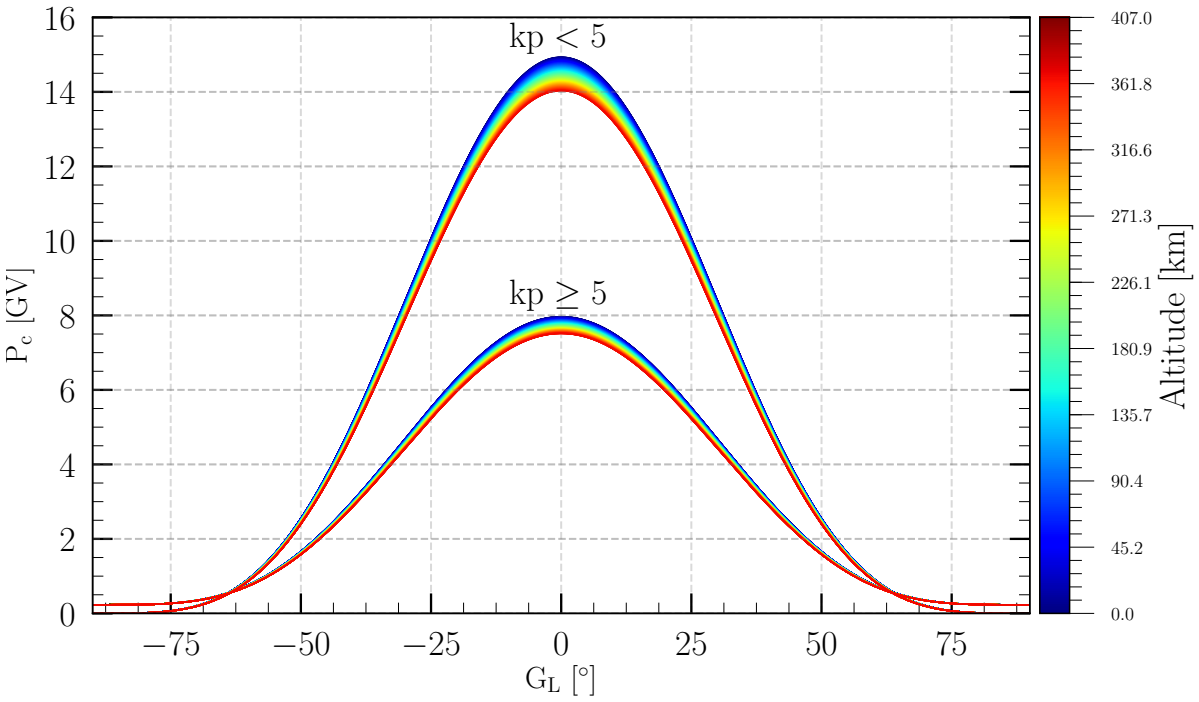

FIGURE 2.4: Analytical solution of P_c determined from Equation 2.10 from sea-level altitude to the International Space Station (ISS). In a virtually undisturbed geomagnetic field, P_c is about 15 GV at the geomagnetic equator compared 8 GV when Kp index is ≥ 5 both at sea-level. There is is significant difference of about 0.9 GV between P_c calculated at the ISS compared to sea-level at the equator, but this effect is negligible at aviation altitudes.

Figure 2.4 shows P_c's dependence on G_L and altitude. At the poles, the field is almost vertical and P_c is almost zero, allowing the maximum number of cosmic-ray to penetrate. However, at the equator, a cosmic-ray with P_c less that 14.9 GV cannot reach the geomagnetic equator from the vertical direction, due to the fact that the geomagnetic field is horizontal to the Earth. The size of this effect also depends on geomagnetic altitude, i.e. at the International Space Station (ISS) P_c is lowered by $\sim$ 0.9 GV with respect to altitude at sea-level, however at aviation altitudes, e.g. $\sim$ 12 km (197.11 g/cm^2) the difference is negligible. There is, however, influence of non-vertical cutoffs not discussed here. For more information on this see e.g. *Bland and Cioni* [1968].

2.5 Atmosphere and Primary Cosmic-ray by-Products

The Earth's atmosphere (see *von Ehrenfried* [2014] for a broad definition as it means different things to different people) is retained by gravity. This region below the geomagnetic field, is composed of five layers (according to its thermal and ionisation structure) from the troposphere to the exosphere and the layers are made up of the gas mixture primarily 78% Nitrogen, 21% Oxygen and about 1% of a mixed of other gasses [*Gratton*, 2015, *von Ehrenfried*, 2014]. For the aviation community, balloon and rocket launches, the [1] troposphere i.e. $\sim 8-10$ km (i.e. $363.016-269.57\ g/cm^2$) near the poles and $\sim 16-18$ km (i.e. $104.89-76.53\ g/cm^2$) in tropical regions with some variation due to weather conditions and the [2] stratosphere extending from the troposphere to about ~ 50 km ($\sim 0.77\ g/cm^2$), are the two most important regions for this work.

Upon getting access through the geomagnetic field, the incident GCRs (and SEPs), known as primaries, traverse down from the exosphere to lower altitudes where they continuously interact with the atmospheric molecules producing a multitude of secondary particles such as neutrons, protons, electrons, etc. Furthermore, this cascade of secondary particles (also called cosmic-ray shower) will undergo further collisions until they have insufficient energy to produce more particles by collision [*Grieder*, 2001]. The particle flux in the atmosphere increases with increasing atmospheric altitude, reaching a maximum reported to be between 16 km (i.e. $\sim 104.89\ g/cm^2$) and 25 km (i.e. $\sim 25.61\ g/cm^2$) in the northern hemisphere; the so called Regener-Pfotzer maximum [*Pfotzer*, 1936, *Regener*, 1933, *Regener and Pfotzer*, 1934]. Above this Regener-Pfotzer maximum the production of these secondary particles dominates, and below this decay and absorption processes dominate over the production of secondary particles. Due to their continuous loss of energy as they penetrate to lower altitudes of the atmosphere, there is a minimum energy of about 500 MeV at TOA required for these primary particles to produce subsequent secondary particles that can be detected at ground-level. When these particles have lost all their energy, they will be completely absorbed in the lower atmosphere [*Schlaepfer*, 2003]. Often, during the cascade production, a small fraction of the initial primary particle with extremely high energy reaches the ground as high energy secondary particles. The average propagation direction of the secondary particles is more or less the same as the incidence direction of the primary particle. A simplified schematic (not drawn to scale) illustrating the primary cosmic-ray interaction with the upper atmosphere and resulting in a cascade of secondary particles is shown in Figure 2.5.

Three major components that are produced in this particle cascade are: The electromagnetic component, the meson component, and the nucleonic component. The nucleonic component

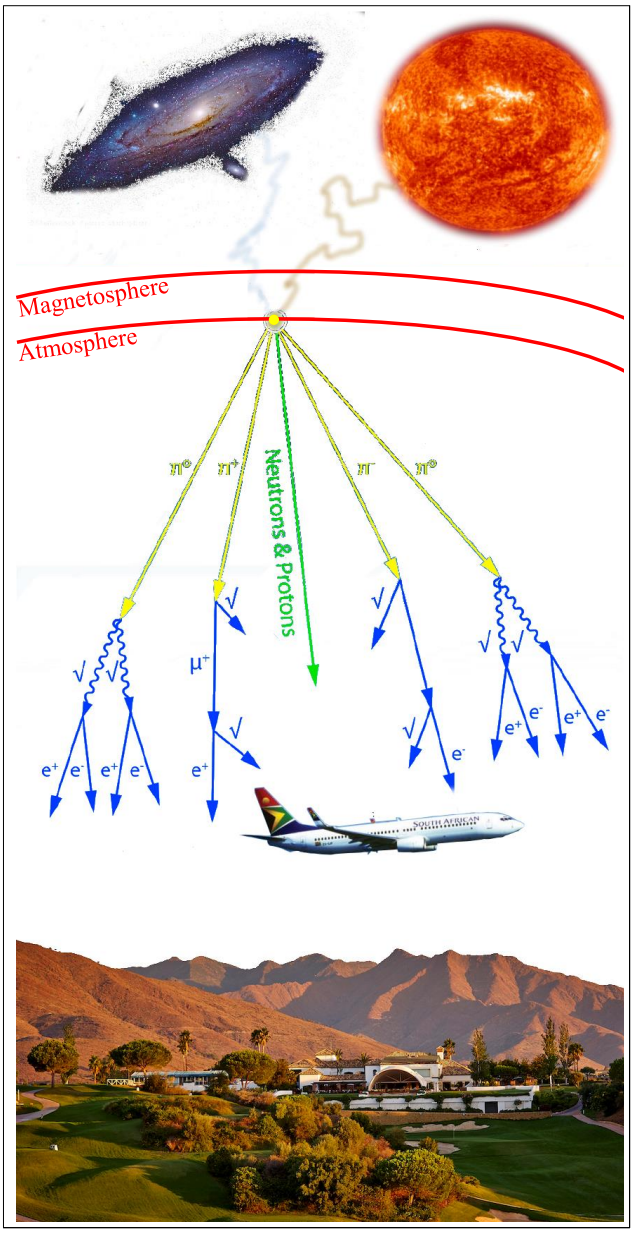

FIGURE 2.5: Primary cosmic-ray interaction with the upper atmosphere and resulting cascade of secondary particles. Image credit: *Mosotho et al.* [2021].

comprises secondary neutrons and protons. The energies of these produced particles cover a wide energy range, while the energy at TOA of the primary particles defines the upper maximum limit. Apart from GCRs, SEPs are often of insufficient energy to contribute to the radiation field at aviation altitudes. However, on other occasions, SEPs are produced with sufficient energy to penetrate the Earth's magnetic field and propagate to the TOA. These particles interact with atmospheric molecules in the same way as GCR particles. For more detailed information on the development of the interaction cascade in the Earth's atmosphere, see [*Allkofer*, 1975, *Allkofer and Grieder*, 1984, *Schlaepfer*, 2003].

2.6 Cosmic-ray Observations

Ground-based cosmic-ray detectors can monitor the cosmic-ray variations with sufficient statistics. These ground-based detectors have been gathering important data for many years; since the early 1950s, long-term ground-based observations have been carried out by means of neutron monitors (NMs), deviating from the traditional ionization chamber, Geiger-Müller counters, muon telescopes, etc. NMs are characterized by the direction from which primary particles impinge on a given point at the TOA arriving at the border of the magnetosphere, i.e. their asymptotic direction (see *Bütikofer* [2018a,b], and for details). Therefore, NMs detect the secondary particles and their count rate ($\mathcal{N}_r$) measurements at a station reflect the TOA flux of primary particles on a given point at the TOA [*Moraal et al.*, 2000, *Moraal and Stoker*, 2010].

NMs setups in the world differ and the most notable are the International Geophysical Year (IGY)-type, NM64-type and neutron moderated detector (NMD)-type. They are useful for the study of not only long-term temporal variations, but also short-term intensity changes. The oldest continuously operating NM in the world is located in Hermanus, Western Cape Province, South Africa. This NM-64, along with the other three NM stations, has been operated by the Centre for Space Research at the North-West University since the late 1950s. The centre has also developed the concept of mini NMs, ideally to re-calibrate these stations. For more information on mini NMs, see *Strauss et al.* [2020], *Krüger* [2006], *Krüger and Moraal* [2010], *Krüger et al.* [2013], *Krüger and Moraal* [2013], *Krüger et al.* [2015], *Usoskin et al.* [2015], *Heber et al.* [2015], *Poluianov et al.* [2015], *Lara et al.* [2016], *Lara and Caballero-Lopez* [2017], *Krüger et al.* [2018], *José Blanco et al.* [2018], *Almutayri* [2019] as these are not discussed in this work. NMs are sensitive to neutrons and protons, and they yield a high counting rate. These South African monitors are part of the worldwide network called the "*Real-Time Database for high resolution NM measurements*" or simply NMDB.[6]

In Figure 2.6, a long term record of 27 days NMs $\mathcal{N}_r$ averages at ground and sea-level is shown as a function of time, together with the original hourly time resolution. The bottom panel shows the $\mathcal{N}_r$ of the Hermanus NM from 1957 up to present, while the second from bottom to top panels show measurements obtained from the South African National Antarctic Expedition (SANAE), Potchefstroom and Tsumeb NMs, respectively. These NMs in the figure are located at geomagnetic P_c ranging from ~0.8 GV to ~9.2 GV, as summariezed in Table 2.1. For statistical comparison between these NMs, the $\mathcal{N}_r$ of each monitor was normalised to 100% in March 4, 1987. The $\mathcal{N}_r$'s response of these monitors is determined by their geographic position

[6] http://www.nmdb.eu/

and atmospheric effects (see e.g., *Pyle* [1997]). SANAE measures the greatest $\mathcal{N}_r$ fluctuations compared to the others simply due to its low geomagnetic P_c.

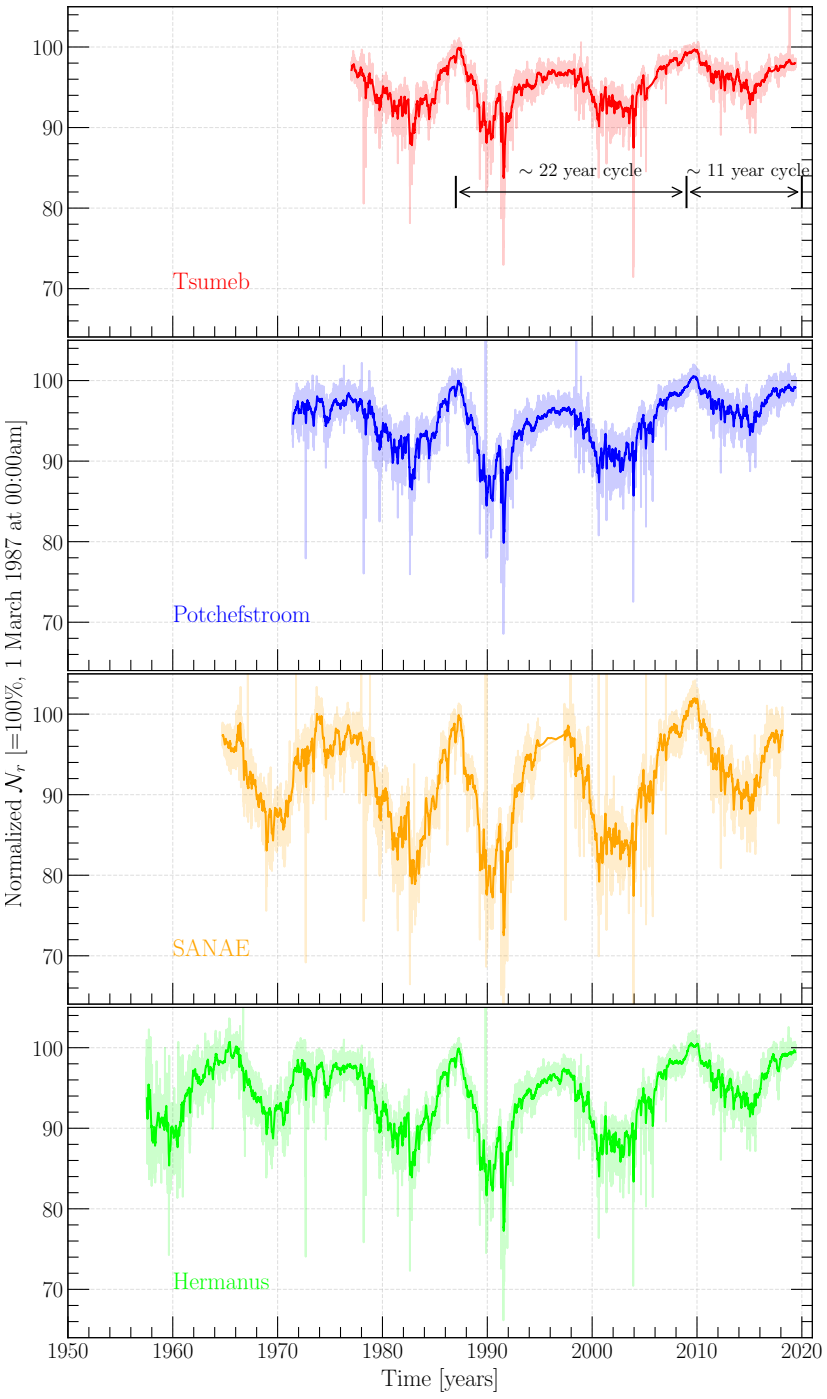

FIGURE 2.6: Hourly NMs $\mathcal{N}_r$ extending up to the early 2020. In all the panels counts rates in the original hourly time resolution is shown in light colour, while the 27 days averages are shown in dark colour. Both the 11 and 22 year cycle are clearly evident. Data source: http://natural-sciences.nwu.ac.za/neutron-monitor-data.

In Figure 2.6, an $\sim$ 11 year cycle, which is anti-correlated with solar activity as illustrated in Figure 2.2 is clear. Sunspot numbers are a measure of solar activity, certainly not the cause of $\mathcal{N}_r$ modulation. Also, evident from Figure 2.6 is an $\sim$ 22 year cycle, related to the Hale cycle

TABLE 2.1: NMs stations and their properties.

Station[a]	Type	Altitude [m]	P_c [GV]	Operation Period
Tsumeb	NM64	1240	9.15	1976−present
Potchefstroom	IGY	1351	6.94	1971−present
SANAE	NM64	52	0.86	1964−present
Hermanus	NM64	26	4.58	1957−present

[a] For more information, visit http://natural-sciences.nwu.ac.za/neutron-monitor-data.

due to the Heliospheric Magnetic Field polarity. This cycle appears to follow an alternating "flattish" to "peakish" solar minimum peak in solar minimum rates [*Barnden and Bercovitch*, 1975, *Kóta and Jokipii*, 1983, *Lockwood et al.*, 2001]. The behaviour of this cycle can be predicted and explained by application of cosmic-ray modulation drift due to solar magnetic field polarity changes every 11 years [*Jokipii et al.*, 1977, *Potgieter and Ferreira*, 2001, *Oh et al.*, 2018, *Krainev*, 2019].

Besides real-time and historical data spanning more than a century, NMs $\mathcal{N}_r$ measurements offer an opportunity for applications of solar energetic particle alerts and these remain the most useful and most widely used tools for assessing aviation radiation exposure for commercial aircrafts. Large, deep, sharp, step-like decreases and increases shown in the NMs $\mathcal{N}_r$ Figure 2.6 are evident. These short−term changes recorded by NMs are believed to be related to transient solar events, which might decrease or increase radiation dosimetric quantities at aviation altitudes. At Earth, a decrease of atmospheric ionization is attributed to geomagnetic storms, which occur as a result of the coronal mass ejections interacting with the geomagnetic field. When this occurs, the magnetic field of the plasma solar wind will temporarily divert some lower energy galactic cosmic-rays away from Earth. This phenomenon is known as a Forbush decrease (FD) (or Forbush effect), named after the American physicist Scott E. Forbush, who studied cosmic-rays in the 1930s and 1940s. FD are known to often occur under quiet geomagnetic conditions. They can be observed not only within the geomagnetic field, but many have been measured for years on various spacecraft in space far away from planets. For more information on these FD see *Forbush* [1938], *Fenton et al.* [1959], *Lockwood* [1971], *Barouch and Burlaga* [1975], *Cane* [2000], *Cane et al.* [1996], *Belov et al.* [2001], *Belov* [2009], as these are not of primary importance in this work.

As a reverse event of a FD, ground-based NMs $\mathcal{N}_r$ often show a large and sharp increase. During the event, SEPs can produce showers of secondary particles with intensities that exceed the galactic cosmic-ray background. However, often the majority of SEPs reach energies of the order of MeV and are totally absorbed in the upper atmosphere. During the 1990s, these ground-level SEPs enhancements [*Simpson*, 1990, *Cliver*, 2008], became internationally known

by the name GLE (meaning, ground-level enhancement or ground-level event). The spectra of these events vary between events and are therefore studied on case by case basis.

The exposure at cruising flight altitudes during strong SEPs events that eventually produce GLEs can significantly enhance the radiation field at these altitudes. As a result, during these strong events, i.e. SEPs and GLEs, flight personnel and passengers might potentially receive doses above the typical GCRs background dose levels [*Lantos*, 2005, *Tuohino et al.*, 2018]. As an indicator of the enhanced radiation field at cruise flight altitudes, NMs measurements are very helpful in studying radiation exposure during GLEs and provide a good basis for further assessment of space weather effects related to accumulated doses at aviation flight altitudes. Recently, *Mishev et al.* [2019], *Mishev et al.* [2018, 2017] and *Mishev and Usoskin* [2018] showed that, using the global NM network (specifically the low cut-off rigidity stations), it is possible to directly or retrospectively obtain a quick estimate of the routine operational dosimetric quantities during GLE events.

The duration of SEP events may be hours to several days. The maximum ionization effect from the GLE is expected during the first hours after the event onset [*Bazilevskaya*, 2005]. GLEs have been recorded and analysed since February 28, 1942 and are numbered in a chronological list since the first event (GLE01) measured by *Lange and Forbush* [1942] using an ionization chamber. There are 72 known events to date and Figure 2.7 shows all measured ground-based GLEs; GLE05 onwards represent a record obtained in the NM era. The list of GLE events is available at http://neutronm.bartol.udel.edu/ and update list in the NM era, see https://gle.oulu.fi/#/.

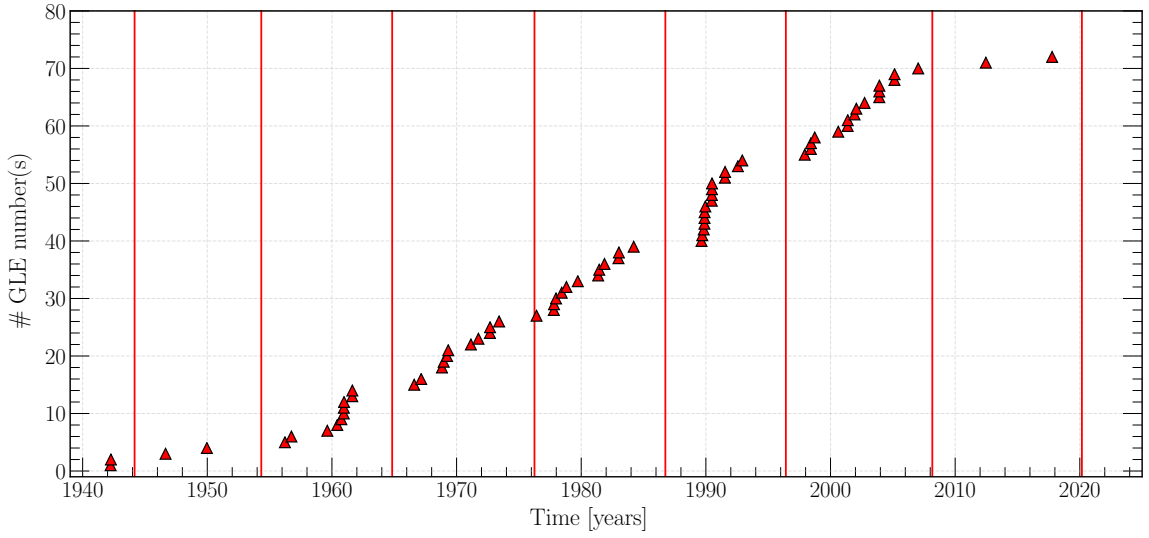

FIGURE 2.7: GLE records since the mid 1950s until the recent 2020 solar minimum. Data source: http://neutronm.bartol.udel.edu/, with updated data in the NM era from https://gle.oulu.fi/#/.

Historically, GLE events are rare, unpredictable, and their occurrence is approximatively expected to be at least once (often more) per year, mostly dominating during solar maximum periods [*Shea and Smart*, 1990]. The red vertical lines on Figure 2.7 mark the beginning of sunspot minima cycles. During solar cycle 23, sixteen GLE events were observed and this is the highest number of GLEs compared to any other cycle, while cycle 24 is the lowest in the NM era. Long gaps with no events can be seen mostly during solar minimum activity. However, GLE27 on 1976 April 30 occurred at (or nearly at) solar minimum. According to *Tylka and Dietrich* [2010], "*no CME observations were available for the 1976 event*". There are limited publications on this GLE event, explaining how or why it occurred out of "season" so to say. In the NMs era, the year 1989 was the year with the most GLE events, a record of seven GLEs.

The first GLE measurement from a South African NM was recorded at SANAE on July 06, 1966. Figure 2.8 shows the percentage increase measured by the four South African NMs during GLE42 of the 29 September 1989 (chosen for demonstration). This GLE is the only event where all four NMs simultaneously registered a significant increase. The SANAE NM registered a 297.5% peak increase, while the Hermanus, Potchefstroom and Tsumeb NMs recorded 105.1%, 105.3% and 62.2%, increases respectively. These $\mathcal{N}_r$'s are expressed as a percent increase over the pre-event galactic background.

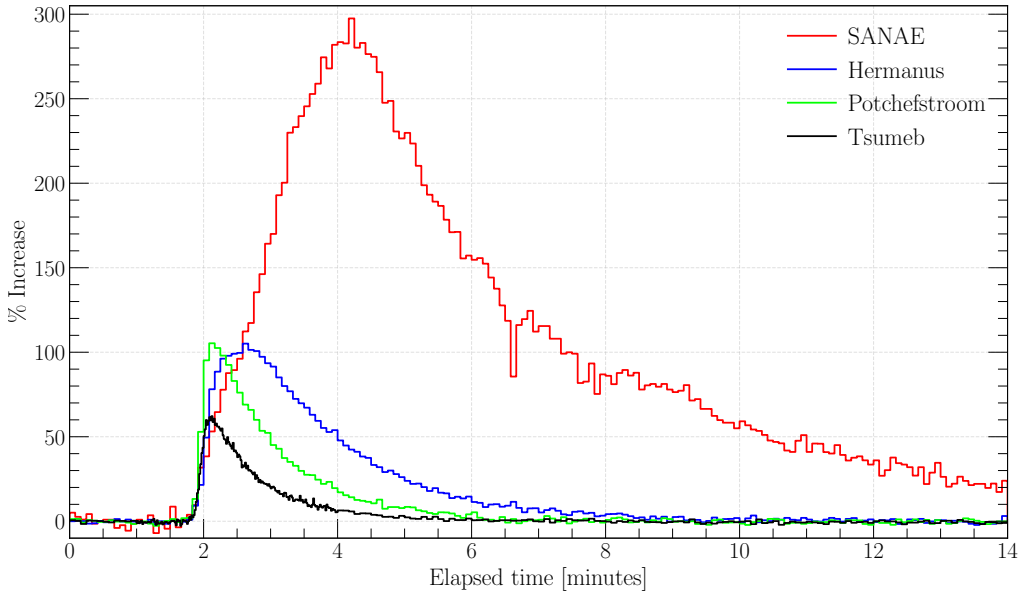

FIGURE 2.8: GLE42 as observed by the South African NM network. Data source: http://natural-sciences.nwu.ac.za/neutron-monitor-data.

GLE identification by ground-based observations has been ongoing since the 1970s and just recently *Poluianov et al.* [2017] proposed a revised "classical" GLE definition, and for weak (or hidden) or events that are below the threshold of GLEs, a proposal was made to classify these event as sub-GLEs. The sub-GLE definition differs from that of the GLE in that no

statistically significant enhancement in the NMs $\mathcal{N}_r$ at sea-level is required, in which case the $\mathcal{N}_r$ must be registered by at least two different high altitude NM station. The definition proposed by *Poluianov et al.* [2017] supports the *Atwell et al.* [2015] definition of a sub-GLE.

The shielding effect of the geomagnetic cutoff and atmosphere as discussed in Section 2.4 and 2.5 makes it impossible for NMs to indirectly measure the particle energy/rigidity spectra at low energies. Cosmic-ray observation at the TOA has the unique advantage of measuring cosmic-rays directly while avoiding the atmospheric effect. Independent studies by *Kühl et al.* [2017] and *Vainio et al.* [2017] demonstrated that a significant number of high energy SEP events, over 25, have been recorded by spacecraft with energies over 500 MeV, but these particles never reached the ground-level and are recorded by NMs. However, high altitude polar NMs measurements have recorded these few events (see *Poluianov et al.* [2017]). These form a base for describing the proposed definitions of sub-GLEs.

The only reliable detectors capable of continuously measuring secondary cosmic-rays with sufficient statistics in the high energy region, i.e. the energy range above several 100 MeV, for real time monitoring, are the ground-based NMs [*Simpson*, 2000]. However, NM stations all over the world provide a single $\mathcal{N}_r$ and hence, spectral information cannot be obtained from the measurements of a single detector. Therefore, to get insights regarding the incoming direction of the event, the angular distribution and the energy spectra, *Mishev et al.* [2017] and *Mishev and Usoskin* [2018] show that the NMDB, providing data from a large number of instruments, can be helpful in this regard.

2.7 Summary

Features of the Sun, the evolution of cosmic-rays from their source to Earth, where they are detected, and also how transient events on the Sun enhance the radiation levels at ground-level and aviation altitudes were discussed. The purpose of this introductory chapter is to introduce the essential science on very interesting subjects concerning aviation radiation exposure for commercial personnel and passengers. In what follows, dosimetric quantities measured/calculated as results of being exposed to ionising radiation will be discussed. For special events in this work, analysis of the mixed radiation field environment at aviation altitudes is restricted to solar energetic particle events producing GLEs and the data used are obtained from NMs.

CHAPTER 3

Radiation Dosimetry

Broadly, radiation is energy in transit, i.e. energy travelling in a form of subatomic particles of matter or as electromagnetic radiation which consists of wave-packets of electromagnetic energy known as photons. When a photon or subatomic particle has sufficient energy to indirectly or directly eject an electron out of orbit from an atom it is referred to as ionizing radiation. Therefore, radiation dosimetry deals with the measurement of energy deposition in matter as a result of being exposed to ionizing radiation. High altitude radiation dosimetry is the science of evaluating, through measurement or calculation, the dosimetric quantities received by the flight personnel and passengers, during flight cruises. There are numerous units used in literature to describe radiation. In the international system of units, for example, Becquerel (or Curie, i.e. 1 Curie $= 3.7 \times 10^{10}$ decays per second) is used to describe radiation emitted by radioactive matter, while for the same type of radiation absorbed by a non-biological body, e.g. dosimetry instruments, the unit Gray (i.e. the deposited energy per unit mass) is used, while the Sievert unit is only used for radiation protection in the case of human beings exposed to ionizing radiation. In this chapter, instruments (relevant for this work) used for detecting and measuring ionising radiation are introduced. Furthermore, basic forms of the interaction of ionising radiation with dosimetry instruments are discussed, as well as, the basic resulting effects of ionising radiation interaction with organic matter, e.g. in human tissue, is discussed with focus on the International Commission on Radiological Protection guidelines and recommendations.

3.1 Dosimetry Instruments

Due to the fact an organic matter does not have senses to detect radiation, instruments used for detecting and measuring ionising radiation are very significant with that regard. Dosimetry at aviation altitudes (and above) requires instruments that are capable of characterizing

dosimetric quantities in matter. Since the discovery of cosmic-rays credited to Hess, breakthroughs in instrumentation from large to portable dosimetry instruments have been achieved and measurements analysis have improved. These breakthroughs have led to many significant improvements in portable instruments, has also increased for the scientific research community, but a need for even better instruments has increased for industrial and personal dosimeters. Dosimeter improvements were made possible by technological advancements where smaller and superior power supplies, longer-life batteries, printed circuit boards and much improved electronics were produced.

The dosimetric quantities on board commercial aircraft at aviation altitudes are routinely monitored using either active or passive radiation detectors for the flight personnel and passengers. A passive detector needs to be "read" at a later stage, whereas an active radiation detector gives instantaneous real time information. With the advances in space dosimetry missions and commercial aviation dosimetry, active detectors are gradually replacing passive detectors. The most commonly used modern detectors for dosimetry science are active detectors which are lighter and easier to use. Apart from being mobile, and being readily transported to almost any location around the world as a unit, their detection efficiency does not change when relocated because they do not need to be dismantled.

The Geiger-Müller counter is one of the oldest radiation detectors and was introduced by Geiger and Müller in 1928 [*Geiger and Müller*, 1928]. It is widely used in the measurement of radiation due to its simplicity, inexpensiveness and ease of operation. It uses a gas filled tube with a central wire at a high voltage to collect the ionization produced by incident radiation. This counter is only capable of detecting ionised radiation. These counters are best used for radiation environments where only a rough estimate of the amount of radioactivity is needed, and often it is used for demonstrations. In the early 1940s, Geiger-Müller counters, together with muon telescopes, were (and are still) widely used as secondary cosmic-rays detectors for monitoring. From the concept of muon telescopes, together with the development of semiconductor technology, fully depleted silicon detectors have become widely used in cosmic-ray physics because of their low noise, high counting rate, and good linearity. Singly, they are capable of determining the energy deposited by the incident radiation in the silicon diodes (SDs), and while in telescope mode (i.e. using a combination of two or more Si detectors) they can be used to determine the linear energy transfer, $\mathcal{L}$, of charged particles [*Beaujean et al.*, 1999, *Ritter*, 2013, *Möller*, 2013, *Labrenz*, 2014, *Labrenz et al.*, 2015, *Berger et al.*, 2019].

Most radiation detectors used for radiation protection are not suitable for measuring high altitude radiation. As an alternative, silicon detectors or tissue equivalent proportional counters are mostly used (see *Rossi and Zaider* [1997], *Beaujean et al.* [2005] and *Nam et al.* [2015]).

Using a gas filled radiation detector, known as the ionization chamber, *Rossi and Rosenzweig* [1955] developed the concept of a tissue equivalent proportional counter (TEPC). The TEPC was originally designed as a dosimeter for direct measurements of energy imparted in microscopic sized volumes of tissue. Modern TEPCs are better than the old ionization chambers where the statistical accuracy of the chambers' count rates was low. The purpose of the TEPC, similar to silicon detectors, is to characterize the radiation environment at high altitude and monitor the exposure of the flight personnel and passengers. TEPCs were used on all NASA space shuttles and on the International Space Station. For operation and application of TEPC, see *Gerdung et al.* [1995].

However, for this work, a dosimeter equipped with a silicon semiconductor sensor was assembled. This dosimeter was selected for its portability in both operation and size. It is described in detail in Chapter 6 and subsequent chapters. For high altitude balloon launches, the Geiger-Müller counters were used and these are described in detail in Chapter 5.

3.2 Radiation Interaction with Matter

As it propagates through matter, radiation interacts with atoms or molecules. Section 2.5 introduced possible interaction processes for ionising radiation in the Earth's atmosphere. In general, ionising radiation, e.g. CRs particles, can interact with other kinds of matter; for insights on particle-matter interactions see *Allkofer* [1975], *Knoll* [2000, 2010], *Harkness-Brennan* [2018]. During the interaction with the target material, charged particles mainly lose energy due to ionization and x-rays emission (see *Bethe and Heitler* [1934], *Evans and Noyau* [1955] for insights as this process is not discussed here). However, neutral particles, e.g. neutrons, mainly lose energy through nuclear processes, while photons lose energy by the photo-electric, Compton effect and pair production [*Srour and McGarrity*, 1988, *Knoll*, 2000, 2010]. In the subsequent sections some basic physical interaction processes of radiation (i.e. from both charged and neutral particles) with matter are briefly described in a more general context. In particular, the incident radiation interacting with silicon target material (with a thickness of 300 μm) will be discussed as this forms part of this work as pointed out in Section 3.1 and further discussed in Chapter 6. The motivation for this discussion stems from the fact that the particle's lose energy during these interaction processes which contributes to the readout signal of radiation detectors and this is very important as it can give a realistic estimate of how much background radiation is likely to be expected, for example, during commercial flights.

3.2.1 Charged Particles Interaction with Matter

The general question in radiation detection, measurements, shielding and dosimetry is: How deep can the incident radiation penetrate the target material? This is different, as it might be expected, for various combinations of incident radiation and the target materials to penetrate on. However, almost every particle known has a specific range of penetration in matter. When heavy charged particles propagate through matter and if the energy of the incident particle is higher than the energy loss due to a single interaction with the target material, this will produces an ongoing process inside the target material over a path length traversed (classically known as penetration depth). All charged particles heavier than electrons and positrons are categorised as heavy charged particles [*Leo*, 1987]. These heavy charged particles mainly loss energy in matter through inelastic scattering either by lifting an electron in an excited state or by ionizing the atom of the target material. Therefore, the total energy loss dE of heavy charged particles, except for electrons and positrons, along a path length dx through the target material can be described by the Bethe-Bloch formula [*Bethe*, 1930, *Bethe*, 1932, *Bloch*, 1933, *Fano*, 1963]. The form of the equation is given as

$$-\frac{d\mathrm{E}}{dx} = \left[\frac{z^2}{v^2}\right]\left[\frac{n_e e^4}{4\pi\epsilon_0 m_e}\right]\left[ln\left(\frac{2m_e v^2}{I(1-\beta^2)}\right) - \beta^2\right], \tag{3.1}$$

where $\beta = \frac{v}{c}$, v and c are speed of the incident particle and the speed of light in a vacuum, respectively. Also, I is the mean effective ionization and excitation potential of the target material. The parameter I is determined experimentally for different materials and *Leo* [1987] compiled a summarised list of values for I, while a more extensive list is provided by *Sternheimer et al.* [1984]. The electron charge is represented by e, while the electron density of the material, i.e. $n_e = N_A Z\rho A$ with N_A being the Avogadro number, and Z, A, and ρ represents the atomic number, atomic mass, and mass density of the target, respectively. The charge of the incident particle is z and the electron mass is m_e, while the energy lost by the incident particle per unit length in the target material is dE/dx. There are correction terms introduced by *Fano* [1963] in the Bethe-Bloch equation, such as the shell correction and the density effects corrections at high energies, however, these are not discussed here, for insights see studies by *Sternheimer et al.* [1984], *Bichsel* [1969], *Sinky* [2005], *Bichsel* [2006], *Walske* [1952, 1956], *Zyla et al.* [2020]. The negative sign on the left-hand side of the equation simply indicates that the dE/dx quantity gives the energy lost by the incident particle and is therefore an overall negative quantity [*Weaver and Westphal*, 2002].

Equation 3.1 does not depend on the mass of the incident particle but it, however, depends on its speed and charge during the interaction with the target material. If the speed of the incident

particle approximately reaches the speed of light, $\beta \approx 1$ as a result of $v \approx c$, the logarithmic term's relevance increases and the dE/dx slightly increases. As a result of the fact that, the interaction time for relativistic particles is small and the estimation of dE/dx inside the target material becomes small. Therefore, in this case, the relativistic particles are termed minimum ionizing particles. However, in a non-relativistic case, i.e. when $\beta < 1$ as a result of $v << c$, only the first term, i.e. $ln\left(2m_e v^2/I\right)$, inside the curly brackets of Equation 3.1 is significant. Hence, the general behaviour of dE/dx for non-relativistic particles can be described by the multiplicative factor which follows from this approximation

$$-\frac{d\mathrm{E}}{dx} \propto \left[\frac{z^2}{v^2}\right]. \tag{3.2}$$

For illustration purposes, this can be understood by noting that, as illustrated by *Dönsdorf* [2013], when the incident particle's v is lower than that of c, it will spend more time in the vicinity of an electron of the target material and therefore the calculated dE/dx from the incident particle to the electron will be larger. Meaning, for non-relativistic energies the dE/dx of a charged particle decreases (increases) with increasing (decreasing) v^2 and energy of the incident particles. In addition, the z^2 factor means that a doubly charged particle of a given speed v is likely to loss energy 4 times compared to a singly charged particle of the same v in the same target material.

To describe dE/dx along the path length traversed in the target material, the concept of the Bragg curve might be useful. If the incident particle energy, atomic mass number and atomic charge number are known, the path length traversed by a particle through the target material (classically this is called the stopping range R), can be estimated. To obtain R in matter through Equation 3.1 [*Leo*, 1987], Equation 3.1 can be integrated over the thickness of the target material

$$R = \int \frac{d\mathrm{E}}{dE/dx}. \tag{3.3}$$

Figure 3.1 shows the dE/dx spectra of a proton particle as it propagates through a silicon target material over the path length defined by R. The broken line indicates the edge of the silicon sensitive area. The highest dE/dx, shows a characteristic maximum known as the Bragg-peak. This peak can clearly be observed towards the end of each spectra. Beyond the peak, dE/dx decreases rapidly to zero giving an indication that the particle has reached its highest energy it can lose in the volume of the target material [*Hasson et al.*, 2013].

It is evident from the figure that, the Bragg-peak dependends on the energy of the incident particles. The energy loss dE/dx by the incident charged particle propagating through the target material is proportional to v^{-2}, which explains the sudden peak observed just before the particle comes to a complete stop. For all the incident particles at the energy ranges considered

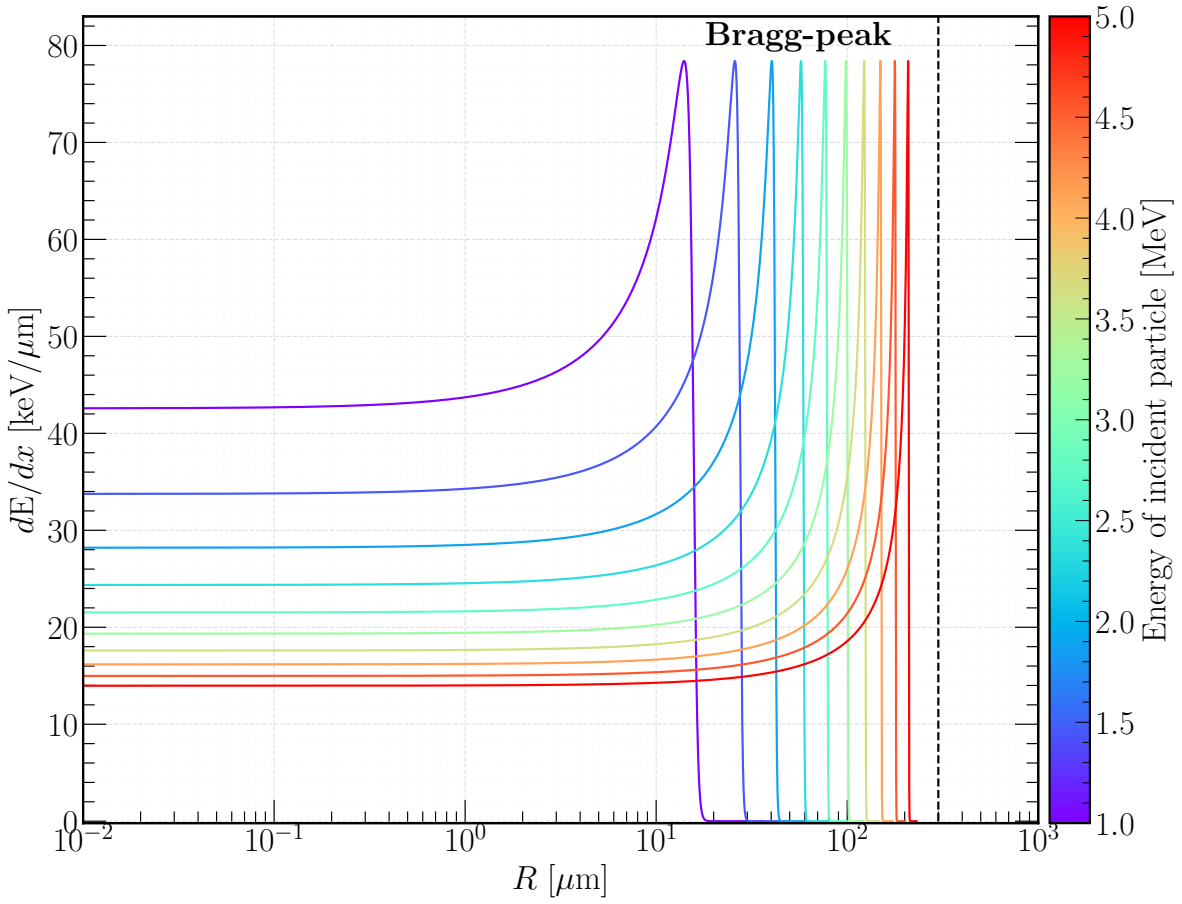

FIGURE 3.1: The Bragg-peak for dE/dx of proton particles penetrating into a silicon target material, with a thickness of the depletion layer about 300 μm, for different incident particle energies.

here, the shape of each dE/dx spectra before and after the Bragg-peak are similar, however, the closer the particle gets to the edge of the target material the Bragg-peak width appears to be getting smaller. It is further shown that by changing the energy of the incident protons, this can potentially increase or decrease the propagation range of proton particles inside the target material. Also shown is that when the incident proton with a certain energy, below 5 MeV, enter the silicon target material, the Bragg-peak of the proton is located inside the sensitive volume of the target material.

3.2.2 Neutrons

Neutrons have no charge, hence, they cannot interact with the electrons of the target material by Coulomb interaction. The interaction processes of the incident neutrons with the electrons in the target material are complex and dependent on their initial energy. However, these interaction can be distinguished between neutron-induced reactions, like (n, p), (n, α), (n, fission) or radiation capture, and elastic scattering. Fast neutrons with energies above 0.5 eV

undergo elastic scattering at nuclei, transferring part of their initial energy to the now energised nucleus. Such a recoil nucleus can then lose its energy by ionisation while propagating through the target material [*Knoll*, 2000, 2010]. The energy transfer, ΔE, of a neutron to the nucleus during elastic scattering depends on the target nucleus mass m_T, scattering angle, θ, the mass of the incident neutron particle, m_N, and the energy, $\mathrm{E_n}$, of neutron. The following equation describes this relationship

$$\Delta \mathrm{E} = 4 \cdot \frac{(m_T \cdot m_N)}{(m_T + m_N)^2} \cdot \cos^2 \theta \cdot \mathrm{E_n}. \tag{3.4}$$

The maximum energy transferable to the target nucleus mass m_T in this equation, i.e. if $\theta = 0$ (for head-on collisions), is calculated assuming that $m_N = 1$, as

$$\Delta \mathrm{E}_{max} \approx 4 \cdot \frac{m_T}{(m_T + 1)^2} \cdot \mathrm{E_n}. \tag{3.5}$$

For a silicon target nucleus ($m_T = 28$), Equation 3.5 shows that neutrons can only transfer up to as factor of 0.133 ($\approx$ 13%) of their primary energy by elastic scattering, while for a hydrogen target nucleus (proton) ($m_T = 1$) fast neutrons can lose all its energy ($\approx$ 100%) in just one collision with a hydrogen target nucleus. The neutron interaction with a hydrogen target nucleus is essential for dosimetry purposes because a human body consists about 10% hydrogen. Also, for dosimetry instruments designed to measure neutrons, fast neutrons have to be moderated by proton-rich materials so that the generated secondary ionised radiation can be detected [*Knoll*, 2000, 2010].

3.2.3 Photons

Similar to neutrons, photons have no charge and they can be classified as the particle of electromagnetic radiation described as either ionizing particles or electromagnetic waves. Photons are non-ionizing at low energies in the order of eV and below. The main interaction process of photons, at these energies, with the target material is coherent scattering of electrons in the atomic shell without any energy loss. However, at higher energies above orders of eV, ionization of target material occurs and the main interaction process of photons with the target material are the pair production, Compton scattering and photo-electric effect. These processes can either lead to a complete or partial transfer of a γ photon energy to electron energy [*Knoll*, 2000, 2010].

Photo-electric Effect

The photo-electric effect involves absorption of the incident photon energy, E_γ, by an electron from the electron shell of the target nucleus. This electron will be excited or emitted from the shell if the absorbed photon energy (hv) is greater than the electron binding energy E_{bin}. The kinetic energy, E, of the outgoing electron is $E = hv - E_{bin}$ [*Knoll*, 2000]. This process will mainly occur at low photon energies. In a silicon target material, the photo-electric effect dominates for photon energies below ~ 60 keV. By definition, the cross section[1] for the photo-electric effect (σ_{pe}) is given as

$$\sigma_{pe} \propto \frac{Z^n}{E_\gamma} \tag{3.6}$$

where Z^n is the atomic number of the target material, with the n index ranging from 4 to 5 [*Knoll*, 2000]. Here, E_γ represents the energy of the incident photon. For higher values of E_γ, i.e. between ~ 60 keV and ~ 16 MeV, the Compton effect dominates photon interaction and supersedes photo-electric effect in silicon.

Compton Effect

During this process, some of the energy of the incident γ photon is transferred to electrons of the target material due to inelastic scattering. The photon loses energy through a wavelength shift that depends on the scattering angle, θ. The scattered photon energy E'_γ can be calculated with

$$E'_\gamma = \frac{E_\gamma}{(1 - \cos\theta) \cdot (E_\gamma / E_0) + 1}. \tag{3.7}$$

where θ is the scattering angle of the photon, E_γ is energy of the incident photon and the rest energy of an electron is $E_0 = 0.511$ MeV. From the equation (see *Knoll* [2000, 2010], the maximum energy transfer $E'_{\gamma,\,\mathrm{max}}$ for back scattered photons (i.e. if $\theta = \pi$) with an energy E_γ can be calculated with

$$E'_{\gamma,\,\mathrm{max}} = \frac{2 \cdot E_\gamma}{2 \cdot E_\gamma + E_0}. \tag{3.8}$$

The cross section for the Compton effect process (σ_{ce}), follows the same relationship as that of Equation 3.6 but for $E_\gamma \sim 0.06 - 16$ MeV [*Allkofer*, 1975, *Knoll*, 2000]. If the photon energy is higher than twice the rest energy of an electron (i.e. $2E_0 = 1.022$ MeV), pair production[1] is the dominating photon interaction in the target material, this effect supersedes the Compton effect in silicon target material for photon energies above ~ 16 MeV.

[1] Photon Cross Section Database, http://www.nist.gov/pml/data/xcom/index.cfm

Pair Production

If the lower energy threshold of the incident γ photon is at least higher than twice the value of the rest energy of an electron ($\sim 2E_0 = 1.022$ MeV), pair production becomes the dominating interaction process [*Allkofer*, 1975, *Knoll*, 2000, 2010, *Blackett et al.*, 1933]. This process describes the interaction between a photon and the Coulomb field of the nuclei in the target material. In this process, the incident γ photon disappears, while an electron-positron pair is created [*Oppenheimer and Plesset*, 1933]. However, if the energy of the incident γ photon E_γ exceeds the required lower energy threshold which is essential for the creation of the pair, this energy is converted into kinetic energy and divided between the electron and the positron [*Blackett et al.*, 1933, *Hubbell*, 2006, *Dönsdorf*, 2013]. The produced electron-positron pair will undergo further electromagnetic interactions inside the target material. The cross section[1] of the electron-positron pair production (σ_{pair}) is

$$\sigma_{pair} \propto Z^2 \cdot \ln E_\gamma, \tag{3.9}$$

where σ_{pair} is proportional to the square of the atomic number Z of the target material and the incident photon energy E_γ *Knoll* [2000, 2010].

3.3 Radiation Protection and Exposure Assessment

Soon after Röntgen's discovery of X-rays, Wolfram Fuchs proposed what today is known as the "first" protection advice; see *Fuchs* [1896]. In the 1920s, the effects of post exposure to ionising radiation prompted the formation of a number of expert bodies to regulate it; see *Clarke and Valentin* [2009] for the historical timeline and evolution of policies. Under a new name given in 1950, the International Commission on Radiological Protection (ICRP[2]) was established in 1928 at the second International Congress of Radiology to address concerns about the ionizing radiation effects being observed in the medical community. At the time it was known as the International X-ray and Radium Protection Committee, but later it was re-organized to account radiation related concerns outside the medical area. Nowadays, its purpose is to establish basic principles and issue recommendations on long-term health effects of radiation exposure and protection.

The *ICRP60* [1991] is one of the publications that address the radiological protection and build on the dose limitation proposed in earlier ICRP documents such as *ICRP26* [1977]. This publication was revised and updated in 2007 in publication *ICRP103* [2007]. Since the

[2] http://www.icrp.org/index.asp

recommendations of publication *ICRP103* [2007], there have been a number of important initiatives in the development of high altitude and space radiation dosimetry. In 2013, the ICRP released a publication entitled "*Assessment of radiation exposure of astronauts in space*" to address the harsh environment that astronauts are exposed to at the TOA and beyond [*ICRP123*, 2013], in response to the *ICRP103* [2007].

Ground-based workers and aircraft flight personnel are exposed to ionising radiation during their occupational activities, and due to this they are classified as being radiation workers; see *ICRP60* [1991]. The mixed radiation field that the aircraft flight personnel and passengers are exposed to at aviation altitudes is very complex compared to the ground-level radiation. In a similar fashion as outlined in Section 2.5, when GCRs and SEPs (or produced secondary particles at lower altitudes) encounter aircraft components, an additional multitude of high energy particles will be produced and scattered into a broad ionizing shower inside the aircraft, see *Knipp* [2017]. In *ICRP132* [2016], the ICRP provides updated guidance on radiological protection from cosmic radiation in aviation, taking into account the previous recommendations in *ICRP60* [1991], *ICRP75* [1997] and *ICRP103* [2007]. The *ICRP132* [2016] publication discusses [1] how flight personnel and passengers are exposed to ionising radiation, [2] the radiation protection principles applicable to the current exposure situation, and [3] the available steps of actions for protection.

The ICRP principles and recommendations form the basis for all exposure of radiation by workers and members of the public of all countries, while leaving the detailed application to national authorities. However, in most countries, aviation radiation is not monitored and the European Union took an initiative by requiring that all its flight personnel be monitored, following recommendations of the *ICRP60* [1991], confirmed by *ICRP103* [2007]. They introduced a revised Basic Safety Standards Directive (see *European Union* [2013]), which included cosmic radiation as occupational exposure. The *European Union* [2013] directives order member countries to perform assessments of cosmic radiation exposure for aircraft flight personnel.

In South Africa, the ICRP system for radiation exposure assessment and protection is incorporated in the National Nuclear Regulator.[3] Dosimetric quantities and dose limits (discussed in the subsequent sections) used in South Africa National Nuclear Regulator are based on *ICRP60* [1991]. Aircraft flight personnel and passengers are not mentioned by the South Africa National Nuclear Regulator. Since aviation radiation was declared a health risk, there has been no dosimetry service which collects data or model occupational exposure in South Africa as a result of cosmic-rays. However, due to the recent appointment of the South African National

[3] http://www.nnr.co.za/

Space Agency (SANSA)[4] by the International Civil Aviation Organization (ICAO)[5] to provide aviation radiation estimates as mentioned in Chapter 1, this will definitely benefit South Africa and enhance its ability to address the unquantified and undocumented radiation levels the flight personnel and passengers are exposed to at aviation altitudes in the Southern Hemisphere. In response to SANSAs appointment the NWU developed educational programs[6,7] to make flight personnel and the public in general aware of the cruise altitude radiation exposure.

3.4 Basic Dosimetric Concepts and Quantities

Commonly used dosimetric parameters for radiation exposure at aviation flight altitudes are introduced and described in this section, with focus on the model calculations at aviation altitudes for commercial aircrafts described in Chapter 4 and subsequent chapters.

3.4.1 Absorbed Dose

The absorbed dose is a measure of the amount of energy absorbed by matter as a result of being exposed to ionising radiation. Here, for dosimetry purposes, matter could be the human body, a particular tissue or organ in the body, or an electronic device. Mathematically, the absorbed dose, $\mathcal{D}$, is described as the amount of energy, dE, deposited in matter/tissue with mass element, dm, by ionizing radiation as

$$\mathcal{D} = \frac{d\mathrm{E}}{dm}. \tag{3.10}$$

The unit of the parameter $\mathcal{D}$ is Gray (Gy) expressed as J/kg where 1 Gy $= 6.2414 \times 10^{12}$ MeV/kg, with 1 eV $= 1.6022 \times 10^{-19}$ J this result in 1 Gy $= 1$ J/kg. In contrast to Kerma, absorbed dose applies to all kinds of ionizing radiation (directly and indirectly). Kerma is a measure of the energy transferred to the medium, whereas the parameter $\mathcal{D}$ is a measure of the energy that actually remains in the medium. The parameter $\mathcal{D}$ does not account for the biological effectiveness of ionizing radiation. The absorbed dose rates, $\mathcal{D}_r$, can be calculated by dividing the absorbed dose by the time of measurement. The parameter $\mathcal{D}_r$ is usually given in $\mu Gy/h$. It is highly dependent on the energy deposition of incident particles and this differs for individual events.

[4] https://www.sansa.org.za/
[5] https://tinyurl.com/y29ykjv7
[6] https://www.facebook.com/NWUSpaceScience/
[7] https://doi.org/10.17159/sajs.2021/7561

For silicon detectors, the calculation of the parameter $\mathcal{D}$ depends on the energy deposition spectra recorded by the detector. The energy loss of all particles depositing energy in the detector is stored in these spectra. Therefore, to calculate the total dose $\mathcal{D}$ in silicon, $\mathcal{D}_{\mathrm{Si}}$, one has to integrate the product of the deposited energy, dE, times the number of particles counted and divided by the detectors mass dm as

$$\mathcal{D}_{\mathrm{Si}} = \mathrm{K} \sum_i \frac{N_i \cdot dE_i}{dm} = \mathrm{K} \sum_i \frac{N_i \cdot dE_i}{\mathrm{dV} \cdot \rho_{\mathrm{Si}}} = \frac{\mathrm{K}}{\mathrm{A} \cdot \mathrm{d} \cdot \rho_{\mathrm{Si}}} \sum_i N_i \cdot dE_i. \tag{3.11}$$

From the equation dV is the volume of the detector, ρ_{Si} is the density of silicon whose value is given as 2.33 g/cm^3, A is the effective area of the detector, d is the thickness of the detectors and N_i is the particles counted by the detector. K is the conversion factor and this constant is used to convert the deposited energy (from MeV units to J) by the particles into the detector to obtain $\mathcal{D}_{\mathrm{Si}}$ in units of Gy.

Traditionally, the conversion from Equation 3.11 to describe the absorbed dose in water is carried out by multiplying values of $\mathcal{D}_{\mathrm{Si}}$ by a factor $F_{\mathrm{Si}\rightarrow\mathrm{H_2O}}$. At commercial aviation altitudes, *Beaujean et al.* [2005] estimate a conversion factor of $F_{\mathrm{Si}\rightarrow\mathrm{H_2O}} = 1.20$. By formulation the total absorbed $\mathcal{D}$ in water is expressed as

$$\mathcal{D}_{\mathrm{H_2O}} = \mathcal{D}_{\mathrm{Si}} \cdot F_{\mathrm{Si}\rightarrow\mathrm{H_2O}}. \tag{3.12}$$

For TOA dosimetry, this conversion factor is incapable of accounting for the presence of particles with higher charge numbers, hence it is only applicable at aviation altitudes (see, *Beaujean et al.* [2005]).

3.4.2 Linear Energy Transfer

The linear energy transfer, $\mathcal{L}$, (a term coined by *Zirkle et al.* [1952]) in radiation protection is described as the radiation energy loss, dE, of charged particles per unit length of a path, dl, through matter [*ICRP103*, 2007]. Experimentally, $\mathcal{L}$ is the energy loss of charged particles interacting with the target material per path length $dEdx$ (as given by Equation 3.1). *Dönsdorf* [2013] acknowledges that, for charged particles which are directly ionizing matter, it is possible to measure $\mathcal{L}$. On the other hand, with indirect ionising radiation such as photons and neutrons it is rather complicated to measure $\mathcal{L}$ and to determine the resulting dosimetric quantities dependent on $\mathcal{L}$ because all secondary radiation which is created in the interaction with matter has to be taken into account. Mathematically, this parameter in silicon detectors is expressed

as

$$\mathcal{L}_{\mathrm{Si}} = \frac{d\mathrm{E}}{dl}. \tag{3.13}$$

The SI unit of the parameter $\mathcal{L}_{\mathrm{Si}}$ is J/m. However, for dosimetric purpose the keV/μm unit is mostly used. Experimentally, $d\mathrm{E} \approx \Delta\mathrm{E}$ where $\Delta\mathrm{E}$ is the measured energy loss and $dl \approx \Delta x$ is the thickness of the SD.

For the calculation of the $\mathcal{L}$ in water, i.e. $\mathcal{L}_{\mathrm{H_2O}}$, the conversion factor and the density ratio of water and silicon are used as

$$\mathcal{L}_{\mathrm{H_2O}} = \frac{d\mathrm{E_i}}{l_{\mathrm{eff}}} \cdot F_{\mathrm{Si}\to\mathrm{H_2O}} \cdot \frac{\rho_{\mathrm{H_2O}}}{\rho_{\mathrm{Si}}}, \tag{3.14}$$

where $\rho_{\mathrm{H_2O}}$ is the density of water whose value is given as 1 g/cm^3 and l_{eff} is the effective length calculated in Appendix C. In principle if the conversion from one form of $\mathcal{L}$ to another through multiplication by a constant is adequate, then the ratio of the two forms of $\mathcal{L}$ as a function of energy should also yield a constant. Since the parameter $\mathcal{D}_{\mathrm{Si}}$ or $\mathcal{D}_{\mathrm{H_2O}}$ does not account for the biological effectiveness of different kinds of ionizing radiation as mentioned, the first step of accounting the biological damage in tissue is the conversion of $\mathcal{L}_{\mathrm{Si}}$ to $\mathcal{L}_{\mathrm{H_2O}}$. This is essential to indirectly estimate the energy deposition in tissue through the detector measurements. Now, according to the Equation 3.14 if the conversion factor and constants are substituted, the $\mathcal{L}_{\mathrm{H_2O}}$ is about half of $\mathcal{L}_{\mathrm{Si}}$. The $\mathcal{L}$ rates, i.e. $\mathcal{L}_r$, can be calculated by dividing the $\mathcal{L}$ by the time of measurement.

3.4.3 Quality Factor

The quality factor, $\mathcal{Q}_f$, is a dimensionless parameter used to characterise the biological effectiveness of different kinds radiation impacts. As explained in the *ICRP103* [2007], the difference in the biological effectiveness occurs as a result of different ionisation density along the tracks of charged particles. In the ICRP, $\mathcal{Q}_f$ is described as a smooth function of the $\mathcal{L}$ of charged particles in water, i.e. $\mathcal{Q}_f(\mathcal{L}_{\mathrm{H_2O}})$, since *ICRP60* [1991]. For charged particles, the $\mathcal{Q}_f(\mathcal{L}_{\mathrm{H_2O}})$ relationship is the most simple and widely used in space dosimetry (see, *ICRP123* [2013]) and aviation dosimetry (see, *ICRP132* [2016]) expressed as recommended by *ICRP103* [2007], i.e.

$$\mathcal{Q}_f(\mathcal{L}_{\mathrm{H_2O}}) = \begin{cases} 1.0, & \text{for } \mathcal{L}_{\mathrm{H_2O}} \le L_i. \\ a_0\left(\frac{\mathcal{L}_{\mathrm{H_2O}}}{L_0}\right) - a_1, & \text{for } L_i \le \mathcal{L}_{\mathrm{H_2O}} \le L_f. \\ a_2\left(\frac{L_0}{\mathcal{L}_{\mathrm{H_2O}}}\right)^{a_3}, & \text{for } \mathcal{L}_{\mathrm{H_2O}} \ge L_f. \end{cases} \tag{3.15}$$

The constants of this piecewise continuous function, i.e. L_0, L_i, L_f, a_0, a_1, a_2 and a_3 are given in Table 3.1. Given that, estimation of dosimetric quantities that rely on $\mathcal{Q}_f(\mathcal{L}_{\mathrm{H_2O}})$ is

still under intense study, it is not surprising that the recommended radiation quality factors associated with them continuously change. The $\mathcal{Q}_f$ has been modified several times and the constants given in Table 3.1 represent the last two modifications.

TABLE 3.1: Constants used to represent the relationship between $\mathcal{Q}_f$ and $\mathcal{L}_{H_2O}$ in Equation 3.15.

	Parameter constants						
Publication	L_0 [keV/μm]	L_i [keV/μm]	L_f [keV/μm]	a_0	a_1	a_2	a_3
ICRP26 [1977]	1.00	3.50	172.5	0.11	0.06	20.0	0
ICRP103 [2007]	1.00	10.0	100	0.32	2.20	300	0.50

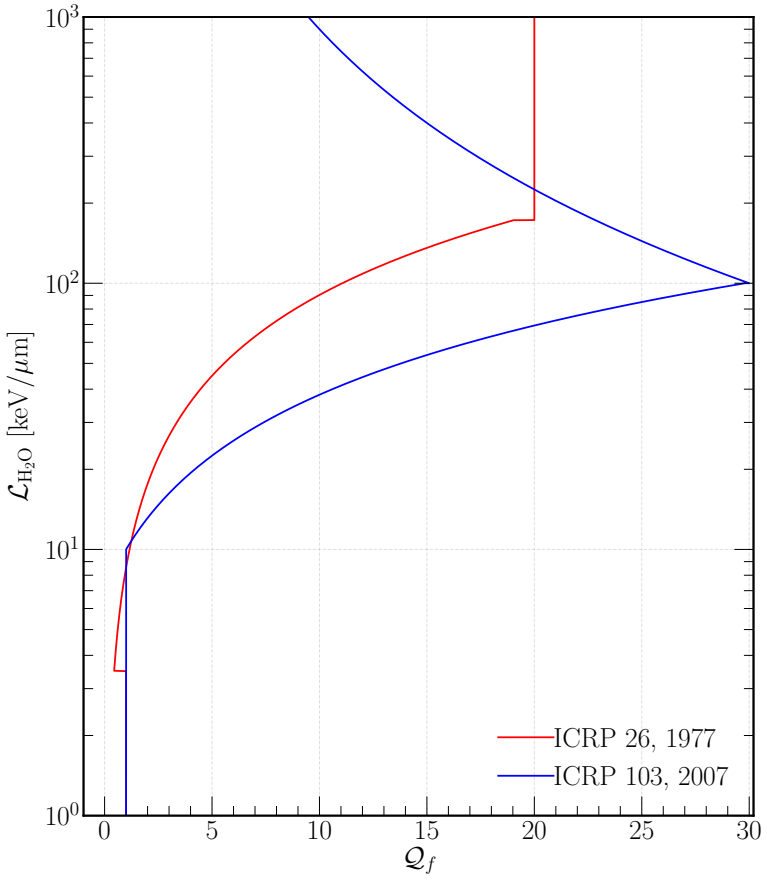

FIGURE 3.2: Quality factor, $\mathcal{Q}_f$, as a function of $\mathcal{L}_{H_2O}$ as given by either *ICRP26* [1977] or *ICRP103* [2007].

Figure 3.2 shows the functional dependence of $\mathcal{Q}_f$ on $\mathcal{L}_{H_2O}$, (Equation 3.15). The values of $\mathcal{Q}_f$ represented in this figure have been derived empirically from biological experiments. The *ICRP26* [1977], *ICRP103* [2007] comparison shows the differences seen in the definition of radiation quality proposed by the ICRP and their evolution with time. Visual inspection from the figure shows that at $\mathcal{L}_{H_2O}$ about 100 $keV/\mu m$, the *ICRP103* [2007] curve has an unfortunate cusp, while the *ICRP26* [1977] curve about 110 $keV/\mu m$ and above flattens. There

is no theoretical evidence to suggest that the $\mathcal{Q}_f$ remain constant for high-$\mathcal{L}_{H_2O}$ in *ICRP26* [1977] or reach a maximum point value and transform immediately from a linear relationship into a power function proportional to $1/\sqrt{\mathcal{L}_{H_2O}}$ in the *ICRP103* [2007]. The ICRP noted that the dependence of $\mathcal{Q}_f$ on $1/\sqrt{\mathcal{L}_{H_2O}}$ is a simplification due to lack of knowledge to assign a more precise relationship. Discussions have been ongoing within NASA[8] about a possibility of replacing quality factors currently being used by the ICRP with a new definition that does not directly depend on $\mathcal{L}$ [*Cucinotta et al.*, 2013]. Hence, the stumbling block is how this new definition can be implemented with instrumentation. The serious shortcoming of the parameter $\mathcal{Q}_f$ concept is that this parameter has not been defined in terms of physically measurable quantities. However, its values can be extrapolated experimentally. In this work, the use of $\mathcal{Q}_f$ and $\mathcal{L}$ concepts is continued while recognizing the possibility that future changes in characterization of biological impact may require the use of new measurement quantities.

3.4.4 Dose Equivalent

The dose equivalent is broadly described as the product of the absorbed dose and the quality factor in *ICRP103* [2007]. In silicon detectors, total dose equivalent can be obtained as

$$\mathcal{H}_{Si} = \langle \mathcal{Q}_f \rangle \cdot \mathcal{D}_{Si}, \tag{3.16}$$

where the SI unit of this parameter also has the quantity J/kg with the name Sievert (Sv) (named after the Swedish scientist Rolf Sievert) used to distinguish it from absorbed by a non-biological body the unit Gray. The mean quality factor is given by $\langle \mathcal{Q}_f \rangle$. In water, dose equivalent parameter, i.e. $\mathcal{H}_{H_20}$, is calculated by multiplying $\mathcal{H}_{Si}$ with the conversion factor $F_{Si \to H_2O}$.

3.4.5 Effective Dose

According to *ICRP103* [2007], the effective dose, $\mathcal{E}_\mathcal{D}$, is recommended for "*the prospective dose assessment for planning and optimisation in radiological protection, and demonstration of compliance with dose limits for regulatory purposes.*" It is also recommended that the effective dose should not be used "*for epidemiological evaluations, nor should it be used for detailed specific retrospective investigations of individual exposure and risk.*" This parameter is given as

$$\mathcal{E}_\mathcal{D} = \sum_T \mathcal{W}_T \sum_R \mathcal{W}_R \mathcal{D}_{T,R}, \tag{3.17}$$

[8] https://www.nasa.gov/

where $\mathcal{W}_R$ is a dimensionless parameter called the radiation weighting factor, while $\mathcal{W}_T$ is the tissue weighting factor. $\mathcal{D}_{T,R}$ is the mean absorbed dose in the corresponding organ or tissue T due to radiation of type R. The parameter $\mathcal{E}_\mathcal{D}$ also refers to energy deposition in a mass element, with units of Sievert (Sv).

Note that the value at ground and sea-level are given as $\mathcal{E}_\mathcal{D}$ (the protection quantity), whereas for the purpose of dose assessment of flight personnel and passengers at aviation altitudes, the parameter $\mathcal{H}$ (the routine operational quantity) is used. The protection quantities, i.e. $\mathcal{E}_\mathcal{D}$, is indirectly measurable, hence a routine operational quantity, $\mathcal{H}$, can be used as an estimation for the protection quantity. However, for some assumptions it is reasonable to use the parameter $\mathcal{H}$ as an estimate for the parameter $\mathcal{E}_\mathcal{D}$. For more information or clarity, see *Bartlett* [2004] and references therein.

3.4.6 Ambient Dose Equivalent

The ambient dose equivalent describes a dose measurement in a specific area. The ambient dose equivalent measurements are done in free air and as a result it underestimates the dose equivalent due to the fact that secondary particles are produced in a human body and this can potentially increase the dose equivalent [*Möller*, 2013]. The ambient dose equivalent is a routine operational quantity for area monitoring, similar to the parameter $\mathcal{H}$. According to the *ICRP103* [2007], the ambient dose equivalent, $\mathcal{H}^*(d)$, is defined as: "*The dose equivalent at a point in a radiation field that would be produced by the corresponding expanded and aligned field in the International Commission on Radiation Units and Measurements* (ICRU) *sphere* (*30 cm diameter soft tissue equivalent sphere with a density of 1 g/cm*^{3}) *at a depth of d mm on the radius vector opposing the direction of the aligned field.*" The SI unit of $\mathcal{H}^*(d)$ is J/kg with a special name known as Sievert (Sv). For strongly penetrating radiation, a depth of 10 mm is recommended and this is denoted by $\mathcal{H}^*(10)$.

3.5 Effects of Ionizing Radiation

The fact that a human body has no organ of perception for ionizing radiation and that some kind of energy deposition can damage the deoxyribonucleic acid (DNA) in our biological cells, produce free radicals and disrupt bonds, radiation exposure is a serious concern and should be monitored and measured. Indirect effects, similar to what one would obtain when irradiating a living tissue with ionizing radiation are discussed below.

A human body comprises mainly water [*Flowers et al.*, 2018]. Naturally, water can be ionised, to demonstrate the impact of ionizing radiation in tissue, water can indirect be used for demonstration. In this case, the absorbing of radiation through water is expected to trigger a series of reactions forming free radicals. Due to the fact that the hydroxyl radicals have an unpaired electron, they are highly reactive and can react with all kinds of biological molecules (e.g. DNA, proteins, etc.), causing damage to the molecules and disrupting bonds and biological processes [*Flowers et al.*, 2018]. These radical species can interact with biomolecules as illustrated in Figure 3.3.

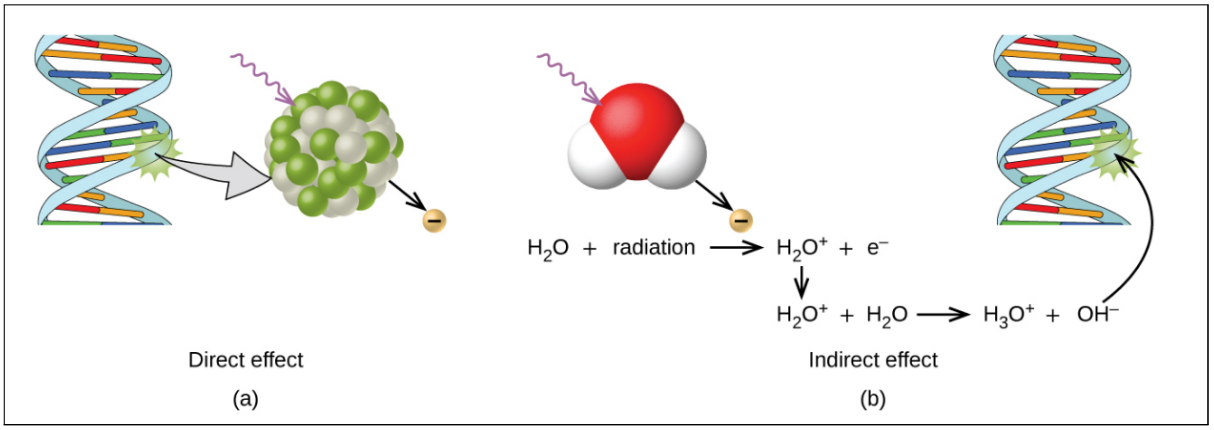

FIGURE 3.3: Ionizing radiation induces direct DNA damage and indirect damage through the radiolysis of water. Image credit: *Flowers et al.* [2018].

The *ICRP103* [2007] outlines and demonstrates this effect through Figure 3.2. When humans are exposed to ionizing radiation, the characteristics of $\mathcal{Q}_f$ in tissue are described as the secondary damage through the formation of free radicals in water as outlined and shown in Figure 3.3. If [1] $\mathcal{Q}_f = 1$, i.e. when the $\mathcal{L}_{\mathrm{H_2O}}$ is below 10 $keV/\mu m$, this is generally considered as not harmful and with good treatment cells damaged by these free radicals can be repaired correctly. Muons, X-rays, photons, positrons and electrons are almost always low-$\mathcal{L}_{\mathrm{H_2O}}$. When [2] $\mathcal{Q}_f$ is between 1 and 30, i.e. $10 < \mathcal{L}_{\mathrm{H_2O}} < 100$ $keV/\mu m$, this represents a case where the cell repair mechanism fails or cells are repaired incorrectly which might potentially lead to cell mutation effects such as cancer[9] cells [*National Research Council*, 2006, *Hellweg and Baumstark-Khan*, 2007]. Here, treatment can be useful to slow down the mutation rate. When $\mathcal{L}_{\mathrm{H_2O}}$ is 100 $keV/\mu m$, this point represents a transition phase where cell mutation stops and all damaged cells start dying. Alpha particles, pions, and neutrons are considered to be high-$\mathcal{L}_{\mathrm{H_2O}}$ radiation. Excluding the range near 10 $keV/\mu m$, and a proton is low-$\mathcal{L}_{\mathrm{H_2O}}$. However, protons are more damaging compared to other low-$\mathcal{L}_{\mathrm{H_2O}}$ radiation (see, *Hada and Sutherland* [2006]). Therefore, when radiation estimates are measured or calculated, protons are sometimes

[9] This work is aware that there are many different forms of cancer and the cell processes that lead to radiation sickness and diseases are publicly not well understood. Hence, the explanation given here is much simpler than the actual process

classified as high-$\mathcal{L}_{H_2O}$ radiation. Then, when [3] $\mathcal{L}_{H_2O} > 100\ keV/\mu m$, $\mathcal{Q}_f$ decreases as cells start dying as a result of being exposed to very high-$\mathcal{L}_{H_2O}$ radiation or a process initiated at $10 < \mathcal{L}_{H_2O} < 100\ keV/\mu m$. The processes at $\mathcal{L}_{H_2O} > 100\ keV/\mu m$ are therefore called programmed cell death, although it is more commonly called apoptosis[10] (from a Greek word meaning "falling off" as leaves from a tree).

3.5.1 Stochastic and Deterministic Effects

When humans are exposed to ionizing radiation, radiation protection measures are necessary because of the relative biological effects. These relative biological effects describe the ability of radiation to induce biological outcomes, for example DNA damage. Generally, the doses are measurable, but the effects are not and they are unpredictable. In order to study the effects of ionizing radiation effectively, high doses have to be measured in a short period of time and low doses for long period of time. If high doses are measured on long-time scales, cells will die almost instantly and the effects will not be known. Similarly, low doses have to be measured on long-time scales for effects to be seen. However, if low doses are measured on a short-time scale, there will not be any damage since cells can repair quickly enough, but for this effects due to exposure will not be notable. Therefore, the probability of damage in human bodies depends on the intensity of the radiation field. This distinguishes between deterministic and stochastic radiation damage.

Deterministic effects such as radiation sickness occur as a result of cells dying following a post exposure to high ionising radiation doses over a short period of time. The seriousness of the effects depends on the magnitude of the doses absorbed. If the amount of absorbed radiation dose involved is large enough, i.e. $\sim$1000$-$2000 mSv, this effect can manifest itself within a period of hours, days or few weeks. At low doses the cell repair mechanism and repopulation can keep up with the rate of cell damage and destruction, but at high doses it cannot. As a result, this type of effect is strongly dependent on the radiation doses. However, these effects need not be considered a health hazard at the low dose of $\sim$0.1 mSv delivered by X-ray scanners because of the threshold dose recommendation in the *ICRP60* [1991] and *ICRP103* [2007] (see reviews by *Wrixon* [2008] and *Stewart et al.* [2012]). In the *ICRP103* [2007], the threshold for deterministic effects is proposed to be above the X-ray scanners threshold, while below this threshold the effect does not occur. However, possible subsequent stochastic radiation damage cannot be excluded below the 0.1 mSv threshold, hence the survivors of deterministic effects are at risk of stochastic effects [*Gusev et al.*, 2001].

[10] A normal, genetically regulated process leading to the death of cells and triggered by the presence or absence of certain stimuli, as DNA damage. https://www.dictionary.com/browse/apoptosis

Stochastic effects occur as a result of cells not dying post exposure to ionising radiation, but the cells' genetic "make-up" is modified. These effects are usually associated with exposure to low doses of ionising radiation and this often shows up years or decades after exposure. However, at no time, even for high ionising radiation doses, is it certain that stochastic effects will result. Therefore, stochastic effects are assumed to have no threshold. Hereditary disorders and incidences of cancer after low dose radiation exposure are examples of a stochastic effect [*ICRP103*, 2007]. However, cancer, as a stochastic effect, results due to DNA modification post exposure to ionizing radiation, where the DNA chain is damaged and repaired incorrectly. It seems reasonably clear that genetic mutations and cancer are interrelated, but the precise mechanisms involved have yet to be clarified. Generally, the term "stochastic" means the process is governed by the laws of probability. The seriousness of cancer is independent of the doses, but the probability of developing cancer is proportional to the doses received. However, due to this fact that the probability of stochastic effects increases with any exposure and during commercial aircraft flights, the intensity of ionising radiation increases with higher altitudes (or lower geomagnetic vertical cutoff rigidity and solar modulation), radiation monitoring is of importance for the aircraft crew.

For more information about the effects of ionizing radiation, see *Failla* [1941], *Hellweg and Baumstark-Khan* [2007], *Flowers et al.* [2018], *Kontomaris et al.* [2019], *Bakar et al.* [2019].

3.6 Summary

The parameter $\mathcal{D}$ is not usually of as much interest from a radiation protection standpoint. As a result, the ICRP and the ICRU established the quality factor, $\mathcal{Q}_f$, which depends on the linear energy transfer, $\mathcal{L}$. When used together, the $\mathcal{D}$ and $\mathcal{Q}_f$ parameters are significant in the calculation of parameters most important for operational radiation protection. However, for routine operational aerial monitoring, the parameter $\mathcal{H}$ and $\mathcal{H}^*(10)$ are mostly used. Modern dosimetry instruments make it possible to measure and monitor these dosimetric quantities. Exposure to ionizing radiation, depending on the type of radiation and the amount of energy deposited, can potentially damage our DNA make-up and set a chain of events in motion that can potentially result in cancer for cases where cells were incorrectly repaired. This makes radiation monitoring with portable dosimeters a priority at aviation altitudes, taking into account the recommendations in the ICRP.

CHAPTER 4

Aviation Radiation Model

4.1 Introduction

Publicly accessible literature relevant for commercial flight dose assessment is widely available. However, the availability of free and reliable computer software tools (CSTools), which can be used to potentially estimate aviation doses, is limited. The 2012 European Radiation Dosimetry Group's (also known as EURADOS[1]) [*Bottollier-Depois et al.*, 2012], report contains comparisons of several modern CSTools used for assessing radiation exposure of flight personnel and passengers due to GCRs and SEPs. Most of these CSTools are based on either measurements taken during aircraft flights or atmospheric modelling simulations or a combination of both.

The CSTool investigated in this work, i.e. the Civil Aeromedical Research Institute (CARI)[2] model from the Federal Aviation Administration, is a physics-based model that take into account a set of mathematical expressions describing the spectra of impinging primary particles, their transport through the geomagnetic field, and the production of the secondary radiation field through the atmosphere that dominates the radiation exposure at aviation altitudes.

To estimate the radiation dose and dose rate experienced by flight personnel, in the past and present, at aviation altitudes by commercial aircrafts using CARI-7/7A at any geographic flight position for a specific date, knowledge of the particles' energy spectra is needed. The overview given in this work for the chosen CSTool is restricted to brief descriptions, while a more detailed discussion, not repeated in this work, is given in the corresponding references. In most publications, the reliability of dosimetric quantities calculated using CSTools depends on the accuracy of the CSTool's fit to measurements. However, because the CSTool calculations

[1] www.eurados.org

[2] https://www.faa.gov/data_research/research/med_humanfacs/aeromedical/radiobiology/cari7/

of dosimetric quantities are simply approximations of measurements expected from dosimeter instruments, uncertainties are expected due to the CSTool's setup, the considered assumptions within the CSTool, and the assumed cosmic-ray spectra at Earth. Therefore, the reliability of CARI-7A in this work, for purposes of characterizing radiation for commercial aircrafts, is assessed on the basis of these points:

- Dose and dose rate simulations must show a clear dependence on the geomagnetic vertical cutoff rigidity (P_c), altitude, solar activity and transient solar events.
- For balloon flight simulations, it must show the dose and dose rate's evolution with altitude, while the Regener-Pfotzer's maximum (Regener-Pfotzer's maximum) dependence on P_c does not change with respect to solar activity levels as reported by *Sarkar et al.* [2017] and references therein.

It is worthwhile to note that the dose and dose rate calculations to be discussed in this work for commercial aircraft do not take into account the aircraft shielding. Therefore, this work assumes that the doses and dose rate distributions inside and outside of the aircraft are the same. The secondary radiation field of interest in this work includes the largest dose contributors, namely the proton and neutron component, which CARI-7A is capable of calculating. As described in the *ICRP103* [2007], the ambient dose equivalent, $\mathcal{H}^*(10)$, (used as an operational quantity) is an adequate approximation for the effective dose, $\mathcal{E}_\mathcal{D}$ (mostly used as a legal regulatory for flight personnel). Therefore, because the flight personnel and passengers (composed of different age groups) are exposed to a wide range of particle species at these altitudes, all interacting with their bodies at the same time, the results presented here are the total ambient dose equivalent, $\mathcal{H}^*(10)$, consisting of contributions of all secondary particles instead of the individual species.

It should be mentioned that an offline CARI CSTool (manually updated) is available free of charge and this CSTool was certified by the United States of America (USA) Federal Aviation Administration (FAA) for routine aviation dose assessment. The CSTool will be briefly described and general results presented. Throughout this chapter, flight altitudes will be mainly given in residual atmosphere (in units of g/cm^2) which decreases with increasing geodetic altitudes.[3]

4.2 The CARI Model

The development of the CARI CSTool for calculating doses and dose rates at aviation flight altitudes and above began in the late 1980s. The latest versions, i.e. CARI−7 and CARI−7A,

[3]Broadly, geodetic altitudes can be defined as the vertical distances above the local ground surface (or sea level)

were developed in 2009 [*Copeland et al.*, 2010, 2012]. This new version was developed to improve several limitations of CARI−6. In addition, one of the improvements from the old version is that CARI−7/7A altitude limit for calculations has been extended from $\sim$ 18.84 g/cm^2 (27 km) to 0.58×10^{-3} g/cm^2 (100 km). A detailed description of CARI−7/7A's development and validation were published by *Copeland* [2017a] and it was first made widely available in February 2017. Since it was released, improvements have been made continuously as motivated by user feedback.

Three physics-based models are employed by CARI-7/7A to transport cosmic-rays through the heliosphere, geomagnetic field, and the Earth's atmosphere respectively. These are: [1] For CARI−7/7A, the transport of GCRs through the heliosphere is calculated using the Badhwar-O'Neill GCR model [*O'Neill*, 2010, *O'Neill*], which solves the spherically symmetric Fokker-Planck equation, while the solar proton contribution is calculated using a simple slant function similar to that used by *Sato* [2016]. [2] Transport through the geomagnetic field is parameterized in vertical cutoff rigidities, P_c as calculated by interpolation from tables calculated by *Shea and Smart* [2001] and *Smart and Shea* [2005]. To account for both quiet and very disturbed geomagnetic conditions in P_c, depending on the state of the planetary Kp index,[4] Equation 2.10 was used. [3] Cosmic-rays are transported through the neutral atmosphere using the Monte Carlo program MCNPX 2.7.0 (available from Oak Ridge National Laboratory). This is used to calculate a database of atmospheric particle spectra resulting from isotropically incident primary GCR particles. All the TOA cosmic-ray spectra models and cutoff rigidities interpolations can be selected at runtime.

The dose and dose rates can be estimated using the provided CARI−7/7A Fortran source code which allows user defined values either at a single or multiple positions at any date and time between 1958 and present. The model makes it possible to choose even known solar storms events for dose and dose rate calculations. Also, users are spoiled for choice due to the availability of several types of radiation doses, namely the whole-body, absorbed dose in a 0.3 (or 0.5) mm silicon chip [*Copeland*, 2017b]; ambient dose equivalent $\mathcal{H}^*(10)$, effective dose $\mathcal{E}_\mathcal{D}$ [*ICRP60*, 1991, *ICRP103*, 2007], and any desired models of GCRs to calculate secondary particle fluence (particles/cm^2) spectra.

The simulation settings for the CARI-7A model were chosen as: Option [1] Galactic radiation received on flights <2> $\longrightarrow$ Option [2] Flight route (s) defined by many waypoints <2> $\longrightarrow$ Option [3] Select input file $\longrightarrow$ Option [4] Select radiation <0> $\longrightarrow$ Option [5] GCR: ISO TS15390:2004-MSU-NYMMIK model <1>, which uses a modulation potential $\longrightarrow$ Option [6] Select dose type - ICRU $\mathcal{H}^*(10)$ Ambient Dose Equivalent <4> $\longrightarrow$ Option [7] Use the

[4] https://omniweb.gsfc.nasa.gov/form/dx1.html

superposition approximation <Y> ⟶ Option [8] Use dates from flight data file <Y>. The modulation potentials used in this work were re-calculated through a procedure described in Appendix A and stored in a file called "SOLARMOD".

4.3 Flight Routes Information

For demonstration, two flight route case studies chosen for characterizing high altitude radiation are presented in this work. For case [1], the commercial flight changes with respect to P_c at a fixed altitude. In this case, three direct flights departing from the Southern to the Northern Hemisphere (i.e. Northbound flights), also three Westbound, and three Eastbound flights, all departing from the same geographic longitude, are discussed. The basic criterion is that all these flights must have flight durations that exceed 7 hours to qualify as long-haul flights. The great circle approximations offer an opportunity to choose only one starting (ending) point (i.e. longitude and latitude) that represents any desired departure (destination) and the corresponding destination (departure).

The choice of the great circle approximations for this demonstration stems from the fact that:

- In most cases, long-haul flights tend to follow a great-circle route to reduce flight cost [*Yang and Sheu*, 2018].
- Data from flight route tracker companies like FlightRadar24,[5] are not always available free of charge and sometimes companies like FlightAware[6] publish free data that are often not reliable and can contain too many data gaps, or there is no data available for that flight.

Northbound flights are presented as: Australia (AUS) (121.90E, 26.39S) → China (ROC) (121.90E, 43.65N), South Africa (RSA) (26.24E, 26.39S) → Bulgaria (BUL) (26.24E, 43.65N) and Argentina (ARG) (70.32W, 26.39S) → United States of America (USA) (70.32W, 43.65N). The Eastbound flights are presented as: RSA (26.24E, 26.39S) → AUS (121.90E, 26.39S), Democratic Republic of the Congo (DRC) (26.24E, 0.52N) → Indonesia (IDN) (121.90E, 0.52N), BUL (26.24E, 43.65N) → ROC (121.90E, 43.65N); while the Westbound flights are presented as: RSA (26.24E, 26.39S) → ARG (70.32W, 26.39S), DRC (26.24E, 0.52N) → Brazil (BRZ) (70.32W, 0.52N), BUL (26.24E, 43.65N) → USA (70.32W, 43.65N), respectively. These flights, in their respective directions, are assumed to depart at the same time, while Eastbound and Westbound depart from the same geographic longitude of 26.24E; with all the Northbound flights set to depart from the same geographic latitude of 26.39S.

[5] https://flightradar24.com/
[6] https://flightaware.com/

For case [2], high altitude stratospheric trajectories from ground-level up to $\sim$ 2.83 g/cm^2 (40 km) (in principle) within a constant P_c are examined. The estimation of stratospheric radiation using balloons is a very old subject of interest and it has been performed since 1911, dating back to Hess' time [*Hess*, 2018]. Recently, many attempts have been made to measure the evolution of radiation levels mainly at mid and high-latitudes; see *Bazilevskaya and Svirzhevskaya* [1998], *Yaniv et al.* [2016], *Sarkar et al.* [2017]. According to *Dyer et al.* [2018] (as suggested by *Nicoll and Harrison* [2014]), small and portable detectors can be developed as a rapid-response system for measuring the evolution and impact of GLE events. However, there are practical issues about launching these detectors any time at any desired location, e.g. at the geomagnetic poles, and assuming they will follow the same trajectory for a fair comparison under similar environmental conditions but on different time scales. Three sites, chosen at ground-level for demonstration of stratospheric radiation levels are: The two geomagnetic poles and the equator (South-East Asia). The equatorial coordinates 2.218°S and 115.6628°E in South-East Asia were chosen. The North magnetic pole coordinates 86.448°N and 175.346°E, and the South magnetic pole coordinates 64.147°S and 135.924°E were chosen based on the IGRF[7] model. In this work it is acknowledged that the chosen geographic location do not remain fixed over decadal periods as discussed in Chapter 2 and several other publications.

The two cases discussed above, will be analyzed during a quiet solar minimum and maximum and also during FD and GLE events, respectively. The chosen dates for a quiet solar minimum and maximum are 2009/12/30 and 2014/04/03, respectively, while GLE69 and the FD of 2005/01/20 and 1991/06/13 are chosen respectively. GLE69 is the second largest in the neutron monitor era.

4.4 Flight Simulation Settings

For aircraft flight route simulations, an INVERSE3D (Python) software library, based on the World Geodetic System 1984 (WGS84) model, was downloaded and used to calculate the great circle routes. During these calculations, the geographic latitude could not be set to zero for equatorial flight routes, because the WGS84 model breaks down. When calculating the great circle distance, the total flight time can also be estimated. From this total flight time, the time elapsed between consecutive geographic coordinates along the flight trajectory can be approximated according to the operational speed of the chosen aircraft. However, different aircraft have different speed profiles and each has a specific procedure for take−off and landing.

[7] https://www.ngdc.noaa.gov/geomag/GeomagneticPoles.shtml

A constant cruise speed of 786 km/h was estimated and assumed for all flights, while the average cruise altitude for this demonstration was assumed to be 197.11 g/cm^2 ($\sim$ 9 km).

For stratospheric flight simulations, trajectories changing with altitude from ground-level were generated using the Cambridge University Spaceflight (CUSF) Standalone Predictor[8] that is mostly used for forecasting meteorological wind profiles for balloon flights. This flight predictor uses a customized data format extracted from the National Oceanic and Atmospheric Administration's (NOAA's) Global Forecast System. The balloon flight output file provides the time (UTC[9]), latitude, longitude and altitude of trajectory coordinates. For analyses, due to different mechanisms involved in the ascent and decent balloon flight trajectory, only the ascent phase was considered.

The data generated from the WGS84 and CUSF flight predictor are used as the user defined option in CARI−7/7A. To facilitate repeated analyses of these flight routes for different solar activity conditions, the CARI−7A Fortran source code was modified to support that.

4.4.1 The Longitude Flight Effect

For a more realistic visualization of the flights projection, all flights from the three departure points are assumed to take−off at the same time. The computed geographic coordinates from the WGS84 model was used in CARI−7A to calculate the dosimetric quantity $\mathcal{H}^*(10)$ and P_c, respectively. Table 4.1 gives an overview of the flights simulations, listing the individual flight routes, distances, durations and the covered P_c interval.

Table 4.1: Great-circle approximation flight information.

Flight route	Flight distance [km]	Flight Time [hour]	P_c [GV]
RSA → AUS	9268	11.8	6.95→7.41
RSA → ARG	9348	11.9	6.95→14.58
DRC → IDN	10648	13.6	14.61→16.19
DRC → BRZ	10748	13.7	14.61→12.55
BUL → ROC	7231	9.2	5.37→5.55
BUL → USA	7289	9.3	5.37→ 1.93

In Figure 4.1 the flight paths of the East and West bound flight routes are shown in blue, while the Northbound flight routes discussed in the next section are shown in red. The West and East bound flights are shown in blue, while north bound flights are shown in red.

[8] https://github.com/jonsowman/cusf-standalone-predictor/
[9] UTC : Coordinated Universal Time

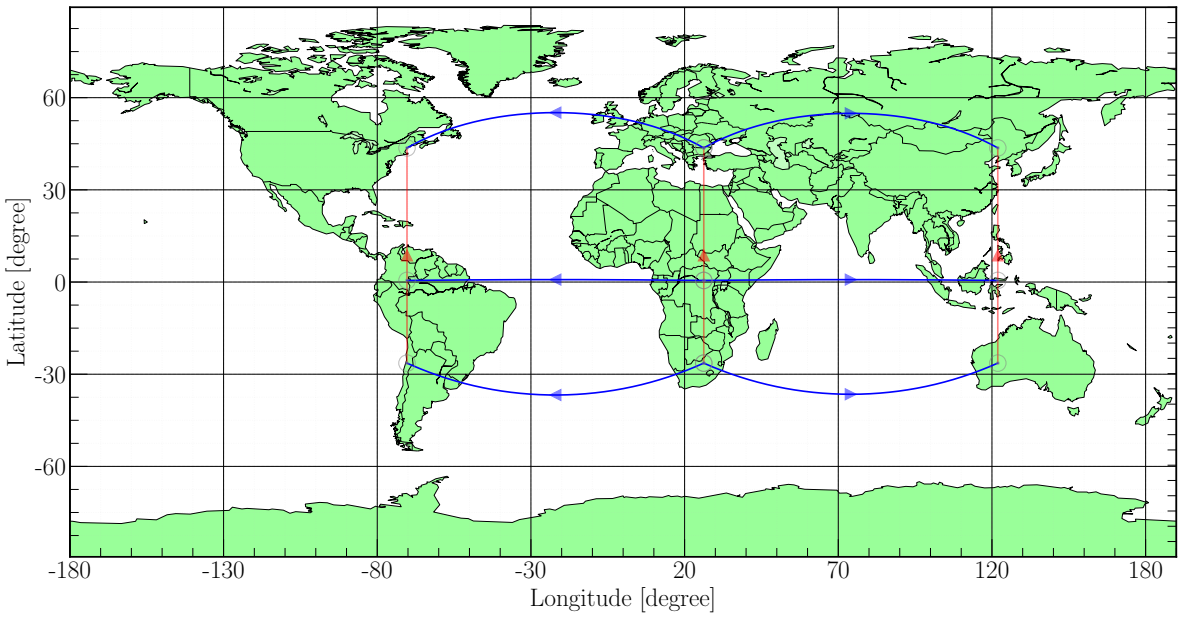

FIGURE 4.1: Representative great circle approximations of the chosen flight routes are shown for demonstration on a world map.

Figure 4.2 shows the constructed $\mathcal{H}^*(10)$ profile for each flight as a function of elapsed flight time at a cruise altitude of 197.11 g/cm^2 ($\sim$ 9 km). The calculated $\mathcal{H}^*(10)$ profile between take−off and the initial aircraft cruising altitude was discarded, along with the final descent. This was done to create a fair comparison between all these flights departing and landing at different altitudes. The summarized results of Figure 4.2 are detailed in Table 4.2, which also presents a comparison between the accumulated total $\mathcal{H}^*(10)$ for all the chosen periods of simulation to a standard chest X-ray dose. There is a fundamental difference between a continuous dose over a year set for a general member of the public from cosmic-rays and radionuclides in the Earth's crust and doses that occur over a few seconds like in chest X-ray, but the comparison is helpful.

Comparing the West and East bound individual accumulated total $\mathcal{H}^*(10)$ in the North, equator and Southern Hemisphere as expected, doses calculated at the quiet solar minimum were higher than those calculated during the solar maximum, except for the East bound flight DRC $\rightarrow$ IDN along the equator. For all results of $\mathcal{H}^*(10)$ calculated for the GLE and FD events, note that the accumulated total $\mathcal{H}^*(10)$ in the table does not tell the whole story, as some flights show that it is possible to get a higher dose during FD events compared to GLE events. For all these flights, the $\mathcal{H}^*(10)$ ratios calculated at solar minimum (GLE) to those at the solar maximum (FD) varied in the range of $\sim$0.9-1.3 ($\sim$0.9-1.1), and it appeared as though the flight BUL $\rightarrow$ USA (DRC $\rightarrow$ BRZ) corresponded to a higher ratio and higher dose accumulation during solar minimum (GLE event). However, the West bound flight DRC $\rightarrow$ IDN corresponded to a lower dose ratio and higher dose accumulation during solar maximum (FD event). Comparing the

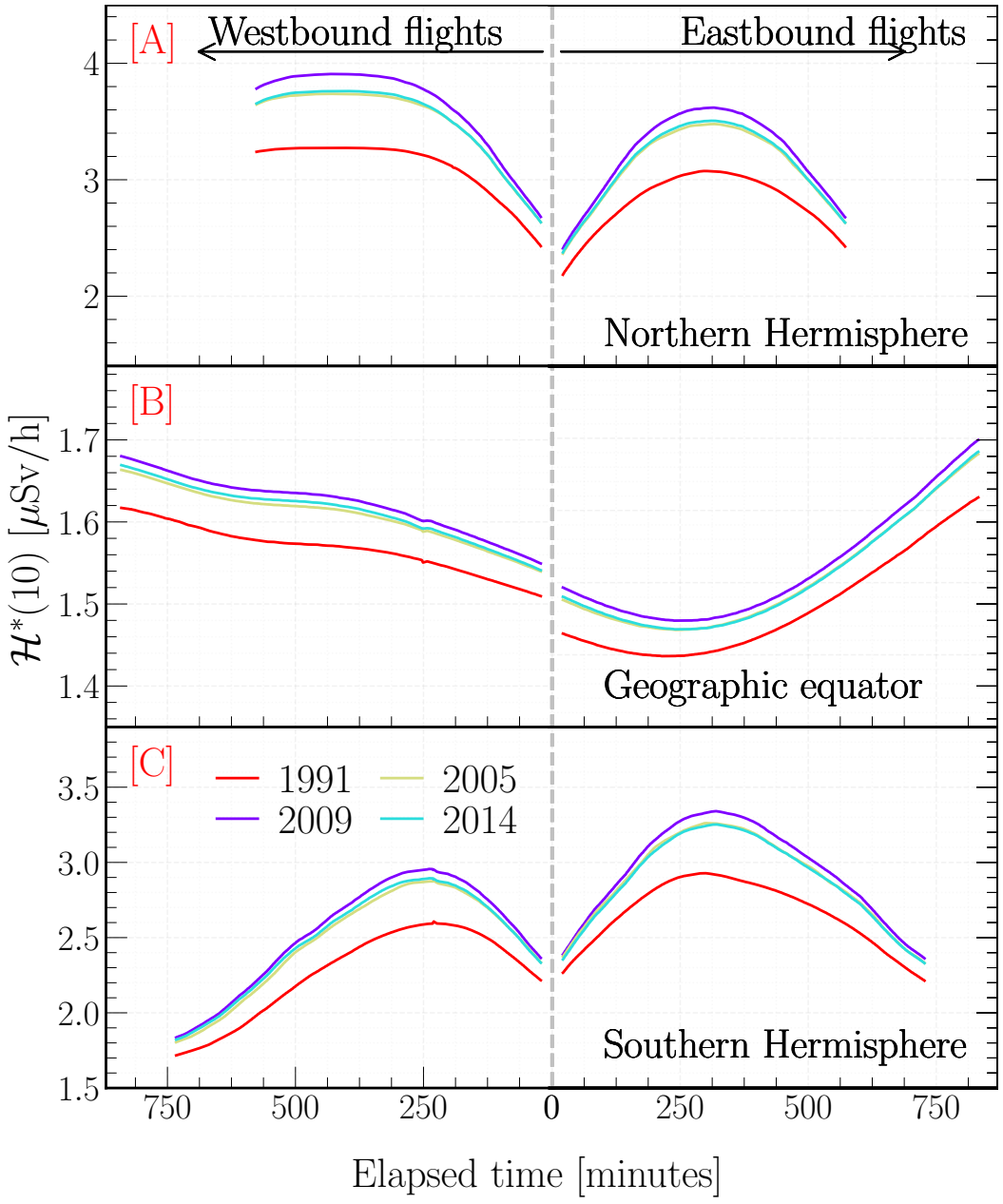

FIGURE 4.2: Calculation of $\mathcal{H}^*(10)$ during the quiet solar minimum and maximum (including the GLE and FD events) for the 6 flights routes listed in Table 4.1. The red, purple, yellow and light blue curves represents the quiet solar maximum (in 1991), quiet solar minimum (in 2009), GLE (in 2005) and FD (in 2014), respectively.

individual accumulated total $\mathcal{H}^*(10)$ to chest X-ray doses, these doses are lower than the chest X-ray doses.

4.4.2 The Latitude Flight Effect

A similar calculation procedure of $\mathcal{H}^*(10)$ performed for the West and East bound flights was performed, but not for Northbound flights. The $\mathcal{H}^*(10)$ result of each flight route listed in

TABLE 4.2: Trans-longitude flight results for various flight routes. Comparison of total dose between quiet solar minimum (r_1) and maximum (r_2) conditions, and doses calculated during the largest GLE recorded and the deepest FD in the NMs era, respectively. The flight routes of the calculated quantities are given in Table 4.1 (i.e. row 1 of Table 4.1 corresponds to row 1 of this table and so on).

r_1 [μSv]	r_2 [μSv]	Ratio (%RD[a])	chest X-ray Equiv.		GLE [μSv]	FD [μSv]	Ratio (%RD[a])	chest X-ray Equiv.	
34.8	31.4	1.1(10.27%)	0.348	0.314	34.1	34.0	1.0 (0.29%)	0.341	0.34
30.1	28.8	1.1 (4.41%)	0.301	0.288	29.4	32.6	0.9 (10.32%)	0.294	0.326
19.7	21.4	0.9 (8.27%)	0.197	0.214	19.6	22.0	0.9 (11.54%)	0.196	0.22
22.1	19.4	1.1 (13.01%)	0.221	0.194	21.9	19.6	1.1 (11.08%)	0.219	0.196
29.8	25.8	1.1 (14.39%)	0.298	0.258	28.8	29.0	1.0 (0.69%)	0.288	0.29
33.7	26.9	1.3 (22.44%)	0.337	0.269	32.4	29.6	1.1 (9.03%)	0.324	0.296

[a]%RD (relative percentage difference): $\frac{|r_1 - r_2|}{\left(\frac{r_1+r_2}{2}\right)} \times 100\%$.

Table 4.3 is plotted in Figure 4.3 as a function of elapsed flight time, with the summarized results in Table 4.4.

TABLE 4.3: Similar to Table 4.1, but now for Northbound flights.

Flight route	Flight distance [km]	Flight Time [hour]	P_c [GV]
ARG → USA	7755	9.9	10.42 → 1.93
RSA → BUL	7755	9.9	6.95 → 5.37
AUS → ROC	7755	9.9	7.41 → 5.55

TABLE 4.4: Similar to Table 4.2, but now for Northbound flights. The flight routes of the calculated quantities are given in Table 4.3 (i.e. row 1 of Table 4.3 corresponds to row 1 of this table and so on).

r_1 [μSv]	r_2 [μSv]	Ratio (%RD[b])	chest X-ray Equiv.		GLE [μSv]	FD [μSv]	Ratio (%RD[b])	chest X-ray Equiv.	
21.2	20.1	1.1 (5.32%)	0.212	0.201	21.0	20.9	1.0 (0.48%)	0.21	0.209
17.4	16.7	1.0 (4.11%)	0.174	0.167	17.3	17.3	1.0 (0.0%)	0.173	0.173
16.1	15.5	1.0 (3.80%)	0.161	0.155	15.9	16.0	1.0 (0.63%)	0.159	0.16

[b]%RD (relative percentage difference): $\frac{|r_1 - r_2|}{\left(\frac{r_1+r_2}{2}\right)} \times 100\%$.

From these flight results, the $\mathcal{H}^*(10)$ ratios calculated at a quiet solar minimum to those at a quiet solar maximum varied in the range of ∼1.0-1.1, while the ratio between FD and GLE events did not show any difference. The far West flight ARG → USA route corresponded to a higher ratio and higher dose accumulation during solar minimum (and during the GLE event), with a lower dose ratio and dose accumulation in the far East flight AUS → ROC. However, the dose accumulation for the far West flight is higher during solar minimum, as compared to

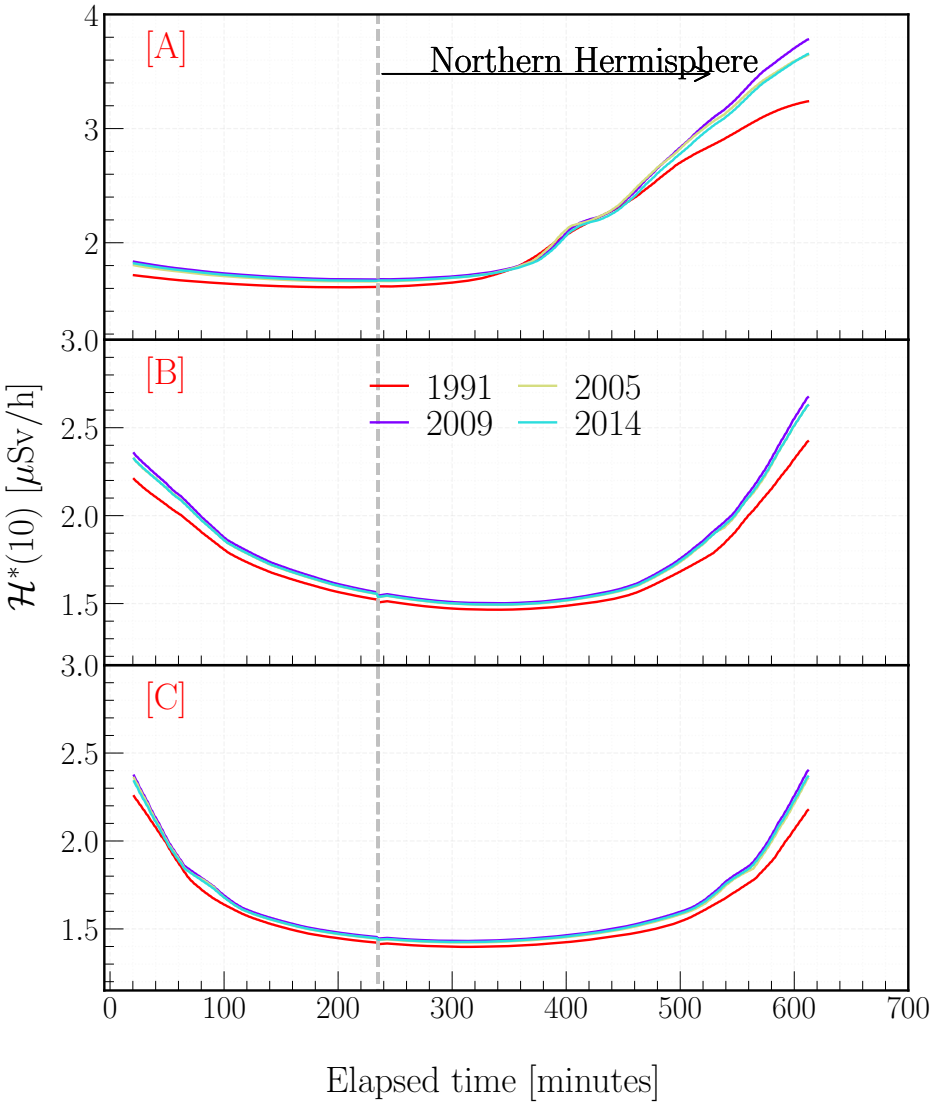

FIGURE 4.3: Flight departure and destination of the three flight routes from the Southern Hemisphere to the Northern Hemisphere during the quiet solar minimum and maximum, and during the GLE and FD events are used for demonstrating dose rates distribution. The colour code is chosen as in the previous figure.

the far East flight during a FD event. Comparing the accumulated total $\mathcal{H}^*(10)$ in terms of X-ray doses, it is found that $\mathcal{H}^*(10)$ is less than that of a single X-ray.

4.4.3 The Altitude Flight Effect

Geomagnetic P_c and altitude are two significant factors in routine aviation dose assessment. Sections 4.4.1 and 4.4.2 clearly demonstrated the P_c dependence of $\mathcal{H}^*(10)$ at commercial flights for a constant cruising altitude. Subsequently, in this section, radiation levels at specified geographic coordinates, are varied with respect to altitude within a constant P_c region, are examined. For all the simulation performed using the CUSF the chosen locations, the launch

altitude 1002.96 g/cm^2 ($\sim$ 250 m), ascent rate (5.0 m/s), descent rate (7.5 m/s), and the desired burst altitude 11.95 g/cm^2 ($\sim$ 30 km) were kept the same. Figure 4.4 presents a spatial 3D representation of all the simulated trajectories from the ground-level to the burst altitude.

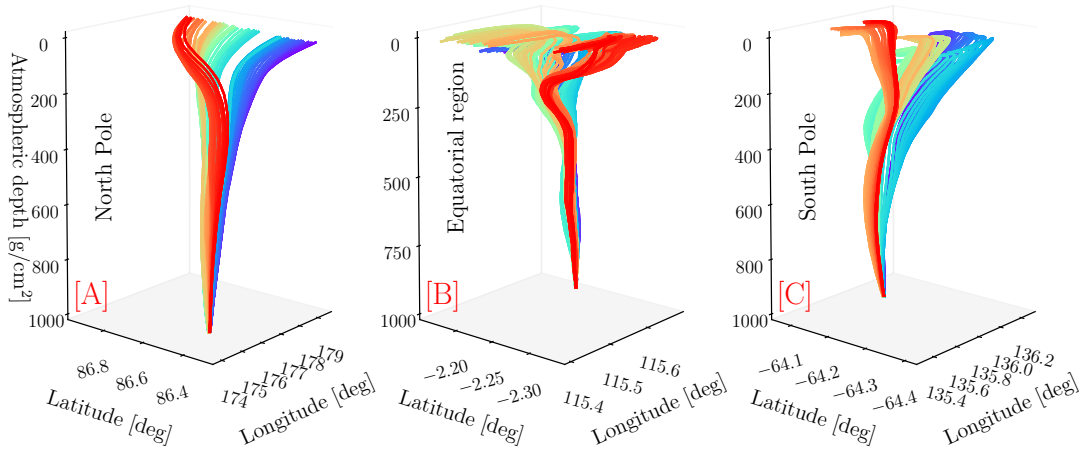

FIGURE 4.4: Three-dimensional (3D) spatial representation of various balloon flight trajectories at different locations. The simulations are carried out at the North pole (panel [A]), equator (panel [B]) and South pole (panel [C]). Different flight trajectories are for different simulation times from 19 (13:00:50) (blue colour) to 26 (14:00:50) November, 2019 (red colour).

All hourly simulations in each location were performed from the 19 (13:00:50) (blue colour) to 26 (14:00:50) November, 2019 (red colour). The corresponding calculated vertical cut-off rigidities at the time of simulations for the North pole, South pole and equator are 0 GV, 0.01 GV, 8.14 GV and 16.51 GV, respectively. The P_c calculations at these locations were internally performed using CARI-7A. Properties of the chosen locations are summarized and presented in Table 4.5.

TABLE 4.5: Simulation locations, dates, coordinates and geomagnetic cutoff rigidity, P_c.

Location	CUSF simulation Date (Time [CAT[c]])	Latitude	Longitude	P_c [GV]
North pole	19/11/2019(13:00:50)−26/11/2019 (14:00:50)	86.448°N	175.346°E	0.00
South pole	19/11/2019(13:00:50)−26/11/2019 (14:00:50)	64.147°S	135.924°E	0.01
Equator	19/11/2019(13:00:50)−26/11/2019 (14:00:50)	2.218°S	115.6628°E	16.51

[c]CAT: Central Africa time

A similar calculation procedure of $\mathcal{H}^*(10)$, performed for aircraft flights, was performed on the balloon trajectories. Balloon flight trajectory $\mathcal{H}^*(10)$ results, with respect to flight time from ground-level and atmospheric depth, are plotted in Figure 4.5 and 4.6 for all four chosen locations. In Figure 4.5, panels [A] to [C] show $\mathcal{H}^*(10)$ as a function of elapsed flight time. With decreasing atmospheric depth, the secondary flux increases and it is expected that $\mathcal{H}^*(10)$ increases, at least until the Regener-Pfotzer maximum, before it decreases. At both

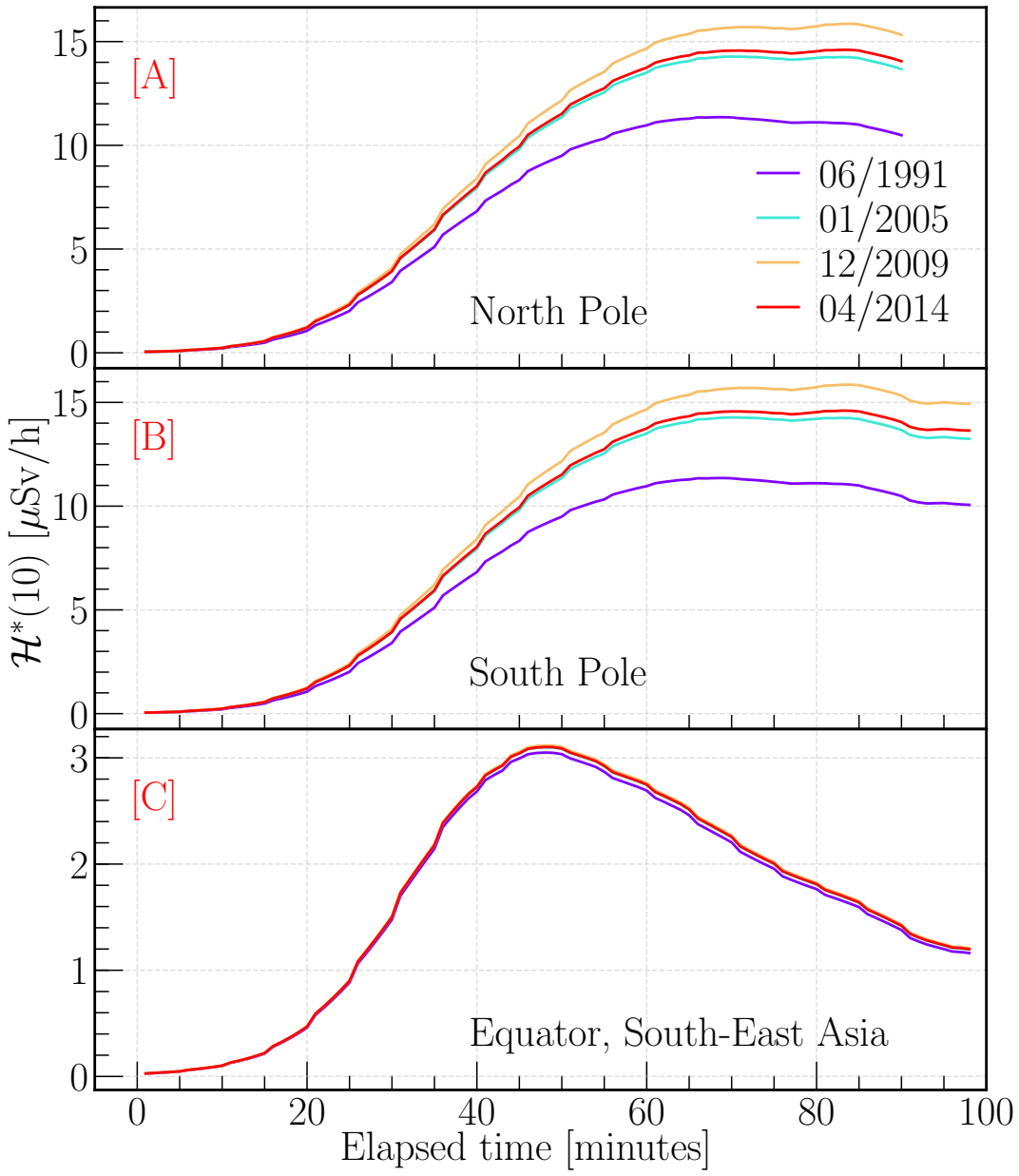

FIGURE 4.5: Time series (vertical profile) of the $\mathcal{H}^*(10)$ during the ascent phase of the investigated balloon flight are shown for demonstration and comparison at different location. At the equator, the Regener-Pfotzer maximum is clearly visible and depends on solar activity and P_c. A clear Regener-Pfotzer maximum is not observed at either geomagnetic pole. The colour code is chosen as in Figure 4.3 and 4.2.

geomagnetic poles, the most noticeable effect of this data profile is that there is no well defined peak representing the Regener-Pfotzer maximum in the $\mathcal{H}^*(10)$ profile. This effect was first shown by *Hands et al.* [2016b] at mid-latitudes (at a P_c ~4 GV) using a low cost portable radiation monitor during a balloon flight. It is not clear what causes this effect and this is still under investigation. In all the other panels, the accumulated total $\mathcal{H}^*(10)$ increases up to the Regener-Pfotzer maximum due to the increase in production of secondary particles within the atmosphere. Beyond the Regener-Pfotzer maximum, $\mathcal{H}^*(10)$ decreases because of the reduced

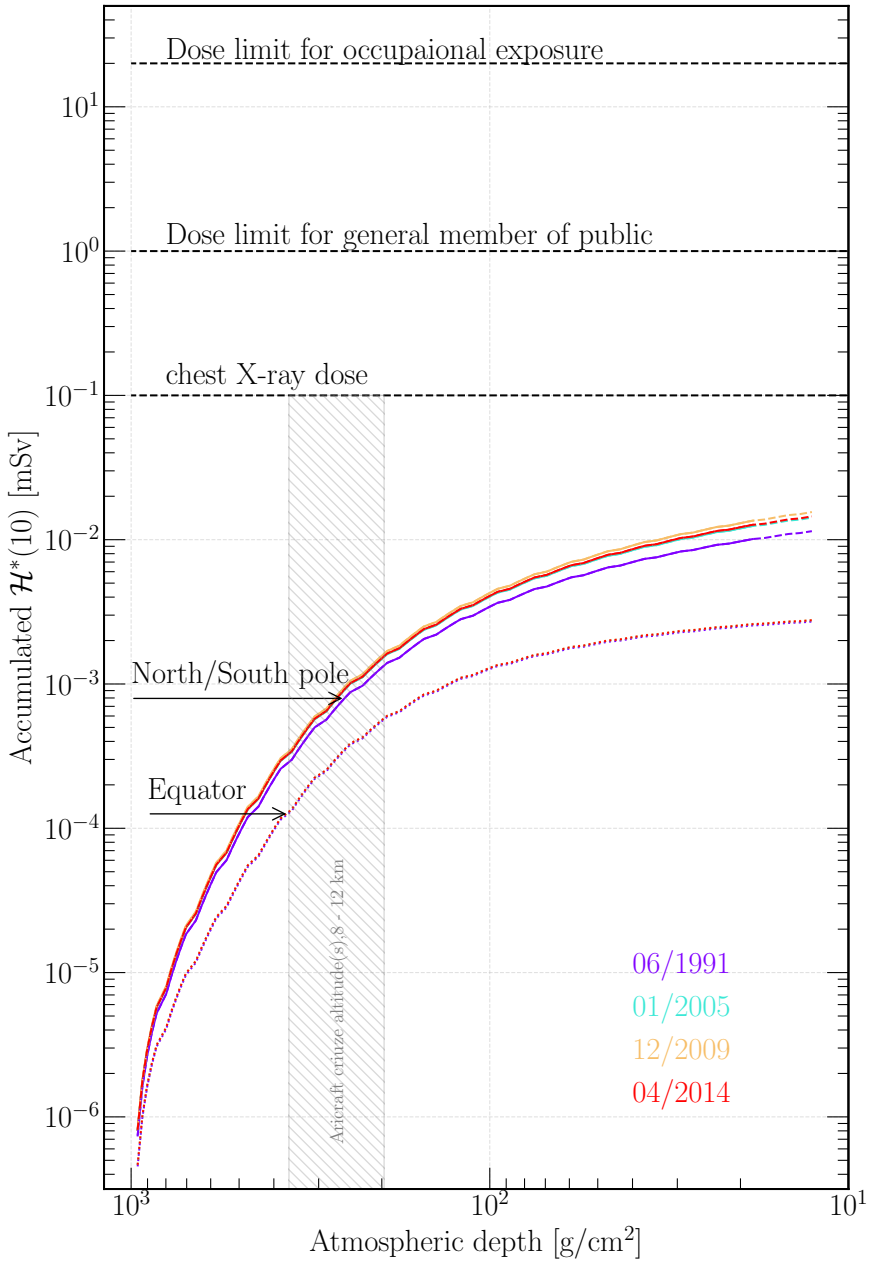

FIGURE 4.6: Vertical profile of radiation dose varying with respect to atmospheric depth from ground-level to 11.95 g/cm^2 (30 km), calculated over several different time scales. The colour code is chosen as in Figure 4.5.

interaction probability of the GCRs in the thinner atmosphere. At the equator, $\mathcal{H}^*(10)$ does not show any solar activity dependence (and geomagnetic disturbances) compared to other chosen locations. At the poles, panel [A] and [B], $\mathcal{H}^*(10)$ profiles are practically the same. Here, the solar activity dependence is clearly visible, with the solar minimum profile being the highest compared to the quiet solar maximum.

The accumulated $\mathcal{H}^*(10)$ dependence with respect to atmospheric depth within a constant P_c region is shown in Figure 4.6. For these flight simulations, $\mathcal{H}^*(10)$ is much less than of a chest

X-ray. It must, however, also be kept in mind that the accumulated dose depends strongly on the amount of time spent at a given altitude and this effect was not investigated here. During a quiet solar minimum the radiation dose at lower flight altitude about 363.02 g/cm^2 at the poles and equator may reach 0.35 μSv, 0.2 μSv and 0.2 μSv, and becomes much higher at 197.11 g/cm^2 than the dose at lower flight altitude reaching 1.67 μSv, 0.95 μSv and 0.59 μSv respectively. However, during a quiet solar maximum the radiation dose at lower flight altitude about 363.02 g/cm^2 at the poles and equator may reach 0.28 μSv, 1.9 μSv and 0.2 μSv, and becomes much higher at 197.11 g/cm^2 than the dose at lower flight altitude reaching 1.3 μSv, 0.84 μSv and 0.59 μSv, respectively.

4.5 Summary

A quantitative comparison of the $\mathcal{H}^*(10)$ profiles between various timescales along aircraft and balloon flights was performed. Along the aircraft flight trajectories flight, the CARI-7 clearly demonstrated the points outlined in section 4.1. The longitude and latitude effects on dose estimation for constant altitudes are shown in Figure 4.2 and 4.3. Contrary to what common sense would suggest, Table 4.2 show that flights (shown in Figure 4.2) with longer duration are not necessarily exposed to larger dose accumulation than short duration flights. However, further comparisons, shown in Table 4.4, show that flights (shown in Figure 4.3) with the same duration do not mean equal dose accumulation, but that this quantity is strongly ordered by P_c. For these flights, the ratios of doses calculated at quiet solar minimum to those at the solar maximum conditions varied in the range of 0.9-1.3, and it appeared as though equatorial flight routes corresponded to lower ratios.

From Figure 4.5, it is noteworthy to point out that for the chosen simulation timescales, in both geomagnetic poles there was no Regener-Pfotzer maximum, while the Regener-Pfotzer maximum at the equator was dependent on both P_c and solar activity. At the equator, because of the nature of the geomagnetic field orientation, the expected $\mathcal{H}^*(10)$ variations with respect to solar modulation for the chosen dates were not observed.

The results shown here indicate that, under normal (or disturbed) solar modulation conditions, the CARI-7A model predicts that it is not possible, on any of the chosen flight routes, to accumulate doses that can reach the 0.1 mSv chest X-ray dose (accumulated in seconds) at normal commercial flight altitudes below 197.11 g/cm^2 (9 km) in just one flight. Instead, this points out that the flight personnel flying at these altitudes may accumulate low doses per flight, but those doses will also accumulate for each flight over the timescale of months to years.

CHAPTER 5

The High Altitude Radiation Monitor

5.1 Introduction

To measure and monitor radiation exposure, at least up to the Regener-Pfotzer maximum, a small, portable, light-weight and battery-powered hand-held radiation detector instrument, known as the High Altitude Radiation Monitor (HARM), was assembled. This acronym was chosen to honour the late Prof. Harm Moraal, who was part of the North-West University (NWU) physics department for 44 years and championed cosmic-ray research in South Africa. This instrument uses a Geiger-Müller counter, capable of detecting ionised radiation, and a number of smaller sensors added to provide additional information. The purpose of HARM its not to replace the already existing dosimeters, but rather to supplement existing dosimeter measurements through a series of students projects. Students/junior-researchers involved have shown the potential to reach out to a broad audience to engage non-scientific communities and public schools to demonstrate the impact of ionizing radiation.

During the development of the HARM, several iterations were performed resulting in different set-ups. This chapter discusses, briefly, different stages of the HARM, i.e. hardware electronics, mechanical work and housing design, functionality and the working principle of the detector, from the first and subsequent upgraded prototypes. The first measurements by the HARM detector during a commercial flight from Johannesburg to Windhoek is reported. As part of public awareness activity, the HARM detector was placed on a high altitude balloon, and these measurements are also shown here. Model calculations (estimations) of radiation levels for the same commercial aircraft flight is shown and the results are used to interpret the measurements. The HARM programme was briefly reported by *Mosotho et al.* [2021], and in this chapter, a broader description of the HARM program is discussed.

5.2 Background and Motivation

Characterizing radiation levels within the atmosphere during transient SEPs, and the ever-present GCRs, at Earth is of significant for the aviation industry, as described in the International Civil Aviation Organizations (ICAO)[1] Space Weather manual. This significance stems from the fact that ionizing radiation exposure of commercial flight personnel and passengers can possibly exceed the recommended general public yearly radiation exposure limit, set by the International Commission for Radiological Protection (ICRP),[2] in a single flight. As the only Space Weather Warning Centre in Africa, the South African National Space Agency (SANSA)[3,4] was appointed by ICAO to provide space weather services and warnings by 2022. As part of the recommendation by ICAO, SANSA must provide radiation estimates to the aviation sector. Therefore, in 2017, the NWU's Centre for Space Research initiated a campaign, known as the HARM programme, as part of the public awareness about atmospheric radiation evolution with altitude from ground-level.

This programme offers opportunities for students to conduct technological and scientific experiments related to cosmic radiation in the atmosphere. The programme has been made available to students not only from NWU, but also from other institutions through a collaboration with SANSA. The importance of this programme is to impart knowledge to the general public about the atmospheric radiation environment's evolution when flying as a function of altitude, geomagnetic cutoff rigidity P_c, solar activity, and flight duration. Apart from that, this programme assists students in gaining experience in designing, testing, and assembling relatively simplistic instruments making significant measurements.

Figure 5.1 shows students who have participated and contributed to the programme so far. The top left image shows Phillip Heita and Jabus van den Berg from the NWU. The top right image shows Londeka Mkhize from the University of KwaZulu-Natal. The bottom left and right shows Portia Legodi from the University of Cape Town and Chris Thaganyana from the University of the Western Cape respectively.

5.3 Housing and Electronics

The housing for the first prototype of HARM consists of a thin plain plastic box with small vents. The housing is 3D Printed, see Figure 5.2. The housing weighs 113 g and it guarantees

[1] https://www.icao.int/Pages/default.aspx
[2] http://www.icrp.org/index.asp
[3] https://www.sansa.org.za/
[4] https://tinyurl.com/y29ykjv7

FIGURE 5.1: Students participating in the HARM programme. These activities events occurred in the following order, i.e. June 2017 [top left], June 2018 [bottom left], November 2018 [bottom right] and December 2019 [top right].

good component protection. From a breadboarding prototype, a picture of the first instruments making up the basic detector system is shown in Figure 5.3. The 3D printed housing encloses the $J305\beta$ Geiger-Müller counter with its power and registration board, the Raspberry Pi (RPi) μ-computer, and the Raspberry Pi Sense HAT. The $J305\beta$ Geiger-Müller counter and its board (called RadPCB, henceforth), and a Raspberry Pi Sense HAT are mounted to the walls of the housing.

FIGURE 5.2: 3D Printing of the HARM housing.

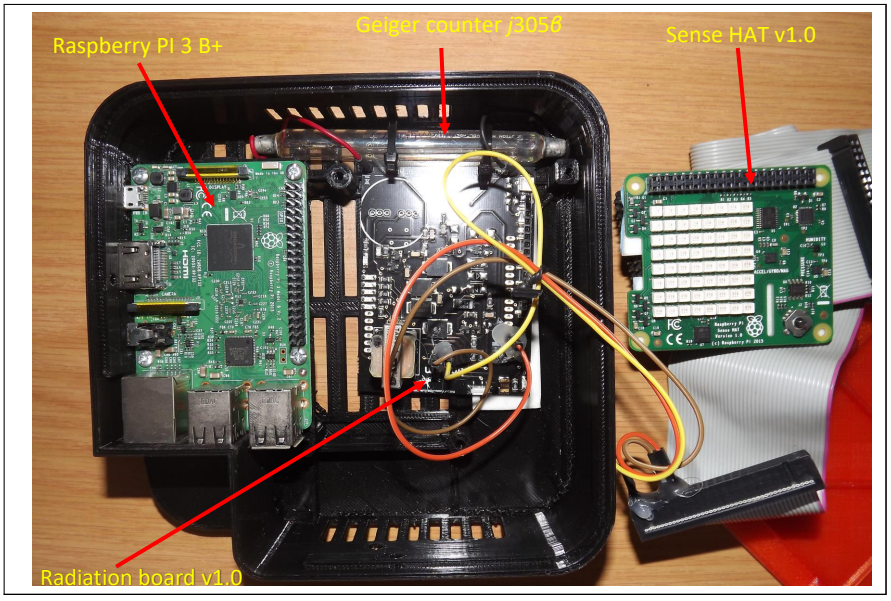

FIGURE 5.3: HARM housing seen from top with open lid.

5.3.1 Raspberry Pi

The RPi is a single board micro computer capable of everything you would expect from a desktop or laptop. The RPi 3 Model B +[5] as shown in Figure 5.3 weighs just ∼ 42 g. This

[5] https://www.raspberrypi.org/

models has 40 pins which are a combination of voltage supplies, grounds and GPIO (general purpose input output). For this HARM set-up, a full Raspbian operating system[6] was installed, updated, and upgraded to the latest version in order to support the RPi GPIO pins.

5.3.2 The $J305\beta$ Geiger-Müller Counter

The Geiger-Müller counter is one of the oldest radiation detectors as mentioned in Section 3.1. The $J305\beta$ cylindrical glass Geiger-Müller counter is filled with a low-pressure gas. The tube contains electrodes, between which there is a potential difference of several hundred volts, but no current flowing. The tube is powered by the RPi through the RadPCB from cooking-hacks.[7] When a high voltage is applied from the RadPCB circuitry to the tube, electrons are accelerated towards the anode and the positive ions are accelerated towards the cathode due to the potential difference between the anode and cathode. The accelerated electrons gain sufficient kinetic energy to produce ionization when ionising radiation is incident on the tube. A short and intense pulse of current is produced and passes from the negative to the positive electrode and this is registered by counting electronics.

Units of measured by Geiger-Müller counters are basically the number of pulses generated, which is read by the RadPCB and its accessories, while the RPi records these events. This means that in one minute there will be "C" counts, i.e. CPM, meaning counts per minute. In all the Geiger-Müller counters this representation is common. However, these measurements give no indication of the energy deposition but they represent the number of pulses, i.e. the number of ionising particles.

Blanco et al. [2009], and many others before, showed the application of Geiger-Müller counters for the detection of cosmic-rays at different levels, i.e. from sea-level, to mountains, and aircraft cruise altitudes, while *Maurin et al.* [2014] demonstrate the reignited interest for stratospheric balloon application since the 1950s, using this type of instrumentation. On ground-level, a Geiger-Müller counters measure the background radiation as a combination of galactic cosmic radiation and radioactive elements from the Earth's crust. This background radiation is highly dependent on where the measurements at ground-level were obtained. The whole $J305\beta$ Geiger-Müller counter circuitry, i.e the tube and RadPCB, weighs ∼50 g and it operates in a temperature ranging from $-20°C$ to $+65°C$[8,9].

[6] http://www.raspberrypi.org/quick-start-guide
[7] https://tinyurl.com/ox76ha5
[8] http://www.libelium.com/v11-files/documentation/waspmote/radiation_board_eng.pdf
[9] https://tinyurl.com/ox76ha5

5.3.3 The Raspberry Pi Sense HAT

The Sense Hardware Attached on Top (Sense HAT)[10,11,12] is a low-cost environmental parameter sensor. This sensor measures environmental parameters such as pressure, temperature and humidity, and it can also measure acceleration and the magnetic field magnitude. These parameters are sampled at a rate of 1 minute when taking measurements. Its size is about 65.1 mm×56.6 mm×13.9 mm, while the whole circuitry weighs ∼20.4 g. This digital sensor has a typical temperature accuracy of ±2°C with an operating range that is optimized from −40°C to +120°C. Operation outside this range is still possible, which will occur at high altitudes during balloon launches. However, the accuracy of the sensor is expected to decrease significantly outside the temperature operating range. The pressure output has an accuracy of ±0.1 hPa in a range from 260 to 1260 hPa.

5.4 Measurement on board an Aircraft

Flying with Portable Electronic Devices (PEDs) is a serious concern for airline companies. Most airlines have limited use of PEDs by passengers during all phases of the flight, and some airlines have provided and implemented guidance on when/how to use the devices. The guidance varies among airlines, with some not permitting passengers to switch on PEDs during take off and the final descent phase of a flight. For the on board measurements presented here (and the RPiRENA measurements in the subsequent chapter), precautionary measures have been followed as prescribed in the relevant in-flight magazines, when available.

The whole HARM set-up uses less power than a standard laptop, and does not radiate any high frequency signals (all wireless connections, such as bluetooth, are disabled). The detector can thus be safely used on board commercial flights. To assess the safety of using cosmic-rays detectors on board, the Deutsche Lufthansa Airlines employed a number experimental devices on the upper deck of a B747−400 aircraft during the measuring campaign of the GSF[13] in 1992/93, with one of those detectors being a Geiger-Müller counter (see *EURADOS WG5* [2004]), which did not interfere with aircraft electronics.

Most of the measurements were conducted from three assembled prototypes, marked #1, #2 and #3. When conducting in-flight measurements, these prototypes were either placed under the passenger seat, on an empty seat or in the overhead storage of the aircraft. To date HARM

[10] https://readthedocs.org/projects/sense-emu/downloads/pdf/latest/
[11] https://github.com/raspberrypilearning/astro-pi-guide
[12] https://thepihut.com/products/raspberry-pi-sense-hat-astro-pi
[13] Forschungszentrum für Umwelt und Gesundheit

was carried in 25 flights over the past three years from July, 2017 to July, 2019, with 76% of those within the South African borders.

5.4.1 The First Flight From Johannesburg to Windhoek

To test the HARM prototype's performance in a mixed radiation field, the first HARM measurements on board an aircraft were during a commercial flight from Johannesburg, O.R Tambo international airport to Windhoek, Hosea Kutako international airport. The measurements were started before the aircraft took-off, completely shut down during take-off (as requested by the flight personnel) and as soon as the aircraft approached cruising altitude it was switched back-on. Again, the device was completely shut down before the final descent and it was switched back on after landing. In Figure 5.4 the count rates of the detector and the selected house-keeping measurements are shown.

In panel [A], the measurements and model calculations are shown as a function of the elapsed time from departure. The scattered error bars in the plot represent the statistical accuracy of the measurements, calculated as a the Poisson error. A two minutes moving average of the data (red solid line) was taken to show a smooth data trend and the light red filling represents the data uncertainties. The average value of the measured count rate at the cruise altitude was 28 per minute; compared to the value at ground-level it is about a factor about 6 higher. Because HARM is unable to directly measure any dosimetric quantities (a Geiger-Müller counter produces only a count rate which cannot be related to a dosimetric quantity in a mixed radiation field), its data and MAIRE model calculation[14] are compared in a qualitative fashion only. From the figure, the model results (blue solid line) show a general agreement with trends of the count rate data (red scattered data), as measured by HARM, within some uncertainties. The modelled average effective dose rate for this flight is about 2.335 μSv/hr at about 269.57 g/cm^2 (i.e. $\sim$10 km) above sea-level for a duration of about 80 minutes, while the HARM measured count rate is 28 per minute, on average.

Subsequently, for an average member of the public, taking only several flights a year, the radiation exposure about 3.8 μSv from flying is negligible. However, if a flight personnel member takes at least 285 of these short-haul flights per year (6 such flights per week), using the same flight path and more or less the same flight time, he/she would receive a dose rate greater than 1 mSv/yr. This is higher than the radiation exposure limit for the general public and illustrates the need to define flight personnel as radiation workers. These assumptions will be more realistic if the atmospheric conditions are the same, i.e. if there are no SEPs events

[14] http://www.radmod.co.uk/maire

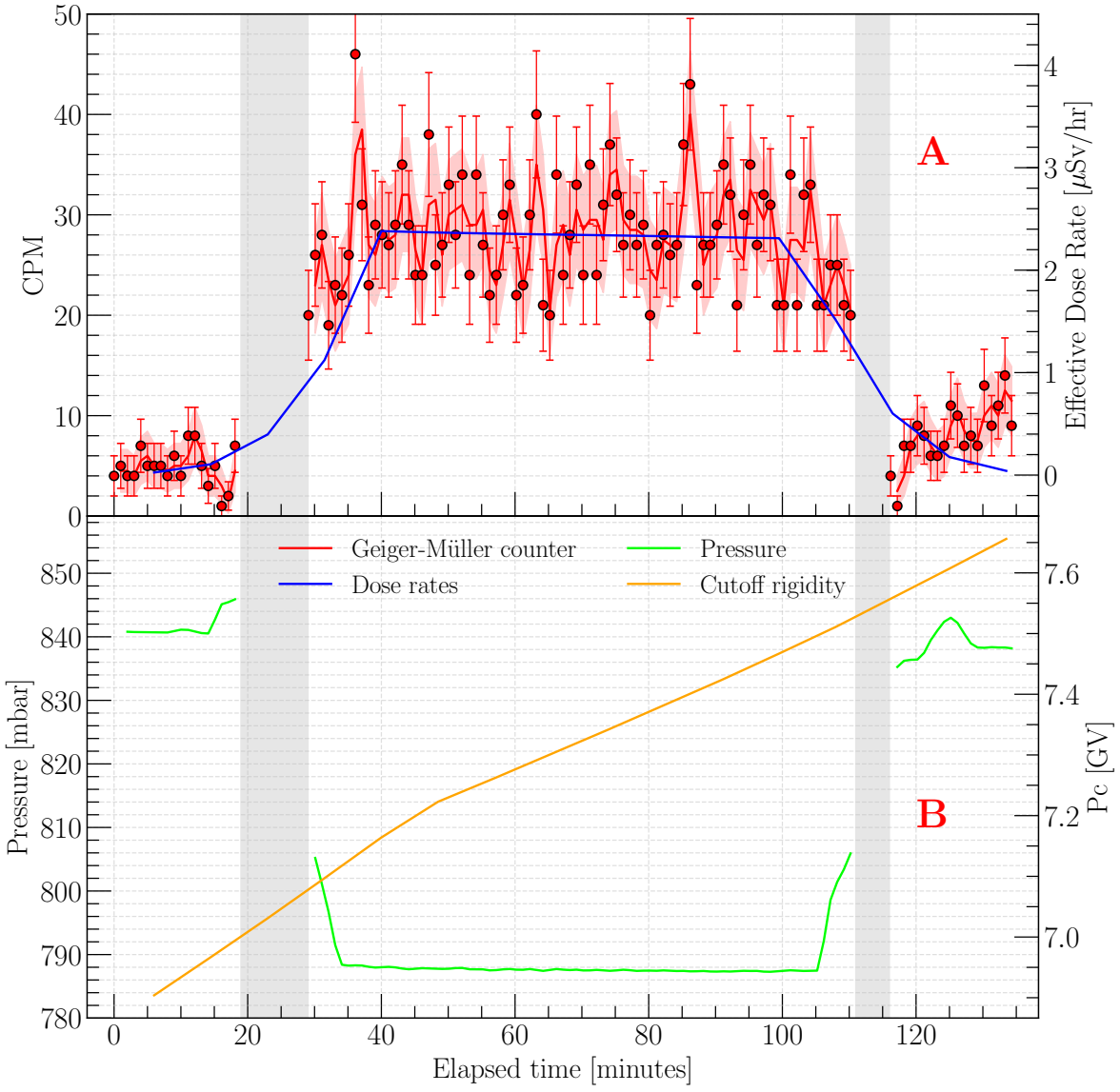

FIGURE 5.4: Counts per minute (CPM; red colour) and model dose rates profile (blue colour). From the HARM's counts rate measurements, it is not possible to calculate any dosimetric quantities such as effective dose rate, here, the calculated effective dose rate simply shows only how strongly the CPM and effective dose rate are related. Bottom panel: Sensor HAT barometric pressure (green colour) and the Pc profile (orange colour). Image credit: *Mosotho et al.* [2021].

which might greatly enhance the atmospheric secondary radiation environment at cruising altitudes. Flight personnel are therefore classified as radiation workers by the ICRP as discussed in Chapter 3 (Section 3.3) and many other governmental bodies[15,16] in Europe and North America. However, this is currently not the case in South Africa.

In panel [B], the aircraft cabin pressure profile is as expected when compared with the count rate profile. The cabin pressure inside the aircraft also changes due to the outside pressure

[15] https://inis.iaea.org/search/search.aspx?orig_q=RN:34007814
[16] http://www.legislation.gov.uk/uksi/2019/1115/made

changing, and this corresponds directly to variations in altitude. As seen from the figure, before take-off a small increase in pressure is seen when the cabin door closes and similarly, when the cabin door opens after landing, a small decrease is observed in the pressure profile. During take-off, since the detector was switched off for 10 minutes, it appears that the cabin pressure started rapidly decreasing and it levelled off at the cruising altitude, recording an average cabin pressure of about 787 mbar. Also shown in the panel is the P_c profile from the MAIRE model calculation changing from 6.904 GV at the O.R Tambo international airport to 7.656 GV at Hosea Kutako international airport. In both panels, the grey shaded areas represent missing measurements as a result of the detector being switched off as requested by the aircraft personnel.

5.5 Measurement on board a Stratospheric Balloon

Several methods can be used to access the troposphere and stratosphere and conduct cosmic-ray research and this includes the use of meteorological rockets[17,18] [*Krause*, 1947, *Perlow*, 1949, *Shafer and Yarygin*, 1961, *Zabori et al.*, 2015, *Zábori et al.*, 2016, *Pont et al.*, 2019], aircrafts (as discussed in the previous section) and mountain top observatories [*Bogdanov et al.*, 2006, *Kubančák et al.*, 2014, *Iskakov et al.*, 2019]. Since the 1950s, interest was reignited to observe the cosmic-ray particles through the experiments of high altitude balloons in the NM era, see *Maurin et al.* [2014].

In South Africa, stratospheric radiation dosimetry studies from ground-level had not been documented before. The NWU (formerly known as Potchefstroom University for Christian Higher Education) conducted balloon launches for 20 years between 1958 and 1978, characterizing ionizing radiation levels with respect to ground-level. However, the outcome of these launches has not been published in accredited journals. Therefore, to address the unquantified and undocumented radiation levels, a first balloon launch was attempted on 28, November 2018, using the HARM set-up to develop the procedures for launching, tracking and recovering of the payload for future balloon launches using the RPiRENA dosimeter. The outcome of this launch were published in *Mosotho et al.* [2021]. This HARM set-up was assembled specifically for a balloon launch and most of the components were replaced to reduce weight. The replaced components are the Sense Hat (with BMP180 barometric pressure sensor)[19] and the RPi 3 Model B + (with RPi zero w).[20] The goal for the first high altitude balloon flight was to

[17] ttp://rexusbexus.net/rexus/rexus-user-manual/
[18] http://rammb.cira.colostate.edu/dev/hillger/wx-rockets.htm
[19] https://tinyurl.com/vsa6tfn
[20] https://tinyurl.com/y4kvlczf

develop the procedures for launching, tracking and recovering of the payload and also testing the HARM electronics at high altitude in a low temperature environment.

To demonstrate the launch procedure and avoid repetition of the first launch, only the second balloon lunch held a year later on 11 December 2019 will be used, while the results are compared to that of the first launch. The core part of the high altitude balloon hardware consists of the payload box, the balloon, and parachute. Comprehensive pre-flight planning needs to be done in advance to make sure that there is a plan in place to deal with circumstances that may show up after a successful launch, leading to successful payload recovery. Therefore, the subsequent sections describe the procedures implemented, individual parts used and design fundamentals, launch, recovery, and data processing techniques implemented.

5.5.1 Launch Permit

Obtaining a launch permit is the most important step to plan a balloon launch. In South Africa, atmospheric space is managed by the Central Aviation Monitoring Unit (CAMU) and regulated by the Civil Aviation Authority (CAA), while the Air Traffic and Navigation Services (ATNS), which is an entity of the Department of Transport of South Africa, is responsible for efficiently running the atmospheric environment within South African borders. The balloon launch permit is granted upon filling an online form for"flexible use of airspace[21]" through the CAMU website at https://www.atns.com/. It is evident from the multiple e-mails sent and responses to these, permission to launch is never granted in a fast and straightforward way. Once permission is obtained from CAMU and ATNS to launch on provided coordinates, the NWU has to be formally made aware of such activity on campus.

5.5.2 Payload Tracking

Tracking is a serious problem during balloon launches. The general idea is to use a Software Defined Radio and decode the received signal with the help of a personal computer. However, because the city of Potchefstroom and the surrounding areas have reliable mobile phone network coverage, the mobile cellphone GPS tracking method was chosen. The choice of cellphone tracking in both the 2018 and 2019 launches was not precisely to track the payload during the entire flight, but to obtain the location when the payload is descending, and especially when it has reached ground-level, where its going to land and when it has done so.

[21] https://www.dictionary.com/browse/airspace?s=t

5.5.3 Payload Box

The payload box is constructed of Styrofoam. The box with a thickness of ∼50 mm guarantees good thermal isolation and shock absorption during the landing impact. Figure 5.5 shows the location of the electronics inside the payload, all wrapped in bubble plastic (excluding the power bank) and mounted to the walls. The payload label has to be created and attached on the payload. This is intended to identify the box if found by a third party not aware of its content; see Figure 5.6. Once the label is attached, the payload is sealed.

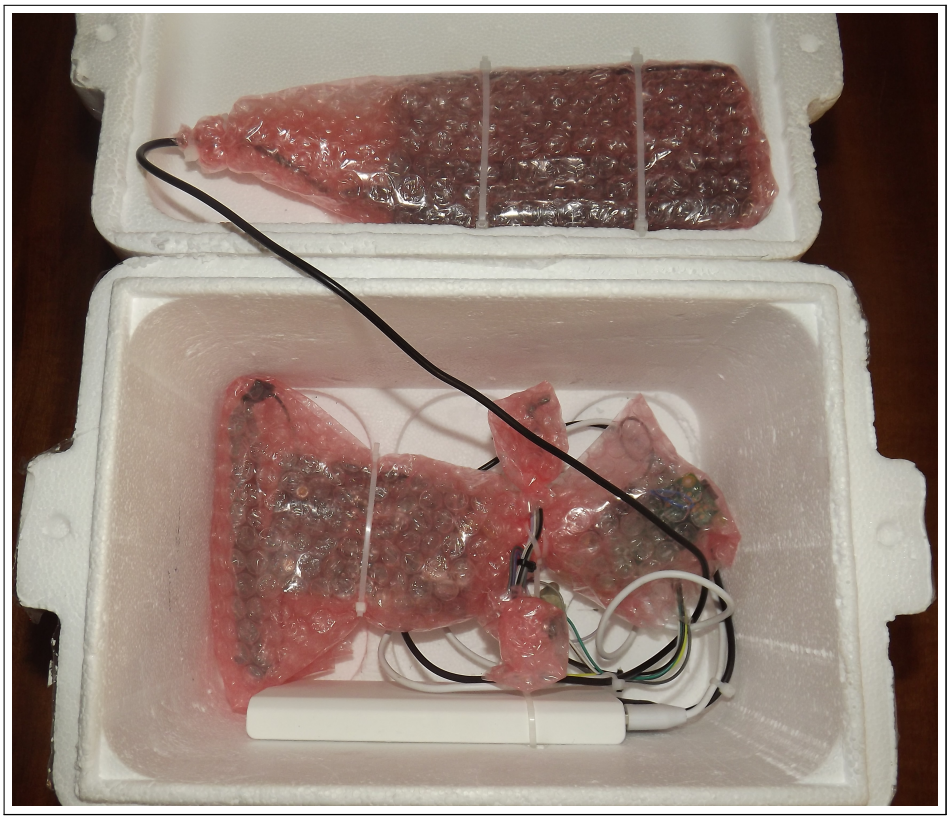

FIGURE 5.5: Payload box seen from top with open hatch. Mobile phone and sensors are wrapped in bubble plastic wrapping.

The type of balloon used in this work is a rubber balloon commonly referred to as meteorological balloon. The rope between the payload box and the parachute is chosen to be ∼60 cm to allow the parachute to deploy freely. The rope between the parachute and the balloon is chosen to be ∼300 cm so that the remains from the balloon burst will hang below the parachute without interfering with the rope below. Table 5.1 lists the weight of the individual components needed to assemble the balloon-to-payload train.

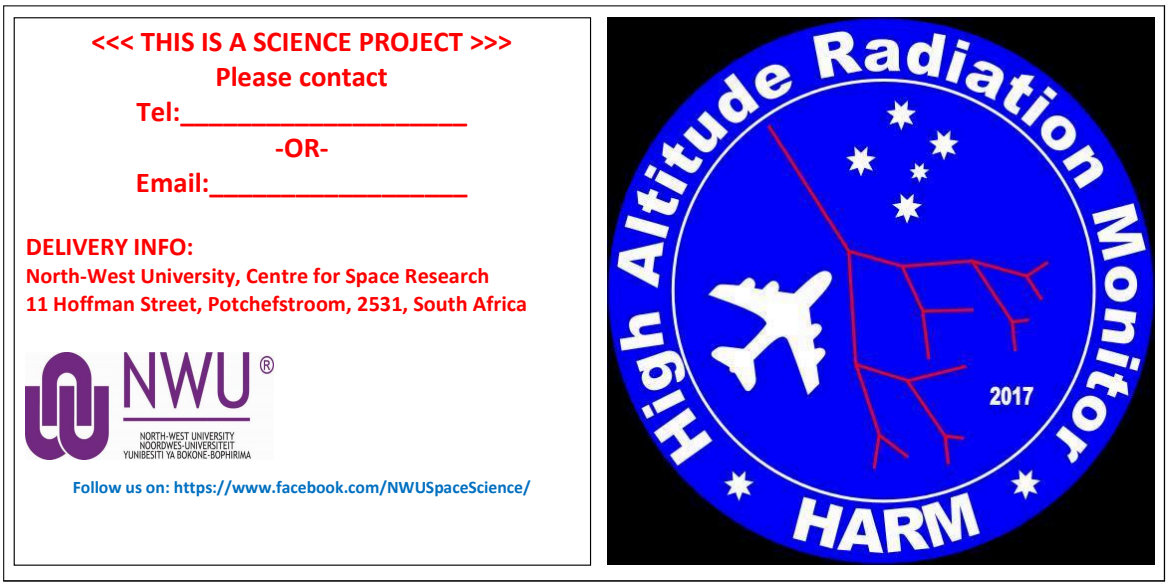

FIGURE 5.6: Payload box label.

TABLE 5.1: Measured weight of individual components and total payload weight. All values apart from the sum are measured values.

Part	Weight
Romoss 10 000 mAh power bank	121.7 g
HUAWEI Y560-L01 cellphone	142.03 g
Empty payload box	110.2 g
Tyvek parachute and lines	80.4 g
Meteorological balloon	1002 g
RPi/RadPCB +Counter/BMP180/DS3231-RTC circuitry	160 g[a]
Fully assembled payload ready to lift off including lines, parachute and balloon.	1.6 kg

[a]The actual mass is 95g, i.e. 9g, 50g, 21g, 4g & 10g, the additional mass results due to the rubber/plastic of tube and connection wires.

5.5.4 Flight Trajectory Prediction

Once permission is granted and the payload prepared, flight predictions are performed to evaluate the flight trajectories. Once the balloon is filled with Helium gas and the balloon-to-payload train released, its flight path is governed by the meteorological conditions along the flight trajectory, which are quite impossible to control. The most important factor is the wind patterns which might guide the balloon (during ascent phase) and parachute (during descent phase) far from the launch site. To forecast the wind pattern and other environmental conditions the windy.com[22] online predictor was used. This predictor can forecast conditions up to 143.79 g/cm^2 (i.e. ∼14 km) altitude above the ground.

[22]https://www.windy.com

An online balloon flight landing predictor, the Cambridge University Spaceflight[23] (CUSF), was used. This flight predictor is widely used during high altitude balloon planning due to its ease of operation. When planning a balloon launch, the first step is to decide on the possible launch windows up to six days ahead of the targeted launch date. For these balloon launches, a python CUSF Standalone Predictor Version 2,[24] discussed in Chapter 4, was used, because it could be manipulated to continuously run simulations in the background. The individual simulated flight path was visualized and based on those flight paths the best time of launch was chosen. The balloon flight trajectories for 11 December 2019 are shown in Figure 5.7 up to an altitude of 11.95 g/cm^2 (∼30 km), forecast within the desired launch times. The solid lines in panel [A] represent the flight trajectories for different times, while the broken buffer-circles lines are used to estimate the distance to the landing site which is represented in panel [B] pertaining to the launch time.

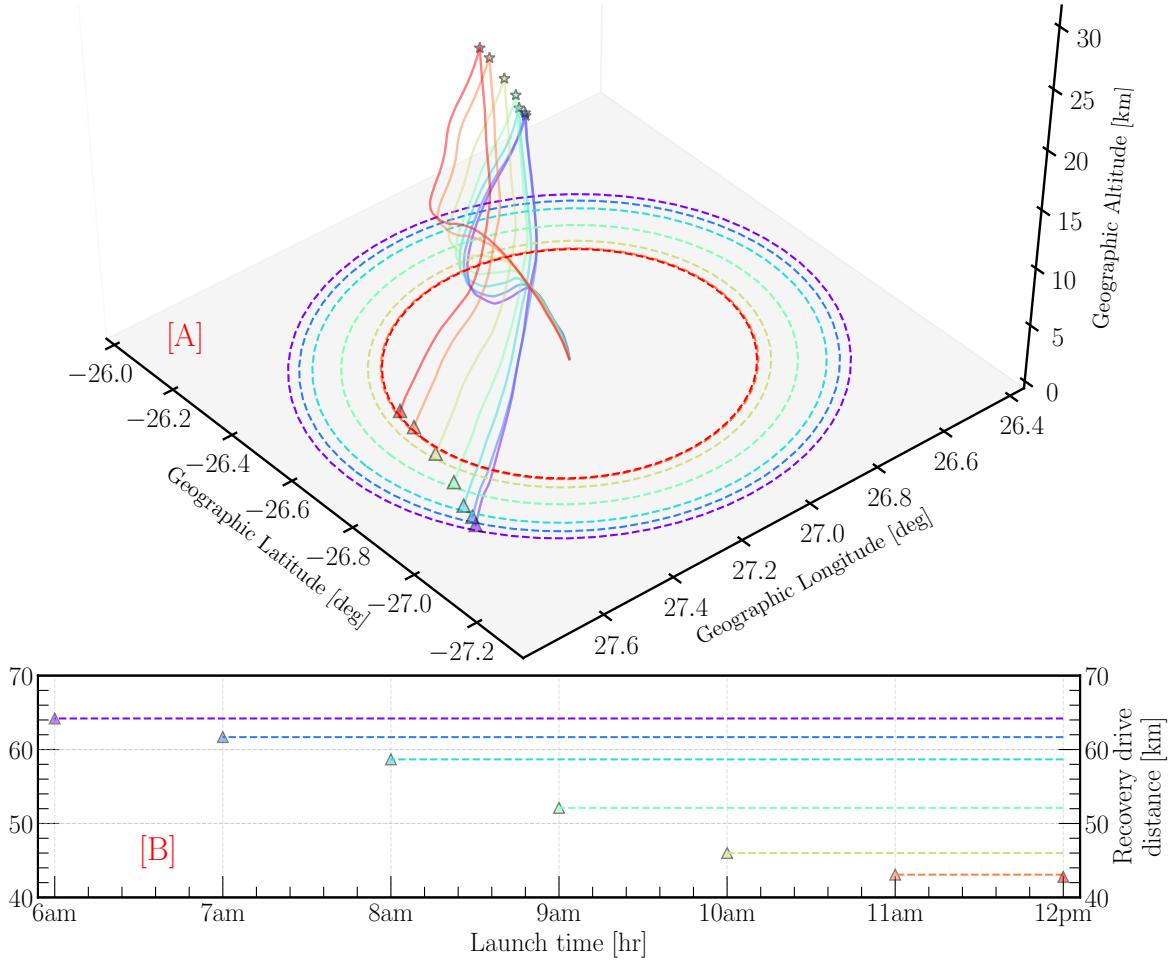

FIGURE 5.7: Six hour (6am-12pm) forecast for identifying a suitable launch time. Panel [A] shows the flight trajectories and the minimum radial landing distance from the launch site, while panel [B] shows the launch times with respect to distance to the landing site.

[23] http://predict.habhub.org/
[24] https://github.com/jonsowman/cusf-standalone-predictor

As a backup to the CUSF Standalone Predictor, the University of Southampton flight predictor, the ASTRA High Altitude Balloon Planner,[25] was often used. This prediction tool is equally capable of running multiple predictions all at once and can produce a heat map of the"possible" landing site based on the most populated landing sites. However, it can only be run manually. Apart from the already mentioned flight predictors, there are several others which can also be used and these are: The S3 Research Flight Predictor,[26] the University of Michigan Flight Prediction Tool,[27] and the University of Wyoming Trajectory Forecaster.[28]

5.5.5 Electronics Testing and Location Tracker

To complete the balloon launch planning, the cellphone tracker and the operation of all the electronics were tested before the launch. Prior to assembling the payload, all sensors and writing of data to the μ-SD card were tested. The power consumption was investigated to ensure that there is enough power for the entire launch and recovery (for at least up to two days).

The payload is expected to spend more than an hour above 269.57 g/cm^2 (i.e $\sim$10 km) altitude for an average launch, depending on weather and wind conditions. During the flight, its practically impossible to avoid hazardous conditions such as electronics icing (or severe tropospheric/stratospheric turbulence). Measurements were performed inside a freezer to decide if more precautions would be needed to properly insulate the payload box or if a thicker box should be used to avoid compromising the working conditions of the electronics. These in-house tests were conducted to simulate the conditions at high altitudes and to verify electronic performance and stability at low temperature environment prior to the launch day.

After these tests were successfully completed, the cellphone tracking was tested. Two tracking apps, i.e. Glympse and Google map location, were used. Glympse was running on mobile data, while Google maps was running offline with the location setting turned on, and the followed path was retrieved when mobile data were switched back on. The idea behind running Google maps with these settings was to see if, during a launch, the payload lose connection during the flight but manages to get one location just before it lands, the whole dataset can be retrieved and a flight trajectory can be constructed to estimate its landing site.

[25] http://astra-planner.soton.ac.uk/
[26] http://www.s3research.com/tools/flightpredictor/
[27] http://vmr.engin.umich.edu/Model/_balloon/index.py
[28] http://weather.uwyo.edu/upperair/balloon_traj.html

5.5.6 Launch Site

The launch site for both launches was selected to be easily accessible, with no nearby obstacles (e.g. building or tall trees). The launch site was inside the NWU next to the Dampad dining hall. Once the payload is sealed, the parachute is attached to the payload, and the inflated balloon is attached to the parachute. A final re-check of the electronics is performed before the payload is released.

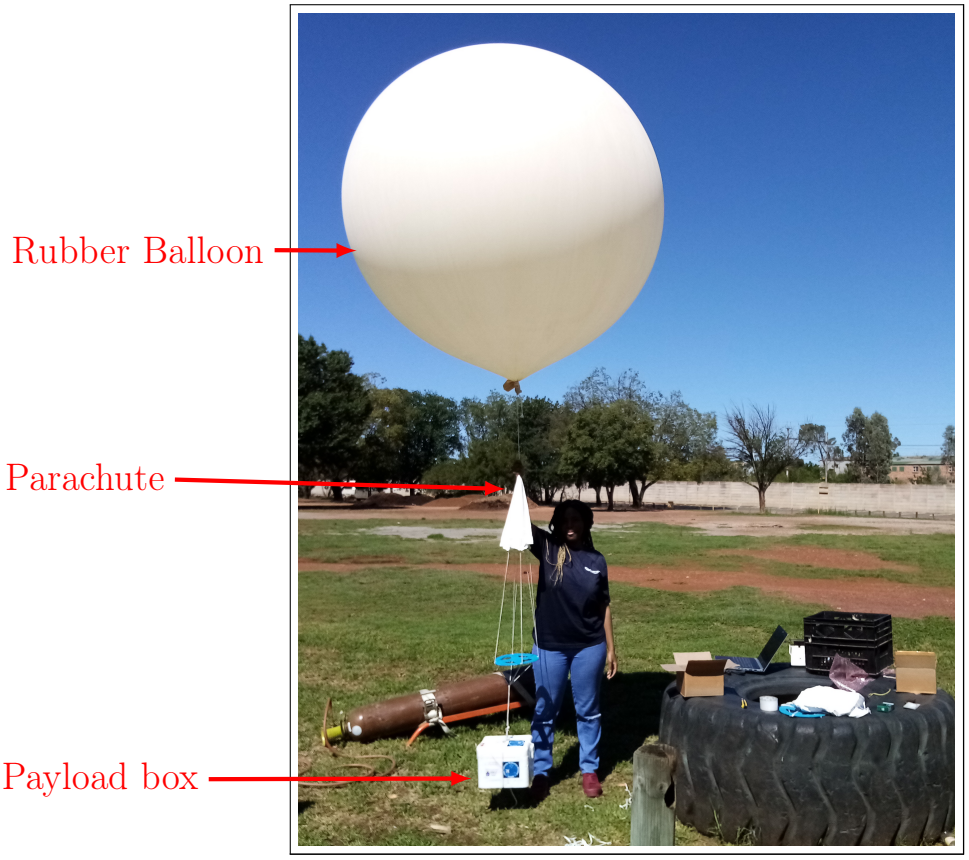

FIGURE 5.8: Picture of the payload box, parachute, and inflated balloon all connected before launch.

A picture in Figure 5.8 shows the overall structure of the high altitude balloon system, i.e. the balloon on the top, parachute between the balloon and the payload, and the payload at the bottom. About 30 minutes before launch, the Air Traffic Control was notified about the status of the launch plans. Once notification was issued and the electronic status verified, a countdown was started, at the end, the payload was released. Shortly after the payload was released, the balloon flight trajectory prediction had to be repeated and compared to the previous predictions to check for major deviations regarding the predicted landing site.

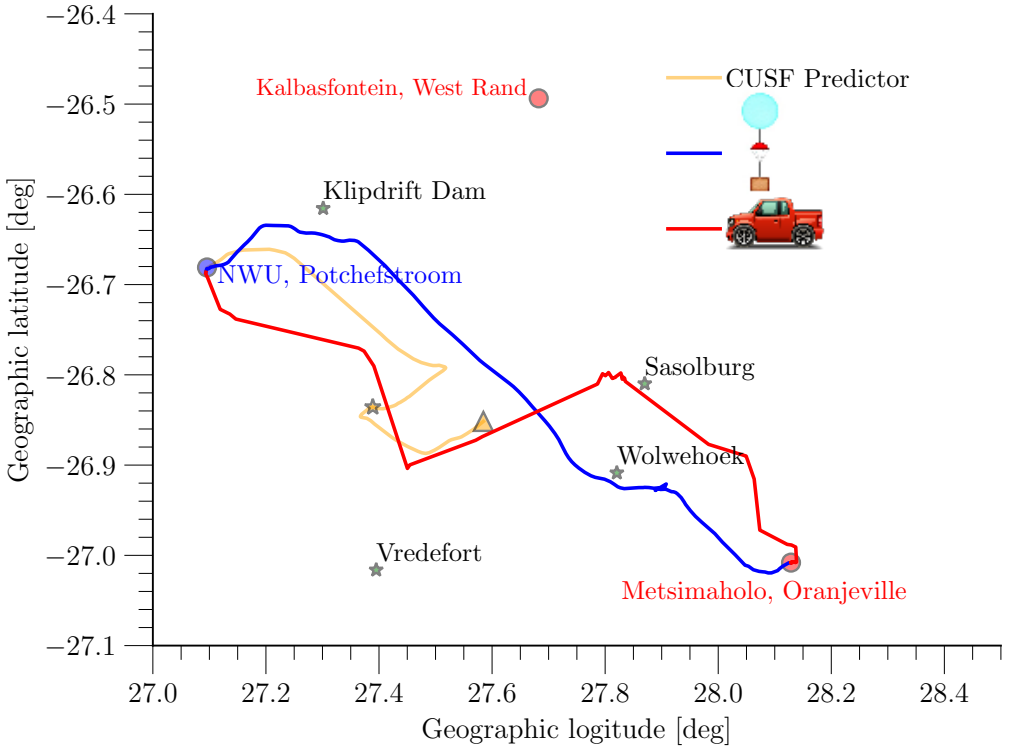

FIGURE 5.9: Balloon flight trajectory (blue), flight path predictor (orange), and return route from the balloon land site to launch site (red).

5.6 Recovery

Due to the absence of a live radio tracker to track the balloon and obtain real-time data of which recovery of the payload is essential. Although the prediction software is not perfect, it does constrain probable flight trajectories based on weather conditions. As shown in Figure 5.9, the CUSF balloon trajectory did not successfully determine the expected landing site for the 2019 launch, but it did estimate the correct direction to the landing site.

The payloads used for both launches were recovered successfully on the same day more than 55.83 g/cm^2 (i.e ∼20 km) away from the predicted landing sites. The cellphone GPS tracker transmitted the exact landing location of the payload after landing. Figure 5.10 shows the condition in which the payload was found at the landing site. The payload electronics were still in good working condition.

5.7 Balloon Flight Results

Figure 5.11 compares the 2018 and 2019 flight results. During the 2018 flight, P_c at the launch site was 6.88 GV and 7.03 GV at the landing site, while in 2019 the landing site's P_c was 7.2

FIGURE 5.10: The state of the payload found at the landing site.

GV. Therefore, P_c changes can be neglected for the data evaluation. In panel [A], the count rates from the counter are shown as circled black dots, while the uncertainty is given as the Poisson error and plotted as red bars. The original time resolution of the detectors is set to one minute, while a two minutes moving average is used to show data trends. The Regener-Pfotzer maximum in both 2018 and 2019 flights are clearly visible as marked by the thin broken lines, though the exact altitude at these peak rate is slightly obscured by the scatter in the data. The shaded grey areas represent the balloon burst altitudes.

Panel [B] shows the atmospheric pressure and temperature profiles. As altitude increases from ground-level, the atmospheric pressure decreases. Pressure is a direct measure for the residual atmosphere which describes the shielding by the atmosphere above the HARM detector. In both 2018 and 2019 flights, pressure value at high altitudes is almost comparable. The plot shows that the temperature inside the box decreased with increasing altitude and it reached about $-10°C$ at the burst altitude during the 2018 flight, while in the 2019 flight the temperature reached about $-20°C$ at the burst altitude. The green vertical line is used to guide the eye, to show that the shaded region in the blue curve might not be the burst altitude. The reason for this misalignment is unclear. However, it can be speculated that a possible reason might be the strong influence of the temperature dropping below the $-20°C$ Geiger-Müller working operation range.[29]

[29] http://www.libelium.com/v11-files/documentation/waspmote/radiation_board_eng.pdf

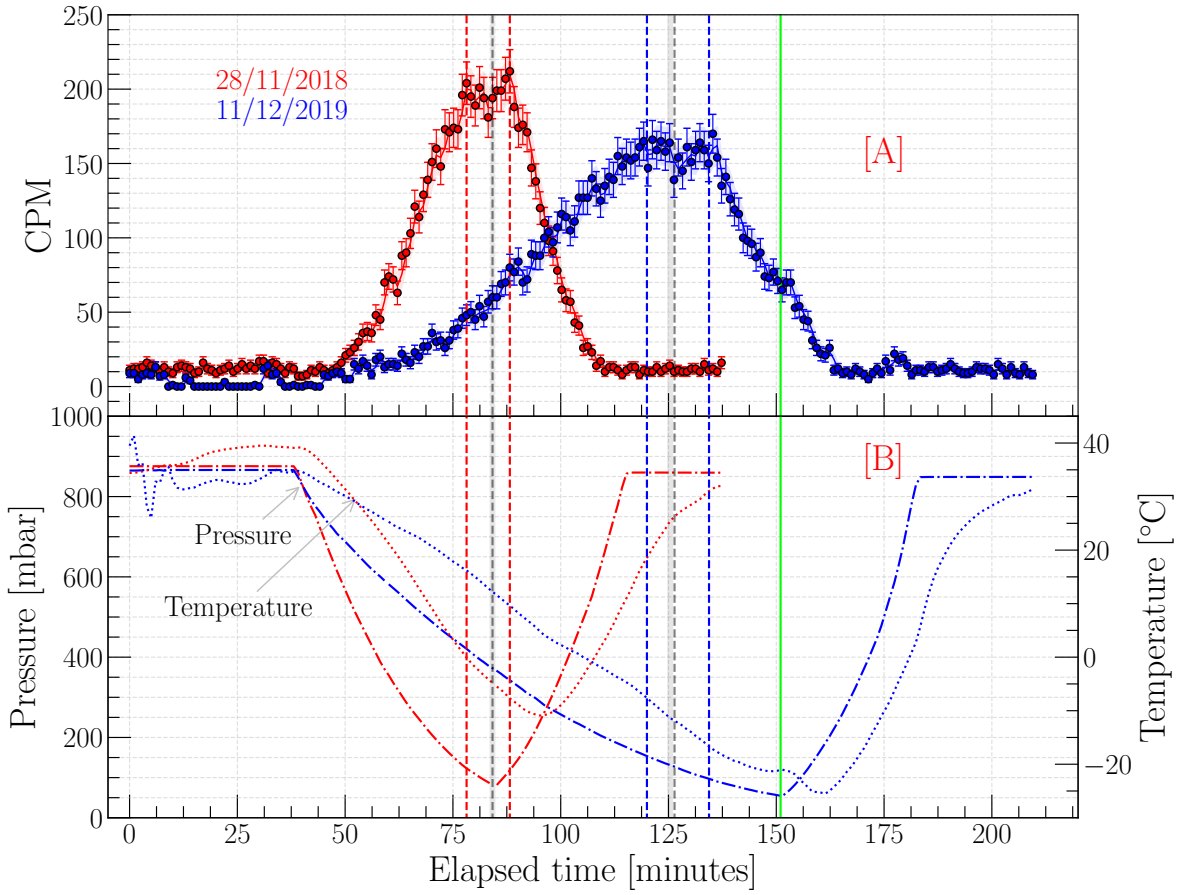

FIGURE 5.11: Panel [A] shows the count rate time profile during the balloon flight in counts per minute. These count rate values are comparable. Panel [B] shows housekeeping data from the flight. The counts per minute (CPM; panel [A]), atmospheric pressure and temperature (panel [B]) are shown as a function of the elapsed time from launch. The red and blue colours represent the 2018 and 2019 measurements, respectively. The grey shaded area represents the burst altitude area, while the blue and red thin vertical lines represent the Regener-Pfotzer maximum before and after the burst altitude. The green vertical line is used to guide the eye and to show that the shaded region in the blue curve might not be the burst altitude.

5.8 Summary

A tested readout electronics system based on a Geiger-Müller counter detector was used to measure stratospheric radiation. The launch procedures, individual parts and design fundamentals, launch and recovery, and data processing were discussed. The HARM instrumentation presented in this work gave satisfactory results. From these measurements, it is not possible to calculate any dosimetric quantities such as dose equivalent (or Ambient dose equivalent). Beyond these scientific expectations, the HARM instrumentation can provide valuable measurements suitable for educational purposes to demonstrate atmospheric radiation variation with changing altitude or (and) geomagnetic cutoff rigidity P_c.

CHAPTER 6

The RPiRENA Dosimeter

6.1 Introduction

In light of the HARM detector's disadvantages, discussed in Section 5.8, one of the goals of this work is to assemble a cosmic-ray detector, based on the RPi, for dosimetry applications on radiation exposure assessment. The assembled dosimeter prototype should ideally be lightweight, relatively small, and portable, to make it suitable for use in different locations on ground-level and at aviation altitudes (or even stratospheric balloons). In this work, a prototype of such an instrument was re-assembled based on the pre-existing RPiRENA (RPi stands for Raspberry Pi and RENA stands for Read-out Electronics for Nuclear Applications) prototype, developed by Professor Stephan Böttcher of the *Christian-Albrechts-Universität zu Kiel*. A detailed description of the RPiRENA project can be found on the website http://www.ieap.uni-kiel.de/et/people/stephan/rpirena/.

This chapter gives an overview of the RPiRENA, describing the dosimeter development steps, the initial tests, and the calibration results.

6.2 RPiRENA Historical Background

Traditionally, the electronics used in radiation detection are expensive, complicated to set up and they are not portable, lightweight or small, and in many cases, not suitable for aviation dosimetry. After the positive-negative (PN) diode was developed in the 1940s, the positive-intrinsic-negative (PIN) diode, a modified version of the PN diode, came into existence in the 1950s. The PIN diode is a semiconductor detector used to convert an optical signal into an electrical signal, i.e. either current or voltage. According to *Ritter* [2013], PIN diodes can be

fabricated to small sizes and are relatively easy to handle. Also, in bias mode operation, these silicon diodes (SDs) provide a high energy resolution and are capable of detecting ionizing radiation within a broad energy range. Furthermore, different from other semiconductor detectors, they do not require cooling for operation and during operation, the signals from the detector can be processed immediately.

Due to these several advantages of using PIN diodes, a cosmic-ray detector based on a RPi known as RPiRENA was assembled. This plug-in board for the RPi implements a four input multi-channel analyser and is capable of reading all four low/high gain channels simultaneously, either in single mode or telescope mode, making it an ideal detector for dosimetry. In single mode, the SDs are sensitive to charged and neutral (especially photons) particles of the incident radiation, while in telescope mode only charged particles are detected. The detection system circuitry draws its power from the 3.3 V and 5 V RPi GPIO pins. According to Stephan Böttcher, the RPiRENA project[1] "*was born out of a big messy compilation of code and designs that accumulated during the work done for the ESA space mission Solar Orbiter,*[2] *several balloon flight missions onboard Bexus balloons*[3] *and the Mars Science Laboratory mission*[4]". This project features open source software and hardware.

6.3 Silicon PIN Diodes

Silicon sensors have been used in various fields of science as positioning detectors in space science and experimental particle physics, and in this work as radiation detectors. For decades, the well established off-the-shelf PIN diodes have been used for dosimetric studies at aviation altitudes, low Earth orbit (see studies by *Beaujean et al.* [2002], *Beaujean et al.* [1999], *Ritter* [2013], *Möller* [2013], *Berger* [2020]), and for space radiation dosimetry (see studies by *Held et al.* [1993], *Spence et al.* [2010], *Zeitlin et al.* [2013], *Porter et al.* [2014], *Berger* [2020]). In this work, two commercial s2744-08 silicon PIN diodes (manufactured by Hamamatsu Photonics[5,6]) in either single or telescope mode, separated by 5 mm, are used. In each SD, the connection pins to the SDs were straightened and shortened so that the attached preamplifier board does not physically make contact with the SDs, as shown in Figure 6.1. These shortened wires ensure that the signal wires transmit as little noise as possible. The preamplifier circuitry is connected to the readout electronics through a ribbon cable terminated with a 10-pole connector which

[1] http://www.ieap.uni-kiel.de/et/people/stephan/rpirena/
[2] https://sci.esa.int/web/solar-orbiter
[3] http://rexusbexus.net/bexus/
[4] https://mars.jpl.nasa.gov/msl/home/
[5] http://www.hamamatsu.com
[6] http://www.alldatasheet.com/datasheet-pdf/pdf/212344/HAMAMATSU/S2744.html

FIGURE 6.1: Complete RPiRENA housing's exterior [panel **A**] and interior [panel **B**]. Close-up of the Hamamatsu SDs s2744-08 in single mode [panel **C**] and telescope mode [panel **D**].

is located underneath the detectors. This readout system, as well as the preamplifiers, are discussed in the next sections.

The SDs were mounted inside a thin aluminium housing with a thickness of 4 mm.[7] This thickness is crucial as it determines the lowest energy that can be detected. The thickness of the SDs is 300 μm,[6] while the width and length of the SDs are 1 cm and 2 cm,[6] respectively. For light, the sensitive effective area is 1 cm^2,[6] while for ionizing radiation, it is 2.31 cm^2.[8] The SDs are connected in reverse to the bias voltage. Based on the data sheet, the SDs require a bias voltage between 40 V (minimum for full depletion) and 100 V (break-down voltage). This bias voltage ensures that the detectors with a thickness of 300 μm are fully depleted. For a

[7] http://www.hammondmfg.com/

[8] The full surface length and width of the diodes, i.e. 2.1 cm and 1.1 cm, are considered for ionizing radiation under the aluminium frame

single SD, the geometry factor (GF) in units of $cm^2 \cdot sr$ is 7.257 $cm^2 \cdot sr$, while for two identical diodes in telescope mode separated by 5 mm, the GF is about 3.74 $cm^2 \cdot sr$ (see Appendix C for a detailed calculation of the geometry factor).

6.4 RPiRENA Housing

Figure 6.1 shows the interior and exterior of the assembled RPiRENA housing, as well as the two PIN diodes' orientation when mounted inside a light proof aluminium housing. As seen from the figure, the aluminium housing enclosing the detector head was separated from the readout electronics to minimise electronic interference. The Printed Circuit Boards (PCB) are located in the upper-right part of the housing.

6.5 Readout Electronics

A block diagram of the RPiRENA's electronics circuitry is shown in Figure 6.2, while Figure 6.3 shows its working principle. Shown in Figure 6.3, are the signal paths from diode 1 (SD1, on top) and diode 2 (SD2, at the bottom) in telescope mode, which are connected to the charge sensitive preamplifiers (CSA). The following electronics shape and amplify the signals in two subsequent amplification stages for low gain (not used in this work) and high gain. In low gain, small signals are amplified, which results in detecting large energy depositions, while high gain results in larger signal amplification covering small energy depositions in the detector. The main processes in this block diagram of three stages, i.e. detection, processing and storage. These are discussed in the following sections.

6.5.1 Detection

When the PIN diode is reverse biased, the entire intrinsic (I) region is quickly filled with free charge carriers from the positive (P) and negative (N) regions. A pair of free charge carriers (known as the electron hole pair) is generated in the SDs during interactions with incident radiation. Within the SDs, the number of electron hole pairs created is proportional to the amount of energy deposited by the incident radiation. However, the amount of ionization energy needed to produce an electron hole pair has been estimated to be about 3.6 eV at room temperature [*Leo*, 1987]. Figure 6.4 illustrates how the s2744-08 SD produces these electron hole pairs (see the red and blue circles).

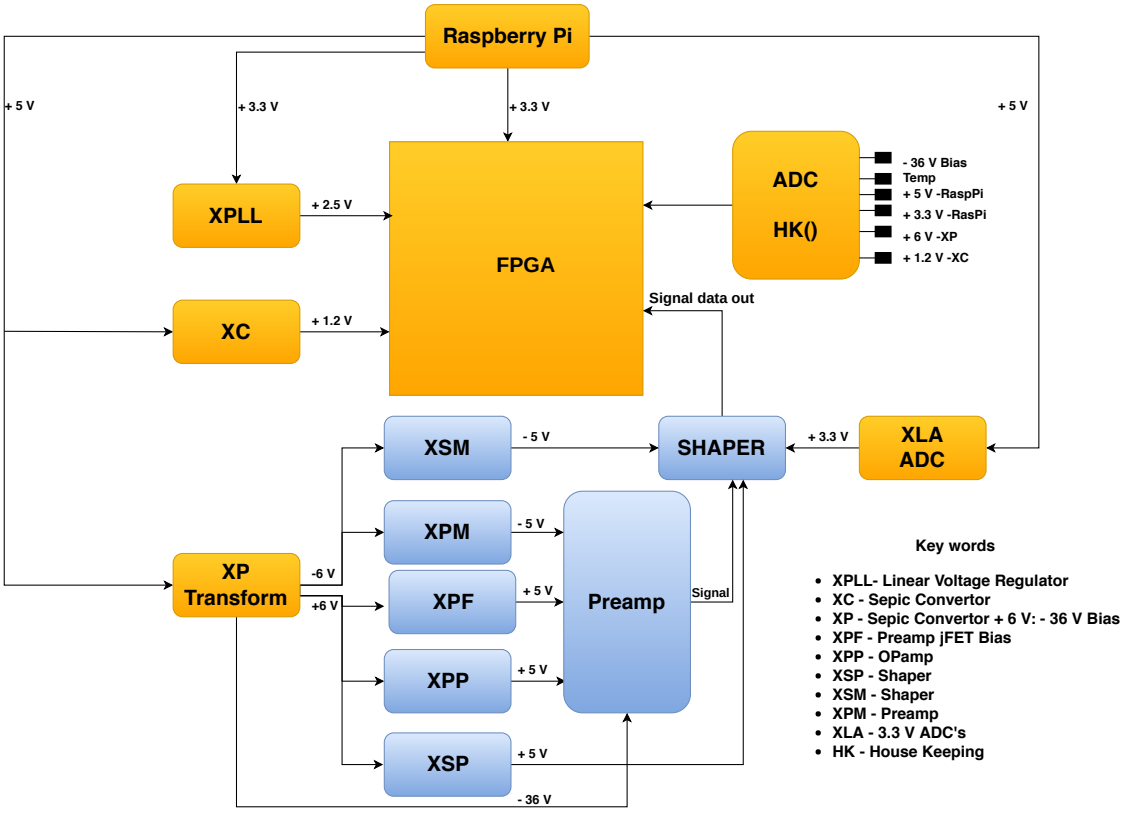

FIGURE 6.2: Schematic representation of the components comprising the RPiRENA detector electronics.

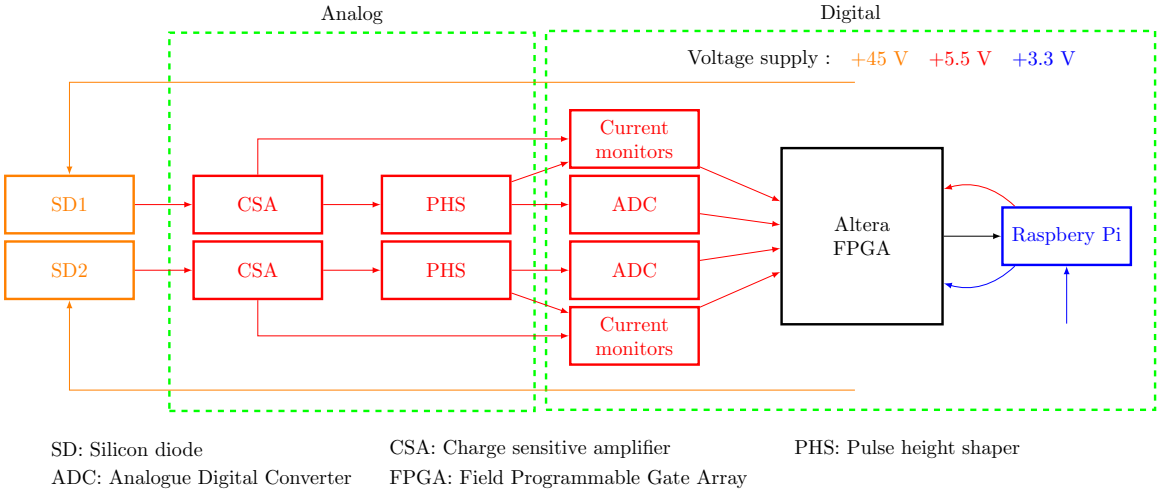

FIGURE 6.3: Readout electronics used together with two SDs. Different modules are divided into an analog and a digital part.

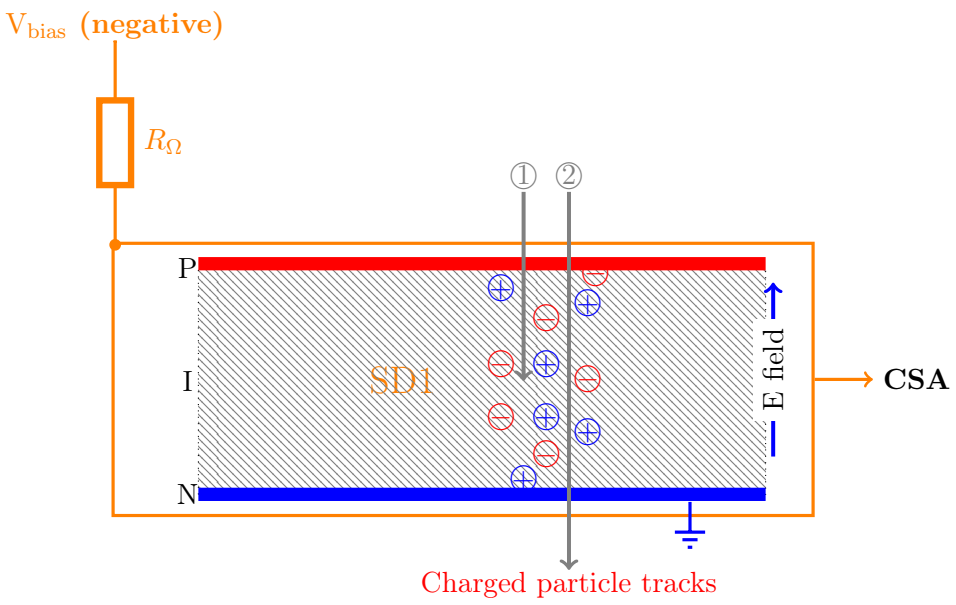

FIGURE 6.4: Schematic view of the RPiRENA's biased PIN diode when used to detect ionizing radiation.

Two scenarios are presented, enumerated 1−2, i.e. [1] for low energy incident radiation, e.g. γ radiation, with energy approximately higher than 3.6 eV, charge carriers are generated across the SD along the tracks of the incident radiation and the incident radiation will be completely absorbed (through the photo-electric effect, see Section 3.2.3) in the diodes if the energy of the incident radiation is less than approximately 60 keV. However, for [2], i.e. a case of very high ionization densities (as discussed in Section 3.2.1), the incident radiation will undergo case [1] and eventually escape the SD, leaving a fraction of its energy in the SD. When energy deposition occurs, this causes the generated carriers to separate and accelerate towards the electrodes. This in turn will cause a short charge pulse (due to the separated charges) that is then processed by the very first part of the amplifier chain, the charge-sensitive amplifier (or charge-sensitive preamplifier). The charge-sensitive amplifier converts this charge pulse into a voltage pulse.

6.5.2 Signal Processing Chain

Charge-sensitive amplifier (CSA), pulse-shaping amplifiers, and the signal processing chains are important building blocks of SDs [*Van der Plas et al.*, 2006]. The major parts of this chain are briefly discussed in the order of information flow, enumerated 1−3, i.e. [1] CSA: As mentioned, the incident particle interactions with the SDs result in the deposition of a fraction (or all) of its energy in the SD, and therefore a short charge pulse will be registered due to the released electron charge. However, the pulse is too small to be sensed directly. Therefore, the pulse will

first be sent to the preamplifier section of the analog electronics, which is an interface between the SDs and the subsequent shaper electronics. [2] Shaping: The shaping stage converts the post-amplified pulse output. Signals from the CSA are sent to the shaping circuitry where it is shaped into a Gaussian pulse, producing a voltage pulse with the peak voltage proportional to the deposited energy. [3] Digitization: Following shaping, the next step is digitization of the signal. For all the pulses generated, amplified and shaped, a threshold is set, corresponding to a minimum energy deposition, below which the instrument will not be sensitive. The pulse magnitude is digitized by a 16 bit analog-to-digital Converter (ADC). A Field Programmable Gate Array (FPGA) is programmed to periodically sample the ADC signals and detect the peak voltage (i.e. the pulse height). Since the pulse height is proportional to the energy deposited, the ADC value is proportional to the energy deposited in the detector.

6.5.3 Storage

The digital voltage of each pulse is stored locally inside the FPGA. The RPi reads the output of the FPGA and stores the pulse height amplitude (PHA) for every event in both SDs, with time stamps, on the μSD-card card attached to the RPi.

6.6 Low-energy Calibrations: Laboratory Radioactive sources

To calibrate the low energy range of the RPiRENA, radioactive sources were used. This dosimeter is most sensitive to charged particles, but also to $\gamma-$rays as mentioned. A wide range of radioactive sources at NWU were available for use. Americium-241 (^{241}Am), Caesium-137 (^{137}Cs), Barium-133 (^{133}Ba) and Bismuth-207 (^{207}Bi) radioactive sources were used. The measurements were performed at the NWU (on January 30, February 4, February 6, 2019), except measurements with ^{207}Bi which were conducted at the *Christian-Albrechts-Universität zu Kiel* on June 12, 2019. For the chosen radioactive sources, the PIN diodes are capable of fully absorbing the released X$-$ and $\gamma-$ray energy. Since the X$-$ and $\gamma-$rays are all at lower energies, the ADC trigger thresholds were set to 15 mV to measure even the lowest energy deposition. Below this value, initial results showed that the diodes are measuring too much noise. Figure 6.5 shows all the radioactive sources used, either placed on top or next to the aluminium housing in the left panels (top to bottom), while the nuclear decays that are expected to be observed from these radioactive sources are shown in the right panels (top to bottom). In telescope mode, the diodes detection surface was positioned perpendicular to the direction of incoming radiation. Measurements were taken for about two hours per radioactive source. The measured spectra from the radioactive sources are shown in the next sections. All

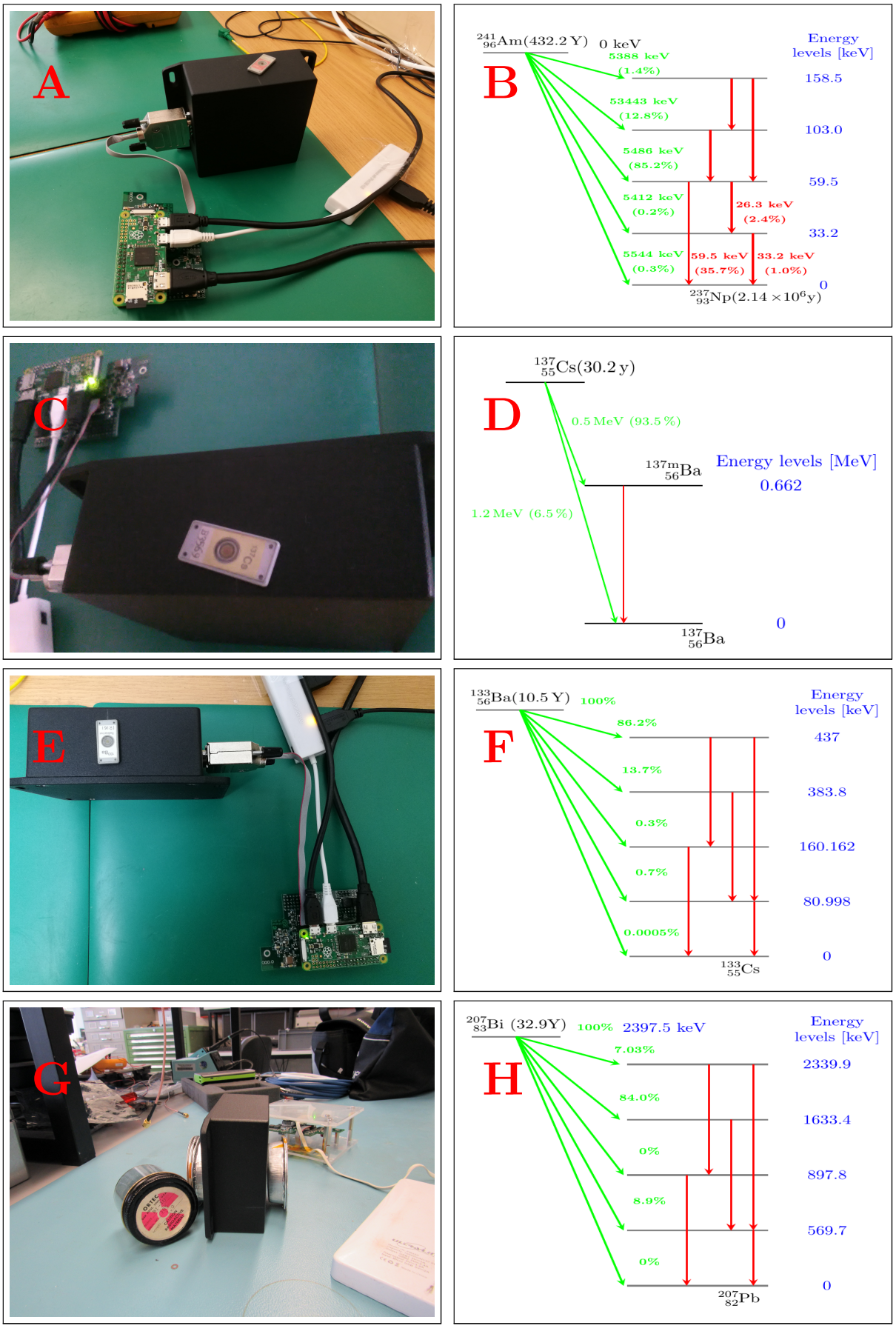

FIGURE 6.5: Left panels (top to bottom) show the radioactive sources used for calibration, while the right panels (top to bottom) show the corresponding (simplified) decay schemes. The decay scheme in panel **B**, was taken from *Khatry et al.* [2017], while those in panel **D**, **F**, and **H**, are from *Knoll* [2000].

spectra, except the ^{241}Am, show a Compton edge, and as shown by *Wüest et al.* [2007] and *Böttcher* [2018] among others, a Compton edge can also be used for energy calibration, as it is done in this work.

6.6.1 Americium-241 source

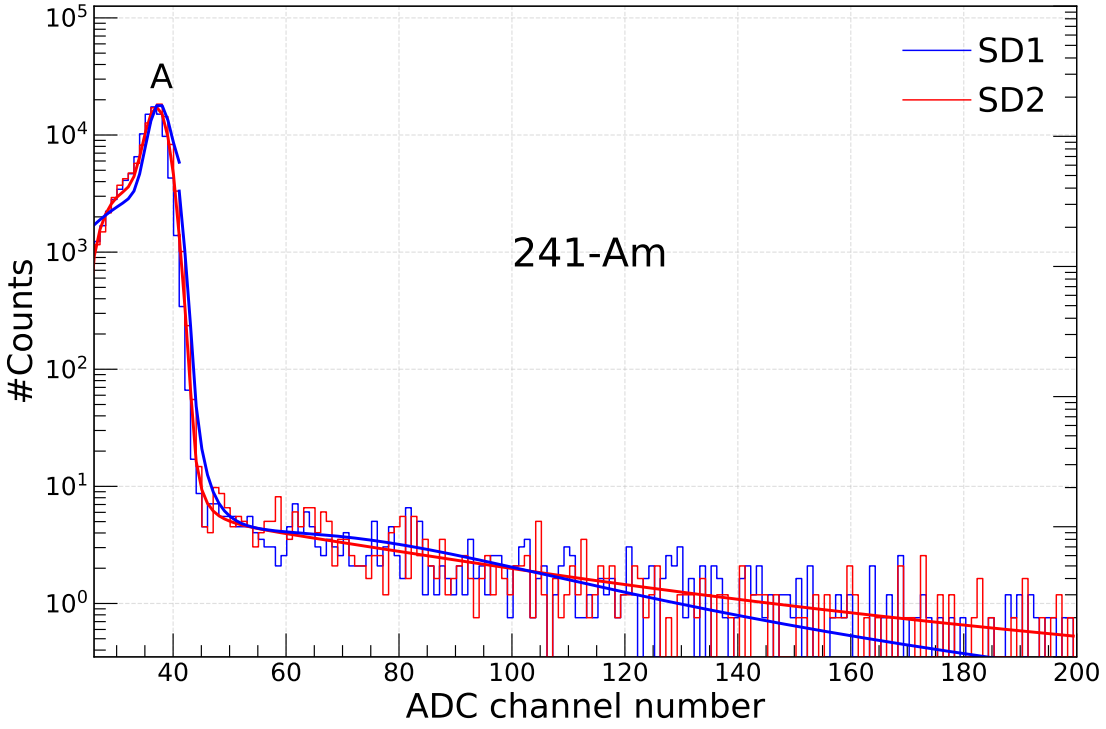

FIGURE 6.6: The ^{241}Am spectrum measured in SD1 (blue curve) and SD2 (red curve) with the solid lines showing data fits. The symbol **A** represents the 60 keV γ peak.

Americium-241 (^{241}Am) is a good calibration source because of the strong 60 keV γ line and most dosimeters are calibrated using this most dominant γ line as the lowest detection limit. Apart from γ lines, α sources offer the advantage of higher energies, in excess of 5 MeV. The α line calibration was not performed in this work, due to the fact that calibrations needed to be performed under vacuum because these α-particles lose energy rapidly in air (see *Knoll* [2000]). Figure 6.6 shows the experimental 60 keV γ line for both SDs. The spectra are truncated and zoomed in for better visualization. The blue colour represents measurements from SD1, while SD2 is represented by red. The measurements of each SD are fitted (here and in subsequent sections) by a normal exponential, plus a Gaussian distribution (solid lines). This shows how the energy loss distribution changes with increasing energy loss within the SDs. Since the ^{241}Am source showed a sharp peak (marked **A** on the plot) of the 60 keV γ line, only this peak was used for calibration that converts the ADC value into an energy deposition. The results of the peak fit parameters are listed in Table 6.1.

6.6.2 Caesium-137 source

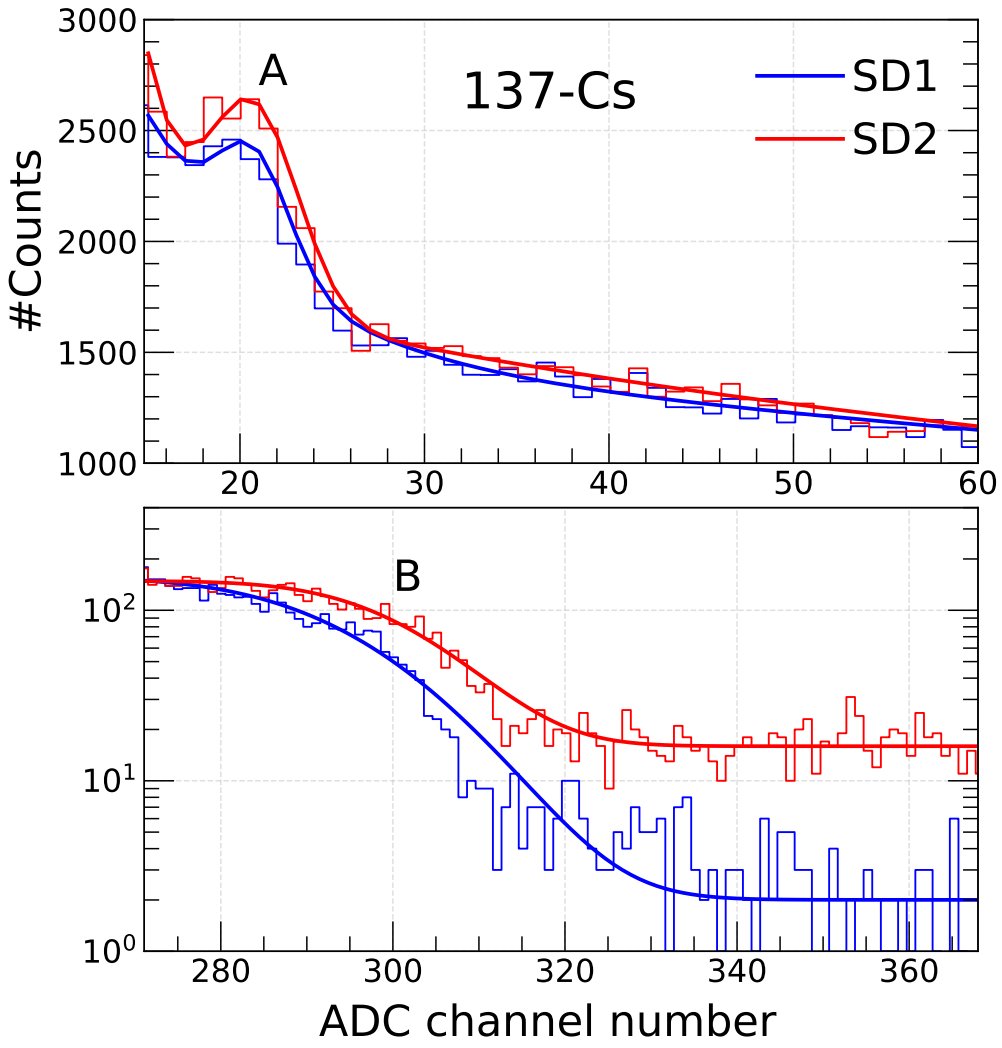

FIGURE 6.7: Same as the previous figure, but now for ^{137}Cs. Symbol **A** and **B** indicate the 32 keV X-ray and 478 keV Compton edges' energies from both SDs.

Measurement with the ^{137}Cs radioactive source was performed following the same procedure as previously discussed. For this ^{137}Cs source, photons with an energy of 0.662 MeV showing the photo-electric effect absorption and Compton scattering are expected [*Knoll*, 2000], along with a Compton edge at 478 keV. Figure 6.7 shows the ^{137}Cs experimental observations for both SDs. However, the Compton edge is clearly seen and indicated on the figure with symbol **B**. Not shown in Figure 6.5, the decay of ^{137}Cs also releases 32 keV characteristics x-rays from the excited daughter nucleus ^{137}Ba [*Frederiksen*, 2017]. This 32 keV X-ray energy is indicated by **A** on Figure 6.7. Because of a lack of better high-energy data, the observed Compton edge will also be used for further calibration. In addition, the Compton edge, peak **B**, was fitted

with the error function of the form

$$g(\mathrm{ADC}_i) = \left(\frac{a_0}{2}\right) \cdot \mathrm{erf}\left(\frac{a_1 - \mathrm{ADC}_i}{a_2^2}\right) + a_3 \tag{6.1}$$

where a_0 and a_3 are the peak amplitudes of the spectrum on the left and right side of the Compton edge, respectively. The error function is represented by erf, while a_1 is the position of the Compton edge and a_2 is the measure for the width of the Compton edge. The ADC_i is the position of the Compton edge estimated by the fit programme, with i being the channel number.

6.6.3 Barium-133 source

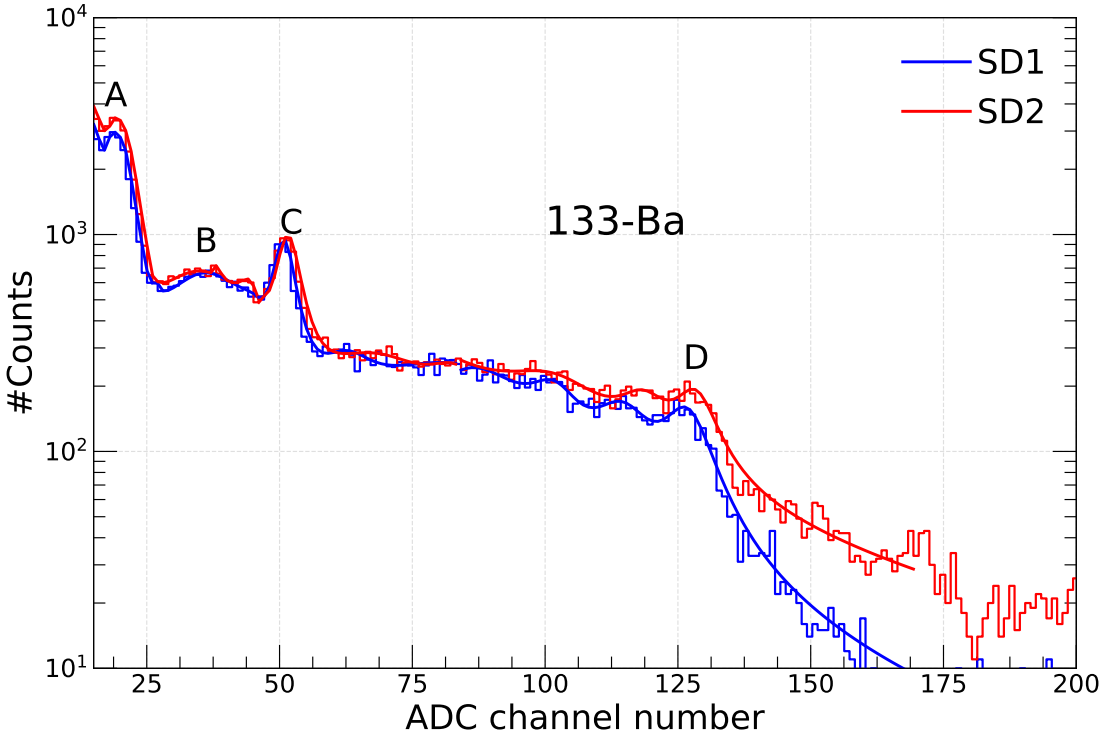

FIGURE 6.8: Same as the previous figure, but now for ^{133}Ba. The symbols **C** and **D** indicate γ line peaks at 81 keV and 207 keV, while X-ray peaks **A** and **B**, with energies of 30.9 keV and 53.2 keV, could also be identified.

A similar procedure as the previous calibrations was applied, but now for ^{133}Ba source. In Figure 6.8, the response of the detection system using this source showed γ line peaks at 81 keV (marked **C** on the plot) and 207 keV (marked **D**), respectively, while X-ray peaks at 30.9 keV (marked **A**) and at 53.2 keV (marked **B**) were observed. Other expected peaks cannot be clearly identified; see also studies by *Wüest et al.* [2007] and *Kim et al.* [2014]. The Compton edge, peak **D**, was fitted with Equation 6.1. The 30.9 keV and 53.2 keV lines, not shown in

Figure 6.5, are once again characteristics X-rays (30.9 keV) and escaping X-rays (53.2 keV) produced in the decay process. For calibration, data from peaks **A**, **B**, **C** and **D** were used.

6.6.4 Bismuth-207 Source

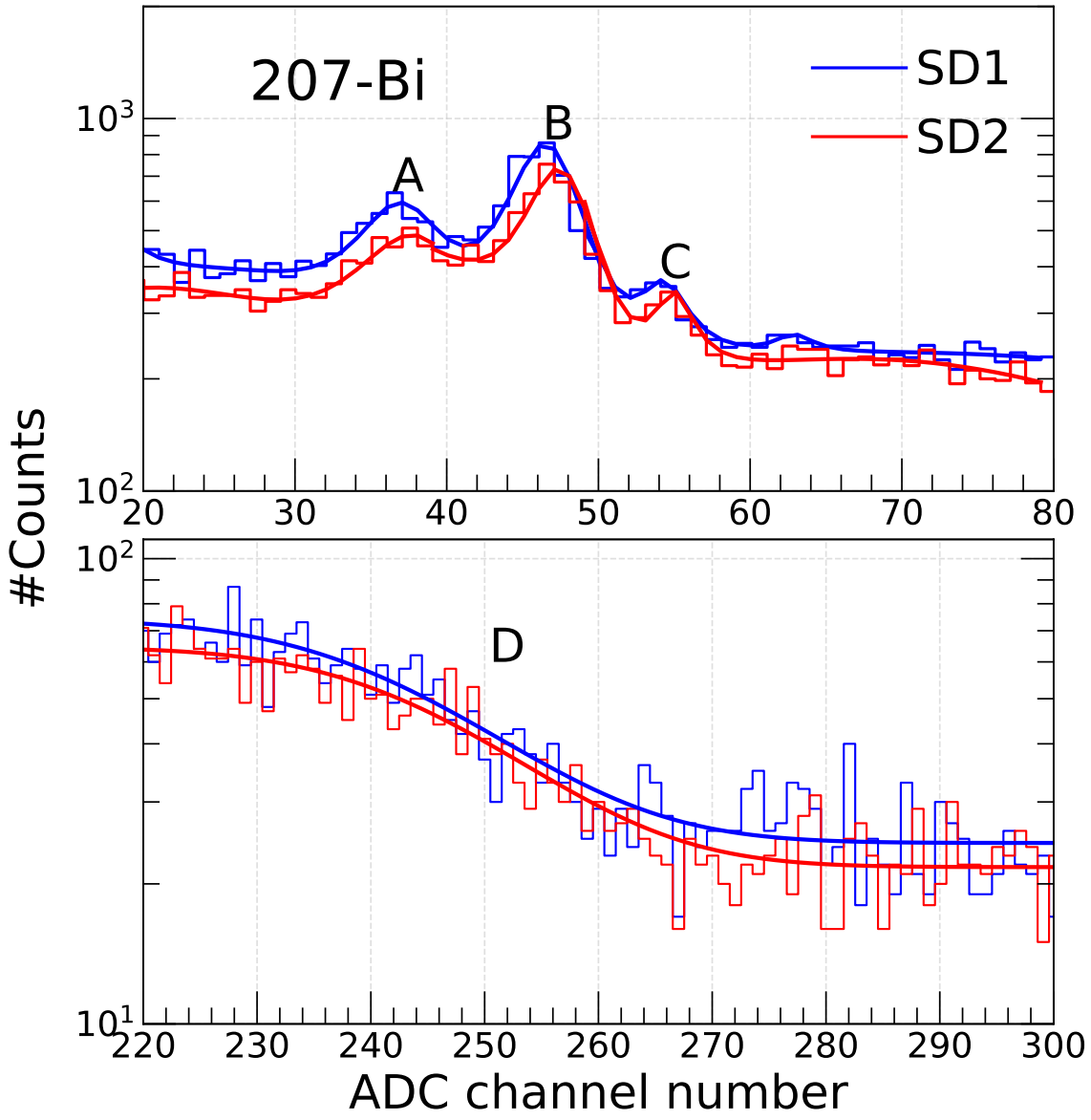

FIGURE 6.9: Same as the previous figure, but now for ^{207}Bi. A, B and C represent the 58, 75 and 85 keV X-ray energy deposition in the SDs, while D represents the Compton edge of the 393.31 keV γ line.

For the ^{207}Bi radioactive source (enclosed in a thin foil), a similar procedure as discussed previously used was followed. In Figure 6.9, X-rays around 58, 75 and 85 keV (marked **A**, **B** and **C** on the plot) were observed, as well as the first Compton edge of the γ line at 393.31 keV marked **D**. The low energy X-ray peaks are all characteristic X-ray lines from ^{207}Pb. Data

from all these peaks were used for calibration. The Compton edge, peak **D**, was fitted with Equation 6.1.

6.7 Energy Calibration

Results from measurements, using the radioactive sources, are recorded in Table 6.1 and plotted in Figure 6.10.

TABLE 6.1: Calibration values and statistical comparisons from both SDs.

Date	**Radioactive source**	**Energy** (keV)	**ADC Channels** SD1	SD2	Ratios (% RD[a])
30.01.2019	^{241}Am-γ	60.0	(37.52 ±0.04)	(38.19±0.04)	1.02 ± 1.00 (1.77 ± 0.00)
04.02.2019	^{133}Ba-γ	80.9	(51.11±0.14)	(52.04±0.15)	1.02 ± 1.07 (1.80 ± 6.90)
	^{133}Ba-(X-ray)	32.0	(18.50±0.47)	(18.58± 0.51)	1.00 ± 1.06 (0.43 ± 8.16)
	^{133}Ba-(X-ray)	53.2	(35.13±0.42)	(35.7± 0.41)	1.02 ± 1.00 (1.61 ± 2.41)
	^{133}Ba-(X-ray)	207	(126.3±0.38)	(128.4± 0.37)	1.02 ± 0.97 (1.65 ± 2.67)
06.02.2019	^{137}Cs-(X-ray)	32.0	(19.65 ±0.52)	(20.66±0.40)	1.05 ± 0.77 (5.01 ± 26.09)
	^{137}Cs-(X-ray)	478	(293.41 ±0.33)	(300.97±0.38)	1.03 ± 1.15 (2.54 ± 1.78)
12.06.2019	^{207}Bi-(X-ray)	58.0	(36.98 ± 0.29)	(36.91 ±0.30)	1.00 ± 1.03 (0.19 ± 3.39)
	^{207}Bi-(X-ray)	75.0	(46.57 ± 0.28)	(46.31 ±0.29)	1.00 ± 1.04 (0.56 ± 3.51)
	^{207}Bi-γ	85.0	(54.19 ± 0.17)	(54.91 ± 0.18)	1.01 ± 1.06 (1.32 ± 28.57)
	^{207}Bi-γ	393.31	(245.41 ± 0.35)	(247.95 ± 0.37)	1.06 ± 1.76 (1.03 ± 5.56)

[a]Relative percentage difference (RD): $\frac{|\text{SD1}-\text{SD2}|}{\left(\frac{\text{SD1}+\text{SD2}}{2}\right)} \times 100\%$.

From these measurements, a linear calibration curve (solid line) was calculated for both SD1 and SD2. The linear regressions are represented by

$$E_i = (\text{A} \pm a_0) \cdot \text{ADC}_i + (\text{B} \pm b_0), \tag{6.2}$$

where E_i is the energy deposition corresponding to the ADC_i value and i represents the channel number. The fit coefficients A, a_0, B and b_0 are listed in Table 6.2.

TABLE 6.2: Linear regression fit parameters for both SDs.

ADC Channels	Fit Coefficients			
	A	$\pm a_0$	B	$\pm b_0$
SD1	1.596	0.008	0.240	1.042
SD2	1.618	0.011	-1.829	1.370
Ratios	1.014	1.375	7.621	1.315

The linearity of the calibration curve shows the stability of the detector system [*Ritter*, 2013]. It can be seen from the SD1 and SD2 data in Table 6.1, along with the regressions, that there is a slight difference between the SDs, ranging between 0.2% to 5%. This is probably due to small uncertainties in the electronics components and manufacturing tolerances. However, the

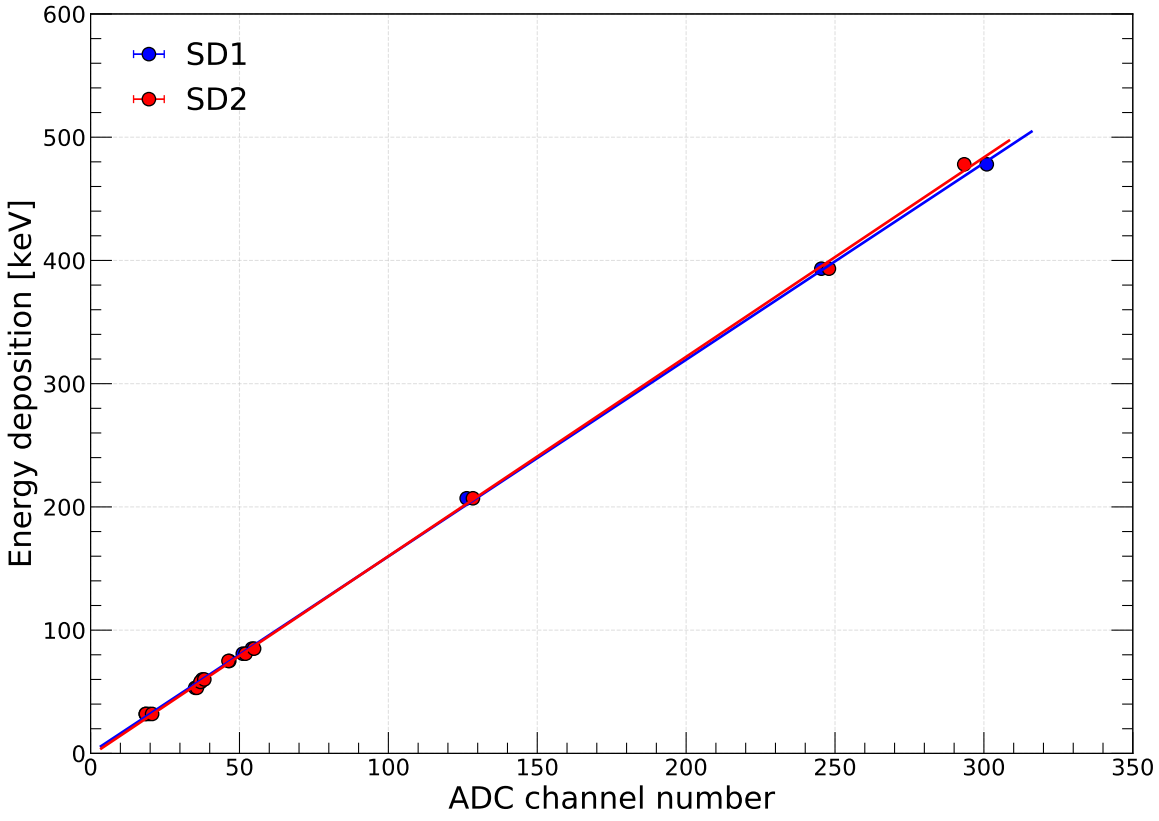

FIGURE 6.10: Calibration data (symbols) and calibration curve (solid lines) that convert ADC channel numbers to deposited energy for SD1 (blue) and SD2 (red).

energy deposition in both SDs is comparable as reflected by the calculated ratios, shown in Table 6.1.

6.8 Summary

This chapter briefly discussed the assembled RPiRENA prototype along with the functionality of the Hamamatsu s2744-08 SDs and the sensor head. The data processing sequence and storage were briefly explained, whereafter the assembled RPiRENA was tested and calibrated, and its reliability verified. The energy deposition threshold in the SDs due to particles having to enter the aluminium housing is not accounted for, but it is assumed to be negligible. Energy losses due to phonons and nuclear recoil is beyond the scope of this work. The calibrated energy deposition was found to be linear within the experimental energy range, as shown in Figure 6.10. The energy deposition in both SDs is shown to be similar, with measurements expected to differ by less than 5%, due to manufacturing tolerance of analogue electronics. Based on the energy deposition response, the detector is expected to give a satisfactory response to the atmospheric radiation field at aircraft cruising altitudes.

CHAPTER 7

RPiRENAs Flight Measurements

7.1 Introduction

The RPiRENA's flight measurements on board an aircraft are discussed. These measurements covered a broad range of geomagnetic cutoff rigidities and aviation altitudes, which are two dominant factors in dose assessment. For all on board measurements, a 15 mV trigger threshold, set for energy calibration in Chapter 6, was used. However, due to the dynamic nature of the radiation environment at aviation altitudes, a threshold re-adjustment was performed several times during data processing to exclude events suspected to be noise.

Possible influences of space weather are a determining factor for understanding and interpretation of the RPiRENA's measurements and calculated quantities. Several hours before and during each flight, the geomagnetic conditions were assessed using the Kp index.[1] No significant contribution of solar energetic particles capable of producing GLEs was reported, during these flights. In addition to space weather and geomagnetic field effects, the measured absorbed dose rates at aviation altitudes are also influenced by changes in the solar modulation of GCRs.

Similar to the previous chapters, all flight altitudes will be mainly given in residual atmosphere (in units of g/cm^2). As a reference, 190 g/cm^2 roughly corresponds to an altitude (or flight level) of 40 kft, 225 g/cm^2 to 36.6 kft, and 270 g/cm^2 to 32.7 kft. The analysis procedure for dosimetric quantities used in this work is similar to that of *Ritter* [2013]. This work follows an International system for airport names, therefore ICAO codes were used throughout.

[1] https://omniweb.gsfc.nasa.gov/form/dx1.html

7.2 Measurement on board an Aircraft: RPiRENA

All flights measurements were obtained in accordance with the airline regulations regarding the safe use of Portable Electronic Devices (PEDs) as discussed in Appendix B. The RPiRENA prototypes were placed either under the passenger seat, on an empty seat, or in the overhead storage of the aircraft when taking measurements.

FIGURE 7.1: Dosimeter position on board an aircraft when taking measurements.

Figure 7.1 shows some of the preferred positions when taking measurements. The actual flight trajectories and the great circle approximations of flights flown with the silicon diodes (SDs) in different setups, discussed in the following sections, are shown in Figure 7.2. The actual flight route is shown in solid curves,[3] while the great circle path (denoted as GC) is shown as broken curves. The assembled RPiRENA's first flight is denoted as Flight 00 in the figure.

7.3 Medium-haul and Long-haul International Flight Measurements

Different SDs setups were applied during these flights measurements. Figure 6.1 shows two setups; setup 1 is shown in panel [C], while panel [D] shows setup 2. In setup 1, SD1 points upwards (i.e. approximately in the zenith direction), while SD2 is rotated by 90° with respect to SD1 orientation. The SD1 and SD2 orientations are denoted as $\Uparrow$ and $\Leftarrow$ respectively. This setup investigates the level of non-isotropy of the radiation field at aviation altitudes, i.e. whether particles reach the detector uniformly from all directions or whether there is a preferred flux from the zenith direction. Measurements obtained in this setup are in single mode, i.e. the events registered in SD1 are not registered by SD2. In setup 2, SD2 points upwards (i.e. in zenith direction) while SD1 points downwards. The SD1 and SD2 orientation,

[3] Some of the actual flight routes were not shown due to the unavailability of data from FlightAware.

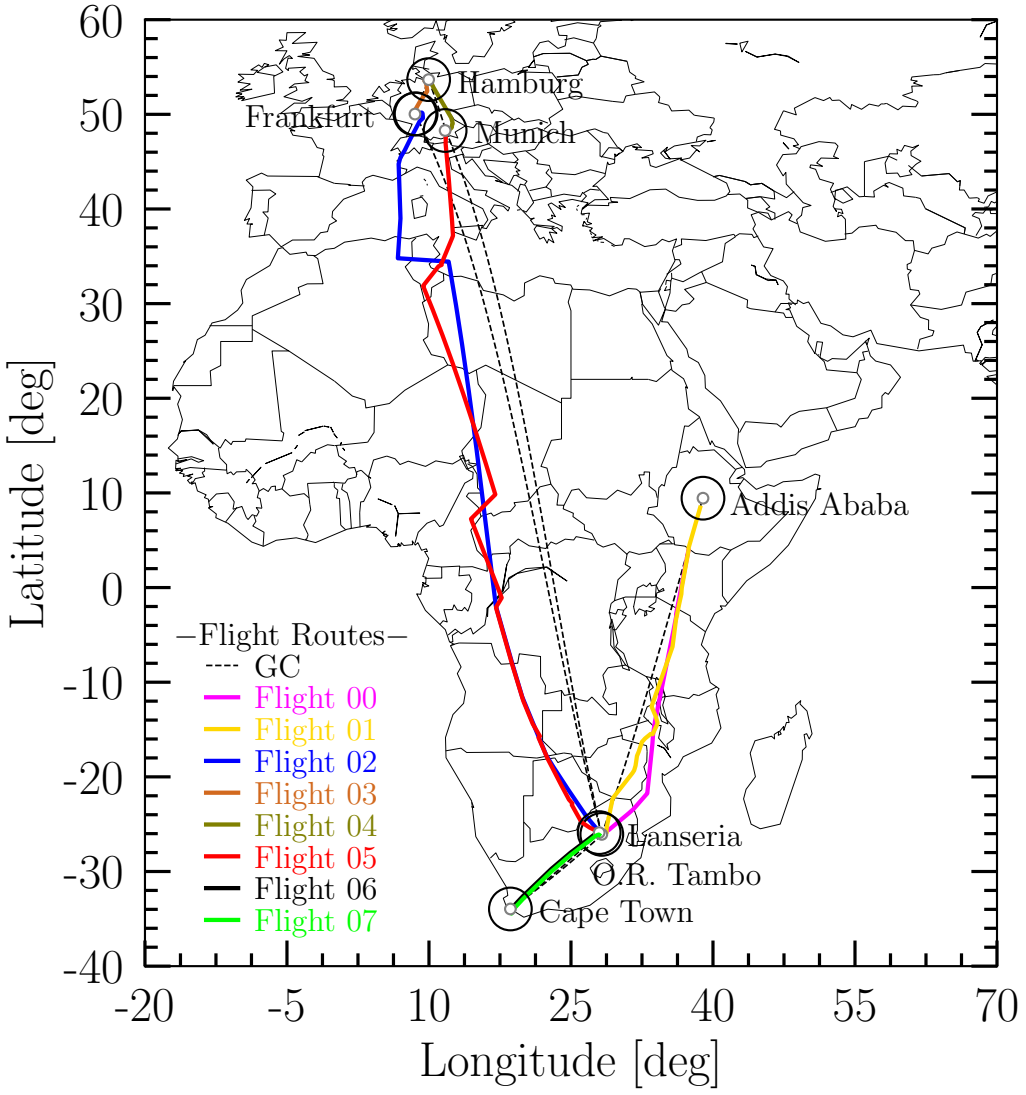

FIGURE 7.2: RPiRENA's flight routes, showing the actual and approximated aircraft routes from departure to destination. Flight route data source: FlightAware.[2]

in telescope mode (SDT), are denoted as ⇓ and ⇑ respectively. Measurements obtained in this setup are used to calculate quality factors directly from determining the linear energy transfer, $\mathcal{L}$, measurements.

Table 7.1 gives an overview of [1] the flight information, e.g. flight routes, cruise altitudes,[4] flight time, aircraft type, and [2] space weather effects, e.g. Kp index and ground based observations, [3] as well as the RPiRENA's SDs orientation at the time of measurement.

Prior, during, and post flight measurements, space weather effects were assessed using a wide range of indicators. Thus, possible influences of space weather on the measurements, shown in Figure 7.3, indicate that the modulation of the GCR component observed with a ground

[4] In column 6, the numbers in brackets indicates the number of times the cruise altitude has changed, this includes the first cruise altitude

TABLE 7.1: Medium-haul and long-haul flight information.

SDs	Aircraft type	Route	Date	Time [hr]	Cruise Altitude [g/cm^2]	$\Delta\mathcal{N}_r$ [%][d]	ΔKp[d]
⇑⇐	B738[a]	FAJS−HAAB	10/03/2019	06.13	243.05−220.81(2)	0.96(100.3)	0.0(0.3)
⇑⇐	B738[a]	HAAB−FAJS	16/03/2019	06.21	231.87−191.29(3)	0.83(099.3)	0.4(2.7)
⇓⇑	A340[b]	FAJS−EDDF	10/06/2019	11.43	255.05−191.29(4)	1.27(101.1)	0.4(0.7)
⇓⇑	A321[c]	EDDM−FAJS	15/06/2019	10.96	267.10−200.56(5)	1.27(100.2)	1.0(1.0)

[a] Boeing 737-800 (twin-jet)
[b] Airbus A340-300 (twin-jet)
[c] Airbus A321-100 (twin-jet)
[d] Modulation level difference, $\Delta\mathcal{N}_r = |\mathcal{N}_r^{\text{max.}} - \mathcal{N}_r^{\text{min.}}|$, while the numbers in brackets indicates the average calculated from departure to destination. Similarly, $\Delta\text{Kp} = |\text{Kp}^{\text{max.}} - \text{Kp}^{\text{min.}}|$ and numbers in brackets indicates the averages.

based NM varied marginally. The maximum variation observed from the Oulu NM[5] was less than 1% for both measuring periods. At the time of these measurements, none of the TOA based instruments showed an increase above the GCR background which would indicate as a contribution by SEPs, or a severe geomagnetic storm disturbance. Therefore, short-term solar activity can be assumed to have less effect on the dosimeter results and these measured rates can be simply attributed to the variations of primary and atmospheric secondary particles (and secondary particles produced on board the aircraft) receiving a constant flux of GCRs. During the time of measurement, the hourly averaged Kp index parameters varied from departure to destination during most flights. However, it was less than 3, as indicated by a red broken curve shown in Figure 7.3. Based on this, it can be assumed from the Kp index that the geomagnetic field was virtually undisturbed. A disturbed geomagnetic field can potentially lead to a significant shift in P_c, see *Smart* [2003], which in turn can potentially affect the radiation field at a given altitude. Furthermore, it can be assumed that space weather effects on the geomagnetic field were negligible during these flight times. A summary of the total measurements time (in hours), at the cruising altitude, in different P_c regions is shown in Figure 7.4, as blue bars.

7.3.1 Count Rates

Flight Route: South Africa – Ethiopia

Two direct flights (round trip) were undertaken on board commercial flights on the 10$^{\text{th}}$ and 16$^{\text{th}}$ of March 2019 from Johannesburg, O.R Tambo International Airport to Addis Ababa, Addis Ababa Bole International Airport to test the dosimeter's performance in a mixed and

[5] The use of NMs is to ideally show and verify that these on board measurements performed are comparable. This NMs gives a rough local estimate of modulation not at the aircraft flight position, but because NMs at various geographic positions in general shows a general trend, this is indented to show modulation changes from departure to destination not taking into account the repeatedly changing P_c's. To do this correctly, a mobile NM is needed.

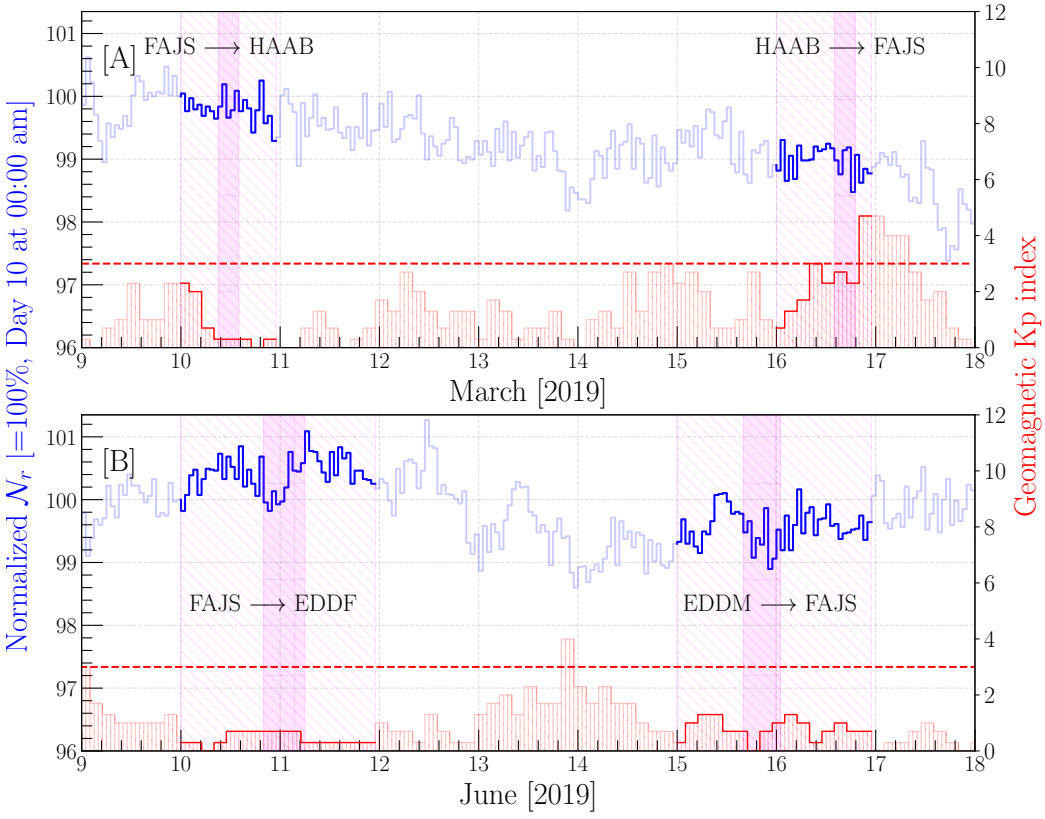

FIGURE 7.3: Modulation of the GCR component (blue colour) observed with the ground based Oulu NM (http://cosmicrays.oulu.fi/), with the Kp index (red colour) showing the condition of the geomagnetic field. The lighter shaded area shows a (the) day(s) of flight measurements, while the dark shaded regions show the time of measurements. The dashed line is used to guide the eye, highlighting virtually undisturbed geomagnetic condition.

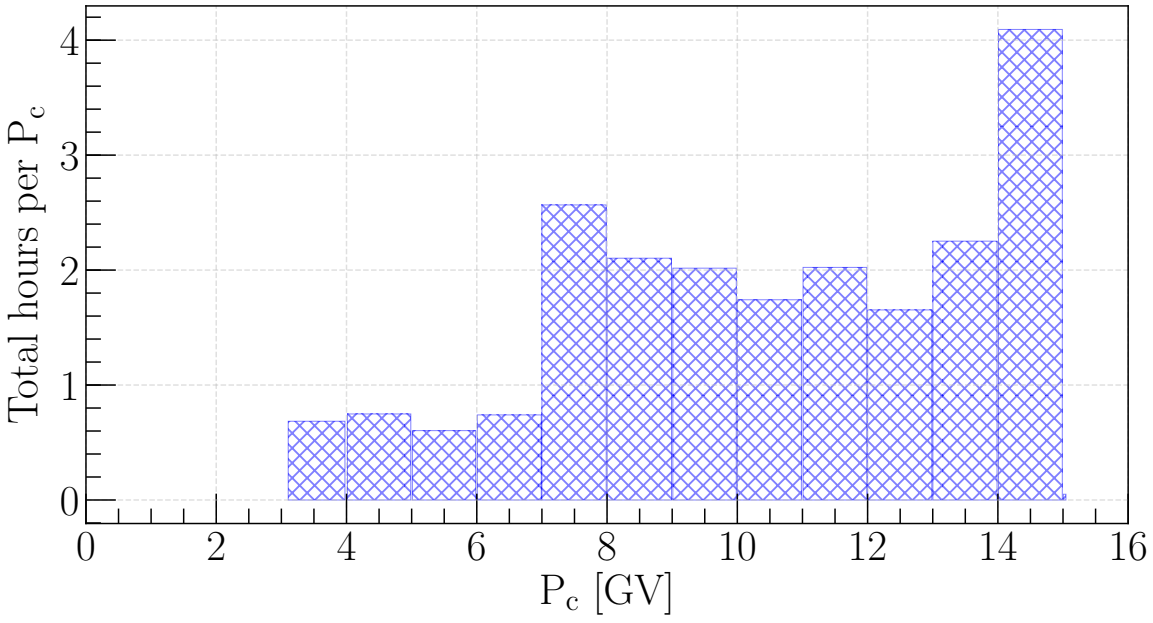

FIGURE 7.4: Total observing time, in hours, in the regions of different cutoff rigidity, P_c.

complex radiation field. The variation of flight altitudes during these flights was approximately 610 m according to FlightAware[6] data. The departure and destination airports are denoted as FAJS, for OR Tambo International Airport and HAAB for Addis Ababa Bole International Airport. These first flights served as a dosimeter test to verify that the system is functioning correctly. During both flights, the HARM prototype was also carried along and measurements using that prototype were obtained. The detectors were switched on for a short period before take-off and after landing to obtain a background count rate ($\mathcal{N}_r$), to compare the background measurements between the take-off and destination site. The measurements were taken for the entire flight from take-off to landing. Flight routes and information were obtained from FlightAware, including the flight's geographic position and cruising altitude. During the individual flight, the geomagnetic field was virtually undisturbed as mentioned earlier. In addition to the GCRs levels, as measured by ground based NM, remained relatively constant. Hence the individual flight measurements were expected to be comparable. The measurements in each medium-haul flight lasted more than 5 hours.

Figure 7.5 shows results from these measurements, showing $\mathcal{N}_r$ with SD2 ($\Leftarrow$) and SD1 ($\Uparrow$) facing in their respective directions. There is significant noise present using a threshold of 15 mV. These are caused by either mechanical vibrations or electrical interference. Therefore, a threshold re-adjustment was performed by placing cut values above the initial 15 mV (i.e. $\sim$24.18 keV for SD1 and $\sim$22.441 keV for SD2) trigger threshold. These trigger threshold re-adjustments of $\mathcal{N}_r$ are colour$-$coded and shown for different re$-$adjusted thresholds between 15 mV (purple colours) and 120 mV (i.e. $\sim$191.76 keV for SD1 and $\sim$192.33 keV for SD2; red colours). In the figure, this filtering approach clearly shows that a cut at 120 mV (i.e. $\sim$191.76 keV for SD1 and $\sim$192.331 keV for SD2) is the most appropriate trigger threshold for both SDs. At these trigger thresholds, an expected flight trajectory profile from the ground-level to the cruising altitude and back to the ground can clearly be seen. The fluctuations in SD1 ($\Uparrow$) are larger than those of SD2 ($\Leftarrow$).

From the flight measurements, $\mathcal{N}_r$ of both SD1 ($\Uparrow$) and SD2 ($\Leftarrow$) are plotted and compared to the HARM detector's measurements, using a threshold 120 mV, in Figure 7.6 panel [A]. The $\mathcal{N}_r$ of SD1 ($\Uparrow$) and SD2 ($\Leftarrow$) with original time resolution of 10 seconds, were subsequently averaged to 1 min intervals, corresponding to the time resolution of the HARM data. The $\mathcal{N}_r$ of HARM is shown in green and those of the RPiRENA's SD1 ($\Uparrow$) in blue, and SD2 ($\Leftarrow$) in red.

The characteristic shape of the $\mathcal{N}_r$ profile seen in the figure is caused by different effects. The altitude effect is clearly seen where the $\mathcal{N}_r$ increases with altitude. The effect of sampling

[6] https://flightaware.com/

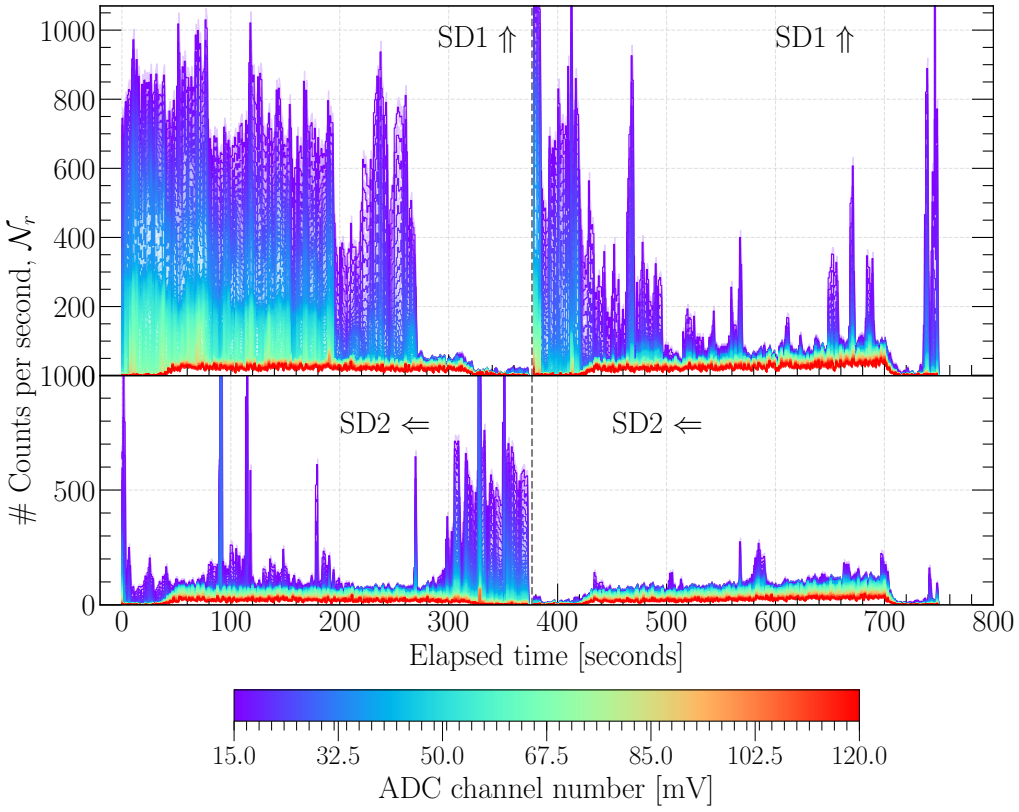

FIGURE 7.5: RPiRENA $\mathcal{N}_r$ for the flights with SD1 (⇑) and SD2 (⇐) pointing in their respective directions. The $\mathcal{N}_r$ is shown for different thresholds, colour-coded from purple (top curve, at 15 mV) to red (bottom curve, at 120 mV). Strong transient noise-like events, evident as sharp spikes, are also visible.

different P_c regions is clearly seen, where $\mathcal{N}_r$ decreases at constant altitude, near the magnetic equator. In the return flight to FAJS, it can be seen that towards the end of the flight, $\mathcal{N}_r$ from both detectors, are higher than those in the first flight close to FAJS even when their P_c's are comparable under quiet geomagnetic conditions. This effect might be due to the higher cruise altitude towards the end of the flight. Furthermore, these two flights indicate that the expectations that measurements obtained over practically the same flight time, P_c, and under similar geomagnetic conditions for nearly the same flight routes, the flight doses are expected to be similar, may be misleading or inappropriate, because of the altitude contribution.

By inspection, these on board measurements shows a general picture consistent with the expected behaviour and it gives an impression that suggests that the RPiRENA performs well after the energy threshold was adjusted to eliminate noise. The performance of the HARM prototype, compared to the RPiRENA measurements, is satisfactory for an initial test. As seen from the figure, the $\mathcal{N}_r$ of HARM is more than a factor of 4 higher than those of the RPiRENA as a result of the filtering approach applied, as well as the larger observing area of the Geiger-Müller counter. It is remarkable how well the $\mathcal{N}_r$'s from the two detectors correlate

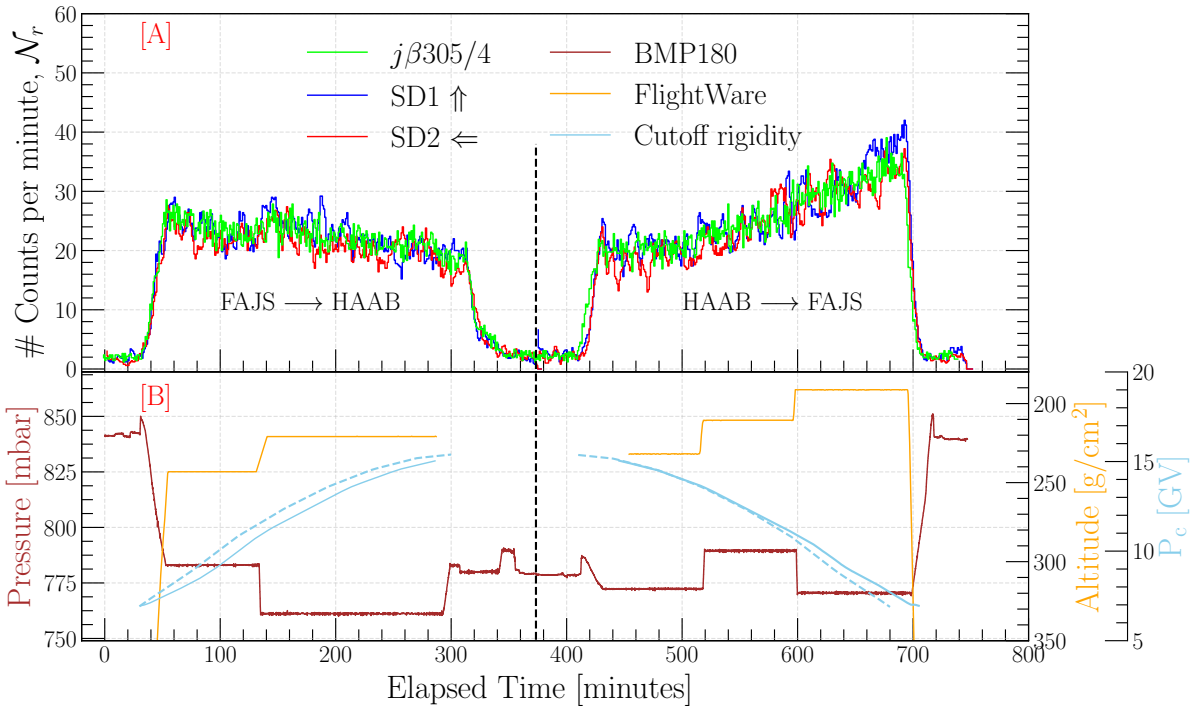

FIGURE 7.6: In panel [A], the RPiRENA $\mathcal{N}_r$ for SD1 (⇑) and SD2 (⇐) are shown in blue and red, while the HARM measurements are shown in green. In panel [B], cabin pressure (in brown), flight cruise altitudes (in orange) and P_c, calculated from the great circle approximation (broken curve lines) and the actual flight routes (solid curve lines) are shown in light blue.

with each other.

In panel [B] of Figure 7.6, the brown curve depicts the cabin pressure and is an indicator of the flight altitudes, which are given by the orange curves. The altitude (and geographic location) data were retrieved from the FlightAware[7] but it contains many data gaps, where minor gaps were interpolated using a cubic spine interpolation. As expected, the cabin pressure at aviation altitudes is lower than at ground-level. As seen from the two profiles, there is a discrepancy between the two approaches at 518 to 600 minutes, as these profiles do not complement each other. It is not clear whether this comes from the pressure data or the FlightAware altitude. To avoid further confusion, further analysis uses only the FlightAware data because it contains geographic coordinates which are needed for P_c calculations along the flight trajectory. In the same panel, P_c is shown in light blue, with the broken lines representing results from the great circle approximation and the actual routes is represented by solid lines.

Flight route: South Africa – Germany

Flight measurements crossing the equator were performed during a flight from OR Tambo International Airport in Johannesburg, FAJS to Frankfurt International Airport in Frankfurt,

[7] https://flightaware.com/

EDDF. The return flight to FAJS was from Munich International Airport in Munich, EDDM. In a flight to EDDF, $\mathcal{N}_r$ for SD1 (⇓), SD2 (⇑), and SDT are calculated and plotted versus time. These measurements were obtained using a trigger threshold of 15 mV and very little noise was present. In Figure 7.7, $\mathcal{N}_r$ of both SDs in single and telescope mode are plotted. $\mathcal{N}_r$ for SD1 (⇓) is shown in red, SD2 (⇑) in blue, and the SDT in green. Unlike, in the previous section where the diodes were orthogonal to each other and the preamplifiers close to SDs, here, the pre-amplifiers were further away from the SDs, seemly reducing the noise levels. In SDT profile, there is noise observed between the 325^{th} and 345^{th} minute, which is assumed to be most likely from the mechanical vibration. This noise was manually removed from the data and the clean data are shown in panel [A] of Figure 7.8. These $\mathcal{N}_r$ are compared to altitude (orange curves) and geomagnetic P_c (light blue curves) in bottom panel [B].

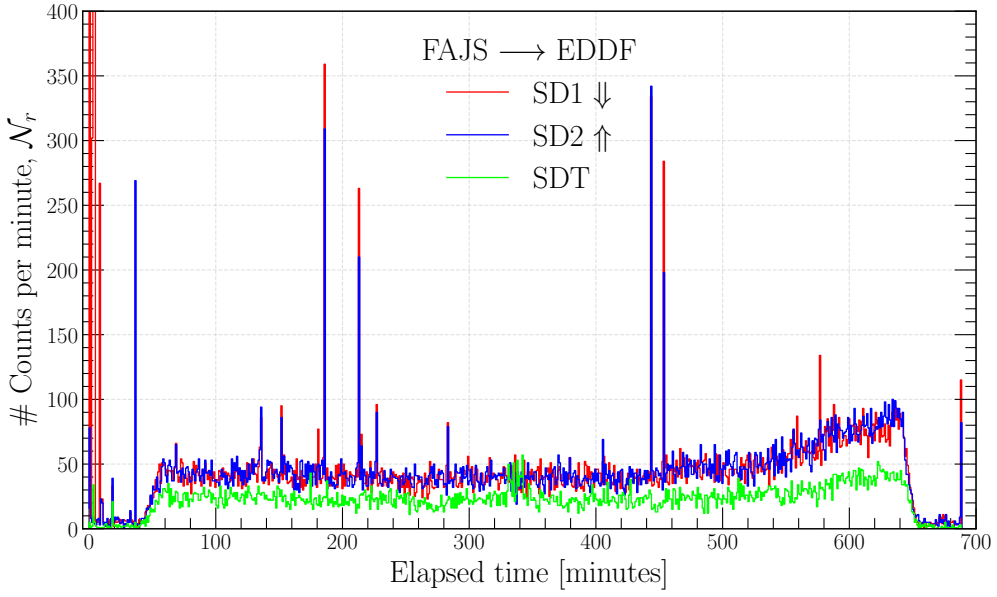

FIGURE 7.7: $\mathcal{N}_r$ for the flight to EDDF from FAJS. $\mathcal{N}_r$ of SD1 (⇓) is shown in red, SD2 (⇑) in blue and SDT in green.

The variation of the flight altitude during the entire flight to EDDF from FAJS was approximately 610 m, according to FlightAware[8] data. The overall shape of the flight profile at aviation altitudes in the southern hemisphere before crossing the equator seems to be "flattish" and over the equator the profile is dominated by higher $\mathcal{N}_r$ towards the flight destination. The changes in P_c showed a negligible effect on $\mathcal{N}_r$ for this route and did not reveal the obvious $\mathcal{N}_r$ decrease towards the equator. The reason for this flatness before crossing the equator is unclear. The return flight to FAJS from EDDM is shown in Figure 7.9. In this flight, the cruising altitude changed by approximately 310 m before crossing the equator and after the equator it was 610 m. Compared to the flight to EDDF, significant changes on $\mathcal{N}_r$ towards

[8] https://flightaware.com/

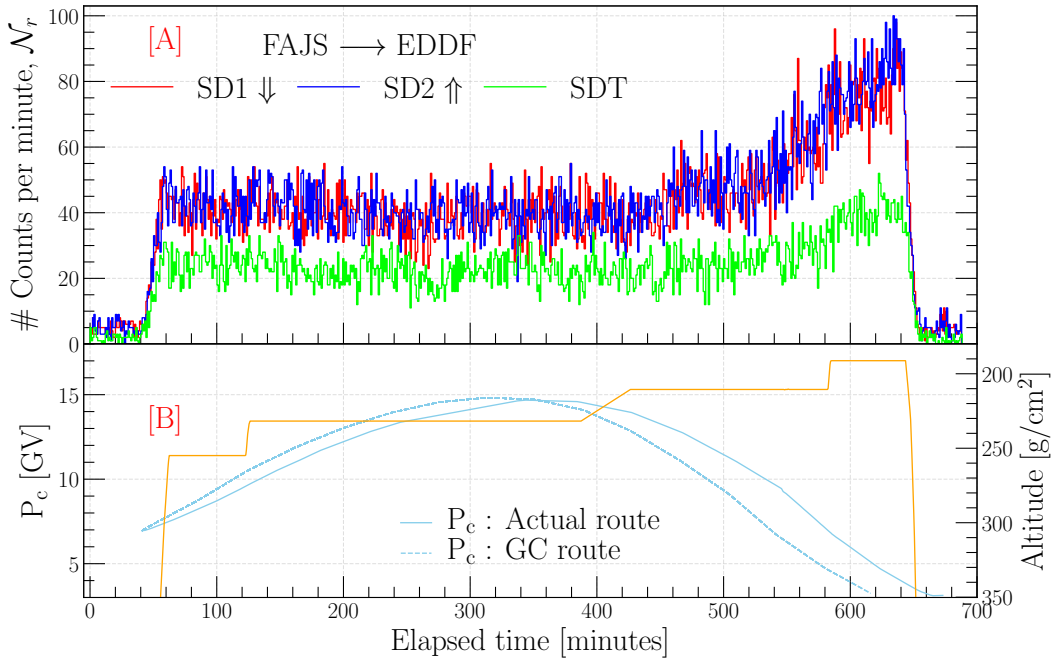

FIGURE 7.8: In the top panel, the same data as in Figure 7.7 was used but after the noise was removed. The bottom panel shows the orange curve indicates the cruise altitude profile, while the light blue curves indicates the actual flight route (solid lines) and great circle (broken lines) profile of the geomagnetic P_c.

and away from the magnetic equator were observed in this flight. The effects of altitude and P_c on these measurements will be discussed separately later.

7.3.2 Energy Deposition Spectra

The energy deposition spectra in silicon are calculated by applying

$$j(E_i) = \frac{\mathcal{N}_i}{GF \cdot T \cdot \Delta E_i} \tag{7.1}$$

where GF is the geometric factor, T the total measurement time in seconds, while energy ΔE_i the is calculated from Equation 6.2 and $\mathcal{N}_i$ is the number of events measured. The spectra derived from these flights are plotted versus the energy deposition in Figure 7.10. Panels [A] and [B] show spectra from FAJS to HAAB and back to FAJS, while panels [C] and [D] show the spectra from FAJS to EDDF and the return flight to FAJS from EDDM. The medium-haul flights (panel [A] and [B]) lasted for about 5 hours, while long-haul flights (panel [C] and [D]) lasted about 11 hours.

A comparison of all flight measurements shows that the intensities from both SDs are comparable for high energy values above the trigger threshold ∼120 mV (i.e. ∼191.76 keV for SD1 and ∼192.33 keV for SD2). For the flight route FAJS-HAAB and back, SD1 (⇑) intensities

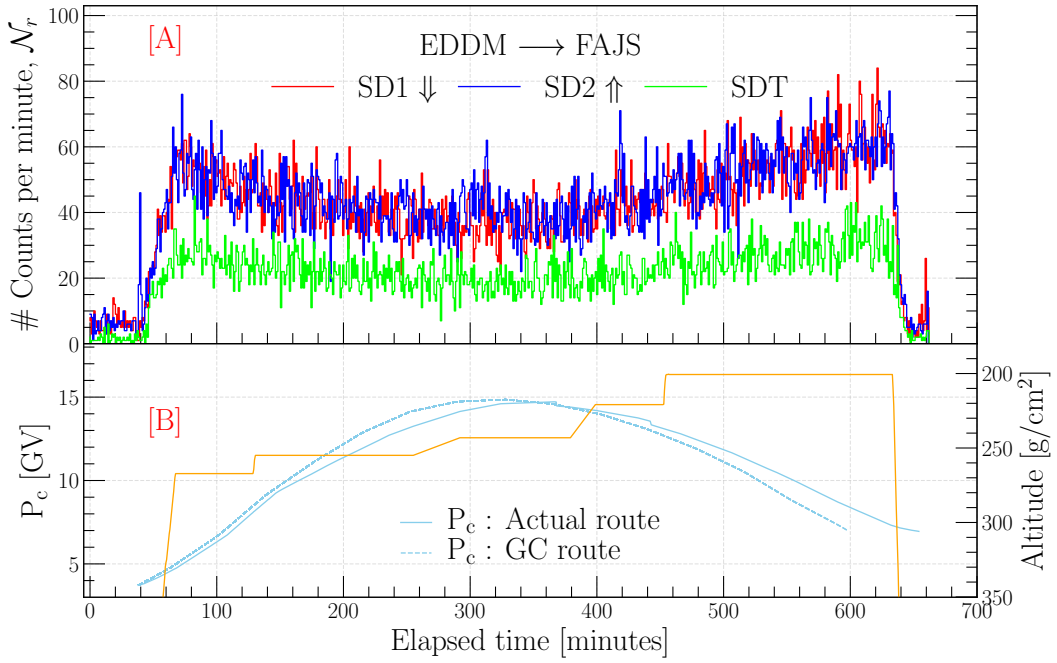

FIGURE 7.9: $\mathcal{N}_r$ for flight from EDDM to FAJS are shown in panel [A]. $\mathcal{N}_r$ is shown for single mode, SD1 (⇓) and SD2 (⇑), and for SDT. Panel [B] shows the cruise altitude profile (orange curve), while the actual flight route (blue solid lines) and great circle (blue broken lines) profile of the geomagnetic P_c.

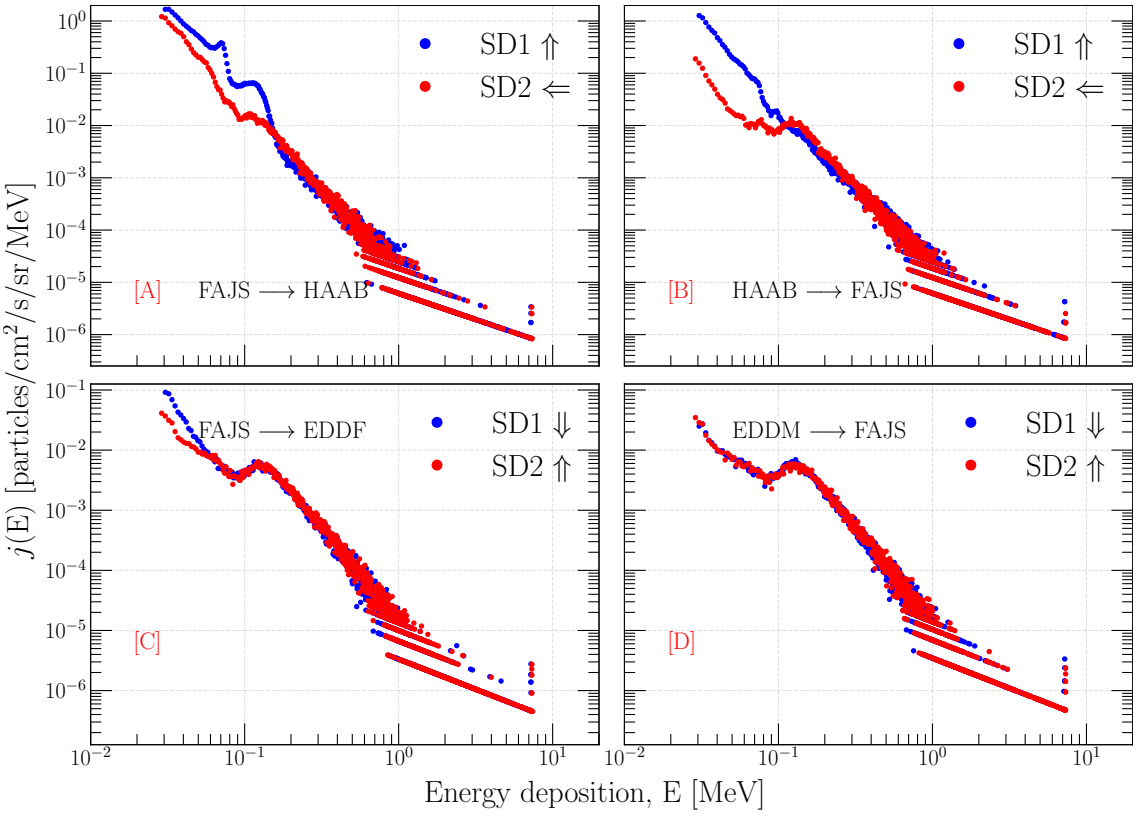

FIGURE 7.10: Energy deposition spectra, for medium-haul (panel [A] and [B]) and long-haul (panel [C] and [D]) flights discussed in this chapter.

are higher compared to those of SD2 (⇐), with large deviations visible at lower energies below 0.1 MeV. These low energy deviations, believed to be noise, were eliminated by increasing the trigger threshold in the subsequent calculations.

The energy deposition spectra for the flights to EDDF and back to FAJS are shown in the bottom panels. The red and blue symbols depict the energy deposition spectra measured from SD1 (⇓) and SD2 (⇑) respectively. For both flights, the overall shape of the spectra is dominated by a single peak. Much less low energy noise was detected during these flights.

7.4 Linear Energy Transfer Spectra and Quality Factor

The dose equivalent can be calculated using the mean $\mathcal{Q}_f$ (quality factor) from the linear energy transfer $\mathcal{L}$ of the particles. The parameter $\mathcal{L}$ is calculated through Equation 3.13, where energy E is calculated through Equation 6.2. The $\mathcal{Q}_f$ calculated from these flight measurements accounts for charged particles in telescope mode. The $\mathcal{L}$ spectra accumulated for the flights to EDDF and a return flight to FAJS from EDDM are shown in Figure 7.11, with respect to $\mathcal{L}$ in water. These spectra were converted from the energy spectrum in silicon using Equation 3.14. Comparing these spectra to those in Figure 7.10, there is no sudden increase in the intensities for these charged particles spectra below the peak intensities.

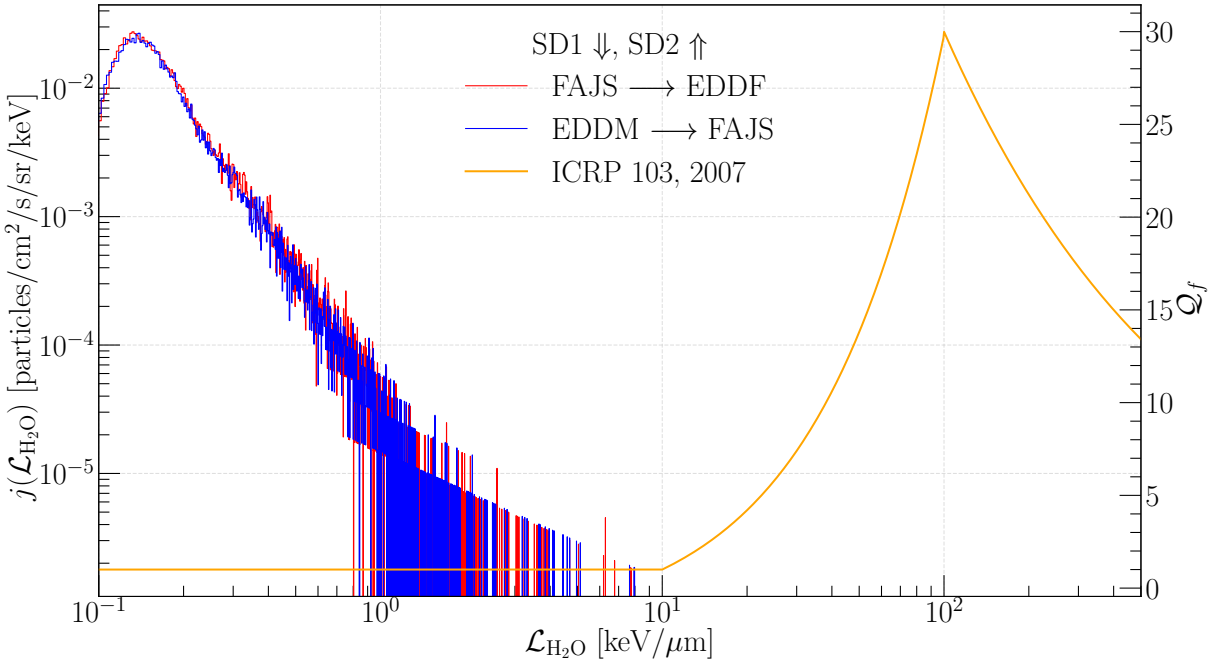

FIGURE 7.11: Energy deposition spectra accumulated for a flight to EDDF (in red) and a return flight to FAJS (in blue) from EDDM. In orange the quality factor is shown as a function of the linear energy transfer, $\mathcal{L}$, defined by *ICRP103* [2007] (see Equation 3.15).

For both flights, the peak intensity and spectra of charged particles were virtually unchanged under similar space weather conditions. This peak of $\mathcal{L}$ appears at about 0.18 keV/μm, consistent with the calculated most probable energy deposition for protons in 300 μm of silicon, using the scaling factor applied by *Beaujean et al.* [2005]. One can see that no particles which contribute to the higher biological effectiveness of ionizing radiation were accounted for above 10 keV/μm. This happened because the amplification in both SDs was performed in the high gain mode, which amplifies small signals and result in detecting large energy depositions, as mentioned in Section 6.5. The real value of the mean quality factor $\langle \mathcal{Q}_f \rangle$ from these data may be underestimated due to measurements obtained from the high gain mode. For both flights, $\langle \mathcal{Q}_f \rangle \approx 1.0$. Nevertheless, compared to other quality factor measurements performed on a similar flight route from EDDM to FAJS using a detector made of SDs, *Möller* [2013] calculated $\langle \mathcal{Q}_f \rangle \approx 1.08$ in 2011.

7.4.1 Dose Rates

The dose rates ($\mathcal{D}_r$) were calculated as described in Section 3.4.1 through Equation 3.11. Measurements from FAJS to HAAB and back are shown in Figures 7.12, while the measurements from FAJS to EDDF, and back to FAJS from EDDM, are shown in Figures 7.12. The $\mathcal{D}_r$ parameters are compared to the CARI-7A model dose rate calculations (in Silicon) due to the availability of flight route data from FlightAware. These dose rates calculations were performed for a 0.3 mm Silicon slab at a given altitude and position.

Flight route: South Africa – Ethiopia

In Figures 7.12, the orange curves in panel [A] indicate the altitude profile during the flight, while the light blue curves in panel [B] indicate the actual flight route (solid lines) and great circle (broken lines) profile of the geomagnetic P_c for the duration of the flight. The colour of the $\mathcal{D}_r$ in these figures are retained from the previous figures for $\mathcal{N}_r$. The same characteristic features, as described previously for the $\mathcal{N}_r$ profiles, can be observed in the SD1 ($\Uparrow$) and SD2 ($\Leftarrow$) $\mathcal{D}_r$ profiles. The measured accumulated flight doses for the two flights are shown in panel [D] and their results are recorded in Table 7.2.

The CARI model calculations were performed only where the altitude data was available.[9] Therefore, a one-to-one comparison of the total accumulated dose rates between the CARI-7A model calculations and dosimeter measurements in this situation might not be meaningful, hence, the comparison is restricted due to the availability of data. However, based on the

[9]Data from FlightAware shows data gaps during the flight decent phase (panel [A]) and take-off (panel [B])

accumulated doses in both SDs, the total dose accumulation in both flights is comparable, with SD1 (⇑) slightly higher than SD2 (⇐).

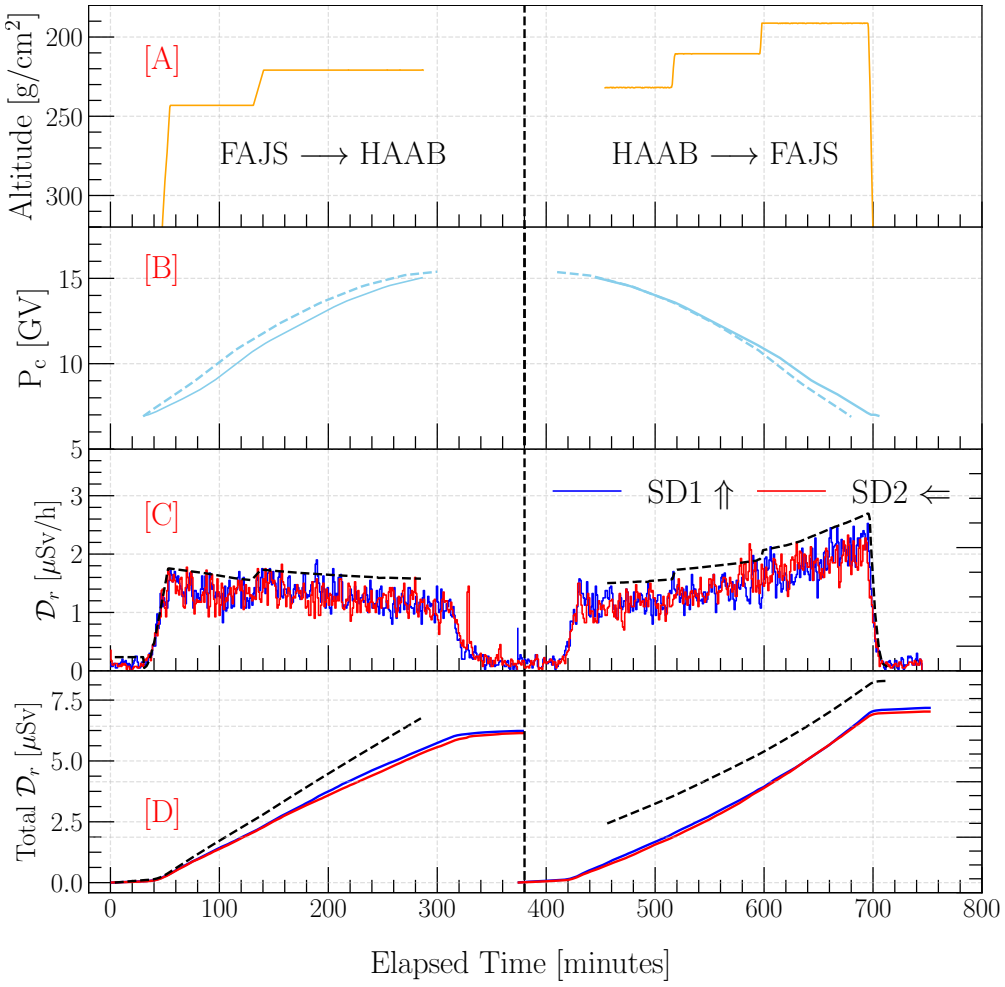

FIGURE 7.12: Panel [A] represents the flight altitudes for the flight to HAAB and back to FAJS, while [B] represents the geomagnetic P_c along the flight route. [C] and [D] represent the absorbed dose rates and the accumulated doses respectively. Note the large data gaps in the altitude profiles during take-off and landing. The solid black lines represents the CARI-7A model dose rate calculations.

TABLE 7.2: Measured accumulated absorbed doses, compared with the CARI-7A calculations for a 0.3 mm Silicon slab.

Route	SD1 [μGy]	SD2 [μGy]	CARI-7A [μGy]
FAJS−HAAB	6.23	6.14	–
HAAB−FAJS	7.18	7.03	–
FAJS−EDDF	11.48	11.46	17.39
EDDM−FAJS	11.04	11.03	15.92

Flight route: South Africa – Germany

For these flight routes, the absorbed dose rates and accumulated doses in Figure 7.13 were compared to the CARI-7A model dose rate calculations (in Silicon). The model results and

measurements for the two flights, in terms of accumulated flight doses, are summarized in Table 7.2. At these altitudes, neutrons are the dominant particle species. The RPiRENA detector is not optimized to detect neutral particles and it appears as though the model dose calculations over estimates the measured doses. However, the model predict higher dose accumulation in the flight to EDDF as compared to the return flight to FAJS from EDDM. The data, however, show that the results were very similar in both flights, with the model calculations about a factor of 1.5 higher than the observation.

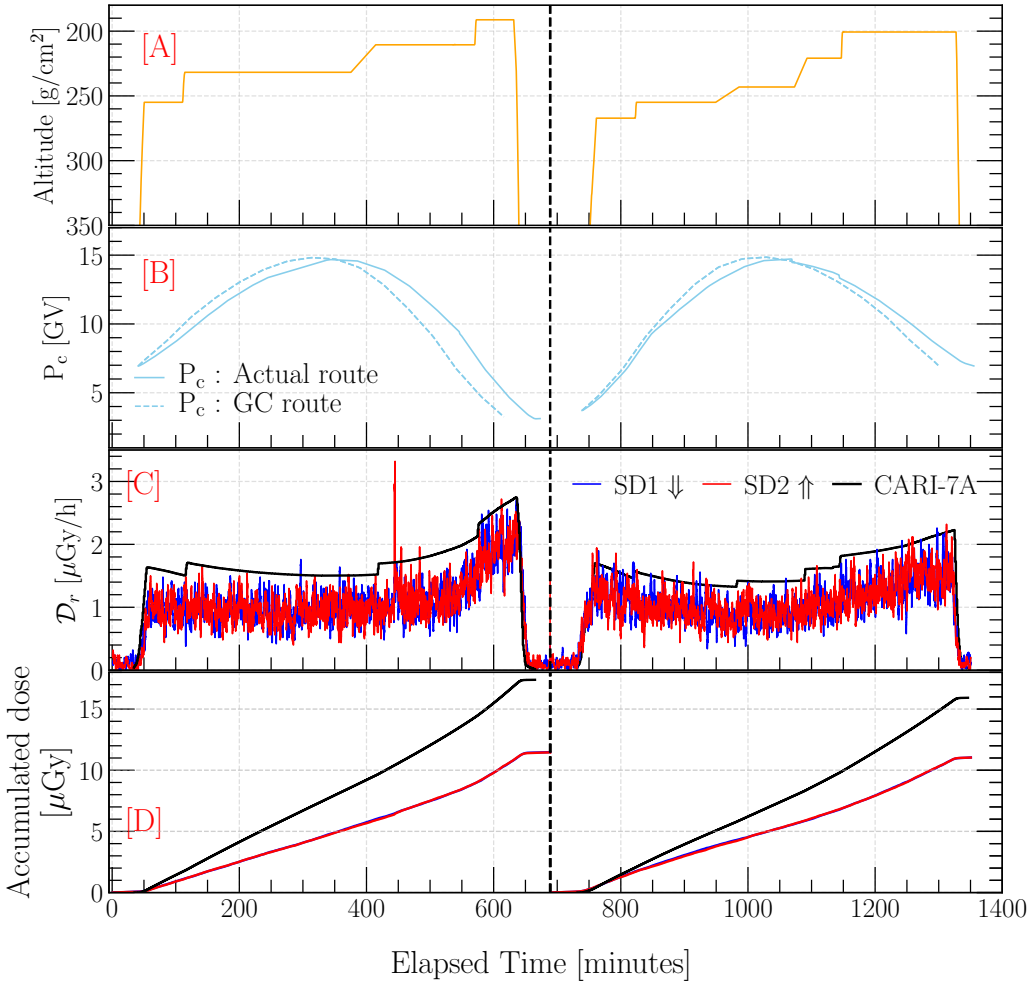

FIGURE 7.13: Same as Figure 7.12, but now for the flight to EDDF, and a return flight to FAJS from EDDM. The solid black lines represents the CARI-7A model dose rate calculations.

7.4.2 Directionality Measurements

For the results of $\mathcal{D}_r$ shown in Section 7.4.1, the ratio between the SDs was calculated for each flight and binned into histograms. The results are shown in Figure 7.14. The distributions are well approximated by Gaussian distributions. The original data are shown as the step-like histogram, which is overlaid by Gaussian fits, shown as the thick curves. For each Gaussian fit,

the mean (μ) and the standard deviation (σ), with its corresponding errorbar, are given at the top of the figure. Comparing these ratios, a small offset from the expected value of 1 clearly illustrates the directional dependence of the radiation field. Based on the calculated ratios, the small offsets observed from the calculated mean $\mu \sim 1$ shows that the directionality of both SDs at aviation altitudes does not seem to be dependent on changes of the cruise altitudes or the change of P_c. For the bottom panels, the ratio of SD1 ($\Downarrow$) to SD2 ($\Uparrow$) is significantly different from unity, illustrating that the top SD is exposed to more ionizing radiation than the bottom SD. This can be due to more shielding for the bottom SD, or an undetermined instrumental effect. For the top panel, the upward facing SD has a slightly higher dose rate than the sideways facing SD. This difference may be due to the directionality of the incoming radiation that peaks in the zenith direction. However, these small offsets between the measurements do not clearly show the strong directional dependence of the radiation field.

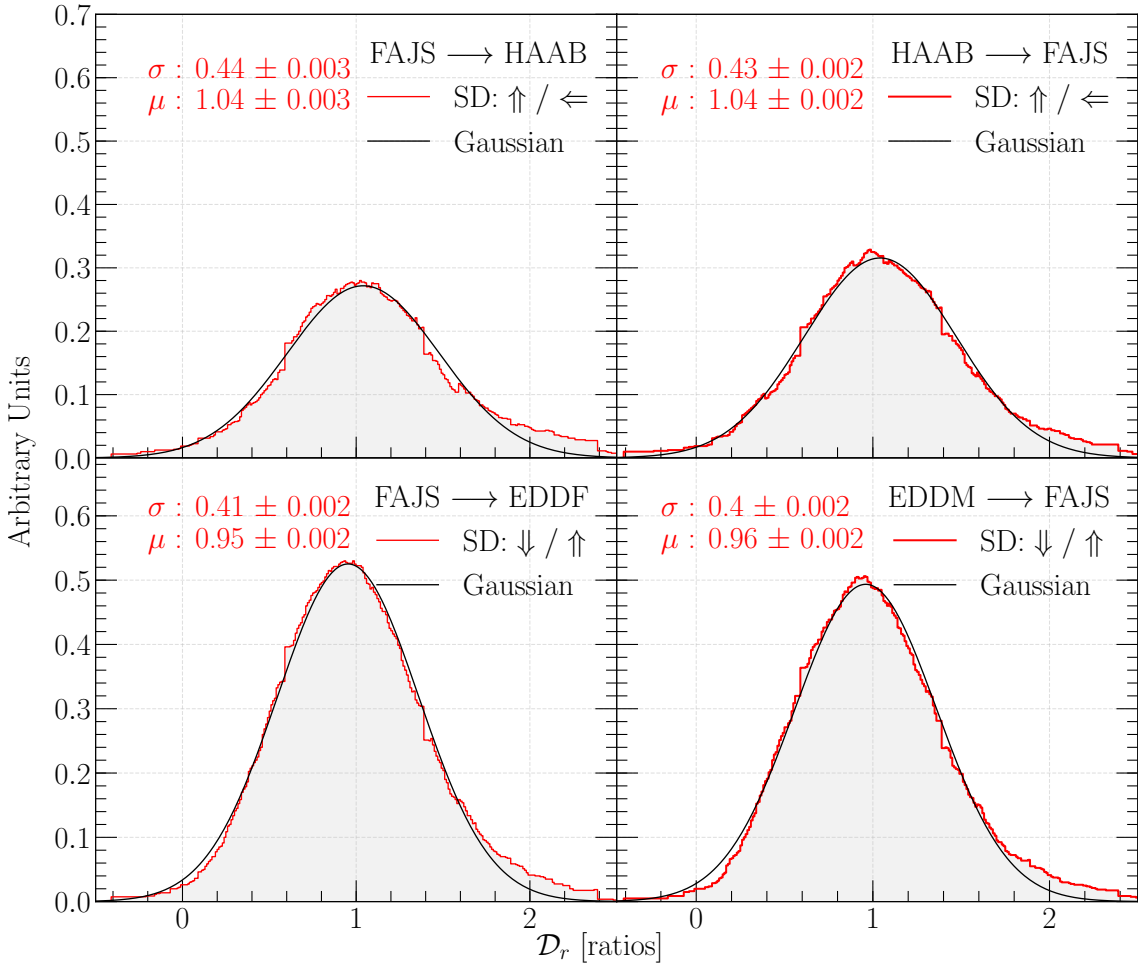

FIGURE 7.14: Distributions of the ratios of $\mathcal{D}_r$ as observed by SD1 and SD2, shown as histograms. The thick curves are Gaussian fits to the data.

7.5 Short-haul Flight Measurements

A short flight campaign was conducted in Germany and South Africa, and the flight results are shown in Figure 7.15. In Germany, this was conducted on two flights, occurring on 10 and 15 June 2019, with cruise altitudes of 363.02 g/cm^2 (i.e. ∼8 km) and 269.57 g/cm^2 (i.e. ∼10 km) respectively. The variation in P_c was largest for the flight Frankfurt (EDDF, 3.39 GV) to Hamburg (EDDH, 2.36 GV), since this flight covered a wider range of latitudes as compared to the flight from EDDH to Munich (EDDM, 4.02 GV).

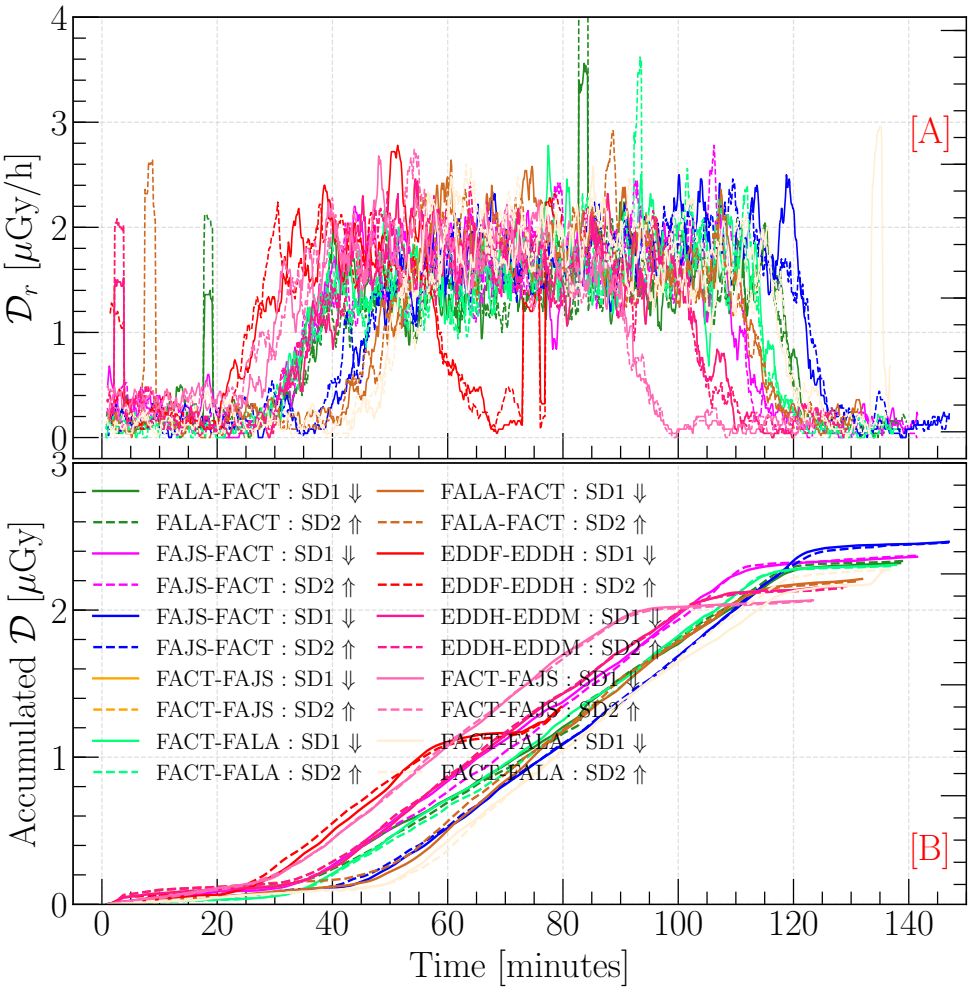

FIGURE 7.15: Dose rates (panel [A]) and accumulated doses (panel [B]) for individual short flight routes over cutoff rigidities changing by less than 2 GV.

In South Africa, this campaign was performed on several local aircrafts in one of the busiest routes in Africa, between Cape town International Airport (FACT) and O.R. Tambo International Airport (FAJS), and also between Lanseria International Airport (FALA) and FACT, covering geomagnetic cutoff rigidities between about 4.54 GV and 7.12 GV, with the cruise altitude assumed to be in the 269.57 g/cm^2 range on average due to the unavailability of some

flight data from FlightAware.[10] These flight measurements were obtained between June 2019 and September 2019. Since most of these flights do not have the flight routes data, model calculations were not performed. These aircraft flights measurements were conducted under solar and geomagnetically quiet conditions.

The dose rate curves and the accumulated absorbed doses for individual flight routes are shown in Figure 7.15. The short-haul flights have a measured average dose rate ∼1.25 μGy/h which is comparable with those measured on long-haul flights. From these 13 flights included in this chapter, covering about 56 hours, resulted in 0.06 mGy of absorbed dose in Silicon. Using a quality factor of $\mathcal{Q}_f = 1$, this translates to a dose equivalent of 0.072 mSv in water. Flying similar routes for 1000 hours[11] per year will therefore result in a total dose equivalent of 1.3 mSv, which is above the radiation exposure limit set for a general member of the public, and illustrates the need to define flight personnel as radiation workers.

7.6 Cutoff Rigidity and Altitude Dependence

In sampling the radiation field and its intensity at aviation altitudes, result measurements are dependent on altitude, P_c, solar activity, and space weather transient events. However, as highlighted earlier, these measurements were obtained in similar geomagnetic and space weather conditions, so that the altitude and P_c dependence can now be investigated separately. Also, it needs to be considered that the radiation field inside the aircraft is strongly influenced by the structure of the aircraft itself, as pointed out by *Ferrari and Pelliccioni* [2004], including factors such as the position inside the aircraft, as well as number of passengers. Since the measurements were performed in a large commercial aircraft, a significant influence of the structure on the measured $\mathcal{D}_r$ was therefore expected.

Because of the few measurement undertaken, covering a wide range in P_c, and altitude, and the unavailability of flight coordinates data from other flights, the measurements from the flight route FAJS-EDDF and EDDM-FAJS were merged together to compare the altitude and P_c effects on the dosimeter measurements. Figures 7.16 and 7.17 show the result of the dose rate, $\mathcal{D}_{Si}$, dependence on P_c, at cruising altitudes and the dose rate, $\mathcal{D}_{Si}$, dependence on cruise altitudes at specific P_c respectively. Smaller dose rates are generally expected at high P_c values, at a constant altitude. However due to the altitude and P_c continuously changing, and the very limited data available, this makes it difficult to point to a major contributor in the measured dose rates as seen from both figures.

[10] https://flightaware.com/

[11] Pilots are allowed to fly a maximum of 1000 hours in a year.

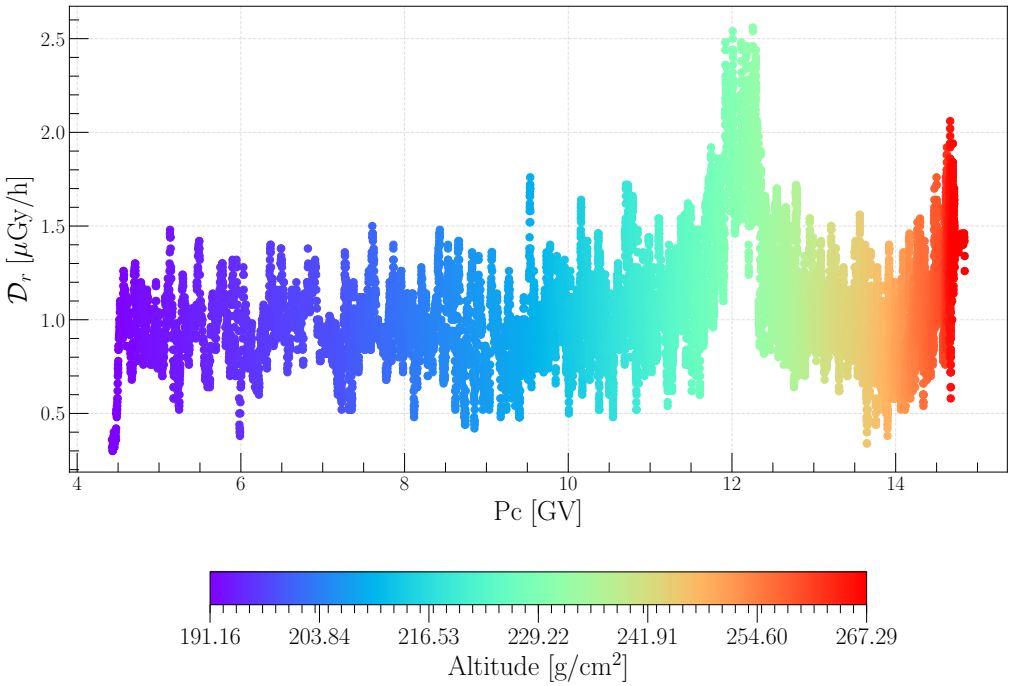

FIGURE 7.16: The dose rate, $\mathcal{D}_{Si}$, dependence on geomagnetic cutoff rigidity, P_c, at cruising altitudes.

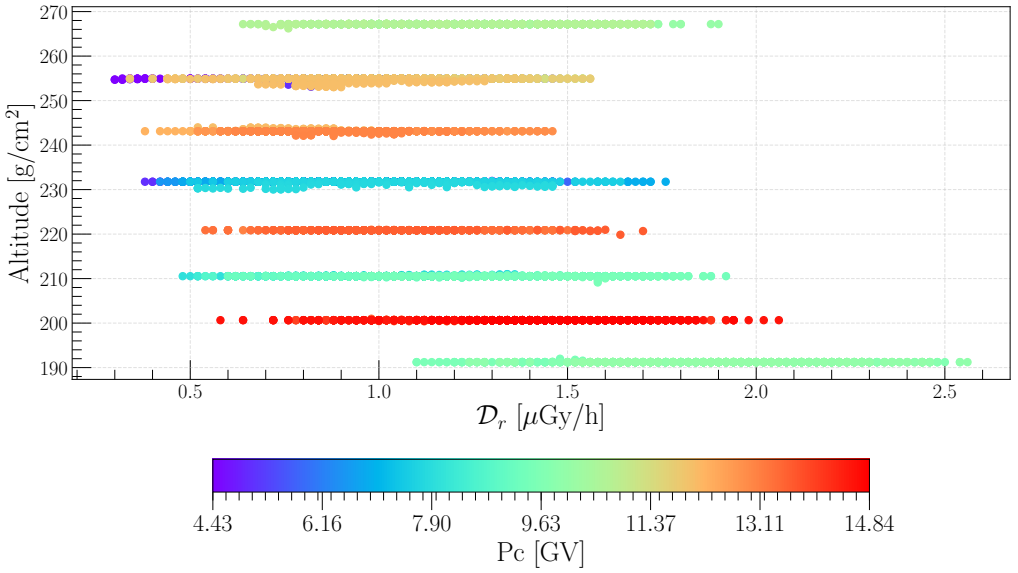

FIGURE 7.17: The dose rate, $\mathcal{D}_{Si}$, dependence on cruise altitudes at specific geomagnetic cutoff rigidities.

7.7 Summary

The assembled RPiRENA performed well, and it was shown to be an active readout device capable of characterizing radiation at aviation altitudes. This dosimeter was assembled because of the limitations of the HARM detector. During the first RPiRENA flight, the HARM detector was also carried on board and measurements obtained. Under the same space weather, geomagnetic, and flight environmental conditions, HARM measurements compared well to the RPiRENA's count rate, as shown in Figure 7.6. Furthermore, in telescope mode, results of the RPiRENA measurements were compared to model calculations and they complement each other fairly well within uncertainties. The model dose calculations over estimates the measured doses, because the assembled RPiRENA detector is not optimized to detect the most dominating particle specie at the altitudes, i.e. the neutron particles.

Geomagnetic cutoff rigidity, P_c and altitude dependence of count and dose rates were observed and quantified. With P_c decreasing and altitude increasing during flights with long duration, this makes it difficult to distinguish the dominant process. More measurements, coupled with detailed modelling, might be able to shed some light on this in future. Comparing the accumulated dose results for long-haul and short-haul flights shows that longer flight durations result in high dose accumulation. This might lead to a partially incorrect conclusion that flights with long duration are associated with larger accumulation of doses, while the accumulated doses from shorter flights are negligible. However, on average, these flight have similar dose rates and flight personnel are exposed to a similarly harmful radiation field.

CHAPTER 8

Summary, Conclusions, and Outlook

The main goal of this work is as titled, "*Cosmic radiation measurements in the Southern Hemisphere, with focus on aviation altitudes*", and this was achieved in this work by presenting the first dedicated dosimetric measurements in the Southern Africa. This was motivated by SANSA's appointment by ICAO, among other agencies, to provide space weather services and warnings to the aviation sector. This chapter serves to outline and expand concise summaries, and the most important conclusions of each of the preceding chapters, with emphasis on the main goals of this work.

In Chapter 1 an overview and layout of this work was given, while the relevant background, concepts, and nomenclature important for radiation exposure assessment at aviation altitudes for flight personnel and passengers were discussed in Chapter 2. The dynamic nature of the radiation field at aviation altitudes is the main concern for the health of flight personnel and passengers and poses a limiting factor for the careers of flight personnel. Therefore, Chapter 3 outlined the relevant background from the ICRP,[1] in line with ICAO's[2] space weather manual, pertinent to radiation exposure at aviation altitudes. The amount of energy deposition that can potentially damage the human DNA make-up, and set up a chain of events that can potentially result in cancer, was discussed.

Chapter 4 presented the CARI-7A[3] CSTool. This CSTool takes into account a set of mathematical expressions capable of describing the local and global dosimetric quantities at aviation altitudes. It was shown how this CSTool can be used to conduct multiple simulations of dosimetric quantities during meteorological balloon flights, and long-haul aircraft flights, over a wide range of cutoff rigidities using the great circle approximation.

[1] http://www.icrp.org/index.asp
[2] https://www.icao.int/Pages/default.aspx
[3] https://www.faa.gov/data_research/research/med_humanfacs/aeromedical/radiobiology/cari7/

Chapter 5 discussed the High Altitude Radiation Monitor (HARM) programme; a public outreach and educational campaign, initiated by the North-West University's Centre for Space Research, about ionising radiation in anticipation of SANSA's project commencement. The project also involved a number of students. The HARM prototypes were carried on 25 flights (to date) over the past three years from July, 2017 to July, 2019, with 76% of those measurements obtained within South Africa's borders. The HARM flight campaign provided radiation measurements at several cruising altitudes, covering measurements from 363.02 g/cm^2 ($\sim$8 km) to 168.35 g/cm^2 ($\sim$13 km). In addition to the aircraft flights, HARM was flown on board two stratospheric balloons, successfully launched from the NWU (Potchefstroom campus). During these flights the count rate's ($\mathcal{N}_r$) dependence on altitude was measured, up to an altitude of almost 55.83 g/cm^2 ($\sim$20 km), and the highest Regener-Pfotzer maximum altitude was determined to be at around 122.81 g/cm^2 ($\sim$15 km).

The problem with measurements obtained using the HARM prototypes is that they do not provide all the information essential for dosimetry purposes, such as the energy deposition. However, the dataset obtained using the HARM prototypes can provide useful information regarding the dynamic nature of the radiation field, within the aircraft at aviation altitudes, and above, up to the Regener-Pfotzer maximum. Continuous radiation exposure monitoring at aviation altitudes, for commercial aircrafts and missions for astronauts, are mostly performed using active and passive dosimeters. An active dosimeter prototype was assembled, implementing two Hamamatsu (s2744-08) silicon diodes (SDs), because of HARM's shortcomings in measuring dosimetric quantities. Chapter 6 briefly discussed the assembling of the RPiRENA prototype, including the mechanical and electronic design, functionality of the SDs, signal processing, energy thresholds, and calibration. Calibration with laboratory radioactive sources was performed, and it was concluded that the RPiRENA detector is sufficient for dosimetric purposes on board commercial aircrafts at aviation altitudes.

In Chapter 7, flight results, obtained on board several domestic and international airlines, were presented. In single mode, count rate $\mathcal{N}_r$ and absorbed dose $\mathcal{D}_r$ profiles were calculated for a flight from South Africa to Ethiopia and back, with one SD pointing upwards (i.e. in the zenith direction), while the other one was rotated by 90° with respect to the first. From the results, altitude and geomagnetic cutoff rigidity dependence on $\mathcal{N}_r$ and $\mathcal{D}_r$, as well as the directionality of the radiation field was observed, and quantified. In general, the RPiRENA detector's ability to sample and characterize radiation on board commercial aircraft was found to be satisfactory. Moreover, the count rate, measured by both the HARM and RPiRENA detectors, compared very well.

In telescope mode, important radiation field parameters were derived from RPiRENA measurements obtained on board long-haul international flights from South Africa to Germany and back. The instrument successfully measured reasonable values of dose quantities (the absorbed dose and quality factor), on board an aircraft. The derived mean quality factor, for both long-haul flights, was found to be ∼1 since there were no counts higher than 10 keV/μm.

The dosimetric quantities calculated in this work are not only important for scientific use, but also for medical purposes, as described in the ICAO Space Weather manual, *ICRP60* [1991], *ICRP75* [1997], *ICRP103* [2007] and *ICRP132* [2016]. Much research is currently devoted to the long term effects of radiation exposure, as experienced during commercial flights. Therefore, due to the good response of the assembled RPiRENA detector, more data from this project will be helpful in understanding and improving the risk estimation for flight personnel and frequent travellers. It will also be important in building a model/CSTool, optimised to use South African ground-based instruments (i.e. from neutron monitors) as input, to perform short-term forecasting of radiation levels for the African continent. The development of such a tool was described in Appendix A.

Future Application and Outlook:

As it stands, further development is ongoing to reduce the size of the assembled RPiRENA prototype. In addition, the RPiRENA software (including the data analysis) is being refined and made more user-friendly. It is expected that the revised RPiRENA detector will be extensively utilized on various flights routes, especially over Southern Africa, in the coming years.

It is hoped that this work will contribute to SANSA's ongoing project to provide space weather services and warnings to the aviation sector and persuade airlines companies to engage with scientific communities regarding flight dosimetry, so that they can successfully raise awarenesses with their flight personnel about radiation exposure during their occupational activities. SANSA's appointment will certainly contribute to address the unquantified and undocumented radiation levels that flight personnel and passengers are exposed to at aviation altitudes in the Southern Hemisphere, and especially in Southern Africa.

Future work with the RPiRENA detector will comprise a detailed comparison between the RPiRENA flight measurements and model calculations. The RPiRENA detector was assembled to measure the energy of the incident radiation in a high gain mode. However, a low gain channel will be added to extend measurements to higher energies where fragmentation calibration of heavy ions will be performed. Based on the CARI-7A model calculations, the highest neutron flux is expected around 76.53−65.36 g/cm^2 (∼18−19 km), near the Regener-Pfotzer maximum. Furthermore, at aviation altitudes, e.g. 197.11 g/cm^2 (∼12 km), neutrons are the

dominant particle species. While the RPiRENA detector is not optimized to detect neutral particles, a detailed comparison between model calculations and RPiRENA measurements on metrological balloons can be used in future to determine whether the RPiRENA measurements are possibly underestimating radiation from the neutron component.

APPENDIX A

Approximate Analytical Solutions of the Parker Transport Equation

The calculation of dosimetric quantities used in Chapters 4, 5 and 7 utilises the modulation parameter (or the so−called solar modulation potential) to estimate the GCR intensity near Earth. These parameters can be reconstructed from ground based stations and (or) spacecraft measurements (see *Usoskin et al.* [2005, 2011], *Usoskin et al.* [2017]; *Ghelfi et al.* [2017]; *Zhu et al.* [2018]). It has, however, been shown by *Mishev et al.* [2013] that modulation parameters depend, not only on the local interstellar spectrum, as shown by *Herbst et al.* [2010], but also on the energy range of interest; see also *Gieseler et al.* [2017] and *Tomassetti* [2017]. Therefore, this appendix deals mainly with the choice of the modulation parameters, how these are related to the underlying diffusion coefficients, and how these may influence the calculated dosimetric quantities. A modified version of the Convection-Diffusion approximation is presented that can accurately reproduce space-born GCRs observations. A method is presented, where the modulation potentials can be calculated from NM measurements, which can be used as input to dosimetry models.

A.1 Parker's Transport Equation

In the form given by *Gleeson and Webb* [1978], the heliospheric transport equation of GCR can be written as

$$\frac{\partial f}{\partial t} = \mathrm{Q} + \vec{\nabla} \cdot \left[\mathcal{K} \cdot \vec{\nabla} f - \mathrm{C} \vec{\mathrm{V}} f \right] + \frac{1}{3\mathrm{P}^2} \frac{\partial}{\partial \mathrm{P}} \left[\mathrm{P}^3 \vec{\mathrm{V}} \cdot \vec{\nabla} f \right], \tag{A.1}$$

where $f = f(r, \mathrm{P}, t)$ is the omnidirectional distribution function of CRs in the fixed frame, Q denotes any possible sources of CRs inside the heliosphere, $\mathrm{C} = -\frac{1}{3} \frac{\partial ln f}{\partial ln \mathrm{P}}$ is the Compton−Getting factor [*Compton and Getting*, 1935, *Gleeson and Axford*, 1968b], $\vec{\mathrm{V}}$ denotes the solar wind velocity, $\mathcal{K}$ is the diffusion tensor used to specify the scattering properties of the heliospheric

magnetic field, and the last term on the right hand side describes the adiabatic losses in the expanding solar wind. Two approximate solutions of the *Parker* [1965] transport equation, namely the Force-Field and the Convection-Diffusion approximations, will be examined in this work. Due to it's simplicity, the Force-Field approximation is by far the mostly used [*Gleeson and Axford*, 1967, 1968a, *Perko*, 1987, *Caballero-Lopez and Moraal*, 2004, *Moraal*, 2011, *Fisk and Axford*, 1969], compared to the mostly neglected Convection-Diffusion approximation [*Parker*, 1958a,b, *L'Heureux et al.*, 1972]. Despite the limited applicability of the Force-Field approximation, as described by *Caballero-Lopez and Moraal* [2004], modified versions of this approximation have been proposed over the years. For recent applications, see *Corti et al.* [2016] and *Gieseler et al.* [2017].

Following *Moraal* [2011] and *Caballero-Lopez and Moraal* [2004], Equation A.1 can be reduced to a simple form if [1] $Q = 0$ (i.e. there are no CRs sources), [2] $\frac{\partial f}{\partial t} = 0$ (i.e. a steady state) and [3] neglecting the adiabatic momentum loss rates (last term of Equation A.1). Further, assuming a time dependent radial flow, i.e. $\vec{\mathrm{V}} = \mathrm{V}(r,t)\hat{r}$, and assuming a spherical symmetry, leads to

$$\kappa \frac{\partial f}{\partial r} - \mathrm{CV}(r,t) f = 0, \tag{A.2}$$

where κ is now the effective radial component of the diffusion tensor. In this work, a factorised form of κ in terms of radial and rigidity as proposed by *O'Gallagher and Simpson* [1967] is used. Here, $\kappa = \kappa(r,\mathrm{P},t) = \beta^{\eta}\kappa_r\kappa_{\mathrm{p}}$ with $\beta = \frac{v}{c} = \mathrm{P}/\sqrt{\mathrm{P}^2 + (\mathrm{A}/\mathrm{Ze})^2\mathrm{E}_0^2}$, where v is the particle speed, c is the speed of light, $\mathrm{E}_0 = 0.938$ GV is the rest mass energy of protons, A=1 is the proton mass number and the proton charge number Ze is 1. $\kappa_{\mathrm{p}} = \mathrm{P}_0\,[\mathrm{P}/\mathrm{P}_0]^{\gamma}$, where $\mathrm{P}_0 = 1$ is written in units of GV so that κ_r will have units of $\mathrm{cm}^2/\mathrm{s}/\mathrm{GV}$. In this work, the remaining parameters are estimated from spacecraft measurements, assuming that γ and η describe the rigidity dependence of κ at high and low energies, respectively. This κ dependence gained popularity in the early 1970s, while its first application at neutron monitor energies was performed by *Moraal et al.* [1973]. After re−arranging Equation A.2 and performing several steps of calculations, the Force-Field modulation parameter can be described as

$$\phi = \phi(r,t) = \int_{\mathrm{P}}^{\mathrm{P}_*} \frac{\beta^{\eta}\kappa_{\mathrm{p}}}{\mathrm{P}} d\mathrm{P} \equiv \int_{r}^{r_*} \frac{\mathrm{V}(r,t)}{3\kappa_r} \mathrm{d}r. \tag{A.3}$$

To describe differential intensity spectra e.g. at 1 AU, one can exploit the fact that the CR distribution function, $f(r,\mathrm{P}) = j(r,\mathrm{P})\mathrm{P}^2$, along characteristics is conserved [*Gleeson and Axford*, 1968a, *Gleeson and Urch*, 1973, *Gleeson and Webb*, 1978, *Moraal*, 2011, *Caballero-Lopez and Moraal*, 2004], which implies that $f(r,\mathrm{P}) = f(r_*,\mathrm{P}_*)$ according to Liouville's theorem. The

CR intensity at the top of the atmosphere (TOA) can be described as

$$j(r, \mathrm{P}) = j(r_*, \mathrm{P}_*) \left[\frac{\mathrm{P}}{\mathrm{P}_*}\right]^2, \tag{A.4}$$

where $j(\mathrm{P}_*)$ is the unmodulated spectra at the boundary of the heliosphere and P_* is calculated through Equation A.3 as

$$\mathrm{P}_* = \mathrm{P} + \phi, \tag{A.5}$$

when $\gamma = 0$ for relativistic particles and $\eta = 1$, while for non-relativistic particles $\gamma = 1$ and $\eta = 1$, P_* is calculated as

$$\mathrm{P}_* = \sqrt{\left[\phi + \sqrt{\mathrm{P}^2 + (\mathrm{A/Ze})^2 \mathrm{E}_0^2}\right]^2 - (\mathrm{A/Ze})^2 \mathrm{E}_0^2}. \tag{A.6}$$

By keeping all the assumptions that lead to Equation A.3, and also assuming that the effect of the Compton getting effect in Equation A.1 is negligible, the CR intensity at the TOA can be described by the Convection-Diffusion approximation as

$$j(r, \mathrm{P}) = j(r_*, \mathrm{P}_*) e^{-M}, \tag{A.7}$$

where

$$M = M(r, t) = \int_r^{r_*} \frac{\mathrm{V}(r, t)}{\kappa} dr = \frac{\Re}{\beta^\eta \kappa_\mathrm{p}}, \tag{A.8}$$

is the so−called dimensionless modulation function, while

$$\Re = \Re(r, t) = \frac{\mathrm{V}(r, t)}{\kappa_r} (r_* - r), \tag{A.9}$$

is referred to as the Convection-Diffusion modulation parameters in this work. Equation A.9 is valid only if κ_r is independent on the radial distance. For a physical interpretation of the approximation, see *Caballero-Lopez and Moraal* [2004]. According to *Gleeson and Urch* [1973], the Force-Field modulation parameter in Equation A.3 is actually ϕ/κ_p instead of ϕ, and this is related to the Convection-Diffusion modulation parameter through

$$\frac{\phi}{\kappa_\mathrm{p}} = \frac{\beta^\eta M}{3} \Longrightarrow \phi = \frac{1}{3}\Re. \tag{A.10}$$

The validity of Equation A.10 will be tested in this work.

A.2 Local Interstellar Spectrum

An overview of the most often used local interstellar spectra (LIS), and their significance in the calculation of modulation parameters, can be found in *Herbst et al.* [2010]. In this work, the LIS used in the calculation of the modulation parameters by most non−commercial flight dose calculators, listed in Table A.1, are compared in Figure A.1. The recent datasets from the Voyager 1 spacecraft [*Stone et al.*, 2013, *Webber and McDonald*, 2013], the Payload for Antimatter Matter Exploration and Light−nuclei Astrophysics (PAMELA), and the Alpha Magnetic Spectrometer (AMS−02) detectors are useful in describing the shape of the LIS both at low and high energies.

TABLE A.1: LIS used by most CSTools.

Source
Nymmik et al. [1992]
Vos and Potgieter [2015]

From the Figure A.1, it can be seen that the LIS strongly differ from each other. These differences can potentially lead to significant differences in the parameterization of the TOA intensities and also in the calculation of dosimetric quantities at aviation altitudes. To further illustrate the differences, the relative deviations of the LIS, with respect to the Voyager 1 and AMS−02 measurements, are shown in the bottom panel [B]. From these deviations, the LIS used in this work, denoted as TW20, compared to others, describe the Voyager 1 observations below 0.1 GeV and the AMS−02 measurements above 10 GeV better. This LIS is given as a function of kinetic energy, T (in GeV), as

$$j_{\mathrm{LIS}}^{\mathrm{proton}}(\mathrm{T}) = j_0 \left(\frac{\mathrm{T}}{\mathrm{T}_0}\right)^{0.179} \left(0.777 \cdot \left(\frac{\mathrm{E}_0}{\mathrm{T}_0}\right) + \left(\frac{\mathrm{T}}{\mathrm{T}_0}\right)^{0.795}\right)^{3.7764}, \tag{A.11}$$

where j_0 is given as 20.98 in units of particles/m^2/s/sr/MeV, while E_0 is the proton rest energy and $\mathrm{T}_0 = 1$ GeV.

A.2.1 Top-of-Atmosphere Parameterization: Spacecraft Data

It is well documented in literature that the Force-Field approximation, in its simplest form, cannot parameterize the TOA intensities during solar maximum at very low energies due to the exclusion of the drift terms [*Jokipii et al.*, 1977, *Isenberg and Jokipii*, 1979]. However, for comparative purposes with the Convection-Diffusion approximation, these are performed nevertheless. In this work, the PAMELA and AMS−02 measurements of the differential proton energy spectra, obtained between July 2006 and May 2017, covering both solar minimum and

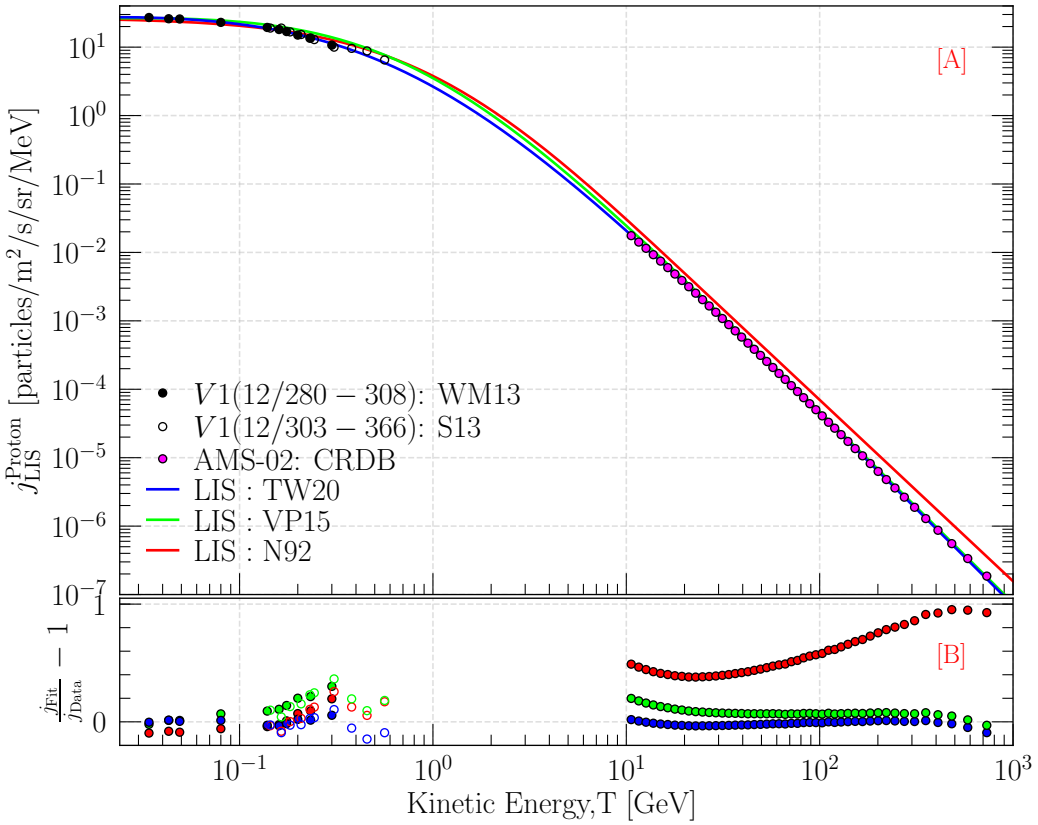

FIGURE A.1: Top panel: The proton LIS measured by Voyager 1 (open symbols, *Stone et al.* [2013] denoted as S13 and shaded black symbols, *Webber and McDonald* [2013] denoted as WM13) and AMS−02 (shaded magenta symbols, Cosmic Ray DataBase at http://tools.asdc.asi.it/CosmicRays is denoted as (CRDB)), while the LIS fits by *Nymmik et al.* [1992] (red solid line, denoted as N92), *Vos and Potgieter* [2015] (green solid line, denoted as VP15) and the LIS used in this work (blue solid line, denoted as TW20) are also shown. Bottom panel: Deviation between the LIS and measurements.

maximum, were used. To modulate the LIS spectrum (Equation A.4) and fit each measurement, the κ parameters, i.e. η and γ, play a significant role. However, for the Force-Field approximation, there are limited options to choose from due to the unavailability of standard integrals to accommodate all possible κ parameter values and still obtain an analytical description. Therefore, for simplicity $\gamma = 1$ and $\eta = 1$ are used, while, for the Convection-Diffusion approximation, these were used as free parameters varying according to solar modulation. The best−fit values of the modulation parameters ϕ and $\Re$ were extracted from the fits for each time interval by minimizing χ^2 in the energy interval between 0.1 and 10 GeV. This energy range incorporates the energy range 1−10 GeV which is the most effective energy range for detection of GCR at ground level by NMs.

Figures A.2 and A.3 give an overview of the PAMELA and AMS−02 proton measurements, averaged for each Carrington rotation, from 07/2006 to 05/2017. These datasets were obtained from https://tools.ssdc.asi.it/CosmicRays/. The parameterized PAMELA and

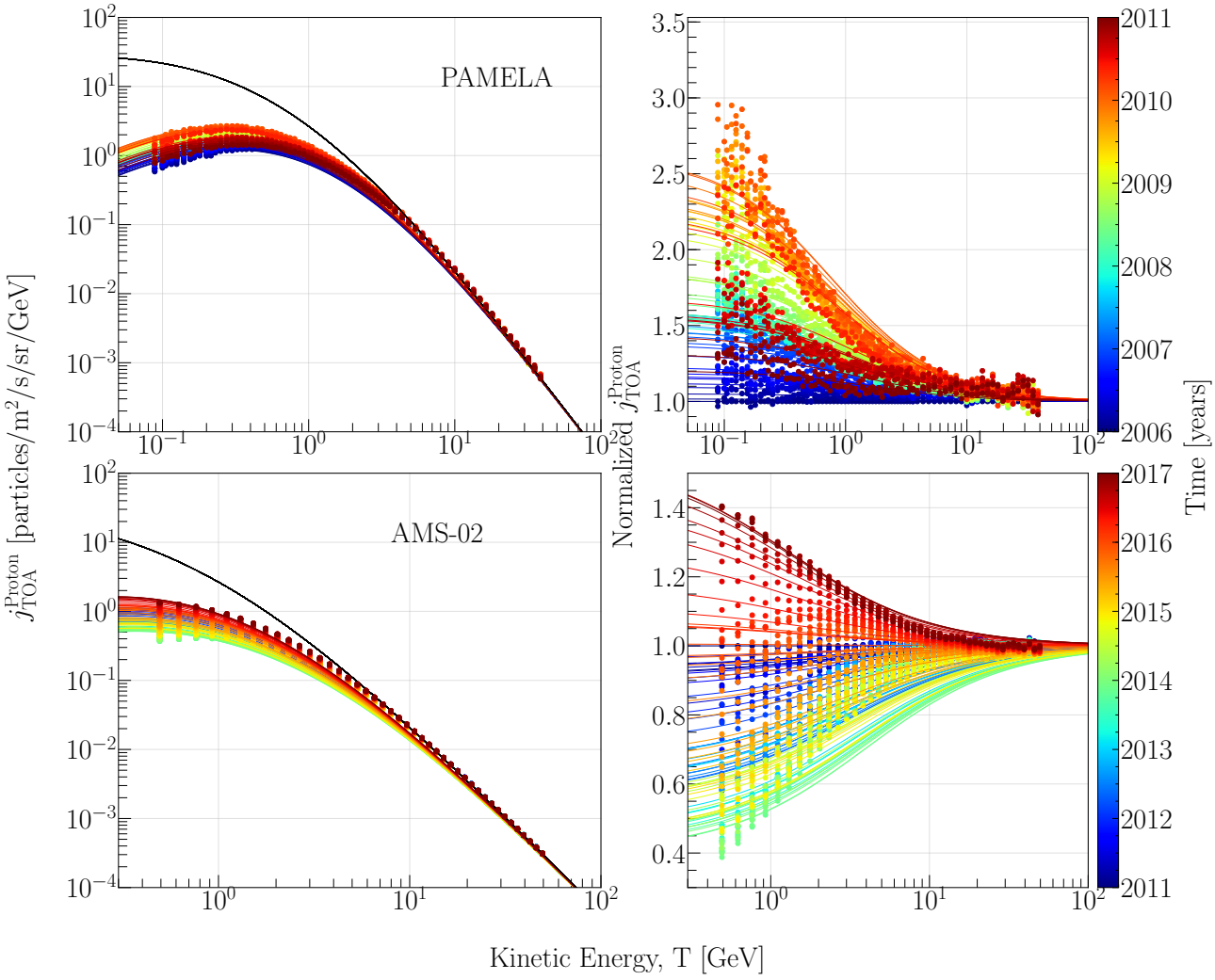

FIGURE A.2: Evolution of the proton energy spectra measured by PAMELA (shaded circles; top panels) and AMS−02 (shaded circles; bottom panels) from the period 07/07/2006 to 09/05/2011 and from 10/06/2011 to 09/05/2017, respectively. The AMS−02 and PAMELA data were taken from http://tools.asdc.asi.it/CosmicRays. The fitted curves are derived from the Force-Field approximation through Equations A.4 and shown in both panels as colour−coded lines, while the black solid lines denotes the assumed LIS.

AMS−02 spectra, using both the Force-Field (Figure A.2) and Convection-Diffusion (Figure A.3) approximations, are also shown as solid lines while the LIS used in this work is shown as black solid lines. Time dependent changes in solar modulation conditions are evident and can be seen in the spread of the colour−coded spectra, varying from blue to brown. The spectral variations are quantified by the calculated normalized ratios. PAMELA and AMS−02 intensities were normalized to the July 2006 and June 2011 spectra respectively. From this, it is clear that the lowest energy GCRs are more modulated than those at high energies. At higher energies, modulation is less pronounced and it can be neglected above ∼10 GeV.

Nevertheless, as it was anticipated, the Force-Field approximation does not correctly fit both

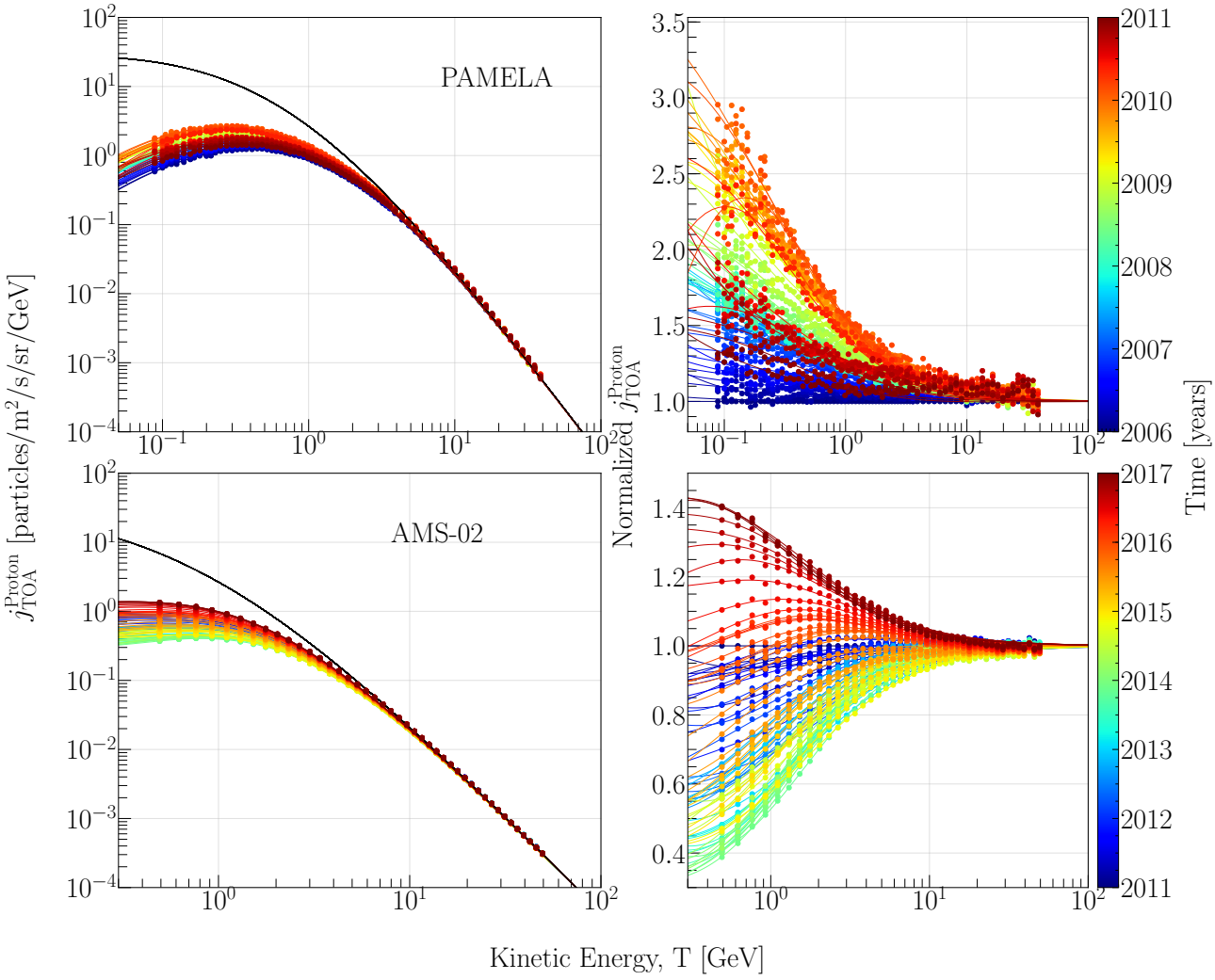

FIGURE A.3: Same as Figure A.2, but for the Convection-Diffusion approximation calculated through Equations A.7 (colour−coded lines), while the black solid lines denotes the assumed LIS.

the PAMELA and AMS−02 datasets, especially at lower energies, while the Convection-Diffusion approximation provides a strong indication that, when analyzed with very precise data such as the PAMELA and AMS−02, it can parameterize the TOA spacecraft measurements better than the Force-Field approximation, as a result of the free κ parameters varying according to solar modulation. In this sense, η can be used in the Convection-Diffusion approximation to mimic drift effects.

A.3 Modulation Parameters: Spacecrafts Data

A.3.1 Time Dependent Modulation Parameters

The fit parameters from the two approximate solutions, for all monthly proton intensities measured by PAMELA and AMS−02, are shown in Figure A.4. From the figure, the results of the modulation parameters (panel [A]) and the κ parameter γ and η (panel [B]), are shown as a function of time. In panel [A], it can be seen that ϕ and $\Re$ evolve, with time, following a well defined pattern over 11−years. The maximum intensities, $j_{\max}$, calculated from both approximate solutions, show an anti−correlation when compared to the modulation parameters ϕ and $\Re$. The $j_{\max}$ intensities show a relatively "flattish" profile during solar maximum compared to the ϕ and $\Re$ profile. However, there is a large difference between ϕ and $\Re$, since ϕ values were estimated using fixed parameters, i.e. $\gamma = 1$ and $\eta = 1$, while those of $\Re$ changed significantly with time. Interestingly, for the Convection-Diffusion approximation, the diffusion coefficient parameters η and γ show a clear temporal dependence and an anti−correlation is evident when compared to each other.

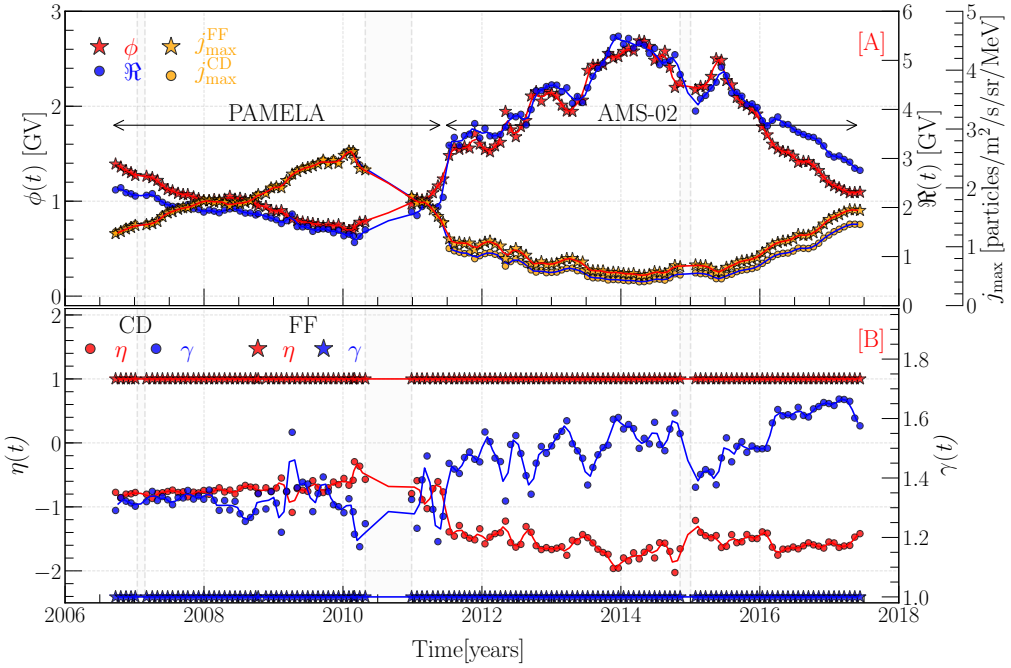

FIGURE A.4: Top panel: Time dependence of the solar modulation parameters ϕ and $\Re$, calculated for for each Carrington rotation, from the fit of Equations A.4 and A.7 to the monthly proton intensities, measured by PAMELA between 2006 and 2011, while intensity measurements by AMS−02 range between 2011 and 2017. The modulated peak intensities show an anti−correlation when compared to the modulation parameters. Panel [B] shows the time series of the best−fit κ parameter γ and η.

Re−plotting ϕ and $\Re$ from panel [A] in Figure A.4, panel [A] of Figure A.5 shows that there is a linear correlation between the maxima produced by the approximations during solar minimum, while during solar maximum the correlation is offset by a factor ranging between 0.1 and 0.2 compared to the solar minimum measurements. Furthermore, panel [B] shows that there is no linear correlation between the calculated modulation parameters sufficient enough to validate Equation A.10. Therefore, for the chosen form of the diffusion coefficient and LIS, the two approximate solutions are not directly comparable using the spacecraft data.

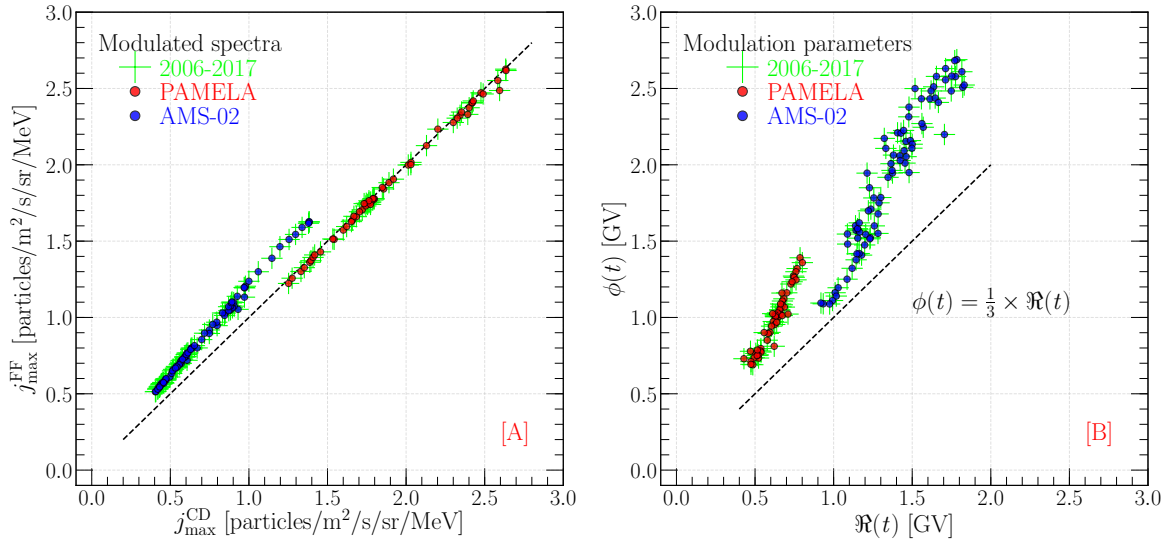

FIGURE A.5: Panel [A] shows the maximum modulated intensities from the Force-Field approximation against the maximum modulated intensities from the Convection-Diffusion approximation, calculated for each Carrington rotation. Panel [B] shows a poor correlation between the calculated modulation parameters, which is insufficient validate Equation A.10 for the chosen diffusion coefficient and LIS.

Again, re−plotting the modulation parameters $\Re$ against η in Figure A.6, an anti−correlation between $\Re$ and η exists. The smaller η gives a larger diffusion coefficient at low energies, while a larger $\Re$ value gives softer spectra of the CR intensities and hence suggesting a smaller γ is required to counter−balance the effect. Due to the non−linear dependence between $\Re$ ∼2.5 GV and ∼4 GV in the figure, this may call for more data to be explored, perhaps during a different solar cycle, to establish whether or not a transition function needs to be proposed between solar maximum and minimum (denoted as F1 and F3) or just one linear function(denoted as F2). In Figure A.7, the κ parameters, calculated from the Convection-Diffusion approximation, show an anti−correlation. The black square symbol represents the κ parameters assumed in the Force-Field approximation. Even here it is not clear what linear function might best represent these parameters for both solar minimum and solar maximum conditions. For calculation in later sections of this appendix F2 was used.

$$\gamma\left(\gamma_0, \eta, \gamma_1\right) = \gamma_0 \cdot \eta\left(t\right) + \gamma_1\left(t\right), \tag{A.12a}$$

$$\eta\left(\eta_0, \Re, \eta_1\right) = \eta_0 \cdot \Re\left(t\right) + \eta_1\left(t\right), \tag{A.12b}$$

with the fit statistics given in Table. A.2.

TABLE A.2: Best−fitted correlation values from modulation parameters and κ parameters calculated from PAMELA and AMS−02 measurements during solar minimum and maximum.

	γ_0	γ_1	$\overline{\epsilon_\gamma}$	R_γ
Figure A.7	−0.252	1.129	0.011	0.801
	η_0	η_1	$\overline{\epsilon_\eta}$	R_η
Figure A.6	−0.327	−0.182	0.012	0.853

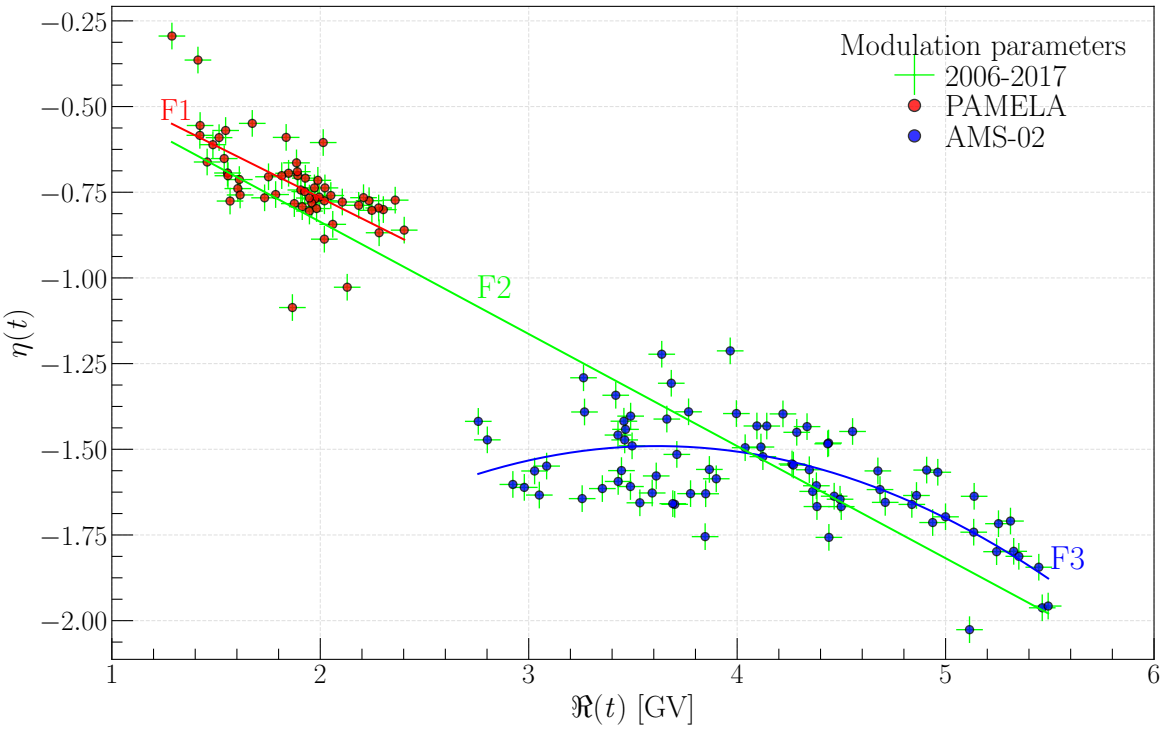

FIGURE A.6: Relationship between η and $\Re$. The different curves i.e. F1, F3, and F2 are regression curves performed for the PAMELA, AMS-02 and a combination of both datasets over solar minimum and solar maximum periods, respectively.

A.3.2 Time Dependence Diffusion Coefficients

In the estimation of κ, the solar wind plasma speed from the OMNI website[1] was averaged for each Carrington rotation from solar minimum to solar maximum at 1 AU for the period of the measurements. During this time, the solar wind speed near the Earth varied between 333−519

[1] https://omniweb.gsfc.nasa.gov/

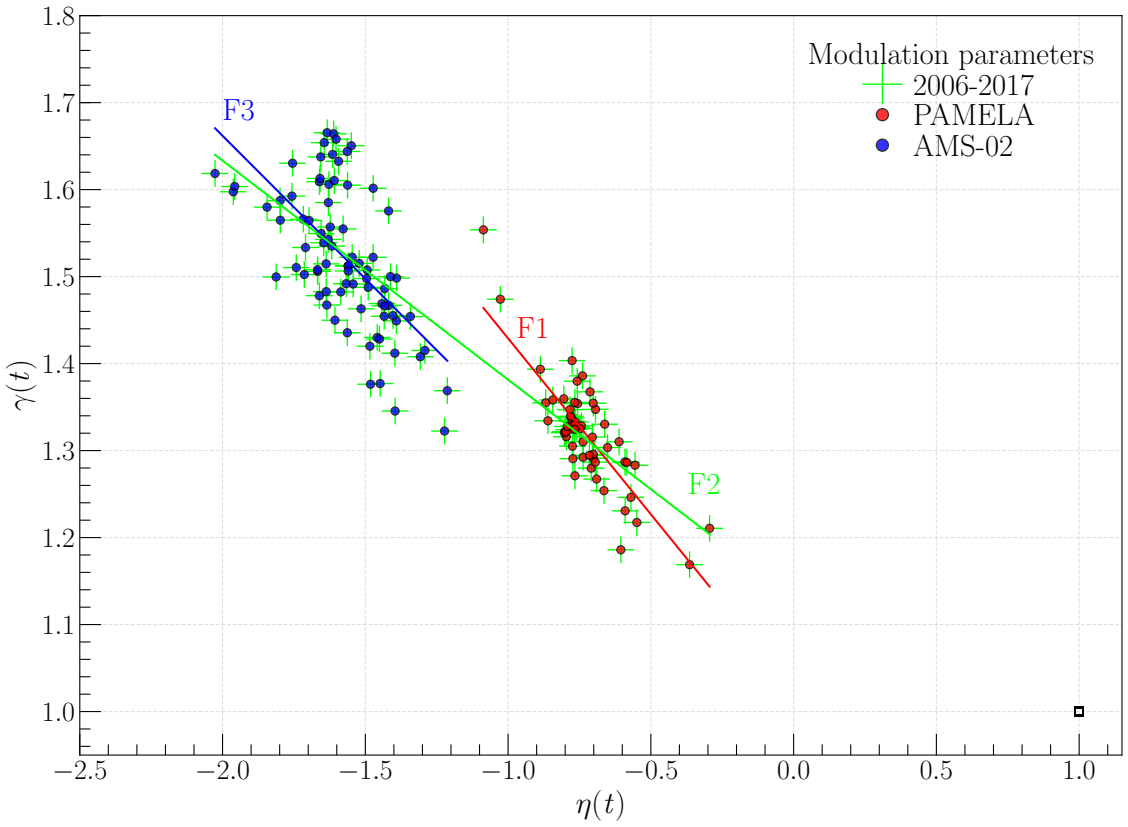

FIGURE A.7: Relationship between γ and η for the Convection-Diffusion approximation. The curves F1, F3, and F2 are linear regression curves performed for the PAMELA (F1), AMS-02 (F3) and a combination of both datasets (F2) over solar minimum and solar maximum periods. The black square symbol represent the κ parameters assumed for the Force-Field approximation.

km/s. A constant solar wind speed of 417.8 km/s was assumed between 2006 and 2011. In the calculation of the radial component of the diffusion coefficients, from Equations A.3 and A.9, both were re−written as

$$\kappa_r^{\mathrm{FF}} = \frac{\mathrm{V}(r,t)}{3\phi(r,t)}(r_* - r) \tag{A.13}$$

and

$$\kappa_r^{\mathrm{CD}} = \frac{\mathrm{V}(r,t)}{\Re(r,t)}(r_* - r), \tag{A.14}$$

where $r_* = 121.6$ AU and at Earth, $r = 1$ AU. The solar wind speed, calculated for both a constant solar wind speed i.e. $\langle \mathrm{V} \rangle = 417.8$ km/s and a time dependent solar wind speed, was used and the resulting calculations compared. These calculated solar wind speed averages, together with the calculated modulation parameters shown in Figure A.4, were incorporated into both Equations A.14 and A.13. Typical values of the diffusion coefficient κ_r, calculated for a constant solar wind flow, were found to be comparable to those calculated for a time dependent solar wind averaged for each Carrington rotation from solar minimum to solar maximum at 1 AU. For the Convection-Diffusion approximation, these values were $(1.3 - 5.5) \times 10^{22}$ cm^2/s/GV

and $(1.2-5.1)\times10^{22}$ cm^2/s/GV calculated for a constant and time dependent solar wind speed, respectively. However, for the Force-Field approximation, a constant solar wind speed[2] produced values in a range $(0.8-3.3)\times10^{22}$ cm^2/s/GV and for the time dependent solar wind speed these values were in a range $(0.9-3.4)\times10^{22}$ cm^2/s/GV.

Panel [A] of Figure A.8 shows the solar wind speed profile (raw data as light red), averages for each Carrington rotation interval (CRI; red symbols) and a moving average of the CRI (red broken line), while panel [B] shows the calculated κ_r for a constant (broken lines) and time dependent (solid lines) solar wind speed for each calculated modulation parameter. For each Carrington rotation, panels [C] and [D] show κ as estimated from the panel [B] quantities and by incorporating ϕ and $\Re$ from Figure A.4. In panels [C] and [D], it can be seen that κ evolves with time, following a well defined pattern. Also, κ increases as the energy increases; this is seen in the spread of the colour−coded κ, varying from blue to brown. Is is also evident that κ will anti-correlate with solar activity. This inverse relation describes the basis of the time dependent GCR modulation phenomenon: an increase (decrease) in diffusion produces high (low) intensities during epochs of solar minimum (maximum). The calculated ratio of the quantities shown in panel [C] and [D] are shown in panel [E] to illustrate the deviations during solar minimum and maximum conditions. These variations imply that estimated dosimetric quantities, calculated from the Force-Field approximation, are expected to be lower than those calculated from the Convection-Diffusion approximation, especially during solar maximum.

A.3.3 Rigidity Dependent Diffusion Coefficients

The rigidity dependence of the diffusion coefficient, resulting from the calculated modulation parameters, is shown in Figure A.9 as a function of rigidity for different times. Due to these apparent changes in the diffusion coefficients, it is evident that particle diffusion had a greater influence on the changes of the TOA intensities between 2006 and 2017. In the left panel, below 1 GeV, κ deviated from a power law due to a changing η. This effect is not present in the right panel where $\eta = 1$ is constant for the Force-Field approximation.

A.4 Modulation Parameters: Neutron Monitor Data

Estimation of modulation parameters using spacecraft measurements is the most widely used direct approach. However, spacecraft time coverage is limited to only a few decades, and neutron monitors (NMs) are mostly preferred. A simple way of extracting a long-term record

[2] Assuming V = 400 km/s and $r_* \approx 150$ AU, *Moraal* [2011] estimated these values to be in a range $(2-6)\times10^{22}$ cm^2/s/GV, while values by *Quenby* [1984] were in a range $(0.3-1.2)\times10^{22}$ cm^2/s/GV

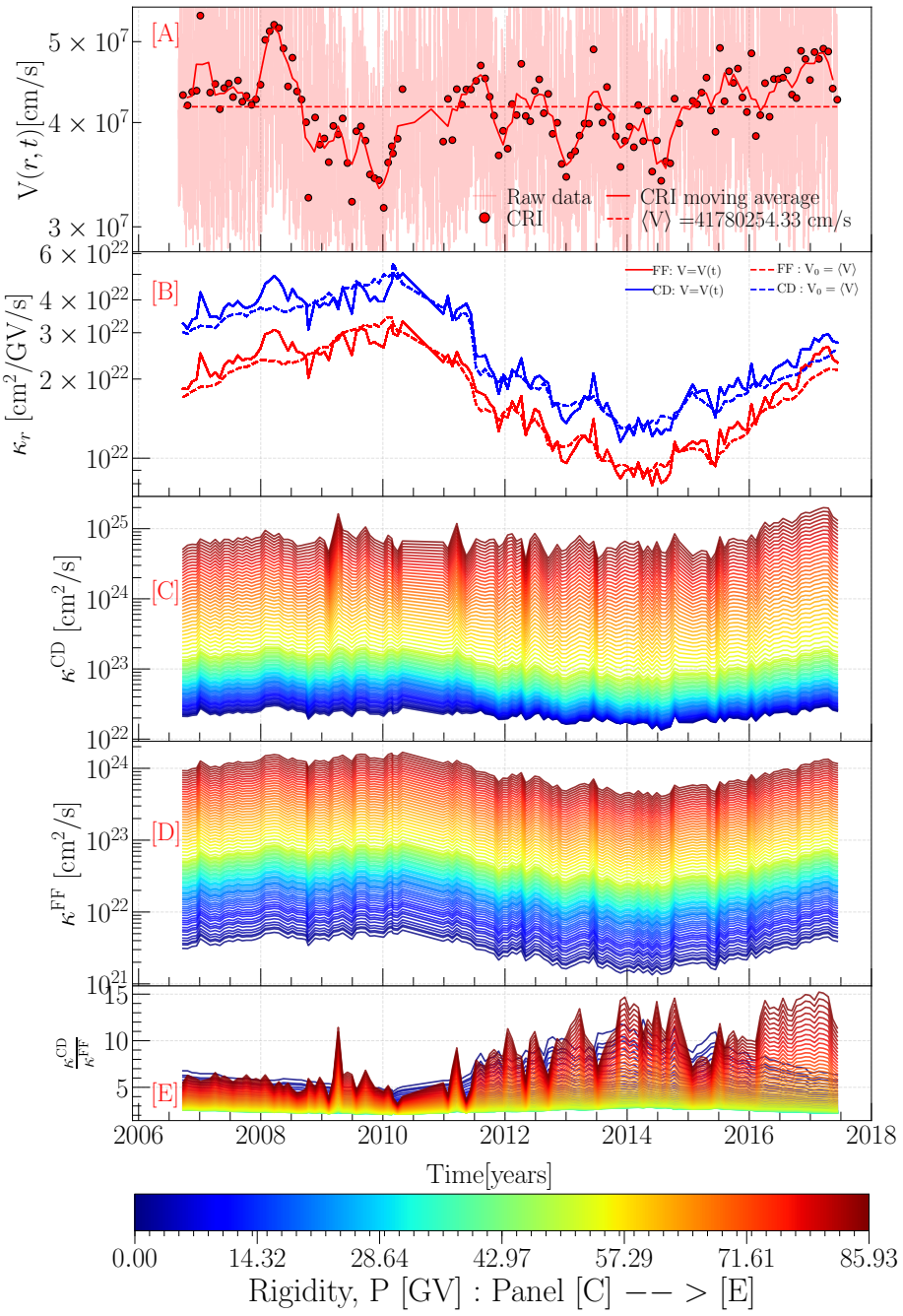

FIGURE A.8: Panel [A] represents the solar wind speed (raw data; light red), averages for each Carrington rotation interval (CRI, red symbols) and a moving average of the CRI (red broken line). Panel [B] represents κ_r for each Carrington rotation, estimated for both a constant (denoted as κ_{V_0}) and a time dependent solar wind speed (denoted as $\kappa_{V(r,t)}$) using values of ϕ and $\Re$ from Figure A.4. Panels [C] and [D] represent, κ for each Carrington rotation, estimated from the panel [B] quantities by incorporating ϕ and $\Re$ from Figure A.4. Panel [E] shows the calculated ratio of the quantities shown in panels [C] and [D] to illustrate the deviations during solar minimum and maximum conditions.

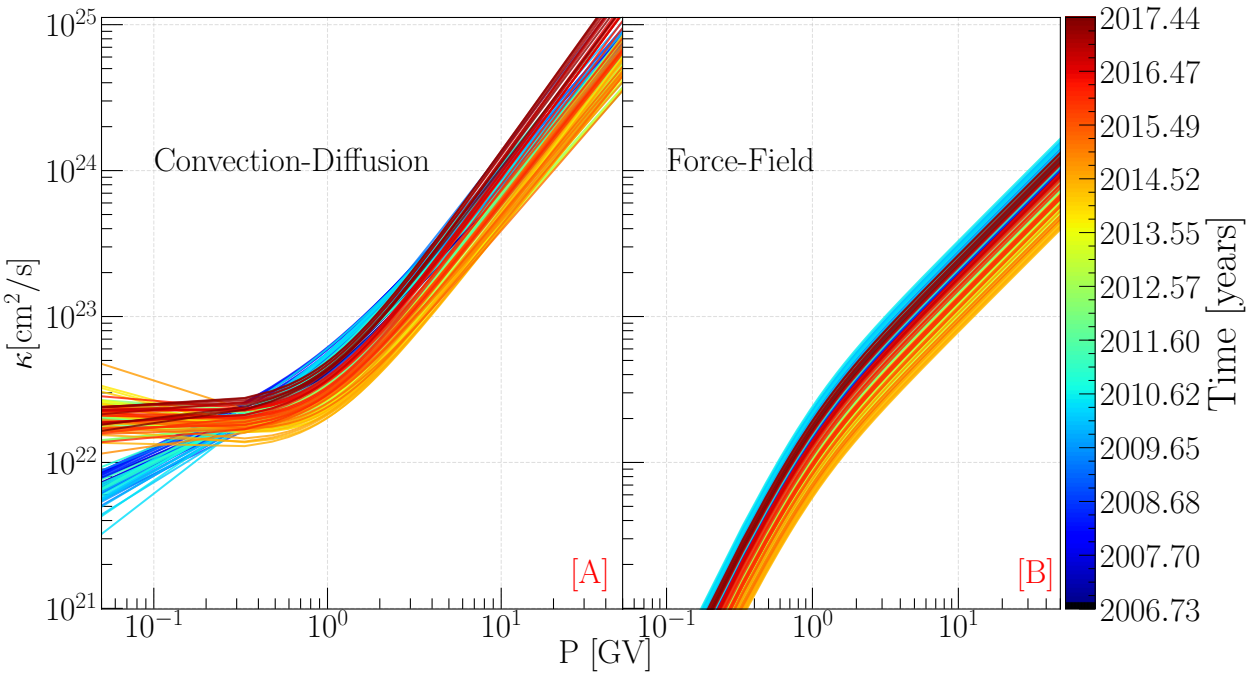

FIGURE A.9: Evolution of the estimated proton diffusion coefficient's rigidity dependence at Earth for different times.

of modulation parameters from NMs data would be to calculate the NM count rate averages for each Carrington rotation, at the same time as when ϕ (and $\Re$) in Figure A.4 were calculated. Through this, a correlation can be performed to establish a relationship between the modulation parameters ϕ (and $\Re$) and NMs count rates. However, this is not a realistic approach, simply because NMs count rates are highly dependent on the geomagnetic cutoff rigidity and altitude, which cannot be simply justified from this type of correlation. Furthermore, to relate the TOA intensities to NMs count rates, a yield function is needed.

In this work, the modulation parameters and diffusion coefficient parameters, calculated from the spacecraft measurements, are used in conjunction with NM data to determine long−term modulation parameters. Using the Force-Field approximation, a generalised and detailed procedure to describe the CR modulation at neutron monitor energies was first performed by *Moraal et al.* [1973]. This approach was recently applied by *Santiago et al.* [2018] to reconstruct a long-term record of solar modulation potentials from ground based neutron monitor stations and spacecraft measurements. Therefore no unnecessary repetition will be included in this work to formulate equations. The reader is rather referred to these publications above for more information. In this work, NM count rates from Hermanus, SANAE, Potchefstroom, and Tsumeb are used, all normalized to 100% in March 1987 for statistical comparison. However, for this demonstration only the SANAE neutron monitor is used when comparing the calculated modulation parameters with pre-existing studies.

At 1 AU, the differential intensity spectra at one time t_1 can be described through the distribution function $f_1 = j_1 {\mathrm{P}_1}^2$, and at a later time t_2 as $f_2 = j_2 {\mathrm{P}_2}^2$. Therefore, at any time, the differential intensity spectra in the Force-Field formalism is given as

$$j_2 = j_1 \left[\frac{\mathrm{P}_2}{\mathrm{P}_1}\right]^2, \tag{A.15}$$

where P_2 is related to P_1 through

$$\mathrm{P}_1 = \sqrt{\left[\Delta\phi + \sqrt{\mathrm{P}_2^2 + (\mathrm{A/Ze})^2 \mathrm{E}_0^2}\right]^2 - (\mathrm{A/Ze})^2 \mathrm{E}_0^2} \tag{A.16}$$

where $\mathrm{E}_0 = 0.938$ GeV is the proton rest mass energy, A is the mass number and Ze is the charge number. In the Convection-Diffusion formalism, Equation A.15 is replaced by

$$\frac{j_2}{j_1} = \exp\left[-\frac{\Delta\Re}{\beta^\eta \kappa_p}\right], \tag{A.17}$$

where $\Delta\Re$ is calculated from Equations A.8–A.9; see also *Stoker et al.* [1971] for more information.

These differential intensities at the TOA at different times are related to the NMs count rates through the atmospheric yield function, $\mathrm{S}(\mathrm{P}, x)$. The yield function used in this work is taken from *Caballero-Lopez and Moraal* [2012]. Therefore, the NMs count rate, $\mathcal{N}_r\left(\mathrm{P_c}, x, t_2\right)$, at a cutoff rigidity P_c, atmospheric depth x, and at any desired time t_2, is given as

$$\mathcal{N}_r\left(\mathrm{P_c}, x, t_2\right) = \int_{\mathrm{P_c}}^{\infty} \left[-\frac{d\mathcal{N}_r\left(\mathrm{P}_1, x, t_1\right)}{d\mathrm{P}_1}\right] \left[\frac{\mathrm{S}_2\left(\mathrm{P}_2, x\right)}{\mathrm{S}_1\left(\mathrm{P}_1, x\right)}\right] \left[\frac{j_2\left(\mathrm{P}_2, t_2\right)}{j_1\left(\mathrm{P}_1, t_1\right)}\right] d\mathrm{P}_2, \tag{A.18}$$

where $-d\mathcal{N}_r\left(\mathrm{P}_1, x, t_1\right)/d\mathrm{P}_1$ is the differential response function calculated from e.g. the in 1987 NM survey. Since *Dorman et al.* [1970] gave $\mathcal{N}_r$ as a function depended on cutoff rigidity and time, $-d\mathcal{N}_r\left(\mathrm{P}_1, x, t_1\right)/d\mathrm{P}_1$ is expressed as the differential response function in the form proposed by *Moraal et al.* [1989] as

$$-\frac{d\mathcal{N}_r\left(\mathrm{P}_1, x, t_1\right)}{d\mathrm{P}_1} = \alpha(t_1) k(t_1) (N_0 - N_1) \mathrm{P}_1^{-k(t_1)-1}, \tag{A.19}$$

where the constants $\alpha = 10.068$ and $k = 0.952$ are taken from *Caballero-Lopez* [2016], while N_0 is assumed to be 100%. The time t_1 is a reference period chosen to be the year in which the chosen NMs were normalized, i.e. in March 1987. In the calculation of the NMs count rates, the modulation parameter change $\Delta\phi(t, t_1)$ is a free parameter with minimum value also dependent on the choice of NM, while in March 1987, this modulation parameter change

$\Delta\Re(t, t_1)$ is 0. To calculate ϕ at any time t, the following formulation can be used

$$\phi(t) = \Delta\phi(t, t_1) + \phi(t_1), \tag{A.20}$$

(see Section 4, Equation [4−9] of *Moraal et al.* [1973]) where $\phi(t_1)$ can be estimated from spacecraft datasets. However, because all the chosen NMs in this work were normalized to 1987 and neither both dataset from AMS−02 nor PAMELA go back that far, an assumption can be made by examining the NMs temporal profile since the early 1950s. The 2008 and 1987 NM count rates are very similar, suggesting that a value of $\phi(t_1) = 0.988$ GV. Similarly, for the Convection-Diffusion approximation, the modulation parameter change $\Delta\Re(t, t_1)$ depends on the choice of a NM, and in March 1987 this modulation parameter change $\Delta\Re(t, t_1)$ is 0. To calculate $\Re$ at any time, the following expressing can be used

$$\Re(t) = \Delta\Re(t, t_1) + \Re(t_1), \tag{A.21}$$

where $\Re(t_1) = 1.8$ GV is again estimated from the 2008 spacecraft measurements, but assumed be representative of the 1987 solar minimum as well.

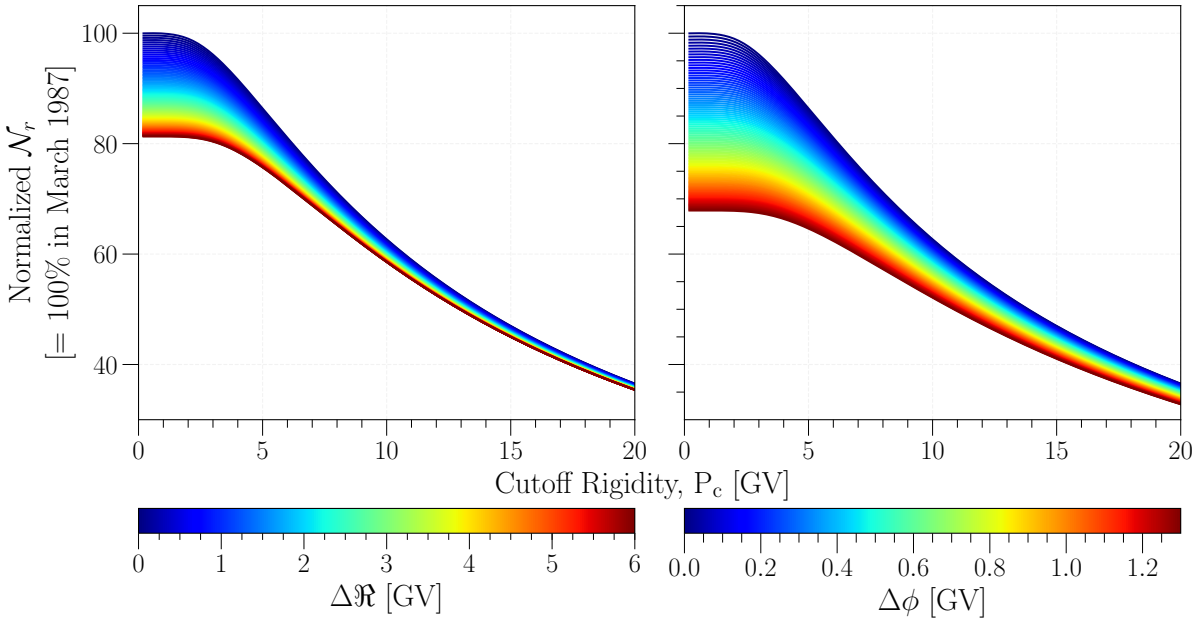

FIGURE A.10: Calculated NM counts rate using the Convection-Diffusion approximation between March 1987 (blue) and June 1991 (brown) in the left panel, while the right panel shows the NM counts rates, for the same period, calculated using the Force-Field approximation. The colour spread between the blue and brown NM counts rates represents modulation changes during the NM era.

To estimate the temporal change of the modulation parameters, $\Delta\phi$ and $\Delta\Re$, from NMs, Equation A.18 was integrated numerically in order to calculate the NMs count rate. For the

Convection-Diffusion approximation, the time dependent diffusion coefficients parameters γ and η, as calculated previously, were used. For the chosen NMs, the same γ, η and $\Delta\Re$ was used for each NMs. However, for the Force-Field approximation, $\gamma = \eta = 1$ were considered. The relationship between the numerically calculated count rate and the cutoff rigidity is shown in Figure A.10.

The calculated NMs count rates from both the Force-Field and Convection-Diffusion approximations are shown in Figure A.11 as a function of $\Delta\phi(t, t_1)$ and $\Delta\Re(t, t_1)$. A third order polynomial equation was used to fit these scatter plots. From these functions it is now possible to use near real-time NM count rates to calculate modulation parameters. These parameters used with the help of Equations A.20 and A.21 can be used to estimate the GCR intensity at Earth, which can be used as input for dosimetric models in order to calculate radiation exposure in the atmosphere. Figure A.12 compares time series of the calculated modulation parameters from *Usoskin et al.* [2011], denoted as U11, *Copeland et al.* [2010], denoted as C10, *Ghelfi et al.* [2017], denoted as G17, and the modulation parameter calculated in this work. These modulation parameters were calculated for NMs with a cutoff rigidity of less than 2 GV. Due to different approaches used to calculate these modulation parameters, results are normalised to each other in March 1987 for statistical comparison. However, one can see that the $\Delta\phi(t, t_1)$ published by *Ghelfi et al.* [2017], using the Oulu NM at ~ 0.8 GV, are in good agreement with the $\Delta\phi(t, t_1)$ calculated in this work for the SANAE NM at a similar cutoff rigidity. These calculated modulation parameters differ by as much as 0.3 GV.

A.5 Summary

PAMELA and AMS−02 observations of the temporal variation of GCR spectra over a whole solar cycle are extremely useful to test approximate solutions of the Parker transport equation. The Convection-Diffusion approximation was found to perform better when compared to the Force-Field approximation when reproducing GCR proton spectra at 1 AU. Simulations show that the Force-Field approximation might over-estimate the TOA intensity during these times. This is mainly because of the general formulation of κ that can be implemented in the Convection-Diffusion approximation that partially reproduces the effect of drifts. Although still in development, the approach outlined in this appendix may subsequently lead to a more accurate description of the TOA proton intensity, and therefore a more accurate description of various dosimetric quantities.

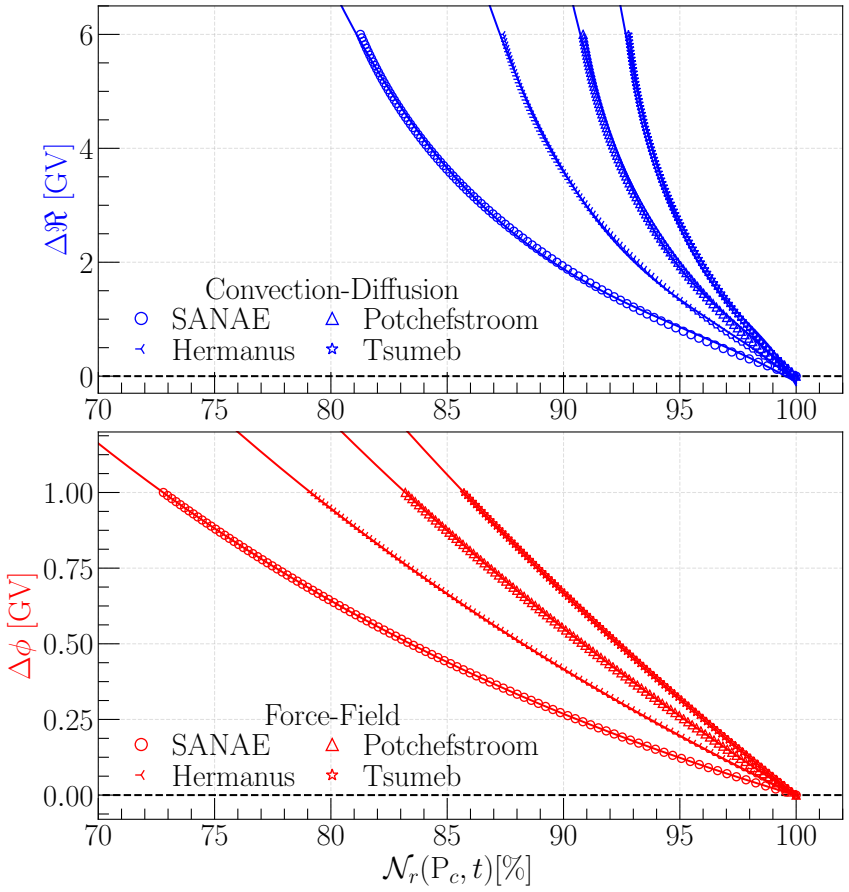

FIGURE A.11: NM count rate, $\mathcal{N}_r\,(\mathrm{P_c}, t)$ (denoted as symbols), calculated from Equation A.20, with $\Delta\phi(t, t_1)$ and $\Delta\Re(t, t_1)$ used as input. These modulation parameters are related to $\mathcal{N}_r\,(\mathrm{P_c}, t)$ by means of a third-degree polynomial (solid lines).

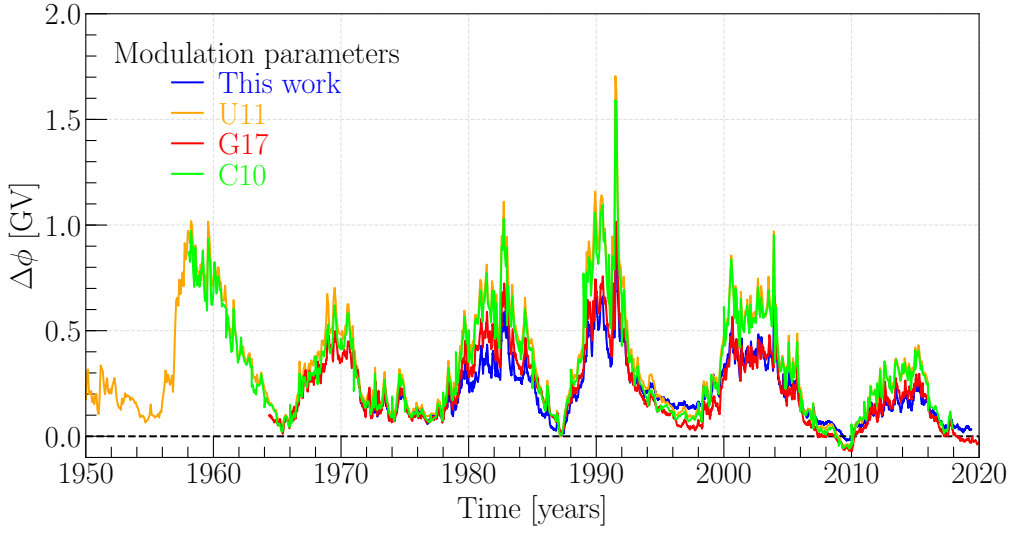

FIGURE A.12: Comparison of reconstructed modulation parameters, calculated using the Force-Field approximation, for NMs with cutoff rigidity less than 2 GV.

APPENDIX B

Portable Electronic Devices

Airlines have restrictions in place regarding the use of Portable Electronic Devices (PEDs) on board by flight personnel and passengers. All airlines share a common concern, namely that the use of PEDs during take-off and landing might pose a safety risk and that PEDs emitting radio signals could interfere with an aircraft's navigation and communication systems. However, updated regulations by Transport Canada,[1] the Federal Aviation Administration (FAA),[2] and the European Aviation Safety Agency (EASA),[3] among others, have made it allowable to use the PEDs for almost the entire flight as long as the devices are not transmitting radio signals.

The FAA has allowed this since October 28, 2013, following studies conducted by the Aviation Rulemaking Committee, appointed by the FAA to review the pre-existing PED policy and guidance. On November 26, 2013 the EASA made it possible for passengers to use their PEDs throughout the flight, regardless of whether the device is transmitting or not. The South African Civil Aviation Authority's[4] policy and guidance are similar to those of the FAA. The usage of PEDs is determined by each specific airline, while all aircraft have to go through an assessment process to ensure that the aircraft is not affected by PEDs. Based on the outcome of the assessment, additional restrictions may be placed on certain aircraft. It is also possible to experience differences within a single airline, depending on the aircraft type. Some airlines do not have clear guidelines easily available to passengers, concerning PED compliance. However, other airlines have clear guidelines, as demonstrated in Figure B.1 and B.2

[1] https://tinyurl.com/uaktk63
[2] https://tinyurl.com/ssj3ze8
[3] https://www.easa.europa.eu/
[4] http://www.caa.co.za/

OUR SAFETY GUIDE

SAA has your safety at heart. Please read these pages carefully

WHEN IN DOUBT, PLEASE CONSULT THE CABIN CREW.

SAFETY PAMPHLET

A safety pamphlet is provided at your seat. Please familiarise yourself with its important information and note the location of your nearest emergency exit.

SMOKING

As per South African Civil Aviation Authority regulations, smoking on board is prohibited. This includes the smoking of any artificial device or e-cigarettes.

SEAT BELTS

Seat belt signs are visible throughout the cabin. Whenever the signs are illuminated, fasten your seat belt. Keep it fastened throughout the flight. If sleeping under a blanket or duvet, fasten the seat belt over it so the cabin crew does not need to wake you in the event of turbulence. On the Airbus 330-300, if you are seated in Premium Class, ensure your shoulder-belt is fastened for take-off and landing. Passengers less than 1.3m in height are not required to make use of the shoulder belt.

SLEEPING ON THE FLOOR IS PROHIBITED

For your own safety, sleeping on the floor is prohibited. In the event of an irregular occurrence and/or emergency, passengers sleeping on the floor would not have access to seat belts and oxygen masks.

PRIOR TO TAKE-OFF AND LANDING

In preparation for take-off or landing, ensure flight mode is selected on your PED and it is switched off, your baggage is stowed, your tray table, footrest, armrest and TV screen are stowed, your window shutter is open, your seat is in the upright position and your seat belt is fastened.

REMAIN SEATED

After landing, remain seated until the aircraft has come to a complete stop and the Commander has switched off the seat belt signs.

LIQUIDS, AEROSOLS AND GELS (LAGs)

When travelling on international flights from South Africa, passengers are restricted from carrying certain LAGs in the aircraft cabin. These rules are aligned to International Civil Aviation Authority standards. Passengers wishing to carry essential liquids with them on board the aircraft must place them in a re-sealable, clear plastic bag with a maximum capacity of one litre and a total diameter of 80cm. No item containing liquid may exceed 100ml and it must fit comfortably inside the sealed bag. If these limitations are not adhered to, items will be confiscated by airport security, and SAA will not be in a position to recover them for passengers. When proceeding through airport security checkpoints, the bag holding these items must be separated from other cabin baggage.

Items that are exempt from LAG restrictions and that may be carried on board, without being placed in a clear plastic bag, are:

- Baby formula/milk and baby food in small containers, provided the child is travelling with the person carrying these.
- Essential and other non-prescription medicines not exceeding 100ml per container, including saline solution and products such as eye drops and contact lens solution.
- Liquids, gels and juice for diabetic passengers who require them for medical reasons.
- Solid cosmetics and personal hygiene items such as lipsticks in tubes, solid deodorants and lip balms. Any duty-free LAG products purchased after security checkpoints should be placed in special security bags at the store, and passengers connecting to further destinations are advised to keep these sealed throughout their journey.

CARRY-ON BAGGAGE

Storage for your cabin baggage is provided either under the seat in front of you or in the overhead stowage compartment. For your own safety and that of the passengers around you, please do not exceed the weight limitations of these compartments and ensure that items placed in them are securely positioned. Be careful when opening the overhead stowage compartments as some luggage may have shifted during the flight.

BUSINESS CLASS

SAA will accept two pieces of cabin baggage, neither of which may exceed 56cm x 36cm x 23cm in dimension and 8kg in weight.

ECONOMY CLASS

SAA will accept one piece of cabin baggage not exceeding 56cm x 36cm x 23cm in dimension and 8kg in weight. These baggage limitations apply to all passengers travelling in Economy Class, regardless of their Voyager or other status.

BASSINETS

The use of the bassinet is restricted by infant size and weight. The bassinet can comfortably accommodate an infant of 75 cm in length. The bassinet is designed to carry a maximum load of 11 kg. In the interest of safety and to prevent exceeding the weight limitation of the bassinet, it is recommended that the weight limitation of the infant not exceed 10 kg. The size and weight limitation of the bassinet must not be exceeded. The infant must fit into the bassinet. **Note:** An infant aged 9 to 12 months has an average length of 74 cm and a weight between 9.2 kg and 11.4 kg.

PORTABLE ELECTRONIC DEVICES (PEDs)

The South African Civil Aviation Authority has granted an exemption to allow SAA passengers to use PEDs during flights. The PEDs are divided into four categories: unrestricted, limited, restricted and prohibited. The table below provides guidance on typical PEDs and when they may be used. All PEDs must be switched off during take-off, climb, approach and landing. In addition, the Commander may prohibit the use of any PED, if this is required in the interest of safety. If at any point during a flight any irregularities or interference are detected in the flight deck, the use of PEDs (including devices with flight mode) must be suspended immediately. In this event, the Commander will make an announcement.

UNRESTRICTED

The items below may be used at any time:

- Hearing aids (including digital devices)
- Electronic watches
- Pagers (receivers only)
- Heart pacemakers
- Devices powered by solar cells
- Devices powered by micro battery cells

LIMITED

The following may only be used before the aircraft doors close prior to take-off and during taxiing after landing:

- Mobile phones
- Tablets
- E-readers
- Laptop computers may only be used when the aircraft doors are open.

RESTRICTED

The following items may only be used in-flight with the permission of the Commander. This is normally indicated by the seat-belt signs being switched OFF during climb and ON during descent. Should circumstances dictate otherwise, the Commander will inform the Senior Cabin Crew Member:

- Laptops with CD-ROM and DVD drive
- Palm-held organisers
- Audio equipment (e.g. CD-player, iPod, MP3 player)
- Computer consoles (e.g. Nintendo DS, PSP)
- Devices capable of recording
- Digital cameras
- GPS hand-held receivers
- Video cameras/recorders (including digital equipment)
- Bluetooth devices with flight mode selected
- Mobile phones with flight mode selected
- Devices using BlackBerry technology with flight mode selected
- Laptops, PDAs, tablets and e-readers with built-in Wi-Fi, with "wireless off" setting selected.

PROHIBITED

The items below are prohibited at all times:

- Devices transmitting radio frequency intentionally
- Walkie-talkies
- Remote-controlled toys
- Display units with cathode ray tubes
- Wireless computer equipment (e.g. mouse)
- PC printers
- PC scanners
- Laser pointers
- CD writers and mini disk recorders in recording mode
- Portable stereo sets
- Pocket radios (AM/FM)
- TV transmitters/receivers
- Telemetric equipment
- Wireless LAN

Cabin Crew members are responsible for enforcing the policy regarding the use of PEDs on board. If the Cabin Crew are unable to confirm that the transmitting function on an intentionally transmitting device has been disabled, then the device should be switched off. After embarkation and prior to the cabin doors being closed, the Senior Cabin Crew Member will make an announcement advising passengers of the conditions under which flight mode may be used. Passengers will be required to select flight mode functionality prior to switching their cellphones off in preparation for the flight. PLEASE NOTE: Flight mode setting is available on many mobile phones and other PEDs. When engaged, it suspends the device's signal-transmitting functions, thereby disabling its capacity to place or receive calls or text messages, while still permitting use of other functions that do not require signal transmission, such as calendars, address books, reading and preparing emails, etc.

FIGURE B.1: SAA PED guidelines for local and international flights.

74

service

KURZ- UND MITTELSTRECKE **FlyNet®** SHORT- AND MEDIUM-HAUL FLIGHTS

A321-100/200

A320-200

A319-100

Surfen Sie über den Wolken

Sie wollen im Flieger mit dem Büro in Verbindung stehen, unterhalten werden und Ihrer Familie schreiben? Mit FlyNet® ist das möglich. Wir führen Sie Schritt für Schritt zur guten Verbindung

Go surfing above the clouds Would you like to stay in contact with your office, communicate with your family or enjoy some excellent entertainment? FlyNet® makes all this possible

INTERNET AN BORD › INTERNET ON BOARD

1. Geräteeinstellungen: Flugmodus aktivieren, danach die WLAN-Funktion des Endgeräts aktivieren. FlyNet®-Netzwerk auswählen und verbinden.
› Settings: Activate flight mode, then the WiFi function. Select the FlyNet® network and connect.

2. Internet-Browser öffnen. Kostenloses FlyNet®-Portal erscheint automatisch als Startseite (sonst: ww2.lufthansa-flynet.com eingeben).
› Open your browser. The free FlyNet® portal will load automatically (if it doesn't pop up, type in: ww2.lufthansa-flynet.com).

3. „Internetzugang" im FlyNet®-Portal anklicken und den weiteren Instruktionen folgen.
› Click "Internet Access" on the FlyNet® portal and follow the instructions.

Fotos: Jens Görlich

Digitale Pannenhilfe

Sie haben Probleme bei der Nutzung von FlyNet®? Hier finden Sie Tipps, wie Sie Ihrem Endgerät Flügel verleihen – und den richtigen Ansprechpartner, falls Sie nicht mehr weiterwissen
› **FlyNet® troubleshooting** Having difficulties with FlyNet®? Here are some tips for what to do and whom to contact for further assistance

Keine Internetverbindung? Beachten Sie, dass die Verbindung erst ab Reiseflughöhe verfügbar ist. Dabei kann es in Ausnahmefällen zu kurzen Unterbrechungen kommen. Das FlyNet®-Portal steht aber durchgehend zur Verfügung.

PROBLEME, ERSTATTUNG, INFORMATIONEN:
Nutzen Sie im kostenlosen Telekom-HotSpot-Portal unter „Hilfe" das Kontaktformular.
E-Mail: HotSpotService@telekom.de

Gebührenfreie Hotline aus Deutschland: 0800 350 2000; aus dem Ausland: 00800 86 87 86 87 (kostenfrei aus der EU, der Schweiz und Norwegen)

› No Internet? A connection is only available at cruising altitude. While brief interruptions may occur, the FlyNet® portal is available throughout the flight.

PROBLEMS, REFUNDS, INFORMATION FOR CUSTOMERS:
Use the contact form under "Help" on the free Telekom HotSpot portal.
Email: HotSpotService@telekom.de

Free hotline from Germany: 0800 350 2000; hotline from all other countries: 00800 86 87 86 87 (toll free from EU countries, Switzerland and Norway)

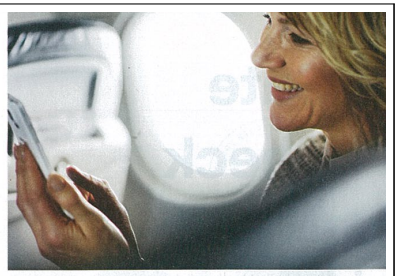

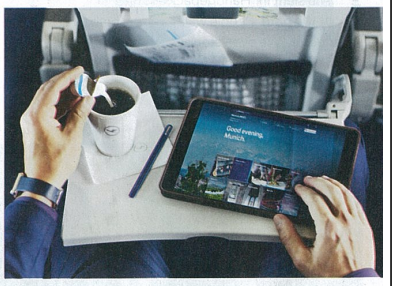

VON GATE ZU GATE › FROM GATE TO GATE

Erlaubte Netzwerkeinstellungen und Verfügbarkeit der FlyNet®-Services im Überblick
› An overview of permitted network settings and availability of FlyNet® services on board

ERLAUBTE NETZWERK-EINSTELLUNGEN AM GERÄT/ › PERMITTED DEVICE SETTINGS	Gate/ Boarding	Taxi	Take-off	Cruise	Landing	Taxi	Disembark/ Gate
Flugmodus/flight mode	OFF	ON	ON	ON	ON	OFF	OFF
WLAN/WiFi	ON	ON	ON	ON	ON	ON	ON
Bluetooth*	ON	ON	ON	ON	ON	ON	ON
Mobilfunknetz/mobile network	ON**	OFF	OFF	OFF	OFF	ON**	ON**
FLYNET® SERVICES							
WLAN/WiFi (FlyNet® Portal)	YES	YES	YES	YES	YES	YES	YES
Internet	–	–	–	YES	–	–	–
Mobilfunknetz/mobile network	–	–	–	–	–	–	–

Anweisungen der Crew zur Benutzung elektronischer Geräte müssen befolgt werden.
Crew announcements concerning the usage of electronic devices have to be followed.

* gilt auch für Lufthansa CityLine
** Mobilfunknetz am Boden/Mobile ground network

FIGURE B.2: PED usage example from Lufthansa for an international flight.

APPENDIX C

Geometric Factor and Effective Thickness

Two silicon diodes (SDs), i.e. the s2744-08 model, manufactured by Hamamatsu Photonics[1] were used this work. The length (a), width (b) and thickness (c) of each SD is 1 cm, 2 cm and 0.03 cm, respectively. The edges of each SD is covered with a coating resin which extends to a maximum of 0.1 mm beyond the upper surface,[2] so that when exposed to the incident light the effective area $\mathcal{A} = a{\cdot}b = 2$ cm^2.[2] However, for ionising radiation, the effective area $\mathcal{A}$ of each SD is 2.31 cm^2 [*Labrenz*, 2014]. For these SDs, the geometrical configuration plays a role for the amount of energy that can be deposited in the SDs. The operation of both SDs is in two different modes i.e. single and telescope mode. Figure C.1 shows two rectangular diodes SD1 and SD2 separated by 5 mm and also the dimensions of both SDs and as well as the incident angles of the incoming radiation are shown. The lower image shows the view of the SD from the side and the middle image shows the view from the top. In the telescope mode, ionizing radiation have to penetrate and hit both telescope SDs nearly simultaneously.

C.1 Single Diode

Following the study of *Sullivan* [1971], the geometry factor (GF) in units of cm$^2 \cdot$ sr is defined by the surface effective area of the detector and the angular coverage of a particle detector. Assuming that the incident particles are isotropic and are interacting with the SD from one side, according to *Sullivan* [1971] the GF of a single SD is simply given by

$$\mathrm{GF} = \mathcal{A} \cdot 2\pi \int_0^{\frac{\pi}{2}} \sin(\theta_2)\cos(\theta_2) d\theta_2 = \mathcal{A} \cdot \pi, \tag{C.1}$$

[1] http://www.hamamatsu.com
[2] http://www.alldatasheet.com/datasheet-pdf/pdf/212344/HAMAMATSU/S2744.html

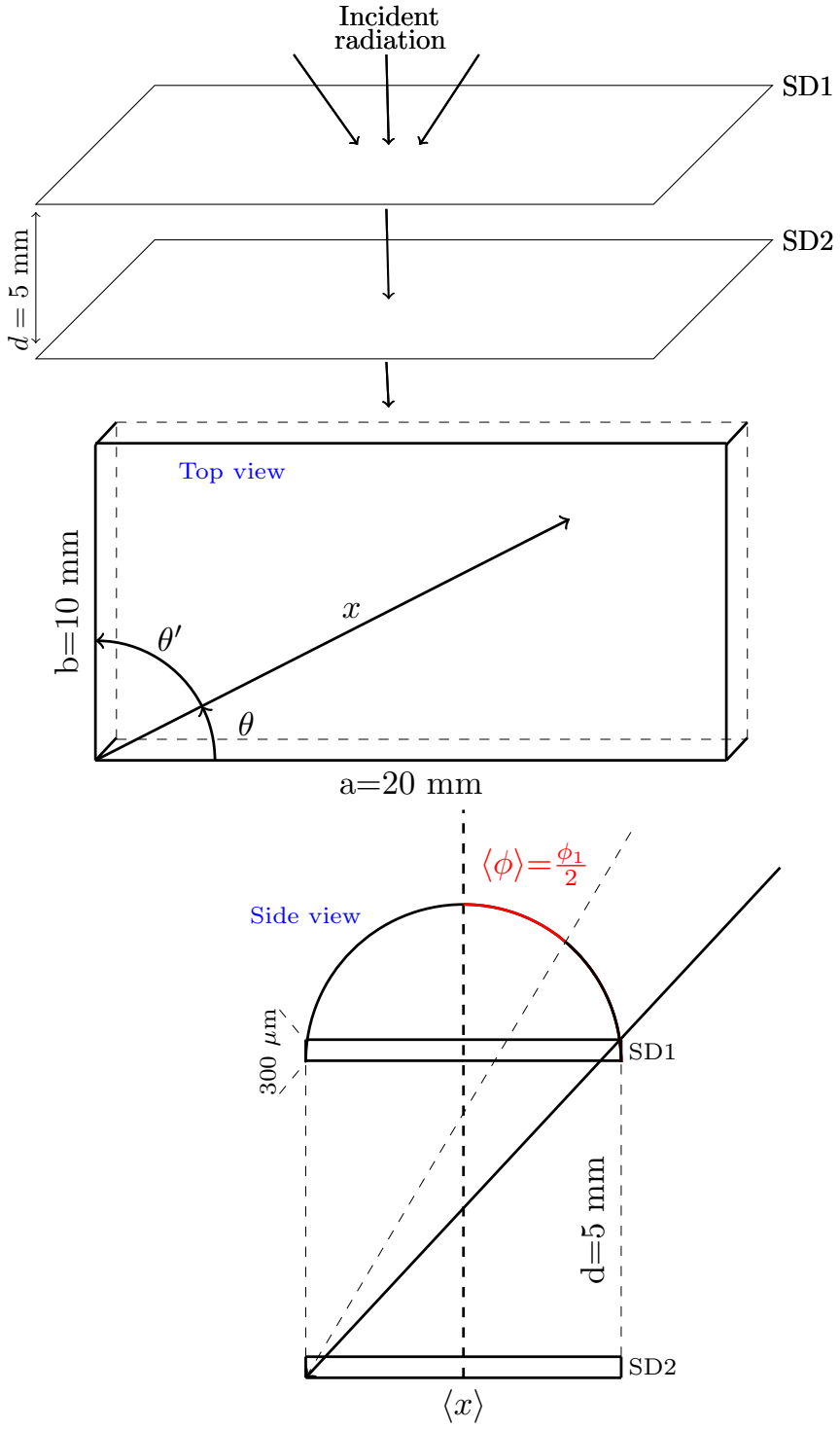

FIGURE C.1: The s2744-08 Hamamatsu diodes in telescope mode. The middle drawing shows the SD's view from the top, while the lower drawing shows a side view.

where θ_2 is the angle of incident and $\mathcal{A}$ is the active effective area of a target material. Therefore, for ionising radiation interacting with the SD, GF $= a{\cdot}b{\cdot}\pi = 7.257$ cm$^2 \cdot$ sr.

C.2 Telescope Diode

For these identical rectangular diodes separated by 5 mm, in telescope mode, the resulting GF is calculated from Equation 11 of *Sullivan* [1971], as

$$\begin{aligned} \mathrm{GF} = {} & d^2 \ln\left(\frac{d^2+a^2}{d^2+a^2+b^2}\cdot\frac{d^2+b^2}{d^2}\right) \\ & + 2a\sqrt{d^2+b^2}\tan^{-1}\left(\frac{a}{\sqrt{d^2+a^2}}\right) \\ & + 2b\sqrt{d^2+a^2}\tan^{-1}\left(\frac{b}{\sqrt{d^2+b^2}}\right) \\ & - 2ad\tan^{-1}\left(\frac{a}{d}\right) \\ & - 2bd\tan^{-1}\left(\frac{b}{d}\right). \end{aligned} \tag{C.2}$$

The resulting GF, in this setup, for the SDs used in this work is 13.197 cm$^2 \cdot$ sr. It can be seen that the GF of the diodes (SD1, SD2) in single mode and telescope mode differ. The ratio of the geometric factors $\mathrm{GF_R}$ for a single diode to diodes in telescope

$$\mathrm{GF_R} = \frac{\mathrm{GF_s}}{\mathrm{GF_T}} = \frac{7.257\ \mathrm{cm^2{\cdot}sr}}{13.197\ \mathrm{cm^2{\cdot}sr}} = 1.819. \tag{C.3}$$

However, this comparison of the single mode to telescope mode $\mathrm{GF_R}$ is meaningless, but shows how the separation d influences the $\mathrm{GF_T}$ estimation.

C.3 Effective Diode Thickness

When isotropic particles interact with both diodes, their trajectory can be projected onto the top diode, as shown in the middle panel of Figure C.1. Here the angle θ is a random variable, varying between 0° and 90°. The average length of this projected tract can now be calculated (numerically) by varying θ. For $\theta \leq \theta_c$, where θ_c is the angle when the trajectory goes along the diagonal of the diode's top projection, $\theta_c = 26.57°$. However, for $\theta > \theta_c$, angle $\theta' = 90° - \theta$. For the SDs used in this work, an average tract length $\langle x \rangle$ of 15.33 mm is obtained from

$$\langle x \rangle = \frac{1}{n}\left[\sum_i \frac{b}{\sin(\theta_i)} + \sum_i \frac{b}{\cos(\theta_i')}\right], \tag{C.4}$$

where i labels all individual calculated x values corresponding to θ_i, while n represents the total number of angles considered.

By examining a side-view of the SDs in telescope mode, the average opening angle of the particle telescope can now be calculated. Using the results of the previous, an angle of $\phi_1 = 90° - 18.07° = 71.93°$ is found. This results in an average opening angle of $2\phi_1 = 143.86°$. When considering isotropic incident particles, the average angle of incidence $\langle\phi\rangle$ is 35.965°. This value is now used to determine the effective thickness l_{eff} of the diodes using

$$l_{\text{eff}} = \frac{300\mu m}{\cos\langle\phi\rangle}. \tag{C.5}$$

For the chosen diodes, the effective length is ≈ 370.67 μm. To calculate the linear energy transfer spectra, Equation C.5 and Equation C.2 are essential.

Bibliography

Aharonian, F., A. Bykov, E. Parizot, V. Ptuskin, and A. Watson, Cosmic rays in galactic and extragalactic magnetic fields, *Space Science Reviews*, *166*(1-4), 97–132, doi:10.1007/s11214-011-9770-3, 2011.

Al Anid, H., B. J. Lewis, L. G. I. Bennett, and M. Takada, Modelling of radiation exposure at high altitudes during solar storms, *Radiation Protection Dosimetry*, *136*(4), 311–316, doi:10.1093/rpd/ncp127, 2009.

Al Anid, H. K., Modelling of aircrew radiation exposure during solar particle events, Ph.D. thesis, Royal Military College of Canada (Canada), 2012.

Allkofer, O. C., Introduction to cosmic radiation, *NASA STI/Recon Technical Report A*, *75*, 46,929, 1975.

Allkofer, O. C., *Introduction to cosmic radiation*, München : K. Thiemig, includes index, 1975.

Allkofer, O. C., and P. K. F. Grieder, *Cosmic Rays on Earth*, Physics data, Fachinformationszentrum Energie, Physik, Mathematik, 1984.

Almutayri, M. M., Preliminary Results from A Mini Neutron Monitor in Central Saudi Arabia, in *36th International Cosmic Ray Conference (ICRC2019)*, *International Cosmic Ray Conference*, vol. 36, p. 1051, 2019.

Anzer, U., Can coronal loop transients be driven magnetically?, *Solar Physics*, *57*(1), 111–118, doi:10.1007/BF00152048, 1978.

Atwell, W., A. Tylka, W. Dietrich, K. Rojdev, and C. Matzkind, Sub-GLE solar particle events and the implications for lightly-shielded systems flown during an era of low solar activity, 2015.

Auger, P., P. Ehrenfest, R. Maze, J. Daudin, and R. A. Fréon, Extensive cosmic-ray showers, *Reviews of Modern Physics*, *11*, 288–291, doi:10.1103/RevModPhys.11.288, 1939a.

Auger, P., R. Maze, and Robley, Extension et pouvoir pénétrant des grandes grebes de rayons cosmiques, *Comptes rendus*, *208*, 1641–1643, 1939b.

Axford, W. I., E. Leer, and G. Skadron, The Acceleration of Cosmic Rays by Shock Waves, in *International Cosmic Ray Conference*, *International Cosmic Ray Conference*, vol. 11, p. 132, 1977.

Babcock, H. W., The Topology of the Sun's Magnetic Field and the 22-YEAR Cycle., *Astrophysical Journal*, *133*, 572, doi:10.1086/147060, 1961.

Bakar, N. F. A., S. A. Othman, N. F. A. N. Azman, and N. S. Jasrin, Effect of ionizing radiation towards human health: A review, *IOP Conference Series: Earth and Environmental Science*, *268*, 012,005, doi:10.1088/1755-1315/268/1/012005, 2019.

Baker, D. N., What is space weather?, *Advances in Space Research*, *22*(1), 7 – 16, doi:https://doi.org/10.1016/S0273-1177(97)01095-8, solar-Terrestrial Relations: Predicting the Effects on the Near-Earth Environment, 1998.

Bakhtiyarov, S. I., *Earth's Natural Protective System: van Allen Radiation Belts*, pp. 225–240, Springer International Publishing, Cham, doi:10.1007/978-3-319-03952-7_19, 2015.

Barnden, L. R., and M. Bercovitch, Field Gradient and Curvature Drifts and Cosmic Ray Transport into the Solar System, in *International Cosmic Ray Conference*, *International Cosmic Ray Conference*, vol. 3, p. 875, 1975.

Barouch, E., and L. F. Burlaga, Causes of forbush decreases and other cosmic ray variations, *Journal of Geophysical Research*, *80*(4), 449–456, doi:10.1029/JA080i004p00449, 1975.

Bartlett, D., Radiation protection aspects of the cosmic radiation exposure of aircraft crew, *Radiation protection dosimetry*, *109*, 349–55, doi:10.1093/rpd/nch311, 2004.

Bartusiak, M., Sounds of the sun, *American Scientist*, *82*, 61–68, 1994.

Baumann, I., and S. Solanki, On the size distribution of sunspot groups in the greenwich sunspot record 1874-1976, *Astronomy and Astrophysics*, *443*, 1061–1066, doi:10.1051/0004-6361:20053415, 2005.

Bazilevskaya, G. A., Solar cosmic rays in the near Earth space and the atmosphere, *Advances in Space Research*, *35*(3), 458 – 464, doi:https://doi.org/10.1016/j.asr.2004.11.019, influence of the Sun's Radiation and Particles on the Earth's Atmosphere and Climate, 2005.

Bazilevskaya, G. A., and A. K. Svirzhevskaya, On The Stratospheric Measurements of Cosmic Rays, *Space Science Reviews*, *85*(3), 431–521, doi:10.1023/A:1005029832052, 1998.

Beaujean, R., J. Kopp, and G. Reitz, Radiation Exposure in Civil Aircraft, *Radiation Protection Dosimetry*, *85*(1-4), 287–290, doi:10.1093/oxfordjournals.rpd.a032853, 1999.

Beaujean, R., J. Kopp, S. Burmeister, F. Petersen, and G. Reitz, Dosimetry inside MIR station using a silicon detector telescope (DOSTEL), *Radiation Measurements*, *35*(5), 433–438, doi:10.1016/S1350-4487(02)00074-4, 2002.

Beaujean, R., S. Burmeister, F. Petersen, and G. Reitz, Radiation exposure measurement onboard civil aircraft, *Radiation protection dosimetry*, *116*, 312–5, doi:10.1093/rpd/nci095, 2005.

Belov, A. V., Forbush effects and their connection with solar, interplanetary and geomagnetic phenomena, in *Universal Heliophysical Processes*, *IAU Symposium*, vol. 257, edited by N. Gopalswamy and D. F. Webb, pp. 439–450, doi:10.1017/S1743921309029676, 2009.

Belov, A. V., E. A. Eroshenko, V. A. Oleneva, A. B. Struminsky, and V. G. Yanke, What determines the magnitude of forbush decreases?, *Advances in Space Research*, *27*(3), 625 – 630, doi:https://doi.org/10.1016/S0273-1177(01)00095-3, 2001.

Berger, T., Long term variations of galactic cosmic radiation on board the international space station, on the moon and on the surface of mars, *Journal of Space Weather and Space Climate*, *10*, 1–20, doi:10.1051/swsc/2020028, 2020.

Berger, T., K. Marsalek, J. Aeckerlein, J. Hauslage, D. Matthiä, B. Przybyla, M. Rohde, and M. Wirtz, The German Aerospace Center M-42 radiation detector-A new development for applications in mixed radiation fields, *Review of Scientific Instruments*, *90*(12), 125,115, doi:10.1063/1.5122301, 2019.

Bethe, H., Zur theorie des durchgangs schneller korpuskularstrahlen durch materie, *Annalen der Physik*, *397*(3), 325–400, doi:10.1002/andp.19303970303, 1930.

Bethe, H., Bremsformel für Elektronen relativistischer Geschwindigkeit, *Zeitschrift fur Physik*, *76*(5-6), 293–299, doi:10.1007/BF01342532, 1932.

Bethe, H., and W. Heitler, On the Stopping of Fast Particles and on the Creation of Positive Electrons, *Proceedings of the Royal Society of London Series A*, *146*(856), 83–112, doi:10.1098/rspa.1934.0140, 1934.

Bichsel, H., Passage of charged particles through matter, doi:10.2172/6675902, 1969.

Bichsel, H., *Charged-Particle-Matter Interactions*, pp. 1373–1387, Springer New York, New York, NY, doi:10.1007/978-0-387-26308-3_91, 2006.

Biermann, L., Kometenschweife und solare Korpuskularstrahlung, *Zeitschrift für Astrophysik*, *29*, 274, 1951.

Biermann, L., Solar corpuscular radiation and the interplanetary gas, *Observatory*, *77*, 109–110, 1957.

Blackett, P. M. S., G. P. S. Occhialini, and E. Rutherford, Some photographs of the tracks of penetrating radiation, *Proceedings of the Royal Society of London. Series A, Containing Papers of a Mathematical and Physical Character*, *139*(839), 699–726, doi:10.1098/rspa.1933.0048, 1933.

Blanco, F., P. L. Rocca, and F. Riggi, Cosmic rays with portable geiger counters: from sea level to airplane cruise altitudes, *European Journal of Physics*, *30*(4), 685–695, doi:10.1088/0143-0807/30/4/003, 2009.

Bland, C., and G. Cioni, Geomagnetic cut-off rigidities in non-vertical directions, *Earth and Planetary Science Letters*, *4*(5), 399 – 405, doi:https://doi.org/10.1016/0012-821X(68)90070-8, 1968.

Bloch, F., Zur bremsung rasch bewegter teilchen beim durchgang durch materie, *Annalen der Physik*, *408*(3), 285–320, doi:10.1002/andp.19334080303, 1933.

Bochsler, P., Composition of matter in the heliosphere, *Proceedings of the International Astronomical Union*, *4*(S257), 17–28, doi:10.1017/S1743921309029044, 2008.

Bogdanov, M., A. Surkov, and A. Fedorenko, Effect of cosmic rays on atmospheric pressure under mountain conditions, *Geomagnetism and Aeronomy*, *46*, 254–260, doi:10.1134/S0016793206020162, 2006.

Bothe, W., and W. Kolhörster, Das wesen der höhenstrahlung, *Zeitschrift für Physik*, *56*(11), 751–777, doi:10.1007/BF01340137, 1929.

Böttcher, S. I., Calibration of HET/EPT Flight Models using data obtained in thermal vacuum, *Technical report*, *6951*, 2018.

Bottollier-Depois, P., J.F. andBeck, M. Latocha, V. Mares, and F. Wissmann, Comparison of codes assessing radiation exposure of aircraft crew due to galactic cosmic radiation, *EURADOS Report 2012-03 (Braunschweig, Germany: European Radiation Dosimetry Group e.V)*, 2012.

Bütikofer, R., *Cosmic Ray Particle Transport in the Earth's Magnetosphere*, pp. 79–94, doi:10.1007/978-3-319-60051-2_5, 2018a.

Bütikofer, R., *Ground-Based Measurements of Energetic Particles by Neutron Monitors*, vol. 444, pp. 95–111, doi:10.1007/978-3-319-60051-2_6, 2018b.

Bykov, A. M., D. C. Ellison, A. Marcowith, and S. M. Osipov, Cosmic ray production in supernovae, *Space Science Reviews*, *214*(1), doi:10.1007/s11214-018-0479-4, 2018.

Caballero-Lopez, R., and H. Moraal, Cosmic-ray yield and response functions in the atmosphere, *Journal of Geophysical Research (Space Physics)*, *117*, doi:10.1029/2012JA017794, 2012.

Caballero-Lopez, R. A., An estimation of the yield and response functions for the mini neutron monitor, *Journal of Geophysical Research (Space Physics)*, *121*(8), 7461–7469, doi:10.1002/2016JA022690, 2016.

Caballero-Lopez, R. A., and H. Moraal, Limitations of the force field equation to describe cosmic ray modulation, *Journal of Geophysical Research (Space Physics)*, *109*, A01101, doi:10.1029/2003JA010098, 2004.

Cade III, W. B., and C. Chan-Park, The origin of "space weather", *Space Weather*, *13*(2), 99–103, doi:10.1002/2014SW001141, 2015.

Cane, H. V., Coronal Mass Ejections and Forbush Decreases, *Space Science Reviews*, *93*, 55–77, doi:10.1023/A:1026532125747, 2000.

Cane, H. V., I. G. Richardson, and T. T. von Rosenvinge, Cosmic ray decreases: 1964-1994, *Journal of Geophysical Research*, *101*(A10), 21,561–21,572, doi:10.1029/96JA01964, 1996.

Carlson, P., and A. De Angelis, Nationalism and internationalism in science: the case of the discovery of cosmic rays, *European Journal of Physics H*, *35*(4), 309–329, doi:10.1140/epjh/e2011-10033-6, 2011.

Carrington, R. C., Description of a Singular Appearance seen in the Sun on September 1, 1859, *Monthly Notices of the Royal Astronomical Society*, *20*(1), 13–15, doi:10.1093/mnras/20.1.13, 1859.

Castellani, V., S. Degl'Innocenti, G. Fiorentini, M. Lissia, and B. Ricci, Solar neutrinos: beyond standard solar models, *Physics Reports*, *281*(5-6), 309–398, doi:10.1016/s0370-1573(96)00032-4, 1997.

Chen, J., Physics of erupting solar flux ropes: Coronal mass ejections (CMEs)—Recent advances in theory and observation, *Physics of Plasmas*, *24*(9), 090501, doi:10.1063/1.4993929, 2017.

Cheng, X., J. Zhang, M. D. Ding, Y. Liu, and W. Poomvises, The driver of coronal mass ejections in the low corona: A flux rope, *Astrophysical Journal*, *763*(1), 43, doi:10.1088/0004-637x/763/1/43, 2013.

Clark, D. H., and F. R. Stephenson, An Interpretation of the Pre-Telescopic Sunspot Records from the Orient, *Quarterly Journal Royal Astronomical Society*, *19*, 387, 1978.

Clarke, R. H., and J. Valentin, The History of ICRP and the Evolution of its Policies, *Annals of the ICRP*, *39*(1), 75 – 110, doi:https://doi.org/10.1016/j.icrp.2009.07.009, iCRP Publication 109, 2009.

Clay, J., Penetrating Radiation, *Proceedings of the Koninklijke Nederlandse Akademie Van Wetenschappen*.

Clette, F., E. W. Cliver, L. Lefèvre, L. Svalgaard, and J. M. Vaquero, Revision of the sunspot number(s), *Space Weather*, *13*(9), 529–530, doi:10.1002/2015SW001264, 2015.

Cliver, E. W., History of research on solar energetic particle (sep) events: the evolving paradigm, *Proceedings of the International Astronomical Union*, *4*(S257), 401–412, doi:10.1017/S1743921309029639, 2008.

Cliver, E. W., History of research on solar energetic particle (SEP) events: the evolving paradigm, in *Universal Heliophysical Processes*, *IAU Symposium*, vol. 257, edited by N. Gopalswamy and D. F. Webb, pp. 401–412, doi:10.1017/S1743921309029639, 2009.

Compton, A. H., and I. A. Getting, An Apparent Effect of Galactic Rotation on the Intensity of Cosmic Rays, *Physical Review*, *47*(11), 817–821, doi:10.1103/PhysRev.47.817, 1935.

Copeland, K., Cari-7A: Development and validation, *Radiation Protection Dosimetry*, pp. 1–13, doi:doi:10.1093/rpd/ncw369, 2017a.

Copeland, K., Radiation Protection Dosimetry, *10*, 1–13, 2017b.

Copeland, K., D. E. Parker, , and W. Friedberg, Alpha particles at energies of 10 MeV to 1 TeV: Fluence absorbed dose, equivalent dose, effective dose, and gray equivalent conversion coefficients calculated using Monte Carlo radiation transport code MCNPX 2.7.A, *Radiation Protection Dosimetry*, *138(4)*, 310–319, 2010.

Copeland, K., W. Friedberg, T. Sato, and K. Niita, Comparison of fluence-to-dose conversion coefficients for deuterons, tritons, and helions, *Radiation Protection Dosimetry*, *148(3)*, 344–351, 2012.

Corti, C., V. Bindi, C. Consolandi, and K. Whitman, SOLAR MODULATION OF THE LOCAL INTERSTELLAR SPECTRUM WITH VOYAGER 1, AMS-02, PAMELA, AND BESS, *Astrophysical Journal*, *829*(1), 8, doi:10.3847/0004-637x/829/1/8, 2016.

Coulomb, C. A., Troisième Mémoire sur l'Electricité et le Magnétiseme, *Histoire de l'Académie Royale des Sciences*, pp. 612–638, 1785.

Cucinotta, F., M. Y. Kim, and L. Chappell, Space radiation cancer risk projections and uncertainties - 2012, doi:10.13140/RG.2.1.1413.3528, 2013.

De Angelis, A., Domenico Pacini, uncredited pioneer of the discovery of cosmic rays, *arXiv e-prints*, arXiv:1103.4392, 2011.

de Angelis, A., Atmospheric ionization and cosmic rays: studies and measurements before 1912, *Astroparticle Physics*, *53*, 19 – 26, doi:https://doi.org/10.1016/j.astropartphys.2013.05.010, centenary of cosmic ray discovery, 2014.

Dönsdorf, E. M., Development of a phoswich detector for neutron dose rate measurements in the earth's atmosphere, Ph.D. thesis, 2013.

Dorman, L. I., S. G. Fedchenko, L. V. Granitsky, and G. A. Rishe, Coupling and barometer coefficients for measurements of cosmic ray variations at altitudes of 260-400 mb, in *International Cosmic Ray Conference*, *International Cosmic Ray Conference*, vol. 2, p. 233, 1970.

Dyer, A. C. R., A. D. P. Ryden, K. A. andHands, C. Dyer, C. Burnett, and M. Gibbs, Zenith: A radiosonde detector for rapid-response ionizing atmospheric radiation measurements during solar particle events, *Space Weather*, *16*, 261–272, 2018.

Eastwood, J. P., The science of space weather, *Philosophical Transactions of the Royal Society of London Series A*, *366*(1884), 4489–4500, doi:10.1098/rsta.2008.0161, 2008.

EURADOS WG5, Cosmic radiation exposure of aircraft crew - compilation of measured and calculated data, *EURADOS*, *Final Report of EURADOS WG5*, 241–259, 2004.

European Union, Council directive 2013/59/euratom of 5 december 2013 laying down basic safety standards for the protection of the health of workers and the general public against the dangers arising from ionising radiation, *Official Journal of the European Communities L13*, *1*, 2013.

Evans, R., and A. Noyau, *The Atomic Nucleus*, @Internat. S.in P. & A. Physics, McGraw-Hill, 1955.

Failla, G., Biological effects of ionizing radiations, *Journal of Applied Physics*, *12*(4), 279–295, doi:10.1063/1.1712910, 1941.

Fano, U., Penetration of protons, alpha particles, and mesons, *Annual Review of Nuclear Science*, *13*(1), 1–66, doi:10.1146/annurev.ns.13.120163.000245, 1963.

Feldman, U., U. Schuhle, K. G. Widing, and J. M. Laming, Coronal composition above the solar equator and the north pole as determined from spectra acquired by the SUMER instrument onSOHO, *Astrophysical Journal*, *505*(2), 999–1006, doi:10.1086/306195, 1998.

Fenton, A. G., K. G. McCracken, D. C. Rose, and B. G. Wilson, The onset times of Forbush-type cosmic ray intensity decreases, *Canadian Journal of Physics*, *37*, 970, doi:10.1139/p59-108, 1959.

Ferrari, A., and R. Pelliccioni, M. andVillari, Evaluation of the influence of aircraft shielding on the aircrew exposure through an aircraft mathematical model, *Radiation Protection Dosimetry*, *108 (2)*, 91–105, 2004.

Fisk, L. A., and W. I. Axford, Solar modulation of galactic cosmic rays, 1, *Journal of Geophysical Research (1896-1977)*, *74*(21), 4973–4986, doi:10.1029/JA074i021p04973, 1969.

Flowers, P. a. T. a. L. a. R. R., S. B. andDonald Carpenetti, A. E. andEmad El-Giar, D. Frantz, P. H. andJennifer Look, G. K. andCarol Martinez andTroy Milliken, V. Moravec, and J. P. andThomas Sorensen andAllison Soult, *Chemistry*, OpenStax, Rice University,Houston, Texas, 2018.

Forbush, S. E., On World-Wide Changes in Cosmic-Ray Intensity, *Physical Review*, *54*(12), 975–988, doi:10.1103/PhysRev.54.975, 1938.

Forbush, S. E., Three unusual cosmic-ray increases possibly due to charged particles from the Sun, *Physical Review Letters*, *70*, 71, 1946.

Foullon, C., D. Heynderickx, and N. Crosby, Toward interplanetary space weather: Strategies for manned missions to mars, *Space Weather*, *3*(7), doi:10.1029/2004SW000134, 2005.

Frederiksen, *Gamma Spectroscopy, the Cs-137 source*, Frederiksen, Viaduktvej 35,Denmark, 2017.

Fuchs, W., Simple recommendations on how to avoid radiation harm, *Western Electrician*, *12*, 1896.

Gaisser, T. K., R. Engel, and E. Resconi, *Cosmic Rays and Particle Physics*, 2016.

Galvin, A. B., et al., Solar Wind Composition: First Results from SOHO and Future Expectations, in *American Astronomical Society Meeting Abstracts #188*, *American Astronomical Society Meeting Abstracts*, vol. 188, p. 49.05, 1996.

Geiger, H., and W. Müller, Electron counting tube for the measurement of the weakest radioactivities, *Sciences*, *16*, 617–618, 1928.

Gerdung, S., P. Pihet, J. E. Grindborg, H. Roos, U. J. Schrewe, and H. Schuhmacher, Operation and Application of Tissue Equivalent Proportional Counters, *Radiation Protection Dosimetry*, *61*(4), 381–404, doi:10.1093/oxfordjournals.rpd.a082805, 1995.

Ghelfi, A., D. Maurin, A. Cheminet, L. Derome, G. Hubert, and F. Melot, Neutron monitors and muon detectors for solar modulation studies: 2. ϕ time series, *Advances in Space Research*, *60*(4), 833–847, doi:10.1016/j.asr.2016.06.027, 2017.

Gibson, S. E., and B. C. Low, A Time-Dependent Three-Dimensional Magnetohydrodynamic Model of the Coronal Mass Ejection, *Astrophysical Journal*, *493*(1), 460–473, doi:10.1086/305107, 1998.

Gieseler, J., B. Heber, and K. Herbst, An empirical modification of the force field approach to describe the modulation of galactic cosmic rays close to earth in a broad range of rigidities, *Journal of Geophysical Research (Space Physics)*, *122*(11), 10,964–10,979, doi:10.1002/2017JA024763, 2017.

Gleeson, L., and G. Webb, Energy changes of cosmic rays in the interplanetary region, *Astrophysics and Space Science*, *58*, 21–39, doi:10.1007/BF00645373, 1978.

Gleeson, L. J., and W. I. Axford, Cosmic Rays in the Interplanetary Medium, *Astrophysical Journal Letters*, *149*, L115, doi:10.1086/180070, 1967.

Gleeson, L. J., and W. I. Axford, Solar Modulation of Galactic Cosmic Rays, *Astrophysical Journal*, *154*, 1011, doi:10.1086/149822, 1968a.

Gleeson, L. J., and W. I. Axford, The Compton-Getting Effect, *Astrophysics and Space Science*, 1968b.

Gleeson, L. J., and I. H. Urch, A study of the force-field equation for the propagation of galactic cosmic rays, *Astrophysics and Space Science*, *25(2)*, 387–404, 1973.

Gordovskyy, M., P. Browning, and R. F. Pinto, Combining MHD and kinetic modelling of solar flares, *Advances in Space Research*, *63*(4), 1453–1465, doi:10.1016/j.asr.2018.09.024, 2019.

Gratton, G., *Initial Airworthiness: Determining the Acceptability of New Airborne Systems*, pp. 15–32, Springer International Publishing, Cham, doi:10.1007/978-3-319-11409-5_2, 2015.

Grechnev, V., A. Kochanov, A. Uralov, V. Slemzin, D. Rodkin, F. Goryaev, V. Kiselev, and I. Myshyakov, Development of a fast cme and properties of a related interplanetary transient, *Solar Physics*, *294*, 139, doi:10.1007/s11207-019-1529-0, 2019.

Grieder, P. K. F., *Cosmic rays at earth: Researcher's reference, manual and data book*, Elsevier, Amsterdam, 2001.

Guo, J., R. F. Wimmer-Schweingruber, Y. Wang, M. Grande, D. Matthiä, C. Zeitlin, B. Ehresmann, and D. M. Hassler, The Pivot Energy of Solar Energetic Particles Affecting the Martian Surface Radiation Environment, *Astrophysical Journal Letters*, *883*(1), L12, doi:10.3847/2041-8213/ab3ec2, 2019.

Gusev, I. A., A. K. Guskova, and F. A. Mettler, *Medical management of radiation accidents, 2nd edition*, New York: CRC, 2001.

Hada, M., and B. M. Sutherland, Spectrum of complex dna damages depends on the incident radiation, *Radiation Research*, *165*(2), 223–230, 2006.

Hale, G. E., On the Probable Existence of a Magnetic Field in Sun-Spots, *Astrophysical Journal*, *28*, 315, doi:10.1086/141602, 1908.

Halley, E., An account of the cause of the change of the variation of the magnetic needle, with an hypothesis of the structure of the internal parts of the earth, *Philosophical Transactions of the Royal Society*, *17*, 563–578, doi:https://doi.org/10.1098/rstl.1686.0107, 1692.

Hands, A. D. P., K. A. Ryden, and C. J. Mertens, The disappearance of the pfotzer-regener maximum in dose equivalent measurements in the stratosphere, *Space Weather*, *14*(10), 776–785, doi:10.1002/2016SW001402, 2016b.

Hands, A. D. P., K. A. Ryden, N. P. Meredith, S. A. Glauert, and R. B. Horne, Radiation effects on satellites during extreme space weather events, *Space Weather*, *16*(9), 1216–1226, doi:10.1029/2018SW001913, 2018.

Hanslmeier, A., *The sun and space weather*, Dordrecht ; Boston : Kluwer Academic Publishers, includes bibliographical references (p. 223-237), 2002.

Hapgood, M., The great storm of may 1921: An exemplar of a dangerous space weather event, *Space Weather*, *17*(7), 950–975, doi:10.1029/2019SW002195, 2019.

Harkness-Brennan, L., Radiation interactions with matter, in *An Introduction to the Physics of Nuclear Medicine*, 2053-2571, pp. 5–1 to 5–10, Morgan and Claypool Publishers, doi:10.1088/978-1-6432-7034-0ch5, 2018.

Hassler, D. M., C. Zeitlin, B. Ehresmann, R. F. Wimmer-Schweingruber, J. Guo, D. Matthiä, S. Rafkin, T. Berger, and G. Reitz, Space weather on the surface of mars: Impact of the september 2017 events, *Space Weather*, *16*(11), 1702–1708, doi:10.1029/2018SW001959, 2018.

Hasson, B. F., D. Yeung, and J. Palta, *Bragg Peak*, pp. 63–64, Springer Berlin Heidelberg, Berlin, Heidelberg, doi:10.1007/978-3-540-85516-3_657, 2013.

Hathaway, D. H., The Solar Cycle, *Living Reviews in Solar Physics*, *7*(1), 2010.

Hathaway, D. H., and S. T. Suess, Solar cycle 23, in *The heliosphere through the solar activity cycle*, edited by A. Balogh, L. J. Lanzerotti, and S. T. Suess, pp. 21–39, Springer-Praxis, Chichester, UK, 2008.

Heber, B., et al., Mini neutron monitor measurements at the Neumayer III station and on the German research vessel Polarstern, in *Journal of Physics Conference Series*, *Journal of Physics Conference Series*, vol. 632, p. 012057, doi:10.1088/1742-6596/632/1/012057, 2015.

Held, P., R. Teucher, G. Klingelhoefer, J. Foh, H. Jaeger, and E. Kankeleit, A Mössbauer Spectrometer for the Mineralogical Analysis of the Mars Surface: First Temperature Dependent Tests of the Detector and Drive System, in *Lunar and Planetary Science Conference*, Lunar and Planetary Science Conference, p. 633, 1993.

Hellweg, C., and C. Baumstark-Khan, Getting ready for the manned mission to mars: The astronauts' risk from space radiation, *Die Naturwissenschaften*, *94*, 517–26, doi:10.1007/s00114-006-0204-0, 2007.

Herbst, K., A. Kopp, B. Heber, H. Steinhilber, H. Fichtner, K. Scherer, and D. Matthiä, On the importance of the local interstellar spectrum for the solar modulation parameter, *Journal of Geophysical Research*, *115*, doi:doi:10.1029/2009JD012557, 2010.

Hess, V., On the observations of the penetrating radiation during seven balloon flights, 2018.

Hess, V. F., Über Beobachtungen der durchdringenden Strahlung bei sieben Freiballonfahrten, *Zeitschrift für Physik*, *13*, 1084–1091, 1912.

Hodgson, R., On a curious Appearance seen in the Sun, *Monthly Notices of the Royal Astronomical Society*, *20*(1), 15–16, doi:10.1093/mnras/20.1.15a, 1859.

Hoyt, D., and K. Schatten, Group sunspot numbers: A new solar activity reconstruction, *Solar Physics*, *181*, 491–491, doi:10.1023/A:1005056326158, 1998.

Hubbell, J., Electron–positron pair production by photons: A historical overview, *Radiation Physics and Chemistry*, *75*(6), 614–623, doi:https://doi.org/10.1016/j.radphyschem.2005.10.008, pair Production, 2006.

Hudson, H. S., Global Properties of Solar Flares, *Space Science Reviews*, *158*(1), 5–41, doi:10.1007/s11214-010-9721-4, 2011.

Hunter, J. D., Matplotlib: A 2D graphics environment, *Computing in Science and Engineering*, *9*(3), 90–95, doi:10.1109/MCSE.2007.55, 2007.

Huttunen, K. E. J., R. Schwenn, V. Bothmer, and H. E. J. Koskinen, Properties and geoeffectiveness of magnetic clouds in the rising, maximum and early declining phases of solar cycle 23, *Annales Geophysicae*, *23*, 625–641, doi:10.5194/angeo-23-625-2005, 2005.

ICRP103, The 2007 Recommendations of the International Commission on Radiological Protection, *Annals of the ICRP*, *37*, 2–4, 2007.

ICRP123, Assessment of Radiation Exposure of Astronauts in Space, *Annals of the ICRP*, *42*(4), 2013.

ICRP132, Radiological protection from cosmic radiation in aviation, *Annals of the ICRP*, *45*(1), 2016.

ICRP26, Recommendations of the ICRP, *Annals of the ICRP*, *1*(3), 1977.

ICRP60, 1990 Recommendations of the International Commission on Radiological Protection, *Annals of the ICRP*, *21*, 1–3, 1991.

ICRP75, General principles for the radiation protection of workers, *Annals of the ICRP*, *27*(1), 1997.

Isenberg, P. A., and J. R. Jokipii, Gradient and curvature drifts in magnetic fields with arbitrary spatial variation., *Astrophysical Journal*, *234*, 746–752, doi:10.1086/157551, 1979.

Iskakov, B. A., M. Khabargeldina, T. K. Sadykov, K. Tastanova, and Y. M. Tautayev, Studies of EAS in the Tien-Shan high-mountain scientific station, *Journal of Physics: Conference Series*, *1337*, 012,004, doi:10.1088/1742-6596/1337/1/012004, 2019.

Jokipii, J. R., E. H. Levy, and W. B. Hubbard, Effects of particle drift on cosmic-ray transport. I. General properties, application to solar modulation., *Astrophysical Journal*, *213*, 861–868, doi:10.1086/155218, 1977.

Jones, F. C., and D. C. Ellison, The plasma physics of shock acceleration, *Space Science Reviews*, *58*(1), 259–346, doi:10.1007/BF01206003, 1991.

José Blanco, J., et al., ORCA: Future Antarctic Cosmic Ray Observatory, in *EGU General Assembly Conference Abstracts*, EGU General Assembly Conference Abstracts, p. 9583, 2018.

Khatry, J., J. Nieminen, J. Smith, and K. Slotten, 10 we radioisotope thermophotovoltaic (rtpv) power source demonstration, 2017.

Kim, H., M. Jeong, Y. S. Kim, J. Ha, and S. Cho, Effect of temperature on silicon pin photodiode radiation detectors, *Journal - Korean Physical Society*, *64*, doi:10.3938/jkps.64.651, 2014.

Kimigis, S., *van Allen, James Alfred*, pp. 2208–2210, Springer New York, New York, NY, doi:10.1007/978-1-4419-9917-7_1409, 2014.

Klein, L. W., and L. F. Burlaga, Interplanetary magnetic clouds at 1 au, *Journal of Geophysical Research (Space Physics)*, *87*(A2), 613–624, doi:10.1029/JA087iA02p00613, 1982.

Knipp, D. J., Essential science for understanding risks from radiation for airline passengers and crews, *Space Weather*, *15*(4), 549–552, doi:10.1002/2017SW001639, 2017.

Knoll, G., *Radiation Detection and Measurement*, Wiley, 2010.

Knoll, G. F., *Radiation Detection and Measurement; 3rd edition*, Wiley, New York, NY, 2000.

Kontomaris, S. V., A. Malamou, G. Balogiannis, and N. Antonopoulou, A simplified approach for presenting the differences between ionising and non-ionising electromagnetic radiation, *Physics Education*, *55*(2), 025,007, doi:10.1088/1361-6552/ab5c00, 2019.

Koskinen, H. E., Physics of space storms: From the solar surface to the earth, *Environmental Sciences*, 2011.

Kóta, J., and J. R. Jokipii, Effects of drift on the transport of cosmic rays. VI - A three-dimensional model including diffusion, *Astrophysical Journal*, *265*, 573–581, doi:10.1086/160701, 1983.

Koyama, K., R. Petre, E. V. Gotthelf, U. Hwang, M. Matsuura, M. Ozaki, and S. S. Holt, Evidence for shock acceleration of high-energy electrons in the supernova remnant SN1006, *Nature*, *378*, 255–258, doi:10.1038/378255a0, 1995.

Krainev, M., Manifestations of Two Branches of Solar Activity in the Heliosphere and GCR Intensity, *Solar-Terrestrial Physics*, *5*(4), 10–20, doi:10.12737/stp-54201902, 2019.

Krause, E. H., High altitude research with v-2 rockets, *Proceedings of the American Philosophical Society*, *91*(5), 430–446, 1947.

Krüger, H., A calibration neutron monitor for long-term cosmic ray modulation studies, Ph.D. thesis, PhD. thesis, Potchefstroom Campus of the North-West University, South Africa, 2006.

Krüger, H., and H. Moraal, A calibration neutron monitor: Statistical accuracy and environmental sensitivity, *Advances in Space Research*, *46*(11), 1394 – 1399, doi:https://doi.org/10.1016/j.asr.2010.07.008, 2010.

Krüger, H., and H. Moraal, Neutron monitor calibrations: progress report, in *Journal of Physics Conference Series*, *Journal of Physics Conference Series*, vol. 409, p. 012171, doi:10.1088/1742-6596/409/1/012171, 2013.

Krüger, H., H. Moraal, and G. Benadé, Mini Neutron Monitors, in *International Cosmic Ray Conference*, *International Cosmic Ray Conference*, vol. 33, p. 3666, 2013.

Krüger, H., H. Moraal, R. Nel, H. G. Krüger, and M. O'Kennedy, The mini neutron monitor programme, in *34th International Cosmic Ray Conference (ICRC2015)*, *International Cosmic Ray Conference*, vol. 34, p. 223, 2015.

Krüger, P., H. Krüger, H. Krüger, C. Diedericks, and D. Malan, New, affordable, open-hardware neutron monitor electronics, *Proceeding of science*, *ICRC2017*, 054, doi:10.22323/1.301.0054, 2018.

Krymskii, G. F., A regular mechanism for the acceleration of charged particles on the front of a shock wave, *Soviet Physics Doklady*, *22*, 327, 1977.

Kubančák, J., I. Ambrožová, R. Bütikofer, K. Kudela, R. Langer, M. Davídková, O. Ploc, and A. Malušek, Liulin silicon semiconductor spectrometers as cosmic ray monitors at the high mountain observatories jungfraujoch and lomnický štít, *Journal of Instrumentation*, *9*(07), P07,018–P07,018, doi:10.1088/1748-0221/9/07/p07018, 2014.

Kühl, P., N. Dresing, B. Heber, and A. Klassen, Solar Energetic Particle Events with Protons Above 500 MeV Between 1995 and 2015 Measured with SOHO/EPHIN, *Solar Physics*, *292*(1), 10, doi:10.1007/s11207-016-1033-8, 2017.

Labrenz, J., Radiation field in low earth orbit : Measurements from matroshka dostel onboard iss, Ph.D. thesis, 2014.

Labrenz, J., S. Burmeister, T. Berger, B. Heber, and G. Reitz, Matroshka DOSTEL measurements onboard the International Space Station (ISS), *Journal of Space Weather and Space Climate*, *5*, A38, doi:10.1051/swsc/2015039, 2015.

Lange, I., and S. E. Forbush, Note on the effect on Cosmic-Ray intensity of the magnetic storm of march 1, 1942, *Terrestrial Magnetism and Atmospheric Electricity*, *47*(2), 185–186, doi:10.1029/TE047i002p00185, 1942.

Lantos, P., Radiation doses potentially received on-board aeroplanes during recent solar particle events, *Radiation Protection Dosimetry*, *118*(4), 363–374, doi:10.1093/rpd/nci356, 2005.

Lara, A., and R. A. Caballero-Lopez, Observations with the Mini Neutron Monitor at Sierra Negra, Mexico, in *35th International Cosmic Ray Conference (ICRC2017)*, *International Cosmic Ray Conference*, vol. 301, p. 129, 2017.

Lara, A., A. Borgazzi, and R. Caballero-Lopez, Altitude survey of the galactic cosmic ray flux with a Mini Neutron Monitor, *Advances in Space Research*, *58*(7), 1441–1451, doi: 10.1016/j.asr.2016.06.021, 2016.

Leo, W. R., *Techniques for Nuclear and Particle Physics Experiments: A How-to Approach*, Springer-Verlag, 1987.

L'Heureux, J., C. Y. Fan, and P. Meyer, The Quiet-Tiem Spectra of Cosmic-Ray Electrons of Energies Between 10 and 200 MeV Observed on OGO-5, *Astrophysical Journal*, *171*, 363, doi:10.1086/151287, 1972.

Lockwood, J., W. Webber, and H. Debrunner, Differences in the maximum intensities and the intensity-time profiles of cosmic rays in alternate solar magnetic field polarities, *Journal of Geophysical Research*, *106*, 10,635–10,644, doi:10.1029/2000JA000307, 2001.

Lockwood, J. A., Forbush Decreases in the Cosmic Radiation, *Space Science Reviews*, *12*(5), 658–715, doi:10.1007/BF00173346, 1971.

MacQueen, R. M., J. A. Eddy, J. T. Gosling, E. Hildner, R. H. Munro, J. Newkirk, G. A., A. I. Poland , and C. L. Ross, The Outer Solar Corona as Observed from Skylab: Preliminary Results, *Astrophysical Journal Letters*, *187*, L85, doi:10.1086/181402, 1974.

Manchester, W., E. K. J. Kilpua, Y. D. Liu, N. Lugaz, P. Riley, T. Török, and B. Vršnak, The Physical Processes of CME/ICME Evolution, *Space Science Reviews*, *212*(3-4), 1159–1219, doi:10.1007/s11214-017-0394-0, 2017.

Mann, I. R., S. Di Pippo, H. J. Opgenoorth, M. Kuznetsova, and D. J. Kendall, International Collaboration Within the United Nations Committee on the Peaceful Uses of Outer Space: Framework for International Space Weather Services (2018-2030), *Space Weather*, *16*(5), 428–433, doi:10.1029/2018SW001815, 2018.

Maurin, D., F. Melot, and R. Taillet, A database of charged cosmic rays, *Astronomy and Astrophysics*, *569*, A32, doi:10.1051/0004-6361/201321344, 2014.

Miller, J. A., Particle Acceleration in Impulsive Solar Flares, *Space Science Reviews*, *86*, 79–105, doi:10.1023/A:1005066209536, 1998.

Mishev, A., S. Poluianov, and I. Usoskin, Assessment of spectral and angular characteristics of sub-GLE events using the global neutron monitor network, *Journal of Space Weather and Space Climate*, *7*, A28, doi:10.1051/swsc/2017026, 2017.

Mishev, A., S. Tuohino, and I. Usoskin, Neutron monitor count rate increase as a proxy for dose rate assessment at aviation altitudes during GLEs, *Journal of Space Weather and Space Climate*, *8*, A46, doi:10.1051/swsc/2018032, 2018.

Mishev, A. L., and I. G. Usoskin, Assessment of the radiation environment at commercial Jet-Flight altitudes during gle 72 on 10 september 2017 using neutron monitor data, *Space Weather*, *16*(12), 1921–1929, doi:10.1029/2018SW001946, 2018.

Mishev, A. L., I. G. Usoskin, and G. A. Kovaltsov, Neutron monitor yield function: New improved computations, *Journal of Geophysical Research (Space Physics)*, *118*(6), 2783–2788, doi:10.1002/jgra.50325, 2013.

Mishev, A. L., I. Usoskin, S. Tuohino, and A. Ibragimov, The upgraded GLE database includes assessment of radiation exposure at flight altitudes, *Journal of Physics: Conference Series*, *1181*, 012,061, doi:10.1088/1742-6596/1181/1/012061, 2019.

Möller, T., Measurement of the radiation exposure for high altitude flights in the polar region, Ph.D. thesis, 2013.

Moore, R., and D. Rabin, Sunspots, *Annual review of astronomy and astrophysics*, *23*, 239–266, doi:10.1146/annurev.aa.23.090185.001323, 1985.

Moraal, H., Cosmic-ray modulation equations, *Space Science Reviews*, *176*, 299–319, 2011.

Moraal, H., and P. H. Stoker, Long-term neutron monitor observations and the 2009 cosmic ray maximum, *Journal of Geophysical Research (Space Physics)*, *115*(A12), doi:10.1029/2010JA015413, 2010.

Moraal, H., P. H. Stoker, and J. J. Henning, Cosmic Ray Modulation at Neutron Monitor Energies Using the Force-Field Solution, in *International Cosmic Ray Conference*, *International Cosmic Ray Conference*, vol. 2, p. 694, 1973.

Moraal, H., M. S. Potgieter, P. H. Stoker, and A. J. van der Walt, Neutron monitor latitude survey of cosmic ray intensity during the 1986/1987 solar minimum, *Journal of Geophysical Research (Space Physics)*, *94*(A2), 1459–1464, doi:10.1029/JA094iA02p01459, 1989.

Moraal, H., A. Belov, and J. M. Clem, Design and co-Ordination of Multi-Station International Neutron Monitor Networks, *Space Science Reviews*, *93*, 285–303, doi:10.1023/A:1026504814360, 2000.

Mosotho, M. G., R. D. Strauss, R. R. Nndanganeni, and J. van den Berg, The north-west university's high altitude radiation monitor programme, *South African Journal of Science*, *117*(1/2), doi:10.17159/sajs.2021/7561, 2021.

Nam, U., et al., Calibration of TEPC for CubeSat Experiment to Measure Space Radiation, *Journal of Astronomy and Space Sciences*, *32*, 145–149, doi:10.5140/JASS.2015.32.2.145, 2015.

National Research Council, *Health Risks from Exposure to Low Levels of Ionizing Radiation: BEIR VII Phase 2*, The National Academies Press, Washington, DC, doi:10.17226/11340, 2006.

Neuhaeuser, R., and D. L. Neuhaeuser, Sunspot numbers based on historic records in the 1610s - early telescopic observations by simon marius and others, 2016.

Nicoll, K. A., and R. G. Harrison, Detection of lower tropospheric responses to solar energetic particles at midlatitudes, *Physical Review Letters*, *112*, 225,001, 2014.

Nymmik, R., M. Panasyuk, T. Pervaja, and A. Suslov, A model of galactic cosmic ray fluxes, *International Journal of Radiation Applications and Instrumentation. Part D. Nuclear Tracks and Radiation Measurements*, *20*(3), 427 – 429, doi:https://doi.org/10.1016/1359-0189(92)90028-T, special Section Galactic Cosmic Radiation: Constraints on Space Exploration, 1992.

O'Gallagher, J. J., and J. A. Simpson, The Heliocentric Intensity Gradients of Cosmic-Ray Protons and Helium during Minimum Solar Modulation, *Astrophysical Journal*, *147*, 819, doi:10.1086/149064, 1967.

Oh, S., Y. Yi, and P. Evenson, Influence of solar wind structure on cosmic ray modulation during epochs of alternate solar magnetic polarity, *Physics of Plasmas*, *25*(10), 102902, doi:10.1063/1.5049599, 2018.

O′Neill, P. M., BO'11 GCR Model Delivery - 20 September 2012, personal communication to Badhwar-O'Neill model users.

O′Neill, P. M., Badhwar-O′Neill 2010 galactic cosmic ray flux model-Revised, *IEEE Transactions on Nuclear Science*, *57(6)*, 3148–3153, 2010.

Oppenheimer, J. R., and M. S. Plesset, On the production of the positive electron, *Phys. Rev.*, *44*, 53–55, doi:10.1103/PhysRev.44.53.2, 1933.

Pacini, D., La radiazione penetrante alla superficie ed in seno alle acque, *Il Nuovo Cimento*, *3*(1), 93–100, doi:10.1007/BF02957440, 1912.

Parker, E. N., The Formation of Sunspots from the Solar Toroidal Field., *Astrophysical Journal*, *121*, 491, doi:10.1086/146010, 1955.

Parker, E. N., Cosmic-ray modulation by solar wind, *Physical Review*, *110*, 1445–1449, doi:10.1103/PhysRev.110.1445, 1958a.

Parker, E. N., Dynamical instability in an anisotropic ionized gas of low density, *Physical Review*, *109*, 1874–1876, doi:10.1103/PhysRev.109.1874, 1958b.

Parker, E. N., Dynamics of the interplanetary gas and magnetic fields, *Astrophysical Journal*, *128*, 664–676, 1958c.

Parker, E. N., *Interplanetary dynamical processes.*, 1963.

Parker, E. N., The passage of energetic charged particles through interplanetary space, *Planetary and Space Science*, *13*, 9–49, 1965.

Perko, J. S., Solar modulation of galactic antiprotons, *Astronomy and Astrophysics*, *184*, 119–121, 1987.

Perlow, G. J., Cosmic ray measurements in rockets, *Scientific Monthly*, *69*(6), 382–385, 1949.

Pfotzer, G., Dreifachkoinzidenzen der Ultrastrahlung aus vertikaler Richtung in der StratosphÄre, *Zeitschrift für Physik*, *102*(1-2), 41–58, doi:10.1007/BF01336830, 1936.

Poluianov, S., I. Usoskin, A. Mishev, H. Moraal, H. Kruger, G. Casasanta, R. Traversi, and R. Udisti, Mini Neutron Monitors at Concordia Research Station, Central Antarctica, *Journal of Astronomy and Space Sciences*, *32*(4), 281–287, doi:10.5140/JASS.2015.32.4.281, 2015.

Poluianov, S. V., I. G. Usoskin, A. L. Mishev, M. A. Shea, and D. F. Smart, GLE and Sub-GLE Redefinition in the Light of High-Altitude Polar Neutron Monitors, *Solar Physics*, *292*(11), 176, doi:10.1007/s11207-017-1202-4, 2017.

Pont, B., et al., REXUS-25 rocket flight of a cubesat cosmic-ray detector, in *36th International Cosmic Ray Conference (ICRC2019) - CRD - Cosmic Ray Direct*, 2019.

Porter, J. A., L. W. Townsend, H. Spence, M. Golightly, N. Schwadron, J. Kasper, A. W. Case, J. B. Blake, and C. Zeitlin, Radiation environment at the moon: Comparisons of transport code modeling and measurements from the crater instrument, *Space Weather*, *12*(6), 329–336, doi:10.1002/2013SW000994, 2014.

Potgieter, M. S., and S. E. S. Ferreira, Modulation of cosmic rays in the heliosphere over 11 and 22 year cycles: a modelling perspective, *Advances in Space Research*, *27*(3), 481 – 492, doi:https://doi.org/10.1016/S0273-1177(01)00080-1, 2001.

Pyle, K. R., Neutron Monitor Sensitivity to Solar Modulation Changes: Altitude vs. Cutoff Rigidity, in *International Cosmic Ray Conference*, *International Cosmic Ray Conference*, vol. 2, p. 197, 1997.

Quenby, J. J., The Theory of Cosmic-Ray Modulation, *Space Science Reviews*, *37*(3-4), 201–267, doi:10.1007/BF00226364, 1984.

Reames, D. V., Particle acceleration at the Sun and in the heliosphere, *Space Science Reviews*, *90*, 413–491, doi:10.1023/A:1005105831781, 1999.

Regener, E., New Results in Cosmic Ray Measurements, *Nature*, *132*(3340), 696–698, doi:10.1038/132696a0, 1933.

Regener, E., and G. Pfotzer, Intensity of the Cosmic Ultra-Radiation in the Stratosphere with the Tube-Counter, *Nature*, *134*(3383), 325, doi:10.1038/134325b0, 1934.

Richardson, I. G., and H. V. Cane, Near-Earth Interplanetary Coronal Mass Ejections During Solar Cycle 23 (1996 - 2009): Catalog and Summary of Properties, *Solar Physics*, *264*(1), 189–237, doi:10.1007/s11207-010-9568-6, 2010.

Ritter, B., The mobile dosimetric telescope : a small active dosimeter for the application in space; development, calibration and measurements, Ph.D. thesis, 2013.

Rossi, B., Interaction between Cosmic Rays and Matter, *Nature*, *132*(3326), 173–174, doi:10.1038/132173b0, 1933.

Rossi, H. H., and W. Rosenzweig, A device for the measurement of dose as a function of specific ionization, *Radiology*, *64*(3), 404–411, doi:10.1148/64.3.404, pMID: 14372080, 1955.

Rossi, H. H., and M. Zaider, Microdosimetry and its applications, *European Journal of Radiology*, *25*, 162–164, 1997.

Santiago, A., A. Lara, O. Enríquez-Rivera, and R. A. Caballero-Lopez, New method to calculate the time variation of the force field parameter, *Journal of Geophysical Research (Space Physics)*, *123*(3), 1731–1737, doi:10.1002/2017JA024914, 2018.

Sarkar, R., S. K. Chakrabarti, P. S. Pal, D. Bhowmick, and A. Bhattacharya, Measurement of secondary cosmic ray intensity at Regener-Pfotzer height using low-cost weather balloons and its correlation with solar activity, *Advances in Space Research*, *60*(5), 991–998, doi:10.1016/j.asr.2017.05.014, 2017.

Sato, T., Analytical model for estimating the zenith angle dependence of terrestrial cosmic ray fluxes, *PLoS ONE*, *11(8):e0160390*, doi:doi:10.1371/journal.pone.0160390, 2016.

Schein, M., W. P. Jesse, and E. O. Wollan, The nature of the primary cosmic radiation and the origin of the mesotron, *Physical Review*, *59*, 615–615, doi:10.1103/PhysRev.59.615, 1941.

Schlaepfer, H., Cosmic rays, *Spatium, International Space Science Institute*, *11*, 2003.

Schwabe, H., Sonnenbeobachtungen im Jahre 1843. Von Herrn Hofrath Schwabe in Dessau, *Astronomische Nachrichten*, *21*(15), 233, doi:10.1002/asna.18440211505, 1844.

Schwadron, N. A., M. Owens, and N. U. Crooker, The Heliospheric Magnetic Field over the Hale Cycle, *Astrophysics and Space Sciences Transactions*, *4*(1), 19–26, doi:10.5194/astra-4-19-2008, 2008.

Seedhouse, E., *Space radiation and astronaut safety*, Springerbriefs in space development, Springer, Cham, doi:10.1007/978-3-319-74615-9, 2018.

Shafer, Y. G., and A. V. Yarygin, Measurements of cosmic rays on geophysical rockets, *Planetary and Space Science*, *8*(3), 165 – 166, doi:https://doi.org/10.1016/0032-0633(61)90261-6, 1961.

Shea, M., and D. Smart, Vertical cutoff rigidities for cosmic ray stations since 1955, *Proceedings of the 27th International Cosmic Ray Conference.*, *10*, 4063, 2001.

Shea, M. A., and D. F. Smart, A Summary of Major Solar Proton Events, *Solar Physics*, *127*(2), 297–320, doi:10.1007/BF00152170, 1990.

Simpson, J. A., Elemental and isotopic composition of the galactic cosmic rays, *Annual Review of Nuclear and Particle Science*, *33*(1), 323–382, doi:10.1146/annurev.ns.33.120183.001543, 1983.

Simpson, J. A., Astrophysical Phenomena Discovered by Cosmic Ray and Solar Flare Ground Level Events: The Early Years, in *International Cosmic Ray Conference*, *International Cosmic Ray Conference*, vol. 12, p. 187, 1990.

Simpson, J. A., The cosmic ray nucleonic component: the invention and scientific uses of the neutron monitor (Keynote Lecture), *Space Science Reviews*, *93*, 11–32, 2000.

Sinky, H. M., Improvements of the Bethe stopping power theory and their application to problems involving radiation in the environment, Ph.D. thesis, Portland State University, 2005.

Smart, a. M., D.F., The limitations of using vertical cutoff rigidities determined from the igrf magnetic field models for computing aircraft radiation dose, *Advances in Space Research*, *32(1)*, 95–102, doi:DOI:10.1016/S0273-1177(03)00501-5, 2003.

Smart, D., and M. Shea, A review of geomagnetic cutoff rigidities for earth-orbiting spacecraft, *Advances in Space Research*, *36*(10), 2012–2020, doi:https://doi.org/10.1016/j.asr.2004.09.015, solar Wind-Magnetosphere-Ionosphere Dynamics and Radiation Models, 2005.

Solanki, S. K., Sunspots: An overview, *Astronomy and Astrophysics Review*, *11*(2), 153–286, 2003.

Spence, H., et al., Crater: The cosmic ray telescope for the effects of radiation experiment on the lunar reconnaissance orbiter mission, *Space Science Reviews*, *150*, 243–284, doi:10.1007/s11214-009-9584-8, 2010.

Srour, J. R., and J. M. McGarrity, Radiation effects on microelectronics in space, *Proceedings of the IEEE*, *76*(11), 1443–1469, doi:10.1109/5.90114, 1988.

Stern, D. P., A brief history of magnetospheric physics during the space age, *Reviews of Geophysics*, *34*(1), 1–32, doi:10.1029/95RG03508, 1996.

Sternheimer, R., M. Berger, and S. Seltzer, Density effect for the ionization loss of charged particles in various substances, *Atomic Data and Nuclear Data Tables*, *30*(2), 261 – 271, doi:https://doi.org/10.1016/0092-640X(84)90002-0, 1984.

Stewart, F. A., et al., ICRP Publication 118: ICRP Statement on Tissue Reactions and Early and Late Effects of Radiation in Normal Tissues and Organs - Threshold Doses for Tissue Reactions in a Radiation Protection Context, *Annals of the ICRP*, *41*(1-2), 1–322, doi:10.1016/j.icrp.2012.02.001, 2012.

Stoker, P. H., B. C. Raubenheimer, and A. J. van der Walt, Anomalous Longterm Modulation of Cosmic Rays during the present Solar Cycle., in *12th International Cosmic Ray Conference (ICRC12), Volume 3*, *International Cosmic Ray Conference*, vol. 3, p. 870, 1971.

Stone, E. C., A. C. Cummings, F. B. McDonald, B. C. Heikkila, N. Lal, and W. R. Webber, Voyager 1 observes low-energy galactic cosmic rays in a region depleted of heliospheric ions, *Science*, *341*(6142), 150–153, doi:10.1126/science.1236408, 2013.

Störmer, C., *The polar aurora*, Oxford University Press, 1955.

Strauss, D., et al., The mini-neutron monitor: A new approach in neutron monitor design, *arXiv e-prints*, arXiv:2007.14711, 2020.

Sullivan, J., Geometric factor and directional response of single and multi-element particle telescopes, *Nuclear Instruments and Methods*, *95*(1), 5 – 11, doi:https://doi.org/10.1016/0029-554X(71)90033-4, 1971.

Tanimori, T., et al., Discovery of t[CLC]e[/CLC]v gamma rays from SN 1006: Further evidence for the supernova remnant origin of cosmic rays, *Astrophysical Journal*, *497*(1), L25–L28, doi:10.1086/311267, 1998.

Tomassetti, N., Solar and nuclear physics uncertainties in cosmic-ray propagation, *Physical Review D*, *96*(10), 103005, doi:10.1103/PhysRevD.96.103005, 2017.

Tousey, R., The solar corona., in *Space Research Conference*, vol. 2, pp. 713–730, 1973.

Tuohino, S., A. Ibragimov, I. Usoskin, and A. Mishev, Upgrade of GLE database: Assessment of effective dose rate at flight altitude, *Advances in Space Research*, *62*(2), 398–407, doi:10.1016/j.asr.2018.04.021, 2018.

Tylka, A. J., and W. F. Dietrich, *Ground-Level Enhanced (GLE) Solar Particle Events at Solar Minimum*, *Astronomical Society of the Pacific Conference Series*, vol. 428, p. 329, 2010.

Usoskin, I., S. Poluianov, H. Moraal, H. Krüger, G. Casasanta, R. Traversi, and R. Udisty, A mini neutron monitor in Central Antarctica (Dome Concordia), in *34th International Cosmic Ray Conference (ICRC2015)*, *International Cosmic Ray Conference*, vol. 34, p. 217, 2015.

Usoskin, I. G., A history of solar activity over millennia, *Living Reviews in Solar Physics*, *14*(1614-4961), 2017.

Usoskin, I. G., K. Alanko-Huotari, G. A. Kovaltsov, and K. Mursula, Heliospheric modulation of cosmic rays: Monthly reconstruction for 1951-2004, *Journal of Geophysical Research (Space Physics)*, *110*(A12), A12108, doi:10.1029/2005JA011250, 2005.

Usoskin, I. G., G. A. Bazilevskaya, and G. A. Kovaltsov, Solar modulation parameter for cosmic rays since 1936 reconstructed from ground-based neutron monitors and ionization chambers, *Journal of Geophysical Research (Space Physics)*, *116*(A2), A02104, doi:10.1029/2010JA016105, 2011.

Usoskin, I. G., A. Gil, G. A. Kovaltsov, A. L. Mishev, and V. V. Mikhailov, Heliospheric modulation of cosmic rays during the neutron monitor era: Calibration using pamela data for 2006–2010, *Journal of Geophysical Research (Space Physics)*, *122*(4), 3875–3887, doi:10.1002/2016JA023819, 2017.

Vainio, R., O. Raukunen, A. J. Tylka, W. F. Dietrich, and A. Afanasiev, Why is solar cycle 24 an inefficient producer of high-energy particle events?, *Astronomy and Astrophysics*, *604*, A47, doi:10.1051/0004-6361/201730547, 2017.

van Allen, J. A., G. H. LUDWIG, E. C. RAY, and C. E. McILWAIN, Observation of high intensity radiation by satellites 1958 alpha and gamma, *Journal of Jet Propulsion*, *28*(9), 588–592, doi:10.2514/8.7396, 1958.

van Allen, J. A., C. E. McIlwain, and G. H. Ludwig, Radiation Observations with Satellite 1958∈, *Journal of Geophysical Research*, *64*(3), 271–286, doi:10.1029/JZ064i003p00271, 1959a.

van Allen, J. A., C. E. McIlwain, and G. H. Ludwig, Satellite Observations of Electrons Artificially Injected into the Geomagnetic Field, *Journal of Geophysical Research*, *64*(8), 877–891, doi:10.1029/JZ064i008p00877, 1959b.

Van der Plas, G., G. Gielen, and W. Sansen, *A Computer-Aided Design and Synthesis Environment for Analog Integrated Circuits*, The Springer International Series in Engineering and Computer Science, Springer US, 2006.

Vaquero, J. M., Historical sunspot observations: A review, *Advances in Space Research*, *40*(7), 929 – 941, doi:https://doi.org/10.1016/j.asr.2007.01.087, 2007.

Verigin, M. I., and W. I. Axford, Konstantin gringauz 1918-1993: Approach to scientific biography, *Physics and Chemistry of the Earth, Part C: Solar, Terrestrial and Planetary Science*, *25*(1), 3–8, doi:https://doi.org/10.1016/S1464-1917(99)00025-2, International Symposium on Space Plasma Studies by in-situ and remote Measurements, 2000.

von Ehrenfried, M. D., *Stratonauts: Pioneers Venturing into the Stratosphere*, pp. 1–3, Springer International Publishing, Cham, doi:10.1007/978-3-319-02901-6_1, 2014.

Vos, E. E., and M. S. Potgieter, New modeling of galactic proton modulation during the minimum of solar cycle 23/24, *Astrophysical Journal*, *815*(2), 119, doi:10.1088/0004-637x/815/2/119, 2015.

Waldmeier, M., Neue Eigenschaften der Sonnenfleckenkurve, *Astronomische Mitteilungen der Eidgenössischen Sternwarte Zürich*, *14*, 105–136, 1935.

Waldmeier, M., Die Zonenwanderung der Sonnenflecken, *Astronomische Mitteilungen der Eidgenössischen Sternwarte Zürich*, *14*, 470–481, 1939.

Walske, M. C., The Stopping Power of K-Electrons, *Physical Review*, *88*(6), 1283–1289, doi:10.1103/PhysRev.88.1283, 1952.

Walske, M. C., Stopping Power of L-Electrons, *Physical Review*, *101*(3), 940–944, doi:10.1103/PhysRev.101.940, 1956.

Walter, M., and A. W. Wolfendale, Early history of cosmic particle physics, *European Journal of Physics H*, *H37*, 323–358, doi:10.1140/epjh/e2012-30020-1, 2012.

Weaver, B., and A. Westphal, Energy loss of relativistic heavy ions in matter, *Nuclear Instruments and Methods in Physics Research Section B: Beam Interactions with Materials and Atoms*, *187*(3), 285 – 301, doi:https://doi.org/10.1016/S0168-583X(01)01143-0, 2002.

Webb, D. F., and T. A. Howard, Coronal Mass Ejections: Observations, *Living Reviews in Solar Physics*, *9*(1), 3, doi:10.12942/lrsp-2012-3, 2012.

Webber, W. R., and F. B. McDonald, Recent voyager 1 data indicate that on 25 august 2012 at a distance of 121.7 au from the sun, sudden and unprecedented intensity changes were observed in anomalous and galactic cosmic rays, *Geophysical Research Letters*, *40*(9), 1665–1668, doi:10.1002/grl.50383, 2013.

Wittmann, A., and Xu Zhentao, A catalogue of sunspot observations from 165 BC to AD 1684, *Vistas in Astronomy*, *31*, 127, doi:https://doi.org/10.1016/0083-6656(88)90189-4, 1988.

Wolf, Abstract of his latest Results, *Monthly Notices of the Royal Astronomical Society*, *21*(3), 77–78, doi:10.1093/mnras/21.3.77, 1861.

Wolf, R., Sonnenflecken beobachtungen in der zweiten hälfte des jahres 1849, *Mittheilungen der Naturforschenden Gesellschaft in Bern*, *1*, 167–168, 1850.

Wolf, R., Mittheilungen über die Sonnenflecken, *Astronomische Mitteilungen der Eidgenössischen Sternwarte Zürich*, *1*, 3–13, 1856.

Wrixon, A. D., New ICRP recommendations, *Journal of Radiological Protection*, *28*(2), 161–168, doi:10.1088/0952-4746/28/2/r02, 2008.

Wüest, M., D. S. Evans, and R. von Steiger, *Calibration of Particle Instruments in Space Physics*, 2007.

Wurz, P., Solarwind Composition, in *The Dynamic Sun: Challenges for Theory and Observations*, *ESA Special Publication*, vol. 11, p. 44.1, 2005.

Yang, Z., and R. Sheu, Effects of flight route variation and great-circle approximation on aviation dose assessment for popular flights from taiwan, *Radiation protection dosimetry*, *184*, doi:10.1093/rpd/ncy186, 2018.

Yaniv, R., Y. Yair, C. Price, K. Nicoll, G. Harrison, A. Artamonov, and I. Usoskin, Balloon measurements of the vertical ionization profile over southern Israel and comparison to mid-latitude observations, *Journal of Atmospheric and Solar-Terrestrial Physics*, *149*, 87 – 92, doi:https://doi.org/10.1016/j.jastp.2016.10.003, 2016.

Zabori, B., A. Gerecs, A. Hurtonyne Gyovai, D. Benyei, F. Naczi, and T. Hurtony, REM-RED Cosmic Radiation Monitoring Experiment On-Board the REXUS-17 Sounding Rocket, in *22nd ESA Symposium on European Rocket and Balloon Programmes and Related Research*, *ESA Special Publication*, vol. 730, edited by L. Ouwehand, p. 539, 2015.

Zábori, B., A. Hirn, S. Deme, I. Apáthy, and T. Pázmándi, Characterization of cosmic rays and direction dependence in the Polar Region up to 88 km altitude, *Journal of Space Weather and Space Climate*, *6*, A12, doi:10.1051/swsc/2016006, 2016.

Zeitlin, C., et al., Measurements of galactic cosmic ray shielding with the crater instrument, *Space Weather*, *11*(5), 284–296, doi:10.1002/swe.20043, 2013.

Zheng, Y., et al., Space radiation and plasma effects on satellites and aviation: Quantities and metrics for tracking performance of space weather environment models, *Space Weather*, *17*(10), 1384–1403, doi:10.1029/2018SW002042, 2019.

Zhu, C. Z., Q. Yuan, and D. Wei, Studies on Cosmic-Ray Nuclei with Voyager, ACE, and AMS-02. I. Local Interstellar Spectra and Solar Modulation, *Astrophysical Journal*, p. 863:119, 2018.

Zirkle, R. E., D. F. Marchbank, and K. D. Kuck, Exponential and sigmoid survival curves resulting from alpha and x irradiation of aspergillus spores, *Journal of Cellular and Comparative Physiology*, *39*(S1), 75–85, doi:10.1002/jcp.1030390408, 1952.

Zyla, P., et al., Review of Particle Physics, *PTEP*, *2020*(8), 083C01, doi:10.1093/ptep/ptaa104, 2020.